

I. Shape Selectivity of Small-pore Molecular Sieves for the Methanol-to-Olefins Reaction
And
II. Synthesis and Topotactic Transformation of Germanosilicate CIT-13

Thesis by
Jong Hun Kang

In Partial Fulfillment of the Requirements for the degree of
Doctor of Philosophy

The logo for the California Institute of Technology (Caltech), featuring the word "Caltech" in a bold, orange, sans-serif font.

CALIFORNIA INSTITUTE OF TECHNOLOGY
Pasadena, California

2019
(Defended 22 May 2019)

© 2019

Jong Hun Kang
ORCID: 0000-0002-4197-9070

All Rights Reserved Except Where Otherwise Noted

ACKNOWLEDGEMENTS

I would first and foremost like to thank to Professor Mark E. Davis for all of his guidance, critical ideas, and deep insights during my 5 years at Caltech. The Countless hours of discussions with him were always full of scientific inspirations and heart-stirring motivations for further research. He has heedfully taken care of all aspects of my academic career. It was a lifetime honor for me to have him as my PhD advisor. I could grow in all aspect of my life in his research group.

I also thank to my thesis committee members, Professor Richard C. Flagan, Professor George R. Rossman, and Dr. Stacey I. Zones from Chevron. I am greatly thankful to Dr. Zones for his valuable insights, helpful suggestions, and critical comments for my research based on his unrivaled experiences in the chemical industry. I am thankful to all collaborators including Professor Lynne B. McCusker, Dr. Stef Smeets, and great scientists from Chevron including Dr. Dan Xie and Dr. Cong-Yan Chen for valuable discussions and help. I would like to thank to Dr. Dan Xie for his helps and advice in crystallographic analyses and solutions for structures.

I want to express my gratitude to Dr. Sonjong Hwang, Dr. Chi Ma and Dr. David VandeVelde for their assistances in collecting data which were indispensable for this thesis. I express my sincere appreciation to Dr. Hwang not only for a number of teachings and scientific discussions regarding solid-state NMR but also for his mentoring and encouragements which let me stand up again and again every time I faced hardship. I also thank to other Caltech staffs including Kathy, Martha, Suresh, Nate, Daniel, and Laura.

Studying in the Davis group and interacting with group members who are the brightest young scholars in the world were great privileges for me. I would like to thank all of the former and current group members: Mark, Josh, Joel, Andrew, Dorothy, John, Marat,

Lucy, Kramer, Emily, Steven, Ben, Michiel, Raimund, Dana, Matt, Viktor, Marcella, and Faisal. I especially express my appreciation to Joel and Michiel for passing on highly refined techniques to synthesize zeolites and molecular sieves which are the most important skills in this field of study. I would also like to thank to Yasho and Mark who provided their shoulders on which I have stood. I also thank to Professor Suk Bong Hong from Postech and Professor Hyunjoo Lee from KAIST for their warm welcomes as Davis group alumni when I visited Korea.

I am also grateful to Professor Chong Rae Park at Seoul National University, Professor Seung Jae Yang from Inha University, and Dr. Taehoon Kim at KIMS for their help and guidance when I was working at Gwanak Campus. Professor Park who served as my M.S. thesis advisor not only taught me knowledge in the classroom, but also offered a unique perspective to see things which have been invaluable in academia. I also want to say thank you to Dr. Jakyu Chun and Jun Young Park from the Department of Materials Science and Engineering for their kind encouragements during my PhD years.

I am also thankful to all of my former comrades in arms including Colonel Wonjae Lee from the Republic of Korea Army. Colonel Lee who was my immediate superior when I was serving my country as a lieutenant, and was one of the very people who recommended me to consider Caltech as the next place to study engineering. I'm also very grateful to other members in my company, who has kept in touch with me even after my honorable discharge for their ceaseless encouragements. I also want to express my acknowledgements to my 101 R.O.T.C. brothers.

I would like to thank to the Samsung Scholarship for full financial support for 5 years of my PhD at Caltech and great opportunities to meet many other scholarship recipients who are among the brightest young researchers in the country. Networking with such people at a single place was an invaluable experience for me.

Finally I express my deepest love and gratitude to my family who wholeheartedly supported me across the largest ocean. My parents are my happiness and my love, and my

brothers are my pride and my hope, and they will be. I show my greatest gratitude to them for their perennial love with all my heart.

ABSTRACT

This thesis presents research results from two projects involving molecular sieves. These investigations concern their synthesis, characterization and use as heterogeneous catalysis

In part I, the shape selectivity in the methanol-to-olefins (MTO) reaction is studied, and a new molecular sieve structure – MTO reaction selectivity relationship is developed. 17 zeolites and 13 phosphate-based molecular sieves having 14 selected cage-type/small-pore topologies (CHA, AFX, SFW, LEV, ERI, DDR, AEI, RTH, ITE, SAV, LTA, RHO, KFI, and UFI) are synthesized. The MTO reaction is performed using these catalysts at the same reaction conditions.

The reaction results lead to the conclusion that the molecular sieve cage topology is the most important structural factor that primarily determines the olefin product distribution. For example, AEI and CHA are synthesized with four different elemental compositions (zeolite, SAPO, CoAPO, MgAPO). Regardless of differences in elemental compositions, very similar product distribution patterns are observed in each of the isostructural groups of molecular sieves. Additionally, other isostructural pairs of SAPOs and zeolites show similar product distributions.

The reaction results from 14 topologies are grouped into four categories. Category I consists of CHA, AFX, SFW, and other GME-related topologies. Catalysts having these topologies show ethylene-to-propylene ratios close to one. Category II is a group of ERI and LEV which generate more ethylene than propylene. Category III is a group of DDR, AEI, RTH, ITE, and SAV which shows propylene selectivities higher than those of ethylene. Category IV is a group of LTA, RHO, KFI, and UFI which possess LTA-cages. These types of catalysts give high butylene selectivities.

The concept of cage-defining ring and its size is introduced as a reliable geometric indicator on the basis of a hypothetical ellipsoid cage model. The cage-defining ring size can be easily calculated from crystallographic information which is available online. A strong correlation is found between the cage-defining ring sizes and the four categories of reaction behavior.

In part II, an extra-large-pore germanosilicate molecular sieve CIT-13 with 14- and 10-ring pores is synthesized using monoquaternary, methylbenzylimidazolium-derivative OSDAs, and the synthesis conditions are optimized. Fluoride-free synthetic pathways for pure germanosilicate CIT-13 and isomorphous aluminum substitution in synthesis of aluminogermanosilicate CIT-13 are also described. The nature of disorder in the arrangement within CIT-13 framework is discussed, and its physicochemical properties compared to a UTL-type germanosilicate IM-12.

A comprehensive network of topotactic transformation and postsynthetic modification pathways starting from germanosilicate CIT-13 (Ge-CIT-13) is described. The moisture-mediated transformation of Ge-CIT-13 into another extra-large-pore CFI-type germanosilicate (Ge-CIT-5) is discovered, and the role of sorbed water in the transformation kinetics studied. The resultant Ge-CIT-5 is the first germanosilicate molecular sieve having a CFI topology, and the corresponding transformation is also the first inter-germanosilicate transformation occurring at room temperature. The microporosity of Ge-CIT-5 matched well with the reference pure-silica CIT-5 synthesized using the sparteine-type OSDA.

The acid-delamination processes of Ge-CIT-13 and Ge-CIT-5 are investigated. Ge-CIT-13 can be transformed into two new frameworks, CIT-14 with 12- and 8-ring pores and CIT-15 with 10-ring pores, on the basis of an ADOR-type topotactic transformation. The inverse sigma transformation of Ge-CIT-13 directly into CIT-14 is also firstly described. The conventional acid-delamination of Ge-CIT-13 does not yield Ge-CIT-5. However, the CIT-15-type material is obtained via the base-delamination pathway from Ge-CIT-5. The postsynthetic alumination of Ge-CIT-13 and Ge-CIT-5 is also achievable.

PUBLISHED CONTENT AND CONTRIBUTIONS

- (1) Jong Hun Kang, Faisal H. Alshafei, Stacey I. Zones, Mark E. Davis, Cage-defining Ring: A New Molecular Sieve Structural Indicator for Light Olefin Product Distribution from the Methanol-to-Olefins Reaction, *ACS Catalysis* **2019**, DOI: 10.1021/acscatal.9b00746.

J.H.K. and M.E.D. designed the research; J.H.K. performed the synthetic experimental research and materials characterizations; J.H.K. and F.H.S. analyzed the reaction products; All authors wrote the paper.

- (2) Jong Hun Kang, Raimund Walter, Dan Xie, Tracy Davis, Cong-Yan Chen, Mark E. Davis, Stacey I. Zones, Further Studies on How the Nature of Zeolite Cavities That are Bounded by Small Pores Influences the Conversion of Methanol to Light Olefins, *ChemPhysChem*, **2018**, 19, 412, DOI: 10.1002/cphc.201701197.

J.H.K., M.E.D., and S.I.Z. designed research; J.H.K., R.W., D.X., T.D., C-Y.C, and S.I.Z. performed experimental research; J.H.K., M.E.D., and S.I.Z. developed the core idea based on the results and wrote the paper.

- (3) Michiel Dusselier, Jong Hun Kang, Dan Xie, Mark E. Davis, CIT-9: a fault-free, gmelinite zeolite, *Angewandte Chemie International Edition*, **2017**, 56, 13475, DOI: 10.1002/anie.201707452.

M.D. and M.E.D. designed the research; M.D. and J.H.K. performed the experimental research; D.X. conducted the computational work and the temperature-variable crystallographic characterization; M.D., J.H.K., and M.E.D. wrote the paper.

- (4) Jong Hun Kang, Dan Xie, Stacey I. Zones, Stef Smeets, Lynne B. McCusker, Mark E. Davis, Synthesis and Characterization of CIT-13, the First Molecular To Possess Pores Bounded 14- and 10-Membered Rings, *Chemistry of Materials*, **2016**, 28, 6250, DOI: 10.1021/acs.chemmater.6b02468.

All authors designed the research; J.H.K. performed the synthetic experiments and characterizations; D.X., S.S., and L.B.M. conducted the crystallographic analyses including the synchrotron X-ray diffraction refinement and disorder analyses; J.H.K., S.S., L.B.M., and M.E.D. wrote the paper.

- (5) Ben W. Boal, Michael W. Deem, Dan Xie, Jong Hun Kang, Mark E. Davis, Stacey I. Zones, Synthesis of Germanosilicate Molecular Sieves from Mono- and Di-Quaternary Ammonium OSDAs Constructed from Benzyl Imidazolium Derivatives; Stabilization of Large Micropore Volumes Including New Molecular Sieve CIT-13, *Chemistry of Materials*, **2016**, 28, 2158, DOI: 10.1021/acs.chemmater.6b00031.

B.W.B. designed the research and drafted the paper; M.W.D. performed the computational work; D.X. conducted the rotational electron diffraction experiment; B.W.B. and J.H.K. conducted the experimental research; All authors wrote the paper.

TABLE OF CONTENTS

ACKNOWLEDGEMENTS.....	iii
ABSTRACT	vi
PUBLISHED CONTENT AND CONTRIBUTIONS.....	viii
TABLE OF CONTENTS.....	x
LIST OF FIGURES	xvii
LIST OF TABLES	xxxiv
Part I. Shape Selectivity of Small-pore Molecular Sieves for the Methanol-to-Olefins Reaction.....	1
Chapter 1. Introduction to Part I: The Methanol-to-Olefins (MTO) Reaction and Small-Pore Microporous Materials.....	2
1.1. Background	2
1.1.1. Small-pore Molecular Sieves	5
1.1.2. Mechanism of MTO Reaction.....	9
1.2. Motivation	11

1.3. Objectives	13
Chapter 2. Small-pore Molecular Sieves and MTO Reaction	15
2.1. Introduction	15
2.2. Experimental	18
2.2.1. Synthesis of Organic Structure-Directing Agents	18
2.2.2. Synthesis of Microporous Materials	22
2.2.3. Characterization of Microporous Materials	32
2.2.4. MTO Reaction	33
2.3. Result and Discussion	34
2.3.1. Materials Characterization.....	34
2.3.2. MTO Reaction Results	42
2.4. Summary	53
Chapter 3. Categorization of Topologies based on Product Distributions and Cage-Defining Rings	54
3.1. Introduction	54
3.2. Categorization of Topologies.....	56
3.2.1. Ethylene-to-Propylene Ratio	56
3.2.2. Butylene Selectivity.....	66

3.2.3. Initial Propane Selectivity.....	69
3.3. Concept of Cage-Defining Ring	71
3.3.1. Basic Idea and Development of Concept	71
3.3.2. Selection of Cage-Defining Rings and Four Categories.....	73
3.4. Summary	76
Chapter 4. Summary and Future Work for Part I.....	79
4.1. Overall Summary and Conclusion.....	79
4.2. Proposed Future Work	82
Part II. Synthesis and Topotactic Transformation of Germanosilicate CIT-13.....	87
Chapter 5. Introduction to Part II: Extra-large-pore Molecular Sieves and Germanosilicates.....	88
5.1. Background	88
5.1.1. Extra-large-pore Molecular Sieves.....	89
5.1.2. Germanosilicates.....	91
5.2. Motivation	94
5.3. Objectives.....	95
Chapter 6. Synthesis and Characterization of CIT-13	97

6.1. Introduction	97
6.2. Experimental	99
6.2.1. Synthesis of OSDAs	99
6.3. Results and Discussion.....	105
6.3.1. Effects of Synthetic Parameters.....	105
6.3.1.1. Germanosilicate System in Fluoride Media	105
6.3.1.2. Aluminogermanosilicate System in Fluoride Media.....	113
6.3.1.3. Germanosilicate System in Hydroxide Media.....	114
6.3.2. Structural Disorder within CIT-13	116
6.3.3. Comparison to Relative Germanosilicates	119
6.4. Summary	122
Chapter 7. Transformation from CIT-13 to CIT-5.....	124
7.1. Introduction	124
7.2. Experimental	126
7.2.1. Preparation of Parent Ge-CIT-13	126
7.2.2. Transformation of Ge-CIT-13 to Ge-CIT-5.....	127
7.2.3. Preparation of Reference Sparteine-CIT-5.....	127
7.2.4. Preparation of IM-12, JLG-18, and ITQ-22.....	128

7.2.5. Characterization	130
7.3. Results and Discussion.....	130
7.3.1. Rate of Transformation.....	130
7.3.2. Role of Sorbed Water within Pore System	136
7.3.3. Characterization of Resultant Ge-CIT-5	143
7.3.4. Comparison to Related Germanosilicate.....	150
7.4. Summary	154
Chapter 8. Topotactic Transformation and Postsynthetic Modification of CIT-13 and CIT-5	156
8.1. Introduction	156
8.2. Experimental	158
8.2.1. Preparation of Parent Materials	158
8.2.2. Hydrolytic Delamination of Weak Acid and Base	158
8.2.3. Alkoxysilylational Pillaring.....	158
8.2.4. Inverse Sigma Transformation	159
8.2.5. Direct Condensation of CIT-13P.....	159
8.2.6. Degermanation and Alumination	159
8.2.7. Characterization	160

8.3. Results and Discussion.....	160
8.3.1. Effects of Initial Germanosilicate Structure on Delamination	160
8.3.2. CIT-14 Formation by Ethoxysilylational Pillaring and Inverse Sigma Transformation	166
8.3.2.1. Ethoxysilylational Pillaring.....	166
8.3.2.2. Inverse Sigma Transformation.....	170
8.3.3. CIT-15 Formation by Direct Condensation	177
8.3.4. Effects of Solution Acidity on Alumination	183
8.3.4.1. Postsynthetic Degermanation and Alumination of Ge-CIT-13.....	183
8.3.4.2. Postsynthetic Degermanation and Alumination of Ge-CIT-5.....	188
8.4. Summary	191
Chapter 9. Summary and Future Work for Part II.....	193
9.1. Overall Summary and Conclusion.....	193
9.2. Proposed Future Work	195
REFERENCES.....	197
Appendix A. Supplementary Information for Part I	220
Appendix B. Supplementary Information for Part II	235

LIST OF FIGURES

- Figure 1.1. Overview of the MTO process. (a) Schematic description of the process. (b) UOP/INEOS MTO process with UOP/Total OCP process. Reproduced with Permission from Ref [8]. Copyright 2012 Wiley-VCH. (c) DICP DMTO process (d) DMTO commercial unit operating in Dalian, Jilin Province, PR China. Reproduced with Permission from Ref [13]. Copyright 2015 American Chemical Society. 4
- Figure 1.2. Schematic description of simplified structures of neutral frameworks and Brønsted acid sites composed of various elemental compositions. CHA cages having corresponding elemental compositions and acid sites. 6
- Figure 1.3. Examples of large-, medium-, and small-pore frameworks and their pore opening dimensions. 8
- Figure 1.4. Proposed mechanisms of the MTO reaction. (a) The original hydrocarbon pool mechanism suggested by Dahl and Kolboe. Reproduced with Permission from Ref [27]. Copyright 1994 Elsevier. (b) The aromatic cycles showing the paring mechanism and side-chain mechanism by Lesthaeghe et al. on ZSM-5. Reproduced with Permission from Ref [31]. Copyright 2009 Wiley-VCH. (c) Dual cycle concept. Reproduced with Permission from Ref [8]. Copyright 2012 Wiley-VCH. 10
- Figure 1.5. Dependence of hydrocarbon pool intermediate structures on cage structures. (a) Hydrocarbon pool carbenium cations which were formed in different topologies of cages. Reproduced with Permission from Ref [13]. Copyright 2015 American Chemical Society (b) Hydrocarbon pool mechanism suggested for DNL-6 having a RHO topology. Reproduced with Permission from Ref [36]. Copyright 2014 Elsevier. 11
- Figure 1.6. Schematic illustration of MTO reaction within a SAPO-34 cage and the main question to answer. 14

Figure 2.1. Selection of topologies.....	18
Figure 2.2. Reactions schemes for the OSDAs used to prepare the molecular sieve catalysts demonstrated in this work: (a) 1,1'-(hexane-1,6-diyl)bis(1,4-diazabicyclo[2.2.2]octanium), (b) N-methylquinuclidinium, (c) N,N'-dimethyl-1,4-diazabicyclo[2.2.2]octanium, (d) N,N-dimethylpiperidinium, (e) 1,2,3,4,5-pentamethylimidazolium, and (f) 1,2-dimethyl-3-(4-methylbenzyl)imidazolium...21	21
Figure 2.3. OSDAs and cage structures of the corresponding resultant AlPO ₄ -based molecular sieves.	27
Figure 2.4. OSDAs and cage structures of the corresponding resultant zeolites.....	32
Figure 2.5. PXRD profiles of as-prepared (a) SSZ-13, (b) SAPO-34, (c) CoAPO-34, and (d) MgAPO-34. SEM images of (e) SSZ-13, (f) SAPO-34, (g) CoAPO-34, and (h) MgAPO-34.	35
Figure 2.6. PXRD profiles of (a) SSZ-99, (b) SSZ-104, (c) SSZ-105, and (d) SSZ-27. SEM images of (e) SSZ-99, (f) SSZ-105, and (g) SSZ-27.....	36
Figure 2.7. PXRD profiles of as-prepared (a) high-silica SSZ-16, (b) SAPO-56, (c) SSZ-52, and (d) STA-18. SEM images of (e) high-silica SSZ-16, (f) low-silica SSZ-16, (g) SAPO-56, (h) SSZ-52, and (i) STA-18.	37
Figure 2.8. PXRD profiles of (a) Nu-3, (b) DMDABCO-LEV, (c) SAPO-35, and (d) SSZ-98. SEM images of (e) Nu-3, (f) DMDABCO-LEV, (g) SAPO-35, and (h) SSZ-98.	38
Figure 2.9. PXRD profiles of (a) SSZ-39, (b) SAPO-18, (c) CoAPO-18, and (d) MgAPO-18. SEM images of (e) SSZ-39, (f) SAPO-18, (g) CoAPO-18, and (h) MgAPO-18.....	39

Figure 2.10. PXRD profiles of (a) SSZ-28, (b) Zeolite RTH, (c) Zeolite ITE, and (d) STA-7. SEM images of (e) SSZ-28, (f) Zeolite RTH, (g) Zeolite ITE, and (h) STA-7(1)...	40
Figure 2.11. PXRD profiles of (a) Zeolite LTA, (b) SAPO-42, (c) Zeolite RHO, (d) DNL-6, (e) Zeolite KFI, (f) STA-14, and (g) UZM-5. SEM images of (h) Zeolite LTA, (i) SAPO-42, (j) Zeolite RHO, (k) DNL-6, (l) Zeolite KFI, (m) STA-14, and (n) UZM-5.	41
Figure 2.12. MTO-reaction time-on-stream profiles of (a) SSZ-13, (b) SAPO-34, (c) CoAPO-34, and (d) MgAPO-34.	44
Figure 2.13. MTO-reaction time-on-stream profiles of (a) high-silica SSZ-16, (b) low-silica SSZ-16, (c) SAPO-56, (d) SSZ-52, and (e) STA-18.	45
Figure 2.14. MTO-reaction time-on-stream profiles of (a) SSZ-99, (b) SSZ-104, and (c) SSZ-27.	46
Figure 2.15. MTO-reaction time-on-stream profiles of (a) Nu-3, (b) DMDABCO-LEV, (c) SAPO-35, (d) SSZ-98, and (e) SSZ-105.	48
Figure 2.16. MTO-reaction time-on-stream profiles of (a) SSZ-39, (b) SAPO-18, (c) CoAPO-18, and (d) MgAPO-18.	49
Figure 2.17. MTO-reaction time-on-stream profiles of (a) Zeolite RTH, (b) Zeolite ITE, (c) STA-7(1), and (d) STA-7(2).	51
Figure 2.18. MTO-reaction time-on-stream profiles of (a) Zeolite LTA, (b) SAPO-42, (c) Zeolite RHO, (d) DNL-6, (e) Zeolite KFI, (f) STA-14, and (g) UZM-5.	52
Figure 3.1. Schematic illustrations of 14 small-pore/cage topologies which were classified into four categories based on their olefin product distributions and the concept of the cage-defining ring.	55

- Figure 3.2. MTO product distributions when the methanol conversion is in the range of 98–100%: (a) four isostructural CHA-type molecular sieves, (b) two CHA-AFX-SFW series as SAPOs and zeolites, and (c) two CHA-related GME-intergrown ABC-6-type zeolites. The reactions are performed at $T = 400\text{ }^{\circ}\text{C}$ and $\text{WHSV}(\text{MeOH}) = 1.3\text{ h}^{-1}$ 59
- Figure 3.3. MTO product distributions when the methanol conversion is in the range of 98–100%. The selectivity data of SAPO-17 are reproductions of Wilson and Barger’s work⁴⁴ and are obtained at $T = 375$ and $425\text{ }^{\circ}\text{C}$. The other reactions are performed at $T = 400\text{ }^{\circ}\text{C}$ and $\text{WHSV}(\text{MeOH}) = 1.3\text{ h}^{-1}$ 62
- Figure 3.4. MTO product distributions when the methanol conversion is in the range of 98–100%: (a) four isostructural AEI-type molecular sieves, (b) three high-silica zeolites having DDR, RTH, and ITE-type topologies, and two SAPO materials having the SAV topology. The reactions are performed at $T = 400\text{ }^{\circ}\text{C}$ and $\text{WHSV}(\text{MeOH}) = 1.3\text{ h}^{-1}$ 64
- Figure 3.5. MTO product distributions of zeolites and SAPO-molecular sieves having LTA, RHO, KFI, and UFI-type topologies when the methanol conversion is in the range of 98–100%. The reactions are performed at $T = 400\text{ }^{\circ}\text{C}$ and $\text{WHSV}(\text{MeOH}) = 1.3\text{ h}^{-1}$ 66
- Figure 3.6. Suggested mechanistic pathways for the formation of butylenes. Z-H and Z⁻ refer to the zeolite Brønsted acid site and its conjugate base, respectively..... 68
- Figure 3.7. Ratios of light olefin selectivities (E; ethylene, P: propylene, B: butylenes) of all catalysts investigated in this work. All reactions are performed at $400\text{ }^{\circ}\text{C}$ and $\text{WHSV}(\text{MeOH}) = 1.3\text{ h}^{-1}$ 69
- Figure 3.8. Effects of heteroatom concentration (Al in zeolites, and Si in SAPOs) and topology on the initial propane selectivities (time on stream = 7–10 min) of catalysts:

(a) zeolites and (b) SAPOs. Some of the initial propane data points of SSZ-17 (Nu-3), ⁴¹ zeolite RTH, ⁴⁸ zeolite LTA, ⁶² zeolite RHO, ¹⁰⁶ SSZ-13, ⁶⁴ and SSZ-39 ⁶⁹ are reproduced from articles previously published by our research group.....	71
Figure 3.9. Determination of the cage-defining ring. (a) A hypothetical ellipsoidal model for the cage-defining ring and its size. (b) Selection of cage-defining ring from a CHA cage.	72
Figure 3.10. Correlation diagram between four categories of topologies and cage-defining ring sizes.	76
Figure 4.1. Possible correlation between the dual-cycle mechanistic concept and the cage-defining ring theory.	82
Figure 4.2. Cage structures, maximum sizes of sphere that can fit within cages, and cage-defining ring sizes of topologies SAT, SWY, and AVL.....	83
Figure 4.3. Inter-categorical transition induced by streaming of zeolites.....	85
Figure 5.1. Examples of extra-large-pore frameworks.....	89
Figure 5.2. Extra-large-pore germanosilicate ITQ-33 (ITT) possessing a 3-dimensional 18/10/10-ring channel system.....	91
Figure 5.3. The ADOR process of UTL-type germanosilicate producing two structurally related frameworks OKO and PCR. Reproduced with Permission from Ref [50]. Copyright 2014 Royal Society of Chemistry.	93
Figure 5.4. Schematic illustration of the full network of transformations of Ge-CIT-13 which will be discussed in Part II of my thesis.	95

- Figure 6.1. Brief graphic description of synthesis and structure of germanosilicate CIT-13. Reproduced with Permission from Ref [170]. Copyright 2014 American Chemical Society. 99
- Figure 6.2. Reactions schemes for the syntheses of the OSDAs used in this work and the structures of them: i. 1,2-dimethylimidazole, ii. 1-methylimidazole, iii. 3-methylbenzyl chloride, iv. 3,5-dimethylbenzyl bromide, 1. 1,2-dimethyl-3-(3-methylbenzyl)imidazolium, 2. 1,2-dimethyl-3-(3,5-dimethylbenzyl)imidazolium, 3. 1-methyl-3-(3-methylbenzyl)imidazolium, 4. 1-methyl-3-(3,5-dimethylbenzyl)imidazolium 101
- Figure 6.3. Reaction scheme for the synthesis of (6R,10S)-6,10-dimethyl-5-azaspiro[4.5]decanium. 101
- Figure 6.4. PXRD profiles of selected crystallization conditions which gave high-purity CIT-13: (a) reference condition, (b) Si/Ge = 3, (c) seeded, (d) $H_2O/T = 7.5$ where $T = Si + Ge$, (e) crystallization temperature 140 °C, (f) 150 °C, (g) 175 °C, and (h) OSDA 4. 107
- Figure 6.5. PXRD profiles of the samples crystallized from different Si/Ge ratios in the gel with (a) OSDA 1 and (b) OSDA 4 for gel compositions $x/(1+x) SiO_2 : 1/(1+x) GeO_2 : 0.5 ROH : 0.5 HF : 10 H_2O$. (x is the Si/Ge ratio of gels; Asterisks * denote impurity peaks.) (c) ^{13}C solid-state 8 k MAS NMR spectra (black) of as-made CIT-13 from OSDA 1 and OSDA 4, overlapped with the ^{13}C solution (in $CDCl_3$) NMR spectra (red) of the corresponding OSDAs. (d) TGA profiles of as-made CIT-13 samples from OSDA 1 and OSDA 4. 110
- Figure 6.6. (a) PXRD profiles of as-prepared CIT-13 using NH_4F (green) and HF (magenta) as the mineralizing fluoride sources. SEM images of CIT-13 resulting from the (b) HF and (c) NH_4F protocols. (d) TGA profiles of as-prepared CIT-13 using NH_4F

(green) and HF (magenta). (e) Ar adsorption and desorption isotherms (log-scale, 87.45 K) of calcined CIT-13 from NH_4F - (green) and HF-protocol (magenta). ... 112

Figure 6.7. Material characterization results of Al/Ge CIT-13. (a) The resultant phases of hydrothermal products ($T = 150\text{--}175\text{ }^\circ\text{C}$, for 1–4 weeks) denoted on a Si-Al-Ge ternary gel composition diagram. (b) PXRD pattern of Al/Ge-CIT-13. (c) 8 kHz MAS solid-state ^{29}Si NMR spectrum of Al/Ge-CIT-13. (d) 12 kHz MAS solid-state ^{27}Al NMR spectrum of Al/Ge-CIT-13. (e) SEM image of obtained Al/Ge-CIT-13 crystallites..... 114

Figure 6.8. (a) Examples of PXRD patterns of CIT-13/OH samples. (b) SEM images of selected CIT-13/OH samples. (d) 8 kHz MAS ^1H -decoupled ^{29}Si solid-state NMR spectra of CIT-13/OH(11) compared to that of CIT-13/F. (e) Argon adsorption isotherms (87.45 K) of CIT-13/OH(11) and a typical CIT-13/F. 116

Figure 6.9. The observed diffraction profile (blue), calculated profile (red), and difference between the two (black) for the Rietveld refinement of as-prepared CIT-13. 117

Figure 6.10. Schematic illustrations of possible disordered models for CIT-13. (a–b) Views along the y-axis showing two possibilities of the *cfi*-layers stacking mode: (a) ABAB and (b) AAAA. (c–d) Projections along the x-axis showing two possibilities of the *d4r* unit arrangements together with OSDA molecules within the interlayer region making (c) straight 10-ring channels and (d) tortuous 10-ring channels..... 119

Figure 6.11. Comparison between the crystal structures of CIT-13 and IM-12. (a) CIT-13 viewed along the [001] direction showing the 14-ring pore, and (b) along the [010] direction showing the 10-ring pore. (c) IM-12 viewed along the [001] direction showing the 14-ring pore, and (d) along the [010] direction showing the 12-ring pore. 121

Figure 6.12. Material characterization results of IM-12 and CIT-13. (a) ^1H -decoupled ^{29}Si solid-state 8 k NMR spectra of IM-12 and CIT-13. Ar adsorption and desorption isotherms at 87.45 K of IM-12 and CIT-13 in (b) linear and (c) log-scale.	122
Figure 7.1. Transformation from Ge-CIT-13 to Ge-CIT-5	126
Figure 7.2. Reaction scheme for the preparation of N-methylsparteinium OSDA.	128
Figure 7.3. Structures of OSDA used to synthesize germanosilicates.	130
Figure 7.4. Transformation of Ge-CIT-13/F (Si/Ge = 4.31) to Ge-CIT-5 over time observed on the basis of PXRD patterns in 2-theta scanning ranges of (a) 4–30° and (b) 5–9°	132
Figure 7.5. Transformation of Ge-CIT-13/F (Si/Ge = 3.87) to Ge-CIT-5 over time observed on the basis of PXRD patterns in 2-theta scanning ranges of (a) 4–30° and (b) 5–9°	133
Figure 7.6. Transformation of Ge-CIT-13/F (Si/Ge = 6.38) to Ge-CIT-5 over time observed on the basis of PXRD patterns in 2-theta scanning ranges of (a) 4–30° and (b) 5–9°	134
Figure 7.7 Transformation of Ge-CIT-13/OH (Si/Ge = 4.33) to Ge-CIT-5 over time observed on the basis of PXRD patterns in 2-theta scanning ranges of (a) 4–30° and (b) 5–9°	135
Figure 7.8. Transformation of Ge-CIT-13/OH (Si/Ge = 3.88) to Ge-CIT-5 over time observed on the basis of PXRD patterns in 2-theta scanning ranges of (a) 4–30° and (b) 5–9°	136
Figure 7.9. Transformation from VPI-5 to $\text{AlPO}_4\text{-8}$	137

- Figure 7.10. Accelerated transformation of Ge-CIT-13/F (Si/Ge = 4.31) to Ge-CIT-5: (a) design of experiment, (b) PXRD patterns in 2-theta scanning ranges of (b) 4–30° and (c) 5–9° 138
- Figure 7.11. NMR spectra of hydrated Ge-CIT-13. (a) 8 kHz MAS ¹H-decoupled ²⁹Si solid-state NMR spectrum and ¹H-²⁹Si CP-MAS solid-state NMR spectrum of hydrated Ge-CIT-13/F[4.31] (II of Figure 7.10) and (b) 8 kHz MAS ¹H solid-state NMR spectra of sorbed water within Ge-CIT-5 produced by exposing Ge-CIT-13/F[4.31] to ambient humidity for 4 months (red, IV of Figure 7.10) and saturated water vapor for 2 days (black, II of Figure 7.10)..... 139
- Figure 7.12. Inhibited transformation of Ge-CIT-13/F (Si/Ge = 4.31) to Ge-CIT-5 by excluding moisture from the system by argon and cyclohexane (CH): (a) design of experiment, and PXRD patterns in 2-theta scanning ranges of (a) 4–30° and (b) 5–9° 141
- Figure 7.13. Structural change of Ge-CIT-13/F (Si/Ge = 4.49) at an elevated temperature (160 °C) over time observed on the basis of PXRD patterns in 2-theta scanning ranges of (a) 4–30° and (b) 5–9° 142
- Figure 7.14. Transformation from (a) Ge-CIT-13/F[4.28] and (b) Ge-CIT-13/OH[3.87] and the resultant Ge-CIT-5's on the basis of 8 kHz MAS ¹H-decoupled ²⁹Si solid-state NMR spectra..... 144
- Figure 7.15. NMR spectroscopy and transformation. (a) 8 kHz MAS ¹H-decoupled ²⁹Si solid-state NMR spectrum of the reference Spa-CIT-5. (b) Calculated ²⁹Si NMR spectra of theoretical pure-silica molecular sieves having CIT-13 and CIT-5 topologies. (100% Lorentzian, width = 5.08 ppm) (c) Frameworks of CIT-13 and CIT-5 seen from the 14-ring channel direction with T-atom labels. 145

Figure 7.16. Argon adsorption isotherms (87.45 K) of Ge-CIT-13/F[4.22] and the resultant Ge-CIT-5 compared to the reference Spa-CIT-5. ("↓" denotes the low-pressure adsorption of Ge-CIT-5)	148
Figure 7.17. The lattice models used to calculate lattice energies: (a) pure-silica *CTH and CFI, and (b) hypothetical germanosilicate (Si/Ge = 3) crystal models of *CTH and CFI whose <i>cfi</i> -layers are exclusively composed of pure silica and whose connecting units— <i>d4r</i> and <i>dzc</i> —are completely composed of germanium oxide.	149
Figure 7.18. Structures of germanosilicates consisting of Ge-rich <i>d4r</i> units and Si-rich layers.	150
Figure 7.19. Structural change of IM-12/OH (Si/Ge = 4.9) over time observed on the basis of PXRD patterns in 2-theta scanning ranges of (a) 4–30° and (b) 5–9°.	151
Figure 7.20. Structural change of JLG-18/F (Si/Ge = 1.9) over time observed on the basis of PXRD patterns in 2-theta scanning ranges of (a) 4–30° and (b) 6–10°.	152
Figure 7.21. Structural change of ITQ-22/OH (Si/Ge = 3.1) over time observed on the basis of PXRD patterns in 2-theta scanning ranges of (a) 4–30° and (b) 6–10°.	152
Figure 8.1. Overview of the network of topotactic transformations and postsynthetic modification pathways discussed in this chapter.	157
Figure 8.2. Schematic illustration of the acid- or ammonium-delamination of Ge-CIT-13 resulting in CIT-13P.	161
Figure 8.3. Typical ²⁹ Si solid-state NMR spectra of CIT-13P.	161
Figure 8.4. Kinetics of the acid-delamination of Ge-CIT-13 and Ge-CIT-5 (a) Design of experiment. PXRD patterns of (b) Parent Ge-CIT-13/F[4.33], (c) Ge-CIT-5, (d) a	

- series of CIT-13P/H samples acid-delaminated for x hours. (e) a series of CIT-5P/H samples acid-delaminated for x hours. (x = 3, 6, 12, 24)..... 163
- Figure 8.5. Time-dependent structural and compositional changes induced by acid-delamination. (a) Interlayer distances of CIT-13P/H/xHRs and CIT-5P/H/xHRs as functions of delamination time calculated from PXRD patterns shown in Figure 6.4(d–e). (b) Si/Ge molar ratios of CIT-13P/H/xHRs and CIT-5P/H/xHRs as functions of delamination time. 164
- Figure 8.6. NMR spectra and morphologies of acid-delaminated germanosilicates. (a) ^{29}Si solid-state NMR spectra of CIT-13P and CIT-5 originated from the same parent Ge-CIT-13/F. SEM images of (b) CIT-13P and (c) CIT-5P..... 165
- Figure 8.7. Pathway from CIT-13 to CIT-14 via the pillaring process. (a) Schematic illustration of the topotactic transformation from Ge-CIT-13 to CIT-14 by the ethoxysilylational pillaring. (b) Examples of alkoxyalkylsilane species which can be used as pillaring agents. (c) Intermediate stage of CIT-13 layers linked with bridging diethoxysilane..... 167
- Figure 8.8. Structure, pore sizes, and expected topological information of CIT-14. 167
- Figure 8.9. Influence of degree of delamination on the formation of CIT-14 (a) Design of experiment. PXRD patterns of the resultant CIT-14 samples in the range of (b) 4–40° and (d) 6–9° 168
- Figure 8.10. Material characterization of CIT-14/ESP. (a) Argon adsorption/desorption isotherm, (b) 8 kHz MAS ^1H -decoupled ^{29}Si solid-state NMR spectrum, and (c) SEM image of CIT-14/ESP/4..... 169
- Figure 8.11. Schematic illustration of the inverse sigma transformation from CIT-13 to CIT-14. 171

- Figure 8.12. Examples of the inverse sigma transformation from CIT-13/OH to CIT-14 examined on the basis of PXRD patterns in the range of (a) 4–30° and (b) 5–10° 172
- Figure 8.13. Trials of the inverse sigma transformation using a high-Ge CIT-13/F and a low-Ge CIT-13/OH examined on the basis of PXRD patterns in the range of (a) 4–30° and (b) 5–10° 172
- Figure 8.14. Silanol characterization after water-degermanation of germanosilicates. (a) ^1H - ^{29}Si CP-MAS NMR spectra of water-degermanated (WDG) ITQ-13, ITQ-22, and IM-12. Reproduced with Permission from Ref [176]. Copyright 2014 American Chemical Society. (b) ^1H - ^{29}Si CP-MAS NMR spectra of water-degermanated Ge-CIT-13/F, Ge-CIT-13/OH, and IM-12 samples having various Si/Ge ratios. WDG stands for ‘water-degermanated.’ 174
- Figure 8.15. 8 kHz MAS ^{29}Si NMR spectra and ^1H - ^{29}Si CP-MAS NMR spectra of the parent CIT-13/OH and the resultant CIT-14 produced via the inverse sigma transformation. 175
- Figure 8.16. Argon adsorption isotherms (87.45 K) of the parent CIT-13/OH, two CIT-14 products from the inverse sigma transformation and the ethoxysilylational pillaring in (a) linear scale and (b) log scale. 177
- Figure 8.17. Schematic illustration of the topotactic transformation from Ge-CIT-13 to CIT-15 by the direct condensation of CIT-13P..... 177
- Figure 8.18. Experimentally demonstrated topotactic transformation from Ge-CIT-13 to CIT-15 investigated on the basis of PXRD patterns. 178
- Figure 8.19. Structure, pore sizes, and expected topological information of CIT-15. 179

- Figure 8.20. Influence of degree of delamination of Ge-CIT-13 on the formation of CIT-15
(a) Design of experiment. PXRD patterns of the resultant CIT-15 samples in the range of (b) 4–40° and (c) 6–12°. 180
- Figure 8.21. Pathway from CIT-13 to CIT-15 and characterizations. (a) Schematic illustration of transformation from Ge-CIT-5 to CIT-15 via ammonium delamination. (b) PXRD patterns of intermediate and resultant products. 183
- Figure 8.22. Schematic illustration of postsynthetic degermanation/alumination of Ge-CIT-13 184
- Figure 8.23. Material characterization of Al-CIT-13 samples. (a) PXRD profiles of aluminated Al-CIT-13 samples and those of the parent Ge-CIT-13s. SEM images of (b) Al-CIT-13(1) and (c) Al-CIT-13(7) samples..... 185
- Figure 8.24. Al-site and defect characterizations of Al-CIT-13 samples. (a) 12 kHz MAS solid-state ^{27}Al NMR spectra of Al-CIT-13 samples. (b) 8 kHz MAS ^1H -decoupled solid-state ^{29}Si NMR spectrum and 8 kHz ^1H - ^{29}Si CP-MAS solid-state NMR spectrum of Al-CIT-13(3) sample. 186
- Figure 8.25. Catalysis of Al-CIT-13. (a) Conversions and yields of the decane hydrocracking/hydroisomerization reaction over Pt-CIT-13 catalyst by reaction temperatures. (b) Product distribution chart of the decane hydroisomerization of Pt-CIT-13. (c) Product distribution chart of the methanol to hydrocarbon reaction over Al-CIT-13 samples..... 187
- Figure 8.26. Schematic illustration of the CIT-13-to-5 transformation followed by the postsynthetic degermanation/alumination of Ge-CIT-13. 188
- Figure 8.27. Material characterization of Al-CIT-5 samples. (a) a series of PXRD patterns showing the entire transformation sequence: Ge-CIT-13 \rightarrow Ge-CIT-5 \rightarrow Al-CIT-5.

(b) PXRD patterns of resultant Al-CIT-5 samples and Si-CIT-5. (c) 12 kHz MAS solid-state ^{27}Al NMR spectrum of an Al-CIT-13 sample.	190
Figure A1. The cage visualizations, selection of the cage-defining rings, and their sizes for CHA and AFX.....	221
Figure A2. The cage visualizations, selection of the cage-defining rings, and their sizes for SFW, LEV, ERI, and DDR.....	222
Figure A3. The cage visualizations, selection of the cage-defining rings, and their sizes for AEI, RTH, ITE, and SAV.....	223
Figure A4. The cage visualizations, selection of the cage-defining rings, and their sizes for LTA, RHO, KFI, and UFI.....	224
Figure A5. Cage visualizations and tree ring plots of CHA, AFX, and SFW cages. (probe molecule radius (r_{probe}): black (1.80 Å), red (2 Å), orange (3 Å), green (4 Å), blue (5 Å)).....	226
Figure A6. Cage visualizations and tree ring plots of LEV and ERI cages. (probe molecule radius (r_{probe}): black (1.80 Å), red (2 Å), orange (3 Å), green (4 Å))	227
Figure A7. Cage visualizations and tree ring plots of DDR, AEI, RTH, and ITE cages. (probe molecule radius (r_{probe}): black (1.80 Å), red (2 Å), orange (3 Å), green (4 Å), blue (5 Å), purple (6 Å)).....	228
Figure A8. Cage visualizations and tree ring plots of SAV, and LTA cages of frameworks LTA, RHO and KFI. (probe molecule radius (r_{probe}): black (1.80 Å), red (2 Å), orange (3 Å), green (4 Å), blue (5 Å), purple (6 Å), cyan (7 Å), light-orange (8 Å))	229
Figure A9. Time-dependent behaviors of ethylene-to-propylene ratios during the MTO reactions over selected catalysts.	230

Figure A10. PXRD profiles of pristine and steamed zeolites having selected types of topologies.	231
Figure A.11. ^1H -decoupled ^{29}Si 8 k MAS solid-state NMR spectra of pristine and steamed zeolites having selected types of topologies.	232
Figure A12. ^1H -decoupled ^{27}Al 10 k MAS solid-state NMR spectra of pristine and steamed zeolites having selected types of topologies.	233
Figure A13. MTO time-on-stream selectivity chart of pristine and steamed zeolites having selected types of topologies.	234
Figure B1. The relation between the gel Si/Ge ratios and the product CIT-13 Si/Ge ratios, characterized using the EDS.	238
Figure B2. The effect of the Si/Ge ratio in the gel on the crystallization of CIT-13 (*: impurity; w: week).	239
Figure B3. The effect of water levels in the gel on the crystallization of CIT-13 (w: week).	240
Figure B4. The effect of the amount of OSDA in the gel on the crystallization of CIT-13 (*: impurity; w: week).	241
Figure B5. The effect of the crystallization temperature on the crystallization of CIT-13 (*: impurity; w: week).	242
Figure B6. SEM micrographs of CIT-13 crystallized at (A) 140°C, (B) 150°C, (C) 160°C and (D) 175°C.	243
Figure B7. SEM micrographs of CIT-13 crystals prepared by heating (A) in a rotating autoclave and (B) in a static autoclave.	243

- Figure B8. XPD patterns of germanosilicate samples that crystallized in the presence of **OSDA 2** and different Si/Ge ratios and in the gel (*: impurity; w: week). Here, the impurity phase was identified as an **MFI**-type material.244
- Figure B9. XPD patterns of germanosilicate samples that crystallized in the presence of **OSDA 3** and different Si/Ge ratios and in the gel (*: impurity; w: week).....245
- Figure B10. XPD patterns of germanosilicate samples that crystallized in the presence of **OSDA 4** and different Si/Ge ratios and in the gel (*: impurity; w: week).....246
- Figure B11. (A) An XPD pattern and (B) SEM image of a sample of the germanosilicate IM-12 synthesized in hydroxide medium (**UTL** framework type). The Si/Ge ratio was determined using EDS to be 4.5. This sample was used for comparison with CIT-13.248
- Figure B12. Porosity characterizations of CIT-13 and IM-13. (a) The Saito-Foley pore size distribution derived from the argon adsorption isotherm shown in Figure 8. (b) The log-plot of the Ar-isotherms of CIT-13, IM-12, zeolite Y and zeolite A. (c) The normalized differentiated log-plot of isotherms in (b) to allow a qualitative comparison. *Zeolite Y and Zeolite A data courtesy of Dr. Joel E. Schmidt.*249
- Figure B13. Transformation of Ge-CIT-13/F[4.11] to Ge-CIT-5 over time observed on the basis of PXRD patterns in 2-theta scanning ranges of (a) 4–30° and (b) 5–9°250
- Figure B14. Transformation of Ge-CIT-13/F[4.22] to Ge-CIT-5 over time observed on the basis of PXRD patterns in 2-theta scanning ranges of (a) 4–30° and (b) 5–9°251
- Figure B15. Transformation of Ge-CIT-13/F[4.27] to Ge-CIT-5 over time observed on the basis of PXRD patterns in 2-theta scanning ranges of (a) 4–30° and (b) 5–9°251
- Figure B16. Transformation of Ge-CIT-13/F[4.65] to Ge-CIT-5 over time observed on the basis of PXRD patterns in 2-theta scanning ranges of (a) 4–30° and (b) 5–9°252

Figure B17. Structural change of Ge-CIT-13/F[4.31] upon extended exposure to saturated water vapor.	252
Figure B18. TGA profile of Ge-CIT-5 produced by exposing calcined Ge-CIT-13/F[4.31] to an ambient atmosphere for 4 months.	253
Figure B19. Channel structures and geometric arrangements of <i>d4r</i> units of studied germanosilicates.	255
Figure B20. Reassembly abilities of various aliphatic amines for the condensation of CIT-13P to CIT-15 investigated on the basis of PXRD patterns.	256
Figure B21. Influence of degree of delamination of Ge-CIT-5 on the formation of CIT-15-like layered materials (a) Design of experiment. PXRD patterns of the resultant layered materials in the range of (b) 4–40° and (d) 6–12°	257

LIST OF TABLES

Table 3.1. Topological information of small-pore frameworks investigated in this work...	75
Table 8.1. Summary of postsynthesis alumination of Ge-CIT-13	184
Table 8.2. Summary of postsynthetic alumination of Ge-CIT-5.....	189
Table B1. Summary of fluoride-based CIT-13 synthesis conditions and results.	235
Table B2. Crystallographic details for the structure refinement of as-synthesized CIT-13.	237
Table B3. Selected bond lengths and angles (\AA , $^\circ$).	237
Table B4. Summary of hydroxide-based CIT-13 synthesis conditions and results. ($x/(x+1)$ SiO_2 : $1/(x+1)$ GeO_2 : 0.5 ROH : y H_2O)	247
Table B5. Collection of all T-O-T angles of *CTH and CFI, and estimated positions and multiplicities of ^{29}Si NMR signals calculated using the empirical model by Thomas et al. (1983) which is visualized in Figure 7.15(b).....	254

**Part I. Shape Selectivity of Small-pore Molecular Sieves for the
Methanol-to-Olefins Reaction**

Chapter 1

Introduction to Part I: The Methanol-to-Olefins (MTO) Reaction and Small-Pore Microporous Materials

In this chapter, the topic of Part I of my thesis is introduced. First, I describe what the MTO reaction is and why it is an important process. Next, a brief introduction to the types of catalysts used for the MTO reaction will be provided. Then, the recent trend in mechanistic studies of the MTO reaction is summarized, particularly focusing on the hydrocarbon pool mechanism. Lastly, my motivations and objectives are outlined.

1.1. Background

Ethylene and propylene are the first and second most-produced petrochemicals in the world, respectively.¹⁻² The majority (ca. 60–70 %) of total worldwide ethylene and propylene are used to produce polymer products—polyethylene and polypropylene.^{1,3} The remainder is used to produce more value-added specialty chemicals like ethylene oxide, propylene oxide, cumene, etc. In these days, it is very hard to find any commercial products in any field of industry which have nothing to do with these light olefins. Indeed, it is no exaggeration to say that they are chemicals supporting the human civilization itself.

The majority of ethylene has been produced from steam cracking (SC) of petroleum sources such as light naphtha, and it is currently the case.⁴ Propylene can be also produced from the same SC process, but has more sources such as fluid catalytic cracking (FCC) of

petroleum gas or dehydrogenation of propane.⁵ All of these processes use various petroleum sources as feeds in common. During the 1970s energy crisis, the oil price skyrocketed from USD 10 to USD 60 per barrel.⁶ Processes using non-petroleum sources such as natural gas or coal started to gather industrial interests. In the early 1970s, Mobil invented a revolutionary synthetic zeolite, ZSM-5, which shows excellent catalytic performances in a number of processes including the methanol-to-hydrocarbon (MTH) process.⁷ The first methanol-to-gasoline (MTG) unit was commercialized in New Zealand by Mobil in 1985, and it produced approximately 30 % of the country's gasoline demand.⁸⁻⁹ The original Mobil MTG process was composed of two steps: syngas-to-methanol and methanol-to-gasoline, as shown in Figure 1.1(a).¹⁰ Syngas can be obtained from such as coal gasification and steam reforming of natural gas.

Scientists of UOP (at that time, Union Carbide) introduced a novel silicoaluminophosphate (SAPO) molecular sieve having a chabazite (CHA) topology which is called SAPO-34 in the early 1980s.^{8,11} In the MTH process, SAPO-34 converted methanol into ethylene and propylene with very high selectivity (80–90%) due to its narrow pore and cage dimension. The CHA cages of SAPO-34 bounded with 8-membered-ring pore openings allows reactants (methanol) and products (light olefins) to diffuse in and out, while traps bulky hydrocarbon intermediates within it. UOP and INEOS (Norsk Hydro) introduced the methanol-to-olefins (MTO) process in 1996; they adopted a combination of fluidized bed reactor and continuous regeneration unit to tackle the issue of limited catalytic lifetime of SAPO-34.¹² This process was further improved by combining the olefin cracking process (OCP) that converts higher olefins to propylene developed by Total.⁸ (Figure 1.1(b))

In 2010, a major advancement was made by the Dalian Institute of Chemical Physics (DICP); the dimethyl ether/methanol-to-olefins (DMTO) process using SAPO-34 which recycles higher olefin to maximize the ethylene and propylene selectivity was developed by DICP which is shown in Figure 1.1(c).^{8,13} On the basis of this DMTO technology, Shenhua

Baotou Coal company and DICP constructed the first coal-to-olefin (CTO) unit (Figure 1.1(d)) in Inner Mongolia in 2010. This is now the largest commercialized CTO process unit in the world, producing 600,000 ton of ethylene and propylene per year. Although the majority of ethylene and propylene are currently produced from SC and FCC, for the last decade, the MTO process has attracted more and more attention from the industry not only because of the volatility of oil price but also because of the expected gap between olefin demand and capacity.¹

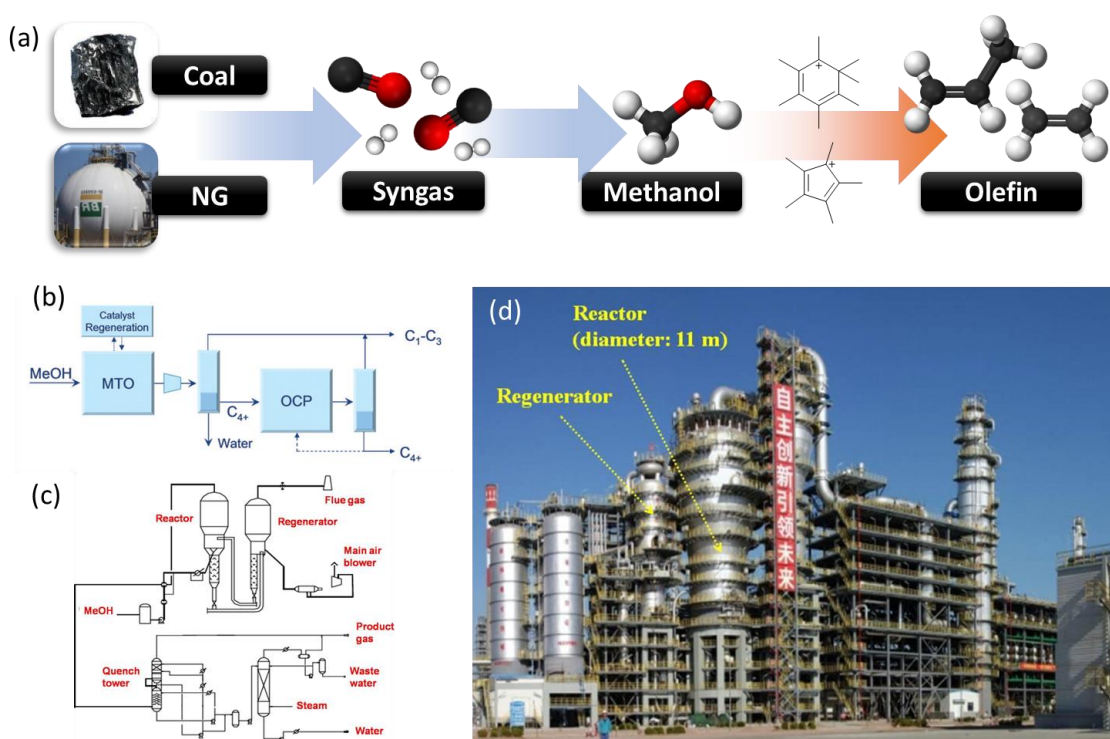


Figure 1.1. Overview of the MTO process. (a) Schematic description of the process. (b) UOP/INEOS MTO process with UOP/Total OCP process. Reproduced with Permission from Ref [8]. Copyright 2012 Wiley-VCH. (c) DICP DMTO process (d) DMTO commercial unit operating in Dalian, Jilin Province, PR China. Reproduced with Permission from Ref [13]. Copyright 2015 American Chemical Society.

1.1.1. Small-pore Molecular Sieves

Molecular sieves refer to crystalline and microporous solid state materials which can have any elemental compositions and any framework charge.¹⁴ *Zeolites* are one class of molecular sieves. In the most rigorous definition, zeolites are the class of microporous crystalline aluminosilicates having alkali (Na^+ , K^+ , etc.) or alkali-earth (Mg^{2+} , Ca^{2+} , etc.) cations and water molecules within their pore systems. The cations can be replaced with protons, generating the Brønsted acid sites on the surface. Some heteroatoms (Ti^{4+} , Sn^{4+} , etc.) within silicate frameworks can exhibit the Lewis acidity. These acidities are the origin of catalytic abilities of zeolites. Up to date, thousands of synthetic zeolites and related metallosilicate molecular sieves have been introduced, particularly for catalytic purposes. For this reason, practically in these days, the terminology ‘zeolite’ is used in a broader meaning referring to any silicate-based molecular sieves. A new terminology ‘*zeotype*’ is used sometimes for this purpose.

Aluminosilicates are accomplished by substituting Al for Si within frameworks. In pure silica, the substitution of Al for Si results in negative charges within the framework due to the difference between the oxidation state of Al (III) and Si (IV) in oxide. This negative charge can hold a proton, thus enabling the material to play a role as a solid acid, as mentioned above. Any neighboring two tetrahedral silicon sites cannot be replaced with aluminum at the same time. In other words, a local tetrahedral structure such as -O-Al-O-Al-O- within silicate frameworks is not possible to exist. This is called the Loewenstein rule.¹⁵ For this reason, the minimum value for Si/Al molar ratio of any zeolites is one. But two aluminum sites can be separated by only one silicon. This is called a *paired site*. Zeolites can have Si/Al ratios from 1 to ∞ . Conventionally, *low-silica* zeolites refer to zeolites having Si/Al ratio close to 1. *High-silica* zeolites are aluminosilicates with small extents of Al-substitution (less than one or two aluminum sites per unit cell, typically Si/Al > 10).

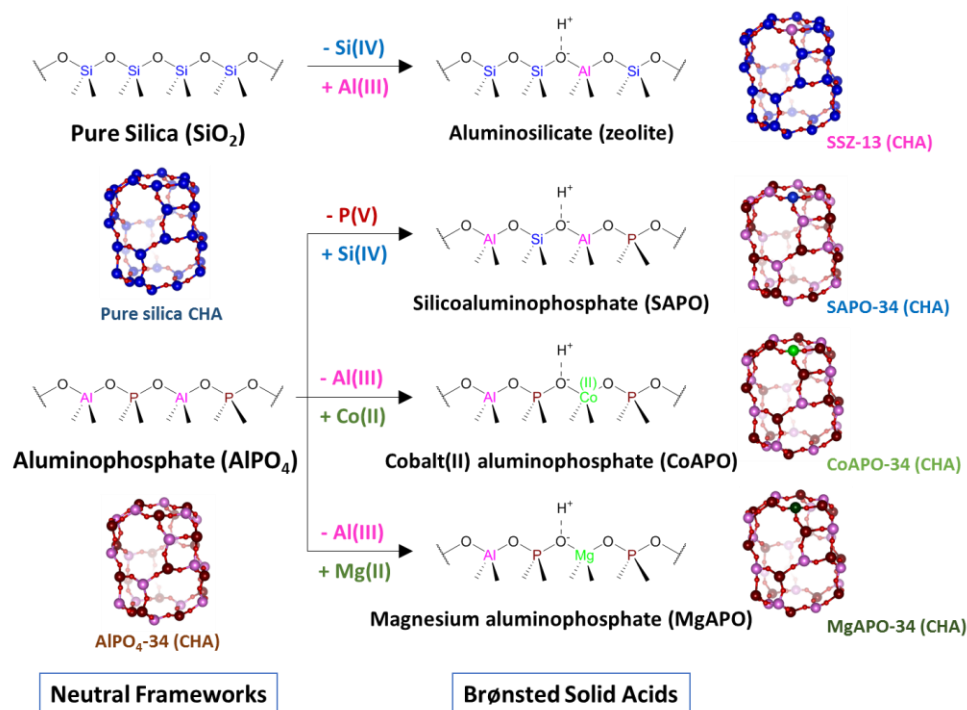


Figure 1.2. Schematic description of simplified structures of neutral frameworks and Brønsted acid sites composed of various elemental compositions. CHA cages having corresponding elemental compositions and acid sites.

The relation between neutral aluminophosphates (AlPOs) and silicoaluminophosphates (SAPO) is analogous to the case of aluminosilicates. In this system, Si (IV) replaces P (V) and generates one acid site. The substitution of Si for one isolated Al site is not possible due to the fact that the Si-O-P bonds cannot be formed in the SAPO systems.¹¹ Instead, in the SAPO system, a domain of AlPO_4 can be replaced with silica-domain having a boundary composed only of Al-O-Si bonds. This site is called an *islanded site*. For this reason, in SAPO materials having islanded sites, the numbers of Brønsted acid sites are not equal to the number of silicon sites. Also, metal ions which can have an oxidation state +2 with a tetrahedral coordination in solid oxides are able to replace Al (III) within the

AlPO₄-frameworks, resulting in metalloaluminophosphates (MAPOs). Magnesium, cobalt (II), manganese (II), and nickel (II) are such metals. Similarly to the cases of zeolites and SAPOs, this substitution generates a Brønsted acid site. However, since substituting M (II) for P (V) is not possible, these MAPOs can have isolated sites only.

Topology is a purely geometric concept, and refers to how the tetrahedral atoms are connected to each other to form the entire *framework*. In some contexts, ‘topology’ and ‘framework’ were used interchangeably. In 2019, the International Zeolite Association (IZA) structure database provides crystallographic data of 245 zeolite frameworks which have been discovered up to date.¹⁶ One topology can have various elemental compositions. For example, the CHA (chabazite)-type framework can be built with pure silica (SiO₂),¹⁷ aluminosilicate (natural chabazite and SSZ-13),¹⁸ aluminophosphate (AlPO₄-34),¹⁹ silicoaluminophosphate (SAPO-34),¹¹ and many metalloaluminophosphates (MAPOs) including magnesium aluminophosphate (MgAPO-34)²⁰ and cobalt (II) aluminophosphate (CoAPO-34),²¹ as shown in Figure 1.2. These CHA-type materials have different elemental compositions, thus having different chemical properties, but share crystallographically the same structure.

The frameworks are denoted using *three-letter codes*. These three-letter codes are abbreviations of the type materials that represent the frameworks. For example, three zeolite frameworks are shown in Figure 1.3. CHA is from the name of natural zeolite *chabazite*. MFI is the abbreviation of ZSM-5 (Zeolite Socony Mobil - *Five*). *BEA came from zeolite *BEta* polymorph A. Asterisks (*) denote the presence of innate structural disorders within frameworks. Zeolite beta is always obtained as disordered crystals possessing intergrown domains of polymorphs A and B. Throughout my thesis, these three-letter codes will be used very frequently without providing any further explanation about name origins. In case of AlPO₄-based molecular sieves, the framework type is denoted as numbers.^{11, 22} For example, SAPO-34 means silicoaluminophosphate molecular sieve having a CHA (-34) topology.

Conventionally, the dimension of pore openings of zeolite is denoted using the number of tetrahedral atoms (T-atoms, T = Si, Al, P, etc.). Most frequently observed pore openings are 8-, 10-, and 12-membered rings. These pore dimensions are conventionally referred to as *small-pore*, *medium-pore*, and *large-pore*, respectively. CHA, MFI, and *BEA shown in Figure 1.3 are representative examples. Pore openings larger than 14-membered rings are called *extra-large-pore*. Rings smaller than 6-membered rings are not considered as porous. For the MTO and MTG processes, small-pore (SAPO-34) and medium-pore (ZSM-5) molecular sieves are used, respectively. These pore sizes determine the product selectivity by limiting the intracrystalline diffusion of product molecules.

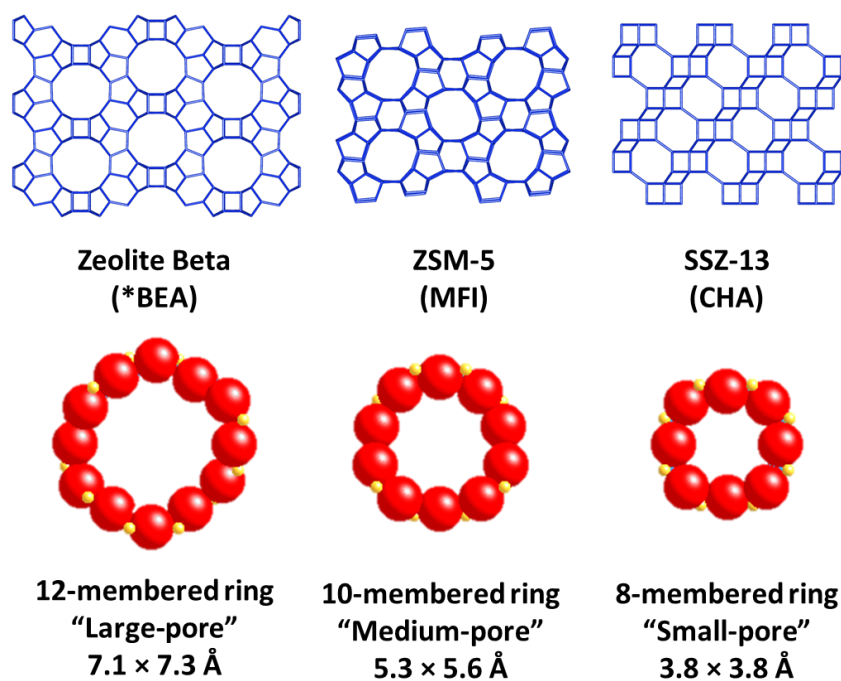


Figure 1.3. Examples of large-, medium-, and small-pore frameworks and their pore opening dimensions.

1.1.2. Mechanism of MTO Reaction

The formation mechanism of hydrocarbons including light olefins from methanol over solid acid molecular sieves has been studied extensively for decades.^{8-9, 13, 23} There has been no doubt that the first step of mechanism is the acid-catalyzed dehydration of methanol via protonated surface methoxyl into dimethyl ether (DME).^{9, 23} However, there has been many theories about the formation of C-C bonds after the formation of DME, such as the oxonium ylide mechanism,²⁴ the carbene mechanism,⁷ the free radical mechanism,²⁵ etc. In the early 90s, Dahl and Kolboe suggested *the hydrocarbon pool mechanism* about the MTO reaction of SAPO-34 (Figure 1.4(a)).²⁶⁻²⁸ The hydrocarbon pool intermediates do not have a specific chemical structure, but are aromatic hydrocarbons or carbocations having multiple ($n = 4-7$) methyl and alkyl groups. (Figure 1.4(b)) This mechanism has been widely accepted up to date, and the most of recent advancements of mechanistic studies about the MTO reaction have been made by further refining Dahl and Kolboe's hydrocarbon pool mechanism.⁸

One of the most recognized mechanistic models for the MTH process is *the dual-cycle concept* suggested by Olsbye and co-workers.⁸ (Figure 1.4(c)) The dual-cycle postulation is established by combining the mechanistic models for ZSM-5 and SAPO-34 into one.⁸ This dual-cycle model has two cycles operating simultaneously: *the alkene cycle* and *the aromatic cycle*. These two cycles are connected with the hydrogen transfer reaction that produces paraffins. Svelle et al. reported that ethylene is exclusively formed from the aromatic cycle while the alkene cycle generates propylene with high selectivity on the basis of their carbon-isotope ($^{12}\text{C}/^{13}\text{C}$) switching experiments.²⁹ Sun et al. showed that both ethylene and propylene are formed from the aromatic cycle.³⁰

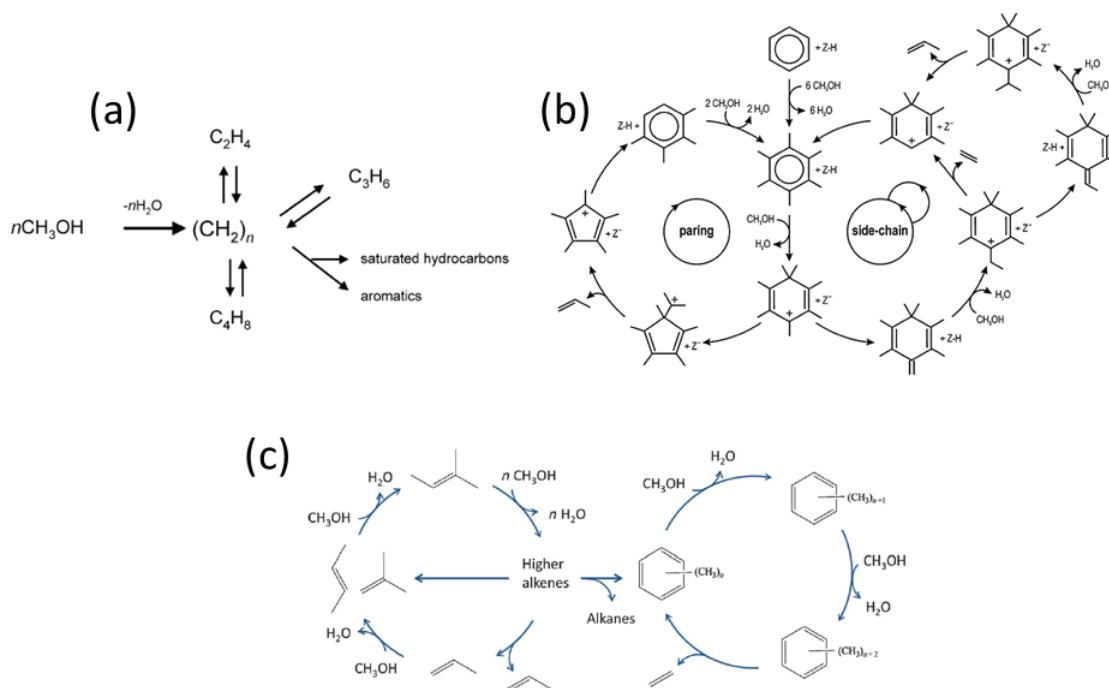


Figure 1.4. Proposed mechanisms of the MTO reaction. (a) The original hydrocarbon pool mechanism suggested by Dahl and Kolboe. Reproduced with Permission from Ref [27]. Copyright 1994 Elsevier. (b) The aromatic cycles showing the paring mechanism and side-chain mechanism by Lesthaeghe et al. on ZSM-5. Reproduced with Permission from Ref [31]. Copyright 2009 Wiley-VCH. (c) Dual cycle concept. Reproduced with Permission from Ref [8]. Copyright 2012 Wiley-VCH.

Most of the mechanistic studies introduced above are about the MTH reactions within the pore systems of ZSM-5 and SAPO-34. The topology is another important factor that determines the type of hydrocarbon pool intermediates. The formation of aromatic intermediates within molecular sieves could be investigated in real time using the *in situ* solid-state ^{13}C nuclear magnetic resonance spectroscopy¹³ and the operando UV-Vis spectroscopy.³² The Liu group of DICP investigated the confinement effects of cage structures on types of hydrocarbon pool intermediates formed during the MTO reactions

within the cages having CHA (SAPO-34 and SSZ-13), LEV (RUB-50 and SAPO-35), and RHO (DNL-6) topologies.^{13, 33-35} As shown in Figure 1.5(a), the larger the cage was, the more methyl groups the carbenium intermediate had.¹³ Also, for each of the catalysts having different topologies, unique hydrocarbon pool cycles could be suggested.^{34, 36}

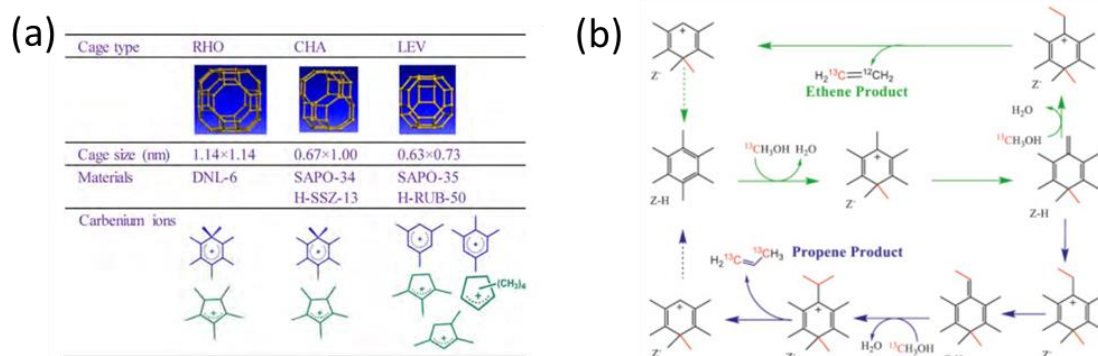


Figure 1.5. Dependence of hydrocarbon pool intermediate structures on cage structures. (a) Hydrocarbon pool carbenium cations which were formed in different topologies of cages. Reproduced with Permission from Ref [13]. Copyright 2015 American Chemical Society (b) Hydrocarbon pool mechanism suggested for DNL-6 having a RHO topology. Reproduced with Permission from Ref [36]. Copyright 2014 Elsevier.

1.2. Motivation

As explained in the previous section, there have been extensive studies regarding the mechanism of the MTO reaction and the structure-reaction intermediate relation. Haw et al. indicated that intermediates having more methyl groups are responsible for the formation of higher olefins.³⁷ Given that a catalyst having larger cages forms hydrocarbon pool intermediates having more methyl groups and eventually shows higher butylenes

selectivities than catalyst having smaller cages,^{13, 34-36} there must be a rule regarding the *intermediate shape selectivity*.

Also, there are many reports which compared olefin product distributions from MTO reactions over several small-pore molecular sieves having different topologies.^{32, 38-45} Y. Bhawe who is one of the previous members of the Davis group also studied the shape selectivity problem by comparing three zeolites having LEV, CHA, and AFX topologies, concluding that the intermediate cage size of CHA is the main reason for its high light olefin selectivities.⁴¹ Pinilla-Herrero et al. investigated four SAPO-based molecular sieves having LEV, AFX, SAV, and LTA topologies.³⁸⁻³⁹ In these works, differences among olefin product distributions were attributed to different pore window sizes.³⁸ On the other hand, Castro and co-workers investigated the MTO reaction products of a set of SAPO-based materials having CHA, SAV, and KFI topology, and concluded that the olefin selectivity distribution is majorly dependent upon the cage topology which has a close relation with the distribution of hydrocarbon pool carbenium intermediates.⁴² These works reached reasonable conclusions on the basis of their experimental results, but no general rule has yet been established.

There has been no reliable way to measure the size of a cage. Some previous reports actually provided dimensions of cages,^{32, 41, 46} but there were large differences among the cage sizes evaluated by them. For example, for the same CHA cage, Bhawe et al.,⁴¹ Chen et al.,⁴⁶ and Goetze et al.³² gave $8.23 \times 8.35 \text{ \AA}$, $12.7 \times 9.4 \text{ \AA}$, and $10.9 \times 6.7 \text{ \AA}$, respectively, which are essentially all different from each other. Dimensions of cages were simply measured by calculating distances between the farthest pair of framework atoms (T or O) in a cage on the basis of crystallographic data provided in the IZA database.¹⁶ But this way of measurements has a fundamental problem because these dimensions do not reflect the actual sizes which are 'felt' by methanol or hydrocarbon pool intermediate molecules.

Yokoi et al. used the free volume to estimate the cage size.⁴⁷ They gave free volumes of 408 \AA^3 for an RTH cage and 415 \AA^3 for a CHA cage, and stated that the former is smaller

than the latter, which is essentially wrong. The size of maximum sphere diameter that can be occluded within an RTH cage is 8.18 Å which is much bigger than CHA of 7.37 Å. The ‘tree ring plots’ I contrived and provided in Chapter 3 also support that RTH is much larger than CHA. I speculate that they included dense layers of the RTH framework within their calculation.⁴⁸ The presence of these dense layers (CIT-10) makes the framework density of RTH (16.1 T-atoms nm⁻³) higher than that of CHA (15.1 T-atoms nm⁻³) despite the fact that an RTH cage is wider than a CHA cage. A statement that ERI is more spacious than CHA could be also found.²³ It is true that an ERI cage is longer than a CHA cage, but the former is apparently narrower than the latter as I will demonstrate in the following chapters. In summary, a reliable way to measure the actual sizes of cages that can have a correlation with the olefin product selectivity distributions should be established.

1.3. Objectives

The primary objective of this work is the creation of a rule regarding the shape selectivity of small-pore molecular sieve cages for the MTO reaction as illustrated in Figure 1.6. The rule must be on the basis of a solid way to measure the effective dimensions of cage structures. The evaluation of dimensions must be easy and straightforward enough to enable one to measure the size of cages without an assist of sophisticated computational tools. Also, the rule should have a predictive ability.

This rule must be deduced from real MTO data obtained at a strictly controlled reaction condition. Considering various non-linear shapes of known MTO-active cages, the reaction data must be obtained from multiple topologies having different elemental compositions (as many as possible). The synthesized catalysts must be as pure as possible to generate reliable reference data.

The following two chapters are about achievements of these goals. For the remainder of Part I of my thesis, in Chapter 2, the selection of topology, the syntheses of required

organic-structure directing agents (OSDA) and molecular sieves, the characterization results, and the time-on-stream MTO data from them will be reported and discussed. In Chapter 3, the olefin product distributions, the categorization of topologies, the concept of cage-defining ring, which is a new way to evaluate the cage dimensions, and how my new concept of correlating the cage-defining ring to product olefin distributions will be discussed. Lastly, in Chapter 4, an overall summary will be provided and future work will be proposed.

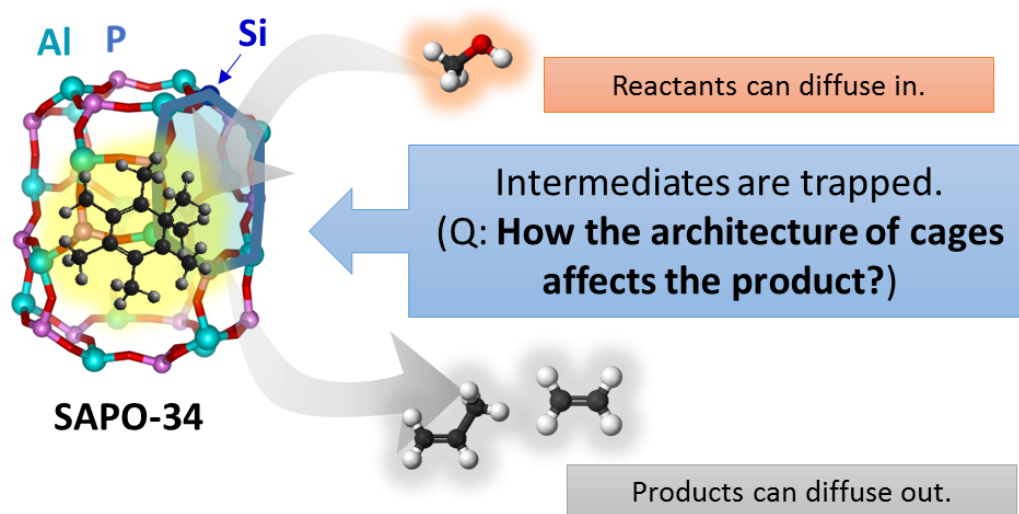


Figure 1.6. Schematic illustration of MTO reaction within a SAPO-34 cage and the main question to answer.

Chapter 2

Small-pore Molecular Sieves and MTO Reaction

In this chapter, the experimental part (syntheses, characterizations, and MTO reactions of molecular sieves) of Part I of my thesis is presented. This chapter and the next chapter (Chapter III) are combined reconstitutions of two of my publications: J. H. Kang et al., *ChemPhysChem* 2018, 19, 412 and J. H. Kang et al., *ACS Catal.* 2019, DOI: 10.1021/acscatal.9b00746. The majority of this chapter is adapted from the Supporting Information (methods and characterization) of my ACS Catalysis paper, but further augmented with the contents from my *ChemPhysChem* paper.

2.1. Introduction

The MTO reaction over small-pore/cage-type molecular sieves is a promising technology which can meet the ever-increasing light olefin demands.^{8, 13, 49} Methanol can be synthesized from syngas which can be obtained from various non-petroleum sources such as coal and natural gas.⁹ The commercialized catalyst for the MTO process is SAPO-34, an AlPO₄-based molecular sieve solid acid having a CHA topology.¹¹ The cage of CHA can effectively trap bulky hydrocarbon pool intermediates and let methanol and light olefins diffuse through its pore openings consisting of 8 tetrahedral atoms. This cage structure of SAPO-34 is the origin of its high selectivity (80–90%) toward light olefins (ethylene and propylene). The first and largest coal-to-olefin plant was constructed in Inner Mongolia in 2010 on the basis of the DMTO process by DICP.¹³

There is a scientific consensus that the mechanism of MTO reaction is based on the hydrocarbon pool cycles (shown in the previous chapter) of various polymethyl aromatic intermediates which are active under the reaction condition.^{8,27} There has been a recognition that the cage structures dictate types of intermediates formed during the reaction.^{23,50} During the recent decade, on the basis of advanced characterization techniques such as the *in situ* solid state nuclear magnetic resonance (NMR) spectroscopy, hydrocarbon pool intermediates formed within cages could be identified.¹ It was confirmed that the types of polymethyl aromatic intermediates are actually controlled by the cage geometry.^{32-34, 36, 46} Also, many attempts were made to correlate the cage structure with the olefin product distributions.^{32, 38-39, 41, 46} Despite these efforts, the global shape selectivity of the MTO reaction has not yet established.

To establish a general rule regarding the shape selectivity, the reaction condition should be controlled first. The reaction temperature is the most important variable that determines the regime of MTO mechanism, and significantly affects the olefin selectivity distributions.^{13,32,46} However, many of the previously reported experiments were performed at different temperatures among which a solid comparison is hard to be made. 350 °C^{40,42-43,51} and 425 °C^{44,52} were the most frequently adopted reaction temperatures other than 400 °C. Furthermore, the number of studied topologies must be as many as possible. Most of the previous studies compared less than 5 topologies. To deduce a valid statement about the shape selectivity, a wide array of molecular sieves having various topologies and compositions must be tested in the same reaction condition. For this reason, in this work, the reaction temperature and the weight-hourly space volume of methanol were strictly controlled at 400 °C and 1.3 h⁻¹.

The molecular sieves tested in this work were selected as follows. Among 245 frameworks which have been discovered up to date, only 34 frameworks have cage structures bounded with 8-ring pore windows.¹⁶ Of course, not all of these frameworks are applicable

to the MTO reaction. Some topologies have been realized only as pure-silica which has no acid site. A topology like tschörtnerite (TSC) has never been realized as aluminosilicates having a Si/Al ratio higher than 1.⁵³⁻⁵⁴ Zeolites having low Si/Al ratios (e.g., less than 3) show too short lifetime to obtain meaningful numbers of data points of nearly complete methanol conversion (i.e., over 98%) due to high paired-site density.⁶⁴ For zeolites, it is important to have moderate-range Si/Al ratios (ca. Si/Al = 4–30) to show optimal MTO activities. Therefore, frameworks having ‘MTO-unfeasible’ elemental compositions were eliminated from the list. Some frameworks have cages which are also present in other frameworks. For example, AFT have CHA and AFX cages, and AFV have CHA and LEV cages.^{16, 55-56} Since CHA, AFX, and LEV are already on the list, to avoid redundancy, these types of ‘combined-cage’ topologies were also ruled out. Frameworks which have elemental compositions not zeolitic neither AlPO_4 -based, such as NPT, were removed.⁵⁷ Finally, 14 frameworks (CHA, AFX, SFW, ERI, LEV, AEI, DDR, ITE, RTH, SAV, LTA, RHO, KFI, UFI) were selected as shown in Figure 2.1. These frameworks were reproduced as zeolites and/or SAPOs/MAPOs in this work. On the top of this list, three zeolites (SSZ-104, SSZ-99, and SSZ-105) having disordered structures of intergrown phases and one zeolite having novel topology (SSZ-27) were provided by Chevron.

Finally, the MTO reactions of the following 30 small-pore/cage-type molecular sieves were investigated: SSZ-13 (CHA), SAPO-34 (CHA), CoAPO-34 (CHA), MgAPO-34 (CHA), SSZ-16 (AFX), SAPO-56 (AFX), SSZ-52 (SFW), STA-18 (SFW), SSZ-99 (CHA/GME intergrowth), SSZ-104 (CHA/ABC-6-type disordered), SSZ-27, Nu-3 (SSZ-17, LEV), SAPO-35 (LEV), SSZ-98 (ERI), SSZ-105 (LEV/ERI intergrowth), SSZ-39 (AEI), SAPO-18 (AEI), CoAPO-18 (AEI), MgAPO-18 (AEI), SSZ-28 (DDR), Zeolite RTH (SSZ-50), Zeolite ITE (ITQ-3), STA-7 (SAV), Zeolite LTA, SAPO-42 (LTA), Zeolite RHO, DNL-6 (RHO), Zeolite KFI, STA-14 (KFI), and UZM-5 (UFI). In this chapter, the syntheses and characterizations of OSDAs and molecular-sieve catalysts are presented. The results of MTO

reactions over catalysts listed above were depicted as the time-on-stream charts. MTO behaviors of these catalysts were analyzed focusing on their transient trends.

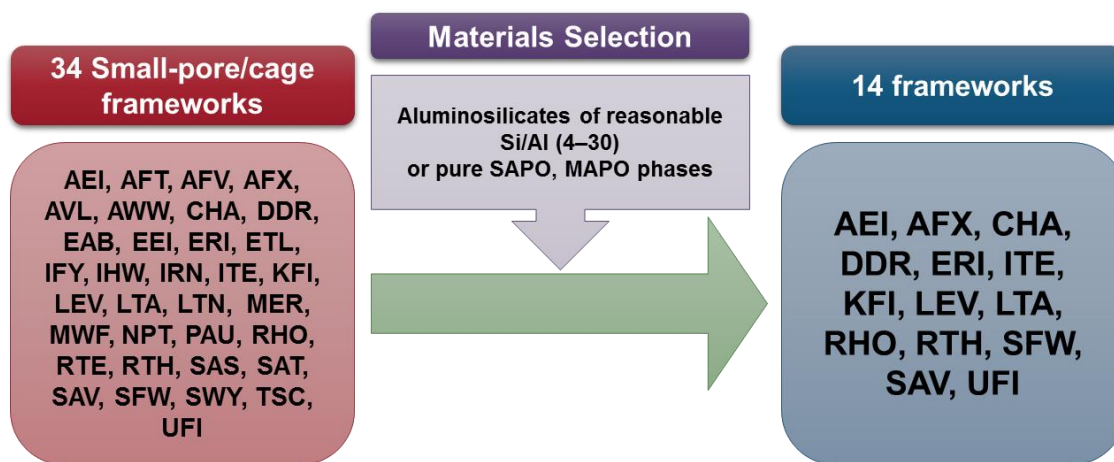


Figure 2.1. Selection of topologies.

2.2. Experimental

2.2.1. Synthesis of Organic Structure-Directing Agents

Materials 1,4-diazabicyclo[2.2.2]octane (DABCO, 99%, Sigma-Aldrich), 1,6-dibromohexane (98%, Sigma-Aldrich), quinuclidine (97%, Alfa Aesar), N-methylpiperidine (99%, Sigma-Aldrich), methyl iodide (99.5%, Cu-stabilized Sigma-Aldrich), 1,2,4,5-tetramethylimidazole (98%, TCI Chemical), 1,2-dimethylimidazole (98%, Sigma-Aldrich), 4-methylbenzyl chloride (98%, Sigma-Aldrich) were used as-received without further purification.

Organic Syntheses The quaternary ammonium OSDAs used in this work were prepared as their halide forms firstly by the S_N2 reactions stated below. The reaction schemes for preparation of the OSDAs are demonstrated in Figure 2.2.

1,1'-(hexane-1,6-diyl)bis(1,4-diazabicyclo[2.2.2]octanium) dibromide (C₆-diDABCO-Br₂) was prepared from the S_N2 reaction of DABCO and 1,6-dibromohexane.⁵⁸ (Figure 2.2(a)) DABCO (67.3 g, 600 mmol, excess) was dissolved in 200 mL of methanol in a 500 ml round-bottom flask, and the solution was heated up to 45 °C. A 50-mL dropping funnel was charged with 1,6-dibromohexane (24.4 g, 100 mmol) dissolved in 100 mL of methanol. The 1,6-dibromohexane solution was slowly added to the DABCO solution dropwise for 30 min while vigorously stirring to prevent the possible oligomerization. The reaction mixture was heated up to the reflux temperature and stirred for 24 hours. After that, the solvent was evaporated using a rotary evaporator. The white solid product was repeatedly washed with an amount of diethyl ether (1 L) to wash out excess DABCO. The product was dried in a vacuum at room temperature. ¹H NMR (500 MHz, D₂O): δ 3.34 (t, 12H), 3.21 (m, 4H), 3.12 (t, 12H), 1.73 (m, 4H), 1.37 (m, 4H). ¹³C NMR (125 MHz, D₂O): δ 64.27, 52.05, 44.16, 25.12, 21.05.

N-methylquinuclidinium iodide was prepared from the S_N2 reaction of quinuclidine and methyl iodide.⁵⁹ (Figure 2.2(b)) 10 g (90 mmol) of quinuclidine was dissolved in 150 mL of chloroform in a 500-mL round-bottom flask, and cooled down using a dry-ice bath. A 50-mL dropping funnel was separately filled with 11.2 mL of methyl iodide (25.5 g, 180 mmol). Methyl iodide was added dropwise to the cooled quinuclidine-chloroform solution slowly because the reaction is highly exothermic. Methyl iodide must be handled in a well-ventilated fume hood because it is very volatile (b.p., 42.4 °C) and toxic if accidentally inhaled. After that, the reaction mixture was stirred at room temperature for extra 72 hours. Solvent and excess methyl iodide were evaporated using a rotary evaporator. Appropriate personal protective equipment (PPE) must be used since toxic vapor containing methyl iodide is generated. The solid product was repeatedly washed with an amount of diethyl ether (1 L). The product was dried in a vacuum at room temperature. ¹H NMR (500 MHz, CDCl₃): δ 3.83 (t, 6H), 3.36 (s, 3H), 2.33 (septet, 1H), 2.10 (m, 6H). ¹³C NMR (125 MHz, D₂O): δ 56.90, 51.83, 23.42, 18.57.

N,N'-dimethyl-1,4-diazabicyclo[2.2.2]octanium diiodide (DMDABCO²⁺(I⁻)₂), N,N'-dimethylpiperidinium iodide (DMP⁺I), 1,2,3,4,5-pentamethylimidazolium iodide (PMI⁺I) were prepared from the S_N2 reactions shown in Figure 2.2(c–e).^{48, 60-61} Synthesis protocols for these OSDAs are analogous to the method for N-quinuclidinium iodide explained above, except for the reactant amines. For DMDABCO²⁺, 16.8 g (150 mmol) of DABCO and 85.2 g (600 mmol) of methyl iodide were used: ¹H NMR (500 MHz, D₂O): δ 4.68 (s, 6H), 3.44 (s, 12H). ¹³C NMR (125 MHz, D₂O): δ 53.45, 44.38. For DMP²⁺, 9.2 g (100 mmol) of N-methylpiperidine and 42.6 g (300 mmol) of methyl iodide were used. ¹H NMR (500 MHz, CD₃OD): δ 3.54 (t, 4H), 3.27 (s, 6H), 2.00 (m, 4H), 1.78 (qnt, 2H). ¹³C NMR (125 MHz, CD₃OD): δ 62.59, 51.25, 20.44, 19.96. For PMI⁺, 18.7 g (150 mmol) of 1,2,4,5-tetramethylimidazole and 63.9 g (450 mmol) of methyl iodide were used. ¹H NMR (500 MHz, D₂O): δ 3.51 (s, 6H), 2.43 (s, 3H), 2.10 (s, 6H). ¹³C NMR (125 MHz, D₂O): δ 142.06, 125.24, 31.26, 9.39, 7.68.

1,2-dimethyl-3-(4-methylbenzyl)imidazolium chloride (12DM34MBI⁺Cl⁻) was synthesized from the S_N2 reaction between 1,2-dimethylimidazolium and 4-methylbenzyl chloride.⁶²⁻⁶³ 14.4 g of 1,2-dimethylimidazolium (150 mmol) was dissolved in 200 ml of toluene. 21.1 g of 4-methylbenzyl chloride (150 mmol) was added slowly. The reaction mixture was heated to 105 °C and the reaction proceeded for 24 hours. After that, the mixture was cooled down to room temperature, and the light yellowish solid was collected by filtration, and washed with a copious amount of diethyl ether (1 L) and dried in a vacuum at room temperature. ¹H NMR (500 MHz, D₂O): δ 7.18 (dd, 2H), 7.13 (d, 2H), 7.05 (d, 2H), 6.50 (s, 2H), 3.61 (s, 3H), 2.41 (s, 3H), 2.18 (s, 3H). ¹³C NMR (125 MHz D₂O): δ 144.14, 139.16, 130.64, 129.67, 127.68, 122.15, 120.89, 51.10, 34.49, 20.07, 8.93.

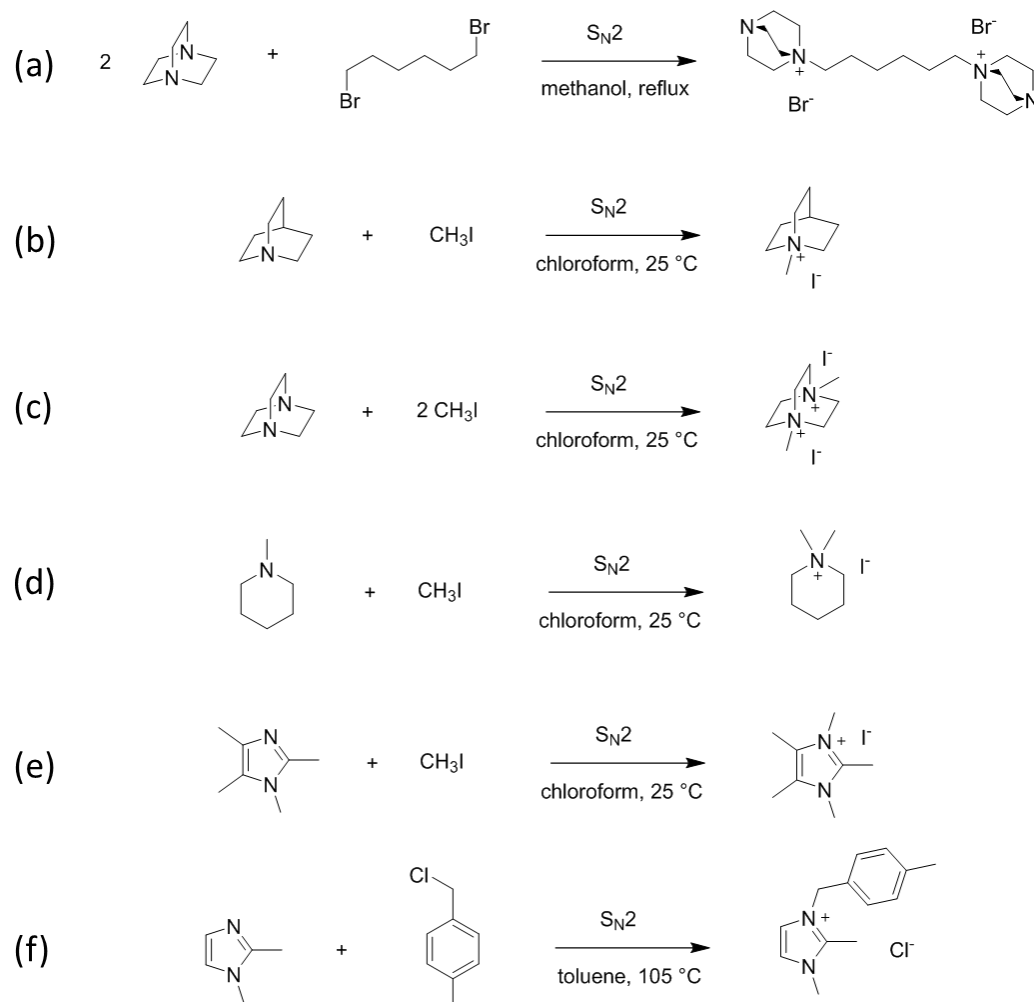


Figure 2.2. Reactions schemes for the OSDAs used to prepare the molecular sieve catalysts demonstrated in this work: (a) 1,1'-(hexane-1,6-diyl)bis(1,4-diazabicyclo[2.2.2]octanium), (b) N-methylquinuclidinium, (c) N,N'-dimethyl-1,4-diazabicyclo[2.2.2]octanium, (d) N,N-dimethylpiperidinium, (e) 1,2,3,4,5-pentamethylimidazolium, and (f) 1,2-dimethyl-3-(4-methylbenzyl)imidazolium.

Ion Exchange Synthesized halide-forms of OSDAs were ion-exchanged to their hydroxide forms. First, organic salts were dissolved in distilled water. And then, desired amounts of ion-exchange resin (DowTM MonosphereTM 550A OH, Dow Chemical) were added to the solution and stirred overnight. The mixing ratio was 1 mmol of OSDA : 3 mL of ion-exchange resin : 6 mL of distilled water. Used resin was separated by filtration and the same procedure was repeated using a new portion of ion-exchange resin. The final aqueous solutions of OSDAs as their quaternary ammonium hydroxide forms were concentrated to 100–200 mL using a rotary evaporator by evaporating excess water. The concentration of OSDA hydroxide was determined using an automatic titrator (Mettler Toledo Titrator DL22).

2.2.2. Synthesis of Microporous Materials

Materials All materials used for syntheses of microporous materials are used as received without further purification steps. Moisture contents of silica or alumina sources were characterized on the basis of thermogravimetric analysis (TGA). For silica sources, colloidal silica (Ludox AS-series, Sigma-Aldrich), fumed silica (Cab-O-Sil[®], ACROS), sodium silicate (Waterglass N[®], 8.9 wt. % Na₂O, 28.7 wt. % SiO₂ in H₂O, PQ Corporation), and tetraethyl orthosilicate (TEOS, 99.9%, Alfa Aesar) were used. For alumina sources, aluminum hydroxide gel (Barcroft 250, 30.6 wt. % of moisture, SPI Pharma), pseudoboehmite (Catapal B, 23.2 wt. % of moisture, VISTA), hydrated alumina (F2000, 33.8 wt. % of moisture, Reheis), sodium aluminate (37.9 wt. % Na₂O, 51.1 wt. % Al₂O₃, 11.0 wt. % H₂O, Alfa Aesar), and aluminum isopropoxide (98%, Sigma-Aldrich) were used. In some cases, zeolites Y were used as silica and alumina sources. Zeolyst CBV500 (Si/Al = 2.6, NH₄-form, 14.3 wt. % of moisture), CBV712 (Si/Al = 6, NH₄-form, wt. 15.1 % of moisture), and CBV720 (Si/Al = 15, H-form, wt. 8.8 % of moisture) were used. For phosphorus source, 85 wt. % orthophosphoric acid in water (Macron) was used. For cobalt sources, cobalt (II)

sulfate hydrate (Sigma-Aldrich) and cobalt (II) acetate tetrahydrate (98%, Sigma-Aldrich) were used. For magnesium source, magnesium acetate tetrahydrate (98%, Sigma-Aldrich) was used. For hydroxide mineralizers, sodium hydroxide (pellets, EMD Milipore), potassium hydroxide solution (45 wt. % in water, Sigma-Aldrich), and cesium hydroxide solution (50 wt. % in water, Sigma-Aldrich) were used. For alkali metal sources, sodium nitrate (99.9%, Sigma-Aldrich) and potassium nitrate (99.9%, Sigma-Aldrich) were used.

The following OSDAs or organic additives were used as-received from the stated vendors: tetraethylammonium hydroxide (TEAOH, 35 wt. % in H₂O, Sigma-Aldrich), tetramethylammonium hydroxide (TMAOH, 25 wt. % in H₂O, Sigma-Aldrich), diethylamine (DEA, Sigma-Aldrich), morpholine (Sigma-Aldrich), cyclohexylamine (Sigma-Aldrich), diisopropylethylamine (DIPEA, Sigma-Aldrich), N,N,N-trimethyladamantylammonium hydroxide (AdaOH, 25 wt. % in H₂O, Sachem), 1,1,3,5-tetramethylpiperidinium hydroxide (TMPOH, 0.788 mmol g⁻¹ in H₂O, Sachem), N,N,N',N'-tetramethylhexamethylenediamine (TMHD, 99%, Sigma-Aldrich), trimethylamine (TMA, 33 wt. % in ethanol, Fluka), tetra-n-butylammonium hydroxide (TBAOH, 55 wt. % in H₂O, Alfa Aesar), hexamethyleneimine (99%, Sigma-Aldrich), 1,4,7,10,13,16-hexaoxacyclooctadecane (18-crown-6 ether, 99%, Sigma-Aldrich), 1,4,8,11-tetraazacyclotetradecane (Cyclam, 98%, Sigma-Aldrich), 4,7,13,16,21,24-hexaoxa-1,10-diazabicyclo[8.8.8]hexacosane (Kryptofix® 222 or just K222, 98%, Sigma-Aldrich), and cetyltrimethylammonium bromide (CTAB, Sigma-Aldrich).

The preparation protocols of the following OSDAs were provided above: 1,1'-(hexane-1,6-diyl)bis(1,4-diazabicyclo[2.2.2]octanium) dihydroxide (C₆-diDABCO-OH₂), N-methylquinuclidinium hydroxide (MQuin⁺OH⁻), N,N'-dimethyl-1,4-diazabicyclo[2.2.2]octanium dihydroxide (DMDABCO²⁺(OH⁻)₂), N,N-dimethylpiperidinium hydroxide (DMP⁺OH⁻) 1,2,3,4,5-pentamethylimidazolium hydroxide (PMI⁺OH⁻), 1,2-dimethyl-3-(4-methylbenzyl)imidazolium hydroxide (12DM34MBI⁺OH⁻).

General Procedures All zeolites and AlPO_4 -based molecular sieves used in this work were prepared on the basis of the general procedures described here unless otherwise mentioned.

For zeolites, firstly, alumina source material was dissolved in alkali and/or OSDA hydroxide solution and stirred until the mixture became clear or translucent. And then, silicon source was added and digested under stirring for extra 24 hours.

For AlPO_4 -based molecular sieves, alumina source was mixed with twofold weight of water and stirred for 2 hours. And using a separate polytetrafluoroethylene (PTFE) beaker, a desired amount of concentrated phosphoric acid was mixed with the same weight of water and transferred to the alumina-water mixtures slowly. This aluminophosphate mixture was stirred for 3 hours. And then, silica or other metal sources and the rest of the desired amount of water (if any) were added to the gel. OSDA was added to the mixture 30 min after the silica addition. The final gel was stirred for extra 24 hours. Excess water was evaporated using an air flow if necessary after that.

Gel having the desired compositions were transferred to a 23-mL PTFE liner for Parr autoclave, and sealed tightly. Crystallizations were performed at desired temperatures in rotary or static convection ovens. Aliquots of the batch were taken periodically, and PXRD patterns of them were acquired to monitor the crystallization progress.

AlPO_4 -based Materials Syntheses The cage structures of AlPO_4 -based molecular sieves used in this work and the structures of OSDAs used to synthesize the corresponding molecular sieves were demonstrated in Figure 2.3.

SAPO-34 was prepared from TEAOH.⁶⁴ The molar composition of the gel was 1 Al_2O_3 : 1 P_2O_5 : 0.075 SiO_2 : 3 TEAOH : 50 H_2O . Catapal B alumina and Ludox HS-40 silica

sol were used as the aluminum and silicon sources, respectively. The crystallization was performed at 200 °C in a static oven for 24 hours.

CoAPO-34 and MgAPO-34 were synthesized by using morpholine as the OSDA.²⁰⁻
²¹ The gel composition was $x \text{ Al}_2\text{O}_3 : 1 \text{ P}_2\text{O}_5 : y \text{ MO (M = Co, Mg) : 2.7 \text{ Morpholine} : 60 \text{ H}_2\text{O}$. For (x,y), (0.8, 0.4) and (0.7, 0.6) were tried. The aluminum, cobalt, and magnesium sources used here were Catapal B alumina, cobalt (II) sulfate hydrate, and magnesium acetate tetrahydrate, respectively. The crystallization was performed at 185 °C in a rotating oven for 72 hours.

SAPO-56 was synthesized using TMHA as the OSDA.⁶⁵ The gel composition was $0.8 \text{ Al}_2\text{O}_3 : 1.0 \text{ P}_2\text{O}_5 : 0.3\text{--}0.6 \text{ SiO}_2 : 2 \text{ TMHA} : 40 \text{ H}_2\text{O}$. Catapal B alumina and Cab-O-Sil fumed silica were used as the aluminum and silicon sources, respectively. The crystallization was performed at 200 °C in a static oven for 96 hours.

STA-18 was synthesized using C₆-diDABCO-Br₂ and TMA as the co-OSDAs.⁵⁸ The gel composition was $1.0 \text{ Al(OH)}_3 : 0.7 \text{ H}_3\text{PO}_4 : 0.3 \text{ SiO}_2 : 0.08\text{--}0.10 \text{ C}_6\text{-diDABCO-Br}_2 : 0.13 \text{ TMA} : 0.28 \text{ TBAOH} : 40 \text{ H}_2\text{O}$. Aluminum hydroxide hydrogel and Cab-O-Sil fumed silica were used as the aluminum and silicon sources, respectively. The crystallization was performed at 190 °C in a rotating oven for 7 days.

SAPO-35 was synthesized using hexamethyleneimine as the OSDA with a gel composition: $1.0 \text{ Al}_2\text{O}_3 : 1.0 \text{ P}_2\text{O}_5 : 0.3\text{--}0.6 \text{ SiO}_2 : 1.5 \text{ hexamethyleneimine} : 55 \text{ H}_2\text{O}$.³⁹ Catapal B alumina and Cab-O-Sil fumed silica were used as the aluminum and silicon sources, respectively. The crystallization was performed at 200 °C in a static oven for 24 hours. SAPO-16 (AST) was observed as the major impurity phase, but it could be separated from SAPO-35 by repeated steps of fractional centrifugation at 500 rpm.

SAPO-18 was prepared from TMPOH.⁶⁶ The gel composition was 1 Al₂O₃ : 0.8 P₂O₅ : 0.172 SiO₂ : 1 TMPOH : 19.2 H₂O. The aluminum and silicon sources were Catapal B (VISTA) alumina and Ludox AS-40 silica sol (Sigma-Aldrich). The crystallization was performed at 190 °C in a rotating oven for 2 days.

CoAPO-18 and MgAPO-18 were prepared from the same diisopropylethylamine (DIPEA) OSDA with a gel composition of 1 Al₂O₃ : 1 P₂O₅ : 0.08 MO (M = Co, Mg) : 1.7 DIPEA : 50 H₂O.⁶⁷ The crystallization was performed at 160 °C in a rotating oven for 8–11 days.

STA-7 was synthesized using Cyclam as the OSDA.⁴² The gel composition was 1.0 Al(OH)₃ : 0.6–0.8 H₃PO₄ : 0.2–0.4 SiO₂ : 0.108 Cyclam : 40 H₂O. The aluminum and silicon sources were aluminum hydroxide dry-gel (Barcroft 250, SPI Pharma) and fumed silica. The crystallization was performed at 190 °C in a rotating oven for 72 hours. In some cases, white fluffy impurity was observed, and required extra purification steps. The desired STA-7 product was slightly yellowish and denser than the white impurity phase. The purification was performed using the fractional centrifugation at 500 rpm in distilled water. The top white phase was removed from the mixture by repeated centrifugation.

DNL-6 was synthesized using DEA and CTAB.⁶⁸ The gel composition was 1.0 Al(OH)₃ : 0.8 H₃PO₄ : 0.2 SiO₂ : 1 DEA : 0.10–0.15 CTAB : 50 H₂O. The aluminum and silicon sources were aluminum isopropoxide and TEOS. The hydrolysis alcohol products (i.e., ethanol and isopropanol) were removed by heating the gels at 80 °C. The crystallization was performed at 160 °C in a rotating oven for 48 hours.

SAPO-42 and STA-14 were synthesized using K222 and TEAOH as the OSDAs.⁴² The gel composition was 1.0 Al(OH)₃ : 0.8 H₃PO₄ : 0.2 SiO₂ : 0.108 K222 : 0.108x TEAOH : 40 H₂O where x = 0–6. When x < 2, SAPO-42 was obtained, and when x > 5, STA-14 was

obtained. This implies that TEA^+ cations can structure-direct the *pau* small cages in this system. The crystallization was performed at 190 °C in a rotating oven for 48 hours.

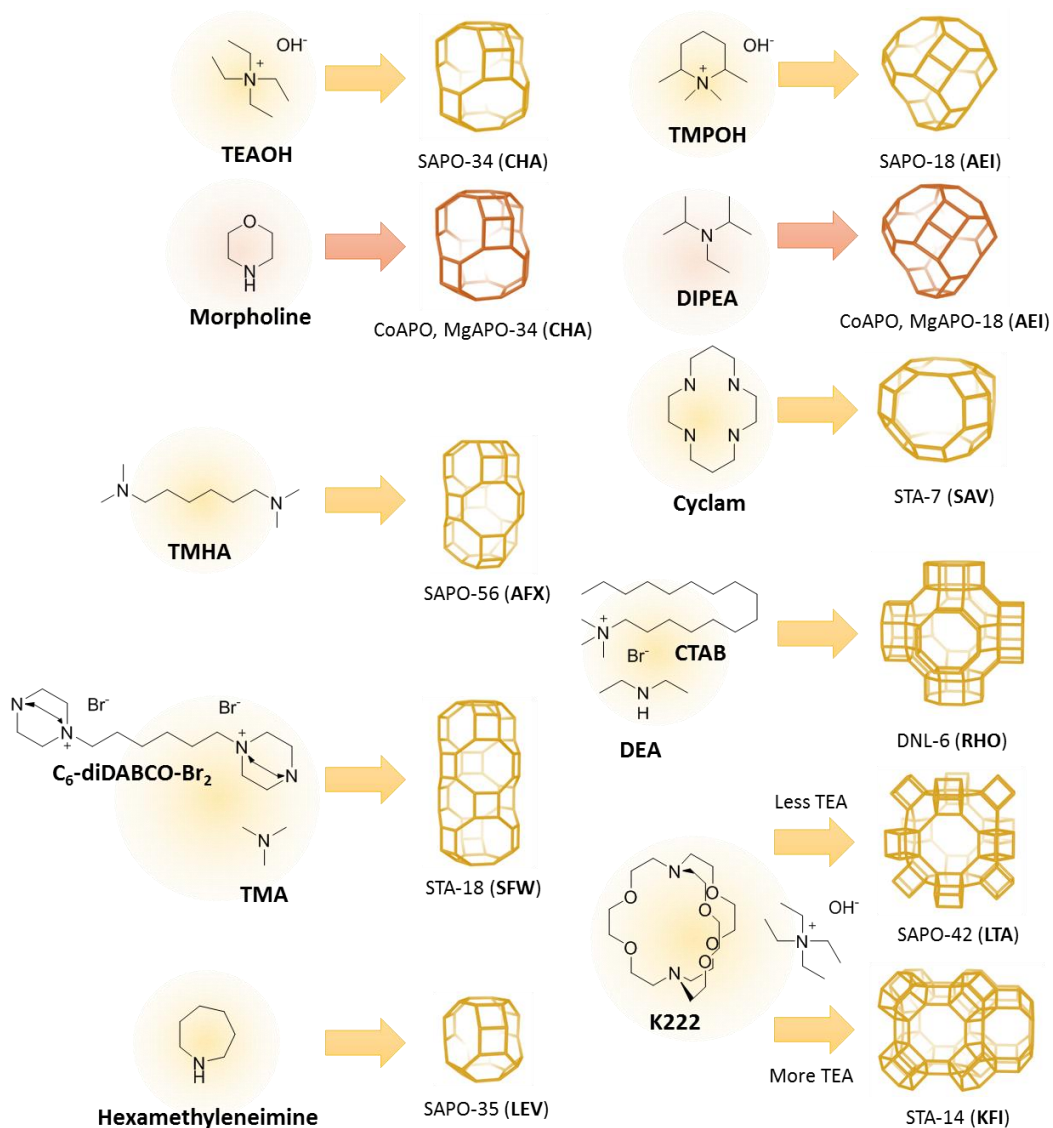


Figure 2.3. OSDAs and cage structures of the corresponding resultant AlPO₄-based molecular sieves.

Zeolites Syntheses The cage structures of zeolites used in this work and the structures of OSDAs used to synthesize the corresponding zeolites were demonstrated in Figure 2.4.

SSZ-13 was prepared using AdaOH as the OSDA.¹⁸ Desired amounts of AdaOH solution, sodium hydroxide and distilled water were mixed. A desired amount of sodium aluminate was dissolved in the mixture and stirred for 1 hour. And then, a desired amount of fumed silica was added. The gel composition was 1 SiO₂ : 0.017 Al₂O₃ : 0.20 AdaOH : 0.20 NaOH : 44 H₂O. The mixture was stirred for 24 hours before starting the crystallization. The crystallization was performed in a 160 °C rotating oven for 6–8 days.

SSZ-39 was prepared by converting commercial Y zeolite using a one-to-one-ratio cis/trans mixture of N,N,3,5-tetramethylpiperidinium hydroxide (TMPOH) as the OSDA. The synthesis was performed without use of sodium hydroxide, modified from ref [69]. Desired amounts of fumed silica, OSDA solution, and distilled water were mixed in a PTFE liner and homogenized by stirring. After that, a desired amount of Zeolyst CBV500 was dispersed in the mixture. Further aging steps at room temperature did not influence the results. The final gel composition was 1 SiO₂ : 0.067 Al : 0.706 TMPOH : 20.38 H₂O. The crystallization was performed in a 140 °C rotating oven for 28 days.

The LEV zeolites used in this work were synthesized using two methods with the following OSDAs: MQuinOH⁵⁹ and DMDABCO(OH)₂.⁶¹ The LEV zeolite synthesized using MQuinOH as the OSDA is known as Nu-3 (or SSZ-17), and has high silica elemental compositions (Si/Al > 10). Desired amounts of MQuinOH solution, sodium hydroxide and distilled water were mixed. A desired amount of Reheis F2000 hydrated alumina was dispersed in the mixture and stirred for 1 hour. Then, colloidal silica Ludox AS-40 was added dropwise. The gel composition was 1 SiO₂ : 0.024 Al₂O₃ : 0.199 MQuinOH : 0.187 NaOH : 40.11 H₂O. The mixture was stirred for 24 hours before starting the crystallization. The crystallization was performed in a 175 °C rotating oven for 6 days.

A lower-silica LEV zeolite was prepared using DMDABCO(OH)₂ as the OSDA. Desired amounts of 20% sodium hydroxide solution, sodium silicate, DMDABCO(OH)₂ solution, and distilled water were mixed in a PTFE liner and homogenized by stirring. Next, a desired amount of Zeolyst CBV720 was dispersed in the mixture. The mixture was stirred for 1 day. A desired portion of water was evaporated using flowing air. The final gel composition was 1 SiO₂ : 0.0147 Al : 0.178 DMDABCO(OH)₂ : 0.580 NaOH : 9.43 H₂O. The crystallization was performed in a 150 °C rotating oven for 3 days.

SSZ-98 was prepared by converting commercial Y zeolite using N,N-dimethylpiperidinium hydroxide (DMPOH) as the OSDA.⁶⁰ Desired amounts of DMPOH solution, potassium hydroxide solution and water was mixed in a PTFE liner and stirred. Next, a desired amount of Zeolyst CBV720 was dispersed in the mixture. The mixture was sealed and transferred to a 150 °C static oven. The final gel composition was 1 SiO₂ : 0.033 Al₂O₃ : 0.267 DMPOH : 0.497 KOH : 38.840 H₂O. The crystallization was performed for 3 days.

Zeolite RTH was prepared using PMIOH as the OSDA.⁴⁸ Desired amounts of TEOS and aluminum isopropoxide were hydrolyzed in a mixture of PMIOH solution by stirring at room temperature for 24 hours. Next, excess amounts of water and alcohol species formed as the results of hydrolysis were evaporated under flowing air. Desired amount of hydrogen fluoride (HF, 45 wt. % in H₂O, Sigma-Aldrich) was added dropwise to the gel. (*Caution: Hydrogen fluoride is a dangerous substance that can cause fatal burns and irreversible damages to human skin, tissue, and bone. It must be handled with appropriate PPE including a lab coat, a respirator, a full-face shield, an acid-apron, a pair of long-sleeve nitrile gloves, etc. with a proper ventilation in a fume hood.*) The viscous transparent gel became powdery as a result of the addition of HF. The resultant fluoride gel was further dried in a fume hood for 1–2 days. A desired amount of distilled water was added to achieve the desired gel composition. The final gel composition was 0.95 SiO₂ : 0.05 Al : 0.5 PMIOH : 0.50 HF : 7.0

H₂O. The crystallization was performed in a 160 °C rotating oven for 2 weeks. Decreasing aluminum contents in gels (below Si/Al = 50) resulted in the formation of high-silica STW impurities.

High-silica LTA zeolite was prepared using 12DM34MBI⁺OH⁻ and TMAOH as the co-OSDAs in fluoride media.⁶² Desired amounts of TEOS and aluminum isopropoxide were hydrolyzed in a mixture of 12DM34MBI⁺OH⁻ and TMAOH solution by stirring at room temperature for 24 hours. Next, excess amounts of water and alcohol species formed as the results of hydrolysis were evaporated under flowing air. Desired amount of hydrogen fluoride (HF, 45 wt. % in H₂O, Sigma-Aldrich) was added dropwise to the gel. (*Caution: Hydrogen fluoride is a dangerous substance that can cause fatal burns and irreversible damages to human skin, tissue, and bone. It must be handled with appropriate PPE including a lab coat, a respirator, a full-face shield, an acid-apron, a pair of long-sleeve nitrile gloves, etc. with a proper ventilation in a fume hood.*) The viscous transparent gel became powdery as a result of the addition of HF. The resultant fluoride gel was further dried in a fume hood for 1–2 days. A desired amount of distilled water was added to achieve the desired gel composition. Pure-silica LTA was added as the seed lastly. The final gel composition was 0.95–0.99 SiO₂ : 0.013–0.048 Al : 0.45 12DM34MBI⁺OH⁻ : 0.05 TMAOH : 0.50 HF : 5.0 H₂O. The crystallization was performed in a 125 °C static oven for 1–3 weeks. Increasing the aluminum contents in gels required longer crystallization times.

Zeolite Rho was synthesized using 18-crown-6 ether as the OSDA as Chatelain et al. have described.⁷⁰ Ludox HS-40 and sodium aluminate were used as the silica and alumina sources, respectively. The gel composition was 1 SiO₂ : 0.1 Al₂O₃ : 0.130 Na₂O : 0.030 Cs₂O : 0.050 18-crown-6 : 10.0 H₂O. The crystallization was performed in a 110 °C static oven for 2–8 days.

Zeolite KFI was synthesized without OSDAs.⁷¹ Zeolyst CBV712 was used as the sole silica and alumina source. Desired amounts of sodium hydroxide, sodium nitrate, and

potassium nitrate were dissolved in distilled water. After that, a desired amount zeolite Y was dispersed in the solution. The final gel composition was 1 SiO₂ : 0.0833 Al₂O₃ : 3.3 Na⁺ : 7.0 K⁺ : 0.56 OH⁻ : 9.74 NO₃⁻ : 117 H₂O. The crystallization was performed in a 140 °C static oven for 3 days. The same procedure was repeated for 3 times by wet-seeding the next batches with a portion of the previous batch used to enhance the crystallinity.

UZM-5 zeolite was prepared based on the charge density mismatch (CDM) synthesis strategy.⁴³ Colloidal silica AS-40 and aluminum isopropoxide were used as the silica and alumina sources, respectively. The final gel composition was 1 SiO₂ : 0.063 Al₂O₃ : 1.0 TEAOH : 0.125 TMAOH : 29.438 H₂O. The crystallization was performed in a 150 °C rotating oven for 10 days.

Other zeolites, high and low silica SSZ-16,⁷² SSZ-52,⁷³ SSZ-105,⁷⁴ SSZ-99,⁷⁵ SSZ-104,⁷⁶ SSZ-27,⁷⁷ SSZ-28,⁷⁸ and ITQ-3-type zeolite,⁷⁹ were thankfully provided by Dr. Stacey I. Zones, Dr. Dan Xie, and Dr. Tracy M. Davis from Chevron Energy Technology Company. The synthesis protocols of these zeolites are disclosed in the cited patents and articles.

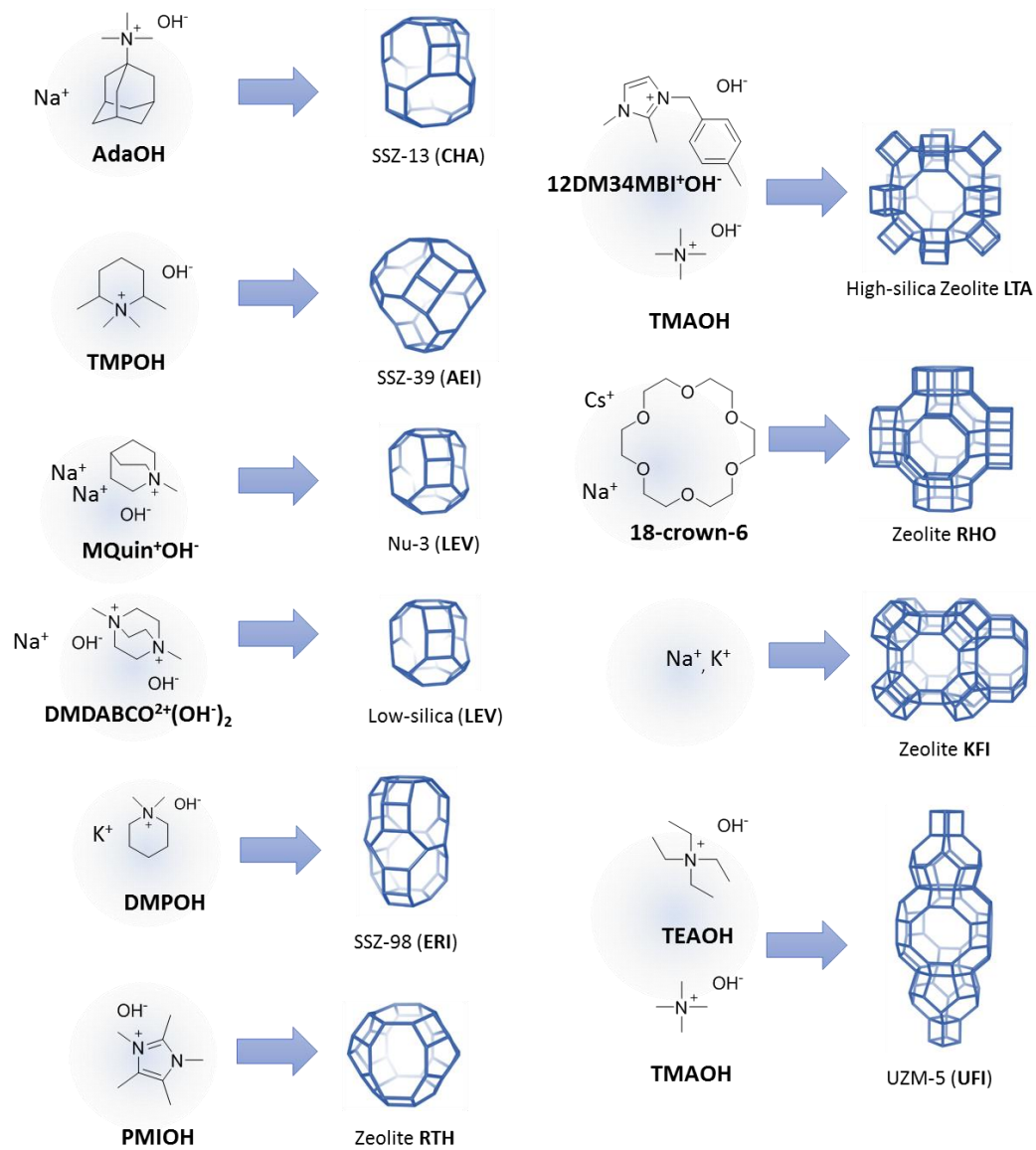


Figure 2.4. OSDAs and cage structures of the corresponding resultant zeolites.

2.2.3. Characterization of Microporous Materials

To identify the product catalysts, powder X-ray diffraction profiles were collected using a Rigaku Miniflex II benchtop diffractometer with Cu K α radiation ($\lambda = 1.54184 \text{ \AA}$).

Morphology and elemental composition of obtained molecular sieves were characterized using a field-emission scanning electron microscope (FE-SEM, ZEISS 1550VP) and an energy dispersive spectrometer (EDS, Oxford X-Max SDD).

2.2.4. MTO Reaction

All catalysts demonstrated in this work were tested in their NH_4 -forms or H-forms, if necessary, by repeated cycles of ion-exchange with 1 M ammonium nitrate solution. (1 g solid : 100 mL solution, 85 °C, 2–5 times until alkali elements are invisible in EDS spectra)

For every reaction, ca. 200 mg of catalyst was pelletized to be 0.18–0.60 mm in granule size. A pelletized catalyst bed was placed in a steel tubular reactor (0.25' in diameter and 6'' in length) between a pair of glass wool blocks. The bed was activated under an air flow at 580 °C for 12 hours. The dry weight of catalyst was estimated on the basis of a TGA profile which was separately acquired. (TGA: PerkinElmer STA6000) The reaction was conducted at strictly 400 °C. The methanol feed was diluted to be 10% in a carrier gas flow (95% He and 5% internal standard Ar, flow rate: 30 mL min^{-1}). Based on the dry weight of the catalyst bed, weight-hourly space volume of methanol (WHSV) was adjusted to be 1.3 h^{-1} . The product distributions were quantified using a GC-MS system (GC: Agilent GC 6890N, MS: Agilent MS 5973N). The reaction outlet flow was sampled every 16 min.

The amount of hydrocarbon products formed over the catalysts were evaluated by calculating the selectivities from the resultant GC-chromatograms. All selectivity values in this work were calculated on the carbon-number basis. The selectivity was defined as follows:

$$\text{Selectivity}(t = \text{TOS}) = \frac{\text{NC} \times n_{\text{product}}(t = \text{TOS})}{n_{\text{MeOH}}(t = 0) - n_{\text{MeOH}}(t = \text{TOS})}$$

where NC , n_{product} , and n_{MeOH} are the number of carbon atoms in a single hydrocarbon molecule, the molar flow rate of the hydrocarbon, and the molar flow rate of the methanol, respectively. The product distributions were calculated by averaging selectivities in the ranges of 98 to 100% methanol conversion.

2.3. Result and Discussion

2.3.1. Materials Characterization

In this section, PXRD patterns and SEM micrographs of obtained molecular sieves were provided. Also, elemental compositions of them are mentioned in the text. The Al contents of zeolites were expressed in Si/Al molar ratios. For AlPO_4 -based materials, M/T ratios ($M = \text{Si, Co, Mg}$; $T = M + \text{Al} + \text{P}$) were offered.

Four CHA-type molecular sieves (SSZ-13, SAPO-34, CoAPO-34, and MgAPO-34) were prepared for the MTO reaction study. PXRD patterns of the resultant materials are shown in Figures 2.5(a-d). All four molecular sieves showed PXRD profiles consistent with the CHA-topology and the previously reported results.^{20-21, 64} Minor differences in intensities and positions of the diffraction peaks are probably due to the difference among their elemental compositions. Figures 2.5(e-h) are the SEM images of these molecular sieves. These CHA-type molecular sieves had polycrystalline rhombohedral-to-cubic morphologies in common, and relatively large sizes (20–30 μm) except for SAPO-34. SAPO-34 showed a higher heteroatom concentration ($\text{Si}/T = 0.123$) than the other two MAPO-34s ($\text{Co}/T = 0.022$ for CoAPO-34, and $\text{Mg}/T = 0.015$).

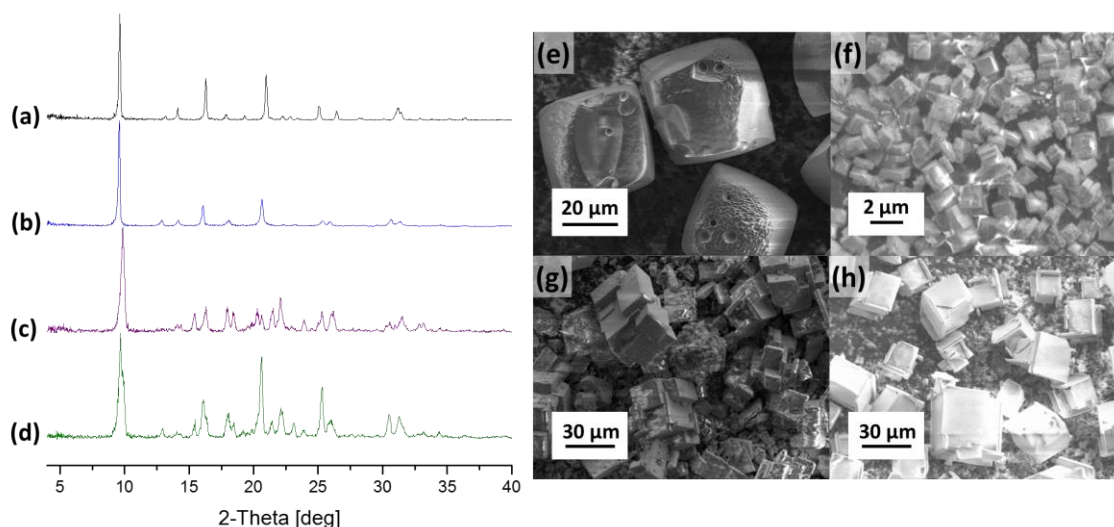


Figure 2.5. PXRD profiles of as-prepared (a) SSZ-13, (b) SAPO-34, (c) CoAPO-34, and (d) MgAPO-34. SEM images of (e) SSZ-13, (f) SAPO-34, (g) CoAPO-34, and (h) MgAPO-34.

SSZ-99 and SSZ-104 are CHA/GME-intergrowth zeolites.⁷⁵⁻⁷⁶ Since both CHA and GME belong to the ABC-6-type frameworks, the two topologies can coexist in one crystal by stacking faults of the *d6r* units along the *c*-axis. Figures 2.6(a, b) show the PXRD profiles of SSZ-99 and SSZ-104. The presence of the diffraction at $2\theta = \text{ca. } 7.5^\circ$ and generally broad shapes of peaks indicates that these are CHA/GME intergrowth zeolites. The crystal sizes were smaller than pure CHA-type molecular sieves shown above, and the Si/Al ratios of these zeolites were relatively low (Si/Al = 3.7 for SSZ-99, and 3.6 for SSZ-104).

SSZ-105 is another intergrowth zeolite of ERI and LEV.⁷⁴ Similarly to the CHA-GME pair mentioned above, both ERI and LEV also belong to the ABC-6 family, but these two frameworks have single-6-ring (*s6r*) layers unlike CHA and GME which are completely composed of *d6r* units. The PXRD profile of SSZ-105 (Figure 2.6(f)) showed broad peaks

related to both LEV and ERI, and it was reported that this diffraction pattern is consistent with the DIFFaX-simulated patterns for ERI-LEV intergrowth crystals.⁷⁴

SSZ-27 is a novel small-pore/cage zeolite having one-dimensional channel system.⁷⁷ It has a unique heart-shaped cage structure (Figure 2.6(h)) which resembles that of ITQ-55 that showed an excellent separation performance for ethylene-ethane mixtures,⁸⁰ but there is a difference in cage-connectivity between SSZ-27 and ITQ-55. The provided SSZ-27 had a Si/Al ratio of 14.7.

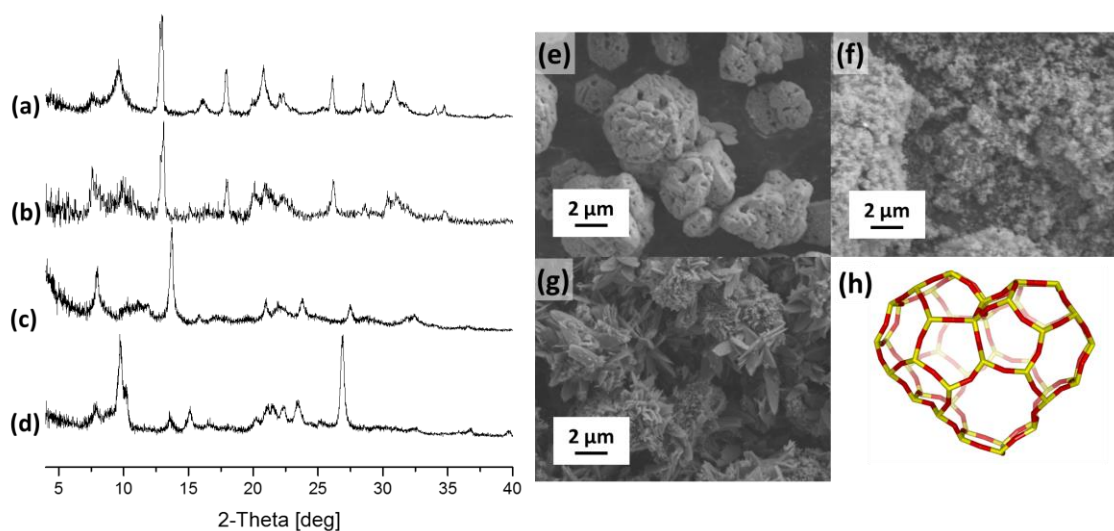


Figure 2.6. PXRD profiles of (a) SSZ-99, (b) SSZ-104, (c) SSZ-105, and (d) SSZ-27. SEM images of (e) SSZ-99, (f) SSZ-105, and (g) SSZ-27.

AFX and SFW are another two topologies belonging to the ABC-6-type frameworks. For AFX-type molecular sieves, two SSZ-16 zeolites and SAPO-56 were prepared. The two SSZ-16 had similar hexagonal morphologies, and the high-silica sample had a bigger crystal size (2–5 μm) than the low-silica sample (ca. 1 μm) (Figure 2.7(e–f)). The Si/Al ratios of the

two SSZ-16 were 14.7 and 6.2, respectively. SAPO-56 had a hexagonal disc-like morphology and a Si/T ratio of 0.137. The SFW topology was also realized as both zeolite and SAPO: SSZ-52⁷³ and STA-18.⁵⁸ The crystal size of SSZ-52 was ca. 1 μm , and its Si/Al ratio was 6.1. STA-18 had a polycrystalline hexagonal plate-like morphology, and the Si/T ratio was 0.176.

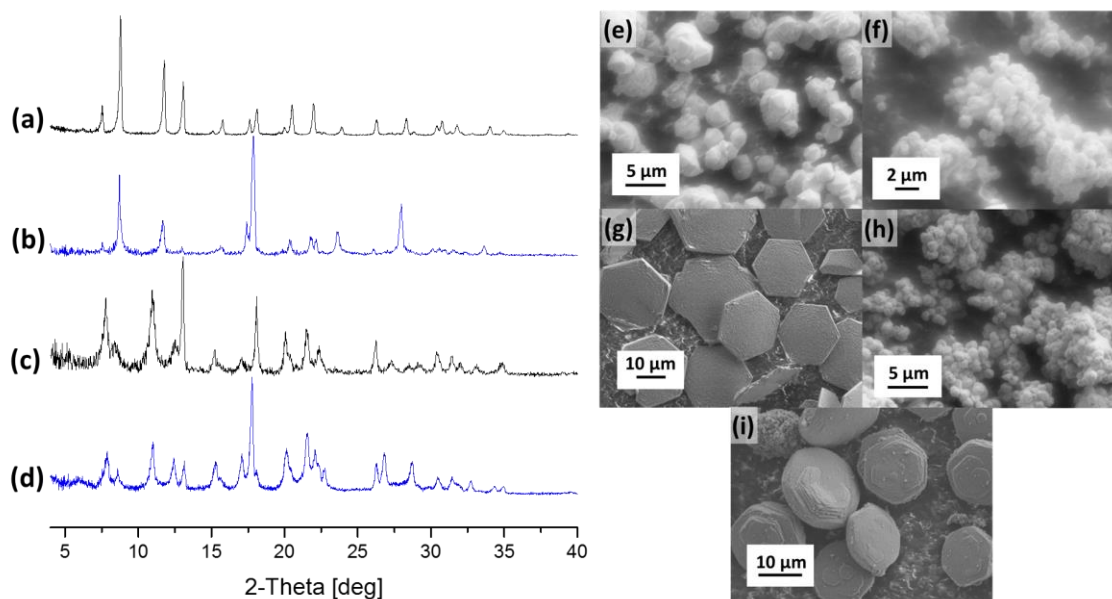


Figure 2.7. PXRD profiles of as-prepared (a) high-silica SSZ-16, (b) SAPO-56, (c) SSZ-52, and (d) STA-18. SEM images of (e) high-silica SSZ-16, (f) low-silica SSZ-16, (g) SAPO-56, (h) SSZ-52, and (i) STA-18.

For the LEV topology, two zeolites from two different OSDAs—MQuin⁺ and DMDABCO²⁺—and SAPO-35 were prepared. In this work, the LEV zeolite synthesized using MQuin⁺ is called Nu-3, and the other is called DMDABCO-LEV. The crystal sizes of both Nu-3 and DMDABCO-LEV were ca. 1 μm . (Figures 2.8(e–f)) The Si/Al ratios of Nu-3 and DMDABCO-LEV were 17.7 and 8.3, respectively. Contrary to the LEV-type zeolite

counterparts, SAPO-35 had a very large (ca. 20 μm) crystal size, and its Si/T ratio was 0.120. The ERI topology was realized as zeolite SSZ-98 which is recently discovered. Crystal size and Si/Al ratio of the synthesized SSZ-98 were 1–2 μm and 6.0, respectively.

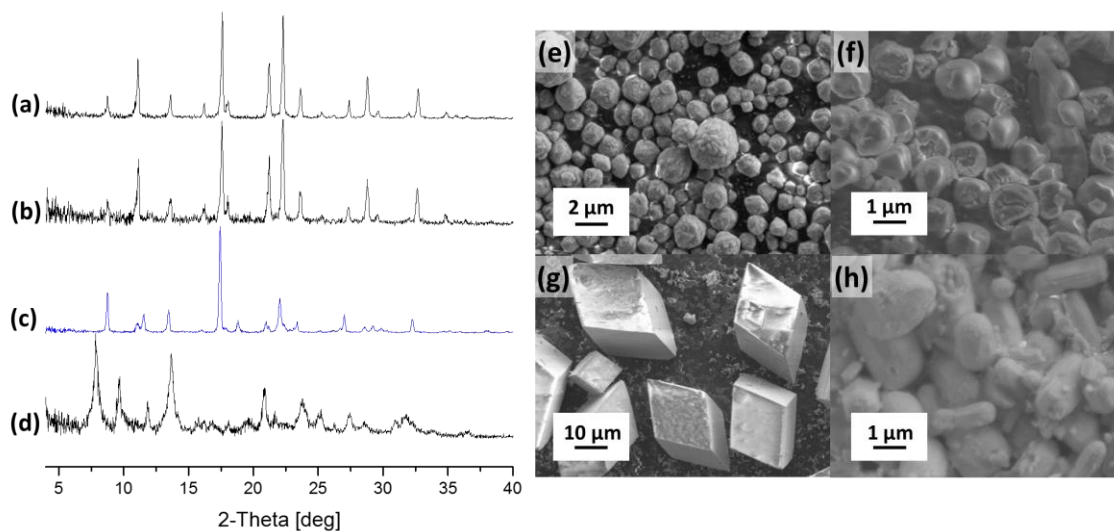


Figure 2.8. PXRD profiles of (a) Nu-3, (b) DMDABCO-LEV, (c) SAPO-35, and (d) SSZ-98. SEM images of (e) Nu-3, (f) DMDABCO-LEV, (g) SAPO-35, and (h) SSZ-98.

AEI is the other topology that was prepared as four different elemental compositions other than CHA. SSZ-39, SAPO-18, CoAPO-18, and MgAPO-18 were prepared and their PXRD patterns and SEM images are shown in Figure 2.9. Generally, the AEI-type molecular sieves had much smaller crystal sizes ($< 1 \mu\text{m}$) than the CHA-type microporous materials (*vide supra*). The Si/Al ratio of SSZ-39 synthesized without alkali cation was 10.0, and heteroatom molar ratios of AlPO_4 -18-based materials were 0.062, 0.073, and 0.031 for SAPO-, CoAPO-, and MgAPO-18, respectively.

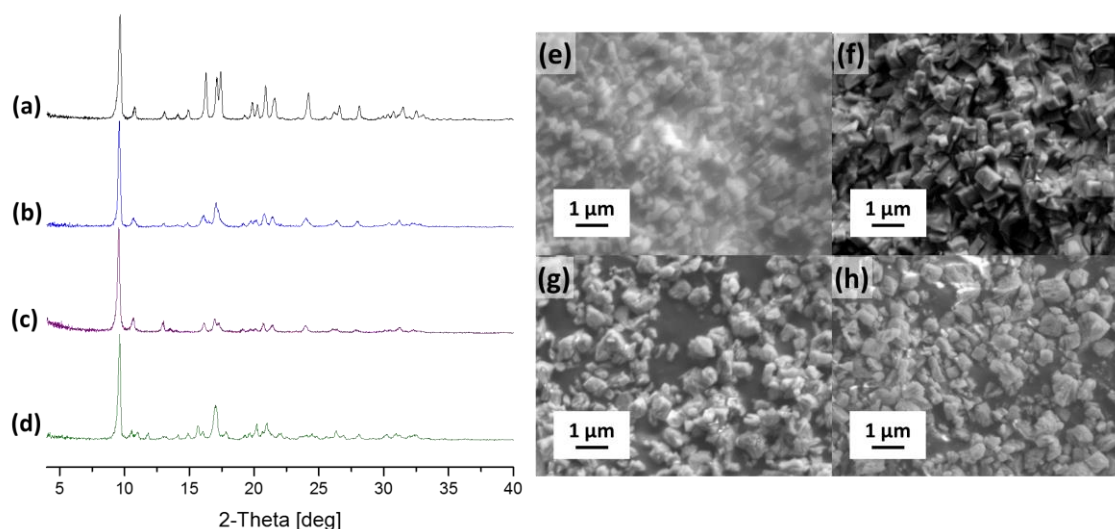


Figure 2.9. PXRD profiles of (a) SSZ-39, (b) SAPO-18, (c) CoAPO-18, and (d) MgAPO-18. SEM images of (e) SSZ-39, (f) SAPO-18, (g) CoAPO-18, and (h) MgAPO-18.

Figure 2.10. shows PXRD patterns and SEM images of several other small-pore zeolites and AlPO_4 -based molecular sieves. Since the frameworks DDR, RTH, and ITE have building units composed of odd numbers of T-atoms (e.g., 5-membered ring), AlPO_4 -based molecular sieves having these topologies cannot exist in principle. Also, zeolites having SAV topology are not discovered yet. Zeolite DDR (SSZ-28, Si/Al = 18.8), RTH (Si/Al = 13.2), and ITE (Si/Al = 18.1) tested in this work had moderately high Si/Al ratios and different morphologies and crystal sizes (Figure 2.10(e–g)). For SAV, Two STA-7 samples were prepared having different Si contents (Si/T = 0.133 and 0.185). They are denoted STA-7(1) (Si/T = 0.133) and STA-7(2) (Si/T = 0.185), respectively. Their crystal morphologies reflected their tetrahedral unit cell symmetries. SEM image of STA-7(1) is shown in Figure 2.10(h). (STA-7(2) is now shown here.)

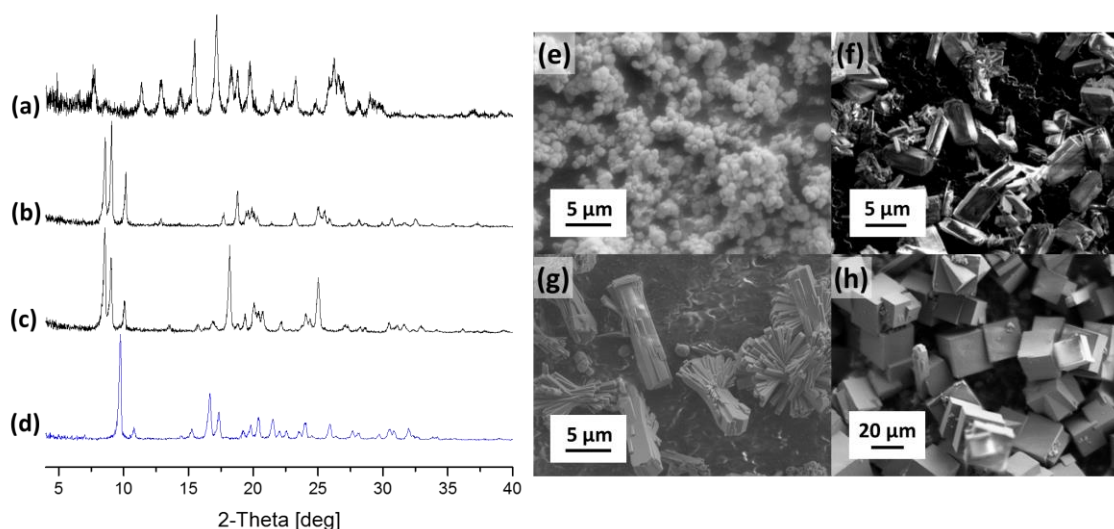


Figure 2.10. PXRD profiles of (a) SSZ-28, (b) Zeolite RTH, (c) Zeolite ITE, and (d) STA-7. SEM images of (e) SSZ-28, (f) Zeolite RTH, (g) Zeolite ITE, and (h) STA-7(1).

Four following topologies having LTA-cages were also prepared as zeolites and SAPO-based materials: LTA, RHO, KFI, and UFI. PXRD patterns and SEM micrographs of these molecular sieves are displayed in Figure 2.11. Similarly to DDR, RTH, and ITE mentioned above, UFI has building units (e.g. *rth* composite building unit) that is composed of odd number of T-atoms. So the topology UFI was realized as its only one known zeolite form, UZM-5. The other three LTA-cage-possessing frameworks are prepared both as zeolites and SAPOs.

High silica LTA zeolite and SAPO-42 represent the LTA framework here. They showed cubic or truncated-cubic topology, and their Si/Al ratio and Si/T ratio were 28.8 and 0.150, respectively. Zeolite RHO and SAPO-RHO (DNL-6) also showed truncated cubic crystal shapes. Zeolite RHO had a relatively low Si/Al ratio, 5.4. DNL-6 demonstrated a moderate Si content (Si/T = 0.140). Also Zeolite KFI had a low Si/Al ratio of 4.0, probably

due to the absence of bulky OSDA cations in its synthesis gel. A SAPO-version of KFI is STA-14, and it had a moderate Si/T ratio, 0.113. STA-14 and SAPO-42 could be synthesized from the same dual-OSDA system of K222 and TEAOH. STA-14 was the preferred product when TEAOH concentration in gels was high ($\text{TEA}^+/\text{K222}$ molar ratio > 5).

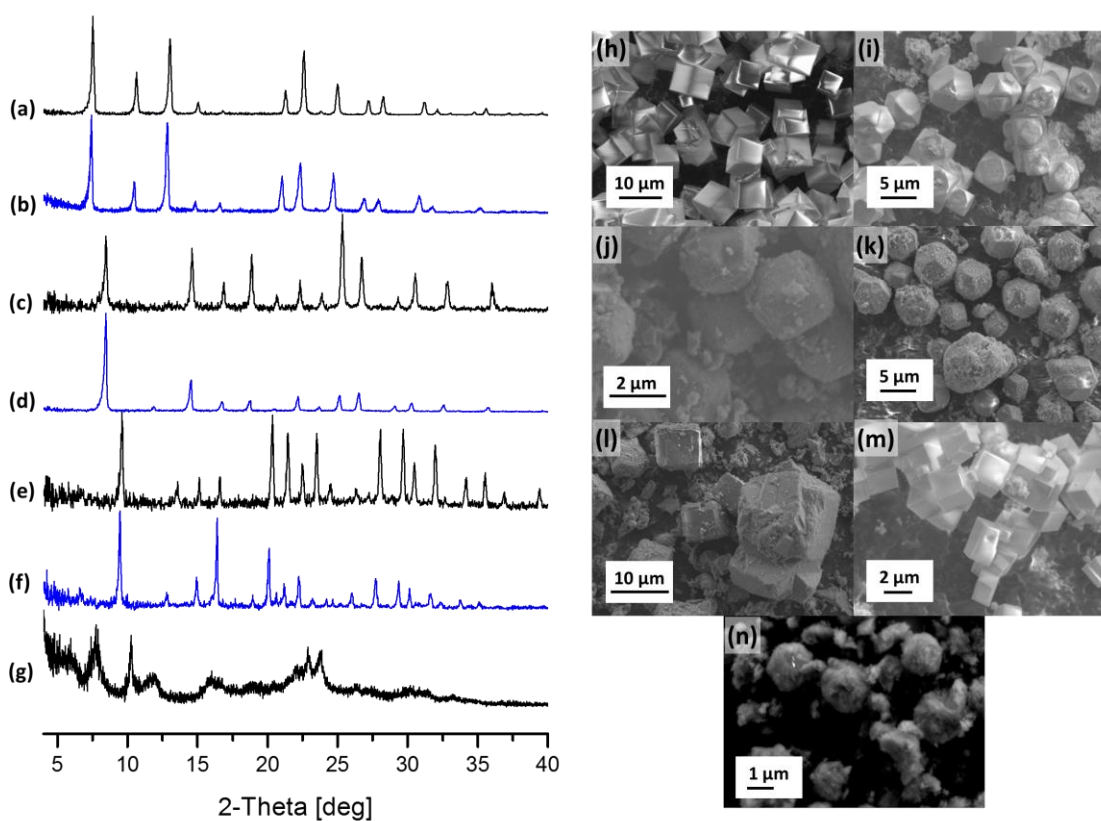


Figure 2.11. PXRD profiles of (a) Zeolite LTA, (b) SAPO-42, (c) Zeolite RHO, (d) DNL-6, (e) Zeolite KFI, (f) STA-14, and (g) UZM-5. SEM images of (h) Zeolite LTA, (i) SAPO-42, (j) Zeolite RHO, (k) DNL-6, (l) Zeolite KFI, (m) STA-14, and (n) UZM-5.

2.3.2. MTO Reaction Results

In this section, the MTO time-of-stream (TOS) selectivity charts of catalysts introduced in the previous section are exhibited. The extents of reactions are monitored by evaluating selectivities of light olefins (ethylene, propylene, and butylenes), alkanes (ethane, propane, and butanes), dimethyl ether (DME) and methanol conversion based on gas chromatograms taken every 16 min. All reactions are conducted at 400 °C with a methanol flow of $WHSV = 1.3 \text{ h}^{-1}$.

The CHA-type molecular sieves are the most extensively studied class of catalysts due to their high selectivities toward light olefins (ca. 85–90%) and excellent thermal stability and lifetime. All CHA-type catalysts shown here exhibited very high ethylene and propylene selectivities. SAPO-34, which is the catalyst being used in commercial processes,¹³ showed the longest lifetime (85% MeOH conversion at 259 min) among all four CHA-type catalysts. However, the lifetime cannot be the unique strength of SAPO-34 because it can be modified by controlling crystal sizes or nature of acid-sites.^{64, 81-83} Most importantly, since these catalysts are continuously regenerated by the co-operating regeneration unit in actual commercial MTO fluidized reactors,^{13, 84} the importance of lifetime performances of catalysts evaluated in an in-lab microscale fixed-bed reactor should not be overestimated.

SSZ-13 showed an ‘ethylene-propylene selectivity crossing’ behavior which has been observed in many previous reports.^{64, 85} Propylene was formed with a relatively constant selectivity, while the ethylene selectivity continuously increased from initial 29.3% to 46.3% at the onset of catalyst deactivation. This behavior different to that of SAPO-34 is known to be due to strong acidity of zeolites stronger than that of SAPOs.⁸⁶ Deimund et al. experimentally showed that this evolution of olefin selectivity significantly depends on the acid-site density of SSZ-13, and suggested that MTO behavior of SSZ-13 would eventually resemble that of SAPO-34 by increasing Si/Al ratio of SSZ-13.⁶⁴ However, regardless of the

acid-site density of the two types of materials, their ethylene-to-propylene selectivity ratios were close to unity.

MTO-catalytic performances of pure CoAPO-34 or MgAPO-34 have been very rare in literature up to date. CoAPO-34 and MgAPO-34 also showed very high overall light olefin selectivities (80–85%), but their lifetimes were shorter than SAPO-34, probably due to their large crystal sizes. Their olefin product distribution were also similar to that of SSZ-13. Cobalt (II) and magnesium can also form Brønsted acid sites within CHA-type AlPO_4 frameworks by replacing aluminum with moderate acidity.²⁰⁻²¹ According to the previous reports, both CoAPO-34 and MgAPO-34 have weaker structural Brønsted acidities than SAPO-34; on the basis of ammonia (NH_3)-temperature programmed desorption (TPD), both Co- and Mg-substituted AlPO_4 -CHA molecular sieves showed maximum ammonia desorption at approximately 350 °C, much lower than ca. 450 °C shown by SAPO-34.²⁰⁻²¹ Ashtekar et al. reported that CoAPO-34 was transformed to crystoballite during calcination at 450 °C,²¹ but such phase transition was not observed in this work. The PXRD pattern of used CoAPO-34 catalyst that had been calcined at 580 °C before its MTO reaction at 400 °C still matched well with a CHA and showed no diffraction peak corresponding to dense crystoballite phase. (not shown)

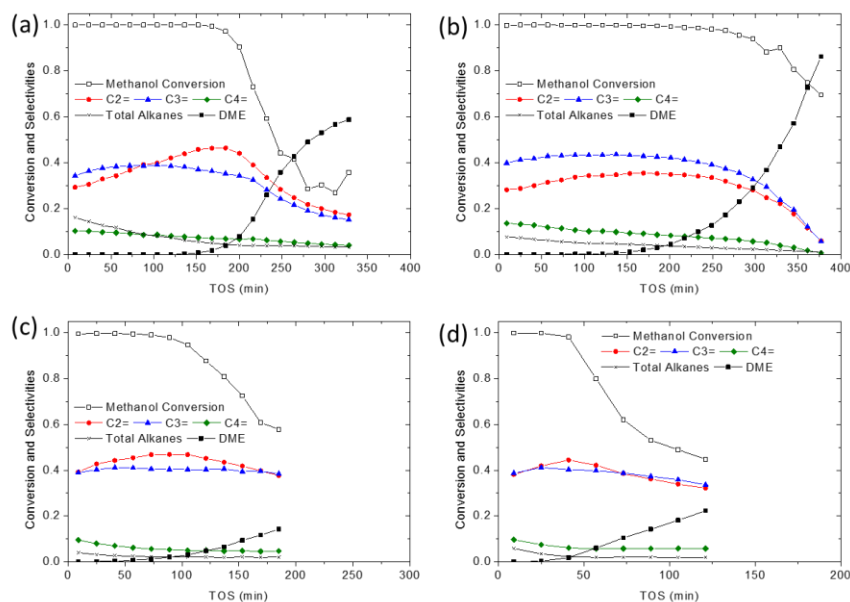


Figure 2.12. MTO-reaction time-on-stream profiles of (a) SSZ-13, (b) SAPO-34, (c) CoAPO-34, and (d) MgAPO-34.

AFX and SFW belong to the ABC-6 class, just like CHA, but have longer cages. Low-silica SSZ-16 and SSZ-52 showed very similar MTO behaviors (Figures 2.13(b–d)) and high-silica SSZ-16 (Figures 2.13(a)) also showed light olefin selectivities very similar to them, except for the initial alkane (propane) selectivity. From these zeolites, ethylene and propylene selectivities started with low values (ca. 10 %) but increased to approximately 35 % at the onset of catalyst deactivation.

The formation of propane particularly noticeable during the initial stage of reaction is known to have close correlation with the formation of polycyclic aromatics. High-silica SSZ-16 showed a lower initial propane selectivity (47.2 %) than that of low-silica SSZ-16 (68.9 %), and this result is consistent with the data observed from a series of SSZ-13 having different Si/Al ratios.⁶⁴ SSZ-52 showed the highest initial propane selectivity (71.5 %) among all catalysts demonstrated in this work. Also, SAPO-56 and STA-18 showed the

highest values of initial propane selectivities (14.8 % and 19.5 %, respectively) among all AlPO_4 -based molecular sieves tested here. Interestingly, all AFX and SFW-type molecular sieves demonstrated transient light olefin selectivities very similar to those of CHA-type materials shown above, even though they have much longer cages. One can discern that ethylene selectivity curves are almost overlapped onto propylene selectivity curves, implying that ethylene selectivity is almost equal to propylene selectivity at all stages of reaction.

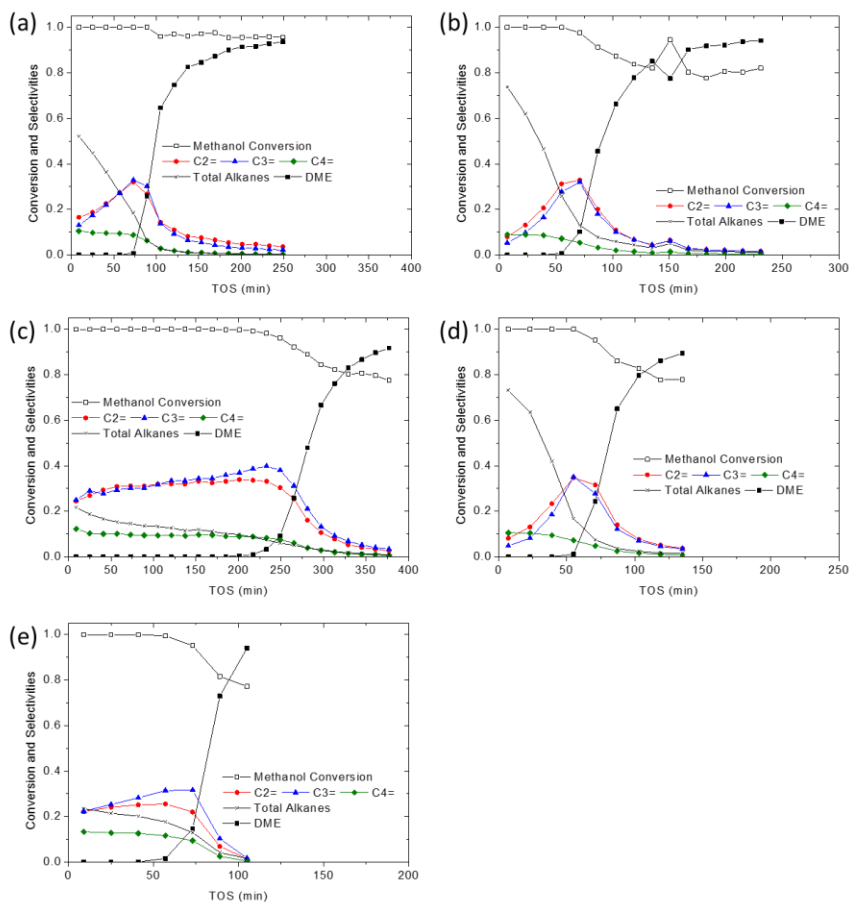


Figure 2.13. MTO-reaction time-on-stream profiles of (a) high-silica SSZ-16, (b) low-silica SSZ-16, (c) SAPO-56, (d) SSZ-52, and (e) STA-18.

SSZ-99 and SSZ-104 are another two zeolites having topologies crystallographically related to CHA. Since these materials have GME-type domains intergrown within the CHA frameworks, it can be said that these two zeolites have much “longer” cages than AFX or SFW, although they are not crystallographically well-defined. SSZ-99 and SSZ-104 showed relatively short lifetimes due to their low Si/Al ratios (3.7 and 3.6, respectively). Also, the initial propane selectivities were high (59.8 % and 59.6 %, respectively), which must be results in consistent with data observed from low-silica CHA having a high density of paired sites.⁶⁴

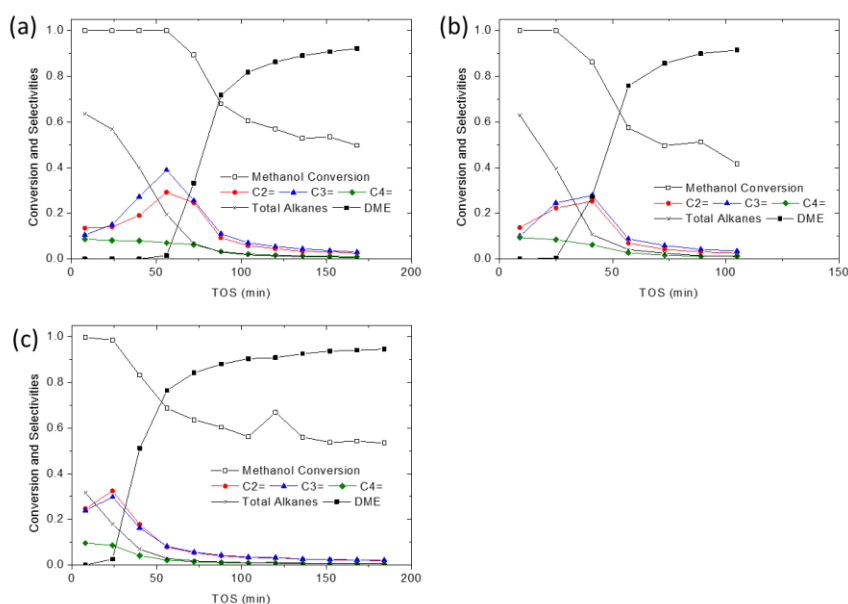


Figure 2.14. MTO-reaction time-on-stream profiles of (a) SSZ-99, (b) SSZ-104, and (c) SSZ-27.

SSZ-27 is the only zeolite that has a one-dimensional channel system among all tested catalysts in this work. Even though a cage can possess a hydrogen pool intermediate, if the presence of such bulky molecules impede the intracrystalline transport of reactants and products, the catalyst will deactivate quickly. Deimund et al. showed that frameworks having

low dimension channel systems have shorter lifetimes and lower amounts of coke build-up than materials (SSZ-13 and SAPO-34) with 3-dimensional channel connectivity.⁸⁷ Presumably due to the highly tortuous one-dimensional channel, SSZ-27 showed a poor lifetime despite its moderately high Si/Al ratio (14.7).

The LEV framework has the smallest cage among all topologies demonstrated in this work. MTO reaction data of two zeolites (Nu-3 and DMDABCO-LEV) and SAPO-35 were illustrated in Figures 2.15(a–c). The zeolites having LEV topology produced higher ethylene selectivities than propylene. Nu-3 having a higher Si/Al ratio (17.7) showed a longer lifetime than DMDABCO-LEV (Si/Al = 8.3). These results are in coherence with the result of AFX shown above and the study on SSZ-13 by Deimund et al.⁶⁴ SAPO-35 yielded more propylene than ethylene, but the ethylene-to-propylene ratio was increased over time of stream. This result is consistent with the previously reported results in literature.³⁸⁻³⁹ The short lifetimes of DMDABCO-LEV zeolite and SAPO-35 seem to be results of the cooperation of high acid-site density and 2-dimensional channel system of LEV.

SSZ-98 ERI showed very high ethylene selectivity, and the ethylene-to-propylene ratio also sharply rose over time. This ratio reached the maximum at the beginning of catalyst deactivation. A transient value of 2.07 was recorded at 95 % of methanol conversion. Another ERI-related intergrown zeolite, SSZ-105 has both ERI and LEV cages cooperating in a single catalyst, and also produced ethylene with very high selectivity. The ethylene-to-propylene ratio reached 2.59 at 98% of methanol conversion, and the overall transient behaviors of olefin selectivities resembled the case of SSZ-98. This implies that the presence of the ERI-type cage is responsible for the high ethylene selectivity in the MTO reaction of related zeolites.

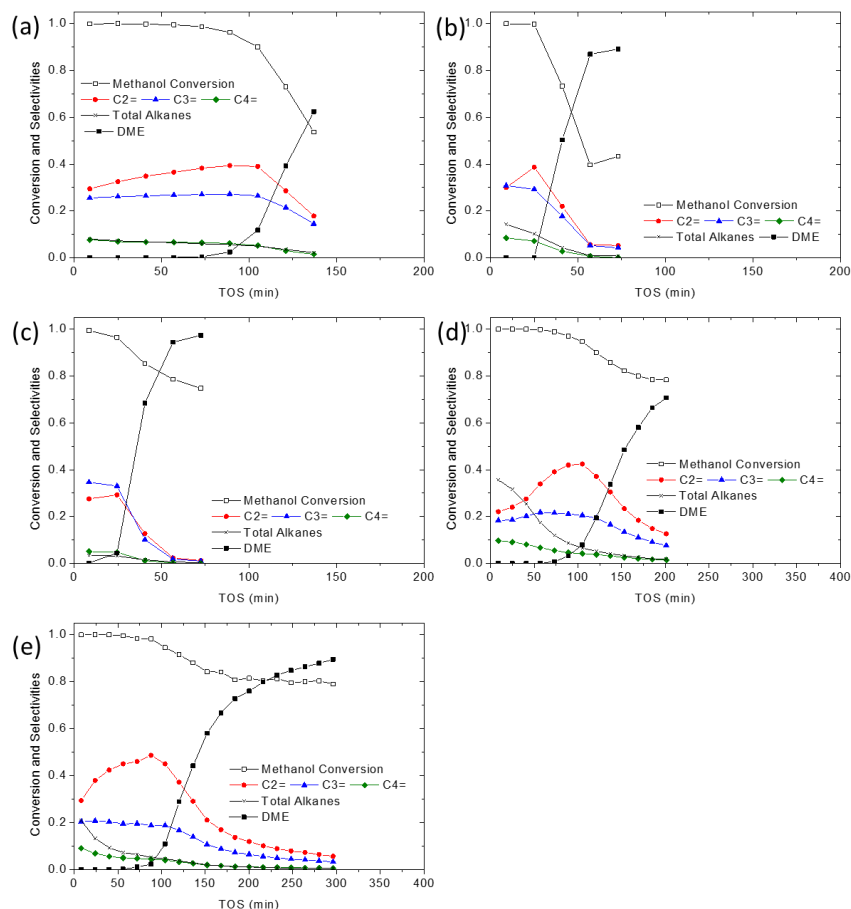


Figure 2.15. MTO-reaction time-on-stream profiles of (a) Nu-3, (b) DMDABCO-LEV, (c) SAPO-35, (d) SSZ-98, and (e) SSZ-105.

Similarly to the case of CHA-type catalysts, zeolite SSZ-39 and three AlPO_4 -based molecular sieves (SAPO-18, CoAPO-18, and MgAPO-18) were tested for the AEI topology. The MTO results of these AEI-type catalysts were separately reported by others,^{46, 67, 69, 88-89} and my results shown in Figure 2.16 were consistent with previous results. From all AEI-type catalysts, propylene was obtained as the predominant olefin product throughout all stages of catalysis. SAPO-18 showed the highest transient propylene selectivity of 50.8 %, and the other three AEI materials also produced high levels of propylene with selectivity

over 40 %. The lifetime of SAPO-18 was the longest (514 min for 85 % methanol conversion), while SSZ-39 and MgAPO-18 was deactivated the earliest. A high initial propane selectivity (34.3 %) was observed from SSZ-39 presumably due to the presence of paired acid-sites in the zeolitic surface.

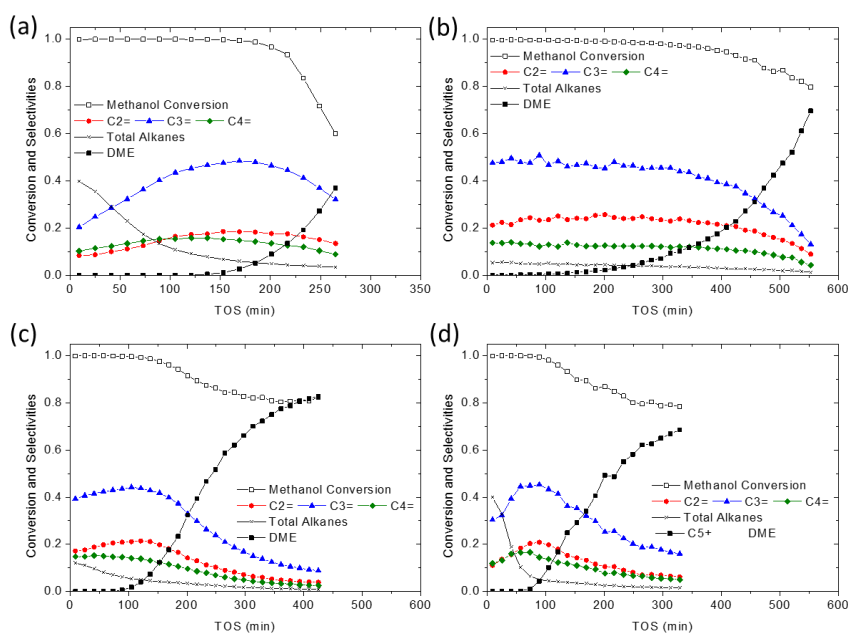


Figure 2.16. MTO-reaction time-on-stream profiles of (a) SSZ-39, (b) SAPO-18, (c) CoAPO-18, and (d) MgAPO-18.

It is noteworthy that the acid strength order of AlPO_4 -based molecular sieves of AEI framework determined by the NH_3 -TPD technique are different to that of CHA. In the case of CHA, SAPO-34 showed the ammonia desorption temperature higher than CoAPO-34 and MgAPO-34, as mentioned above ($\text{MAPO-34} < \text{SAPO-34}$).²⁰⁻²¹ However, it was reported that the ammonia desorption from SAPO-18 occurred at a low temperature (ca. 350 °C), lower

than the desorption temperatures of SAPO-34 and other AEI-type catalysts such as MgAPO-18 and CoAPO-18 (SAPO-18 < MAPO-18, SAPO-34).^{67, 88, 90} This difference in acidity may have affected each of MTO results of the tested AEI-type catalysts. However, it must be emphasized that, just like the CHA-series, all four AEI-type catalysts showed very similar MTO behaviors, particularly in terms of olefin product distribution.

Figure 2.17 shows MTO data of zeolite RTH and ITE, and two SAV-type SAPO molecular sieves, SAT-7. Similarly to the case of the AEI-type catalysts just shown above, these catalysts also yielded olefin product distributions with predominant propylene selectivities. RTH and ITE are structurally related frameworks having cages which are 2-dimensionally interconnected.¹⁶ Both zeolites showed high propylene selectivities with the lowest transient ethylene-to-propylene ratios lower than 0.5. (0.30 for RTH and 0.42 for ITE) These results are consistent with the literature.⁴⁷⁻⁴⁸ The high initial propane selectivity of zeolite RTH (47.1 %) which is higher than that of zeolite ITE (26.2 %) seems to be related to its moderately low Si/Al ratio resulting in the more paired Al-sites, given that the cage dimension of the two related topologies are very similar.

SAV is one of the four frameworks (CHA, AEI, SAV and KFI) that are composed only of the d6r units.¹⁶ Here, MTO behaviors of two STA-7 catalysts having different Si contents (Si/T = 0.133, denoted as STA-7(1); Si/T = 0.185, denoted as STA-7(2)) were investigated. The olefin product distributions and lifetimes of these SAV-type catalysts did not show a significant correlation to Si contents. It was previously reported that olefin product distributions from MTO reactions of SAV-type catalysts have a weak correlation to the acid-site density by Pinilla-Herrero et al.³⁸ STA-7(2) showed an initial propane selectivity (11.5 %) higher than that of STA-7(1) (8.9 %). Since no islanded-Si site was detected in the ¹H-decoupled ²⁹Si NMR spectra (not shown) of these SAV-type catalysts, the initial propane selectivities of these STA-7 samples must be explained on the basis of another reason other than the concentration of paired acid sites.

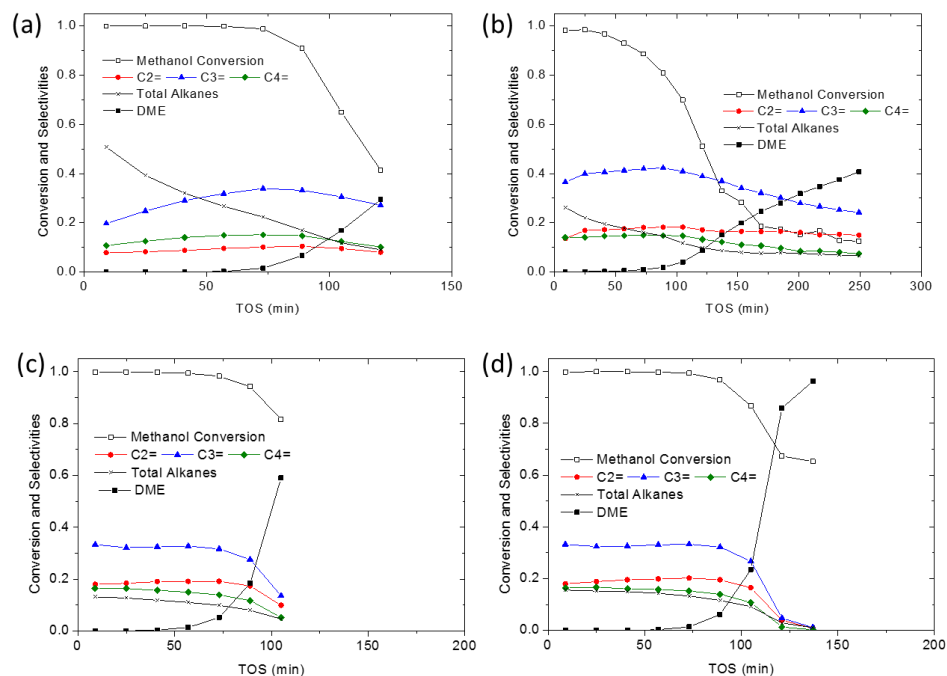


Figure 2.17. MTO-reaction time-on-stream profiles of (a) Zeolite RTH, (b) Zeolite ITE, (c) STA-7(1), and (d) STA-7(2).

The last group of catalysts investigated in this work is the group of LTA, RHO, KFI, and UFI. Unlike the other catalysts shown above, molecular sieves belonging to this group did not show any consistency regarding the ethylene-to-propylene ratios. Zeolite LTA and DNL-6 showed almost 1:1:1 selectivity ratios for ethylene, propylene, and butylenes. While zeolite RHO and KFI showed ethylene selectivities higher than propylene selectivities, SAPO-42 and STA-14 preferably converted methanol to propylene rather than ethylene. UZM-5 was deactivated quickly due to its low dimensionality (2D) of channel connectivity and low Si/Al ratio. These complex patterns shown by this group of molecular sieves will be discussed in the next chapter.

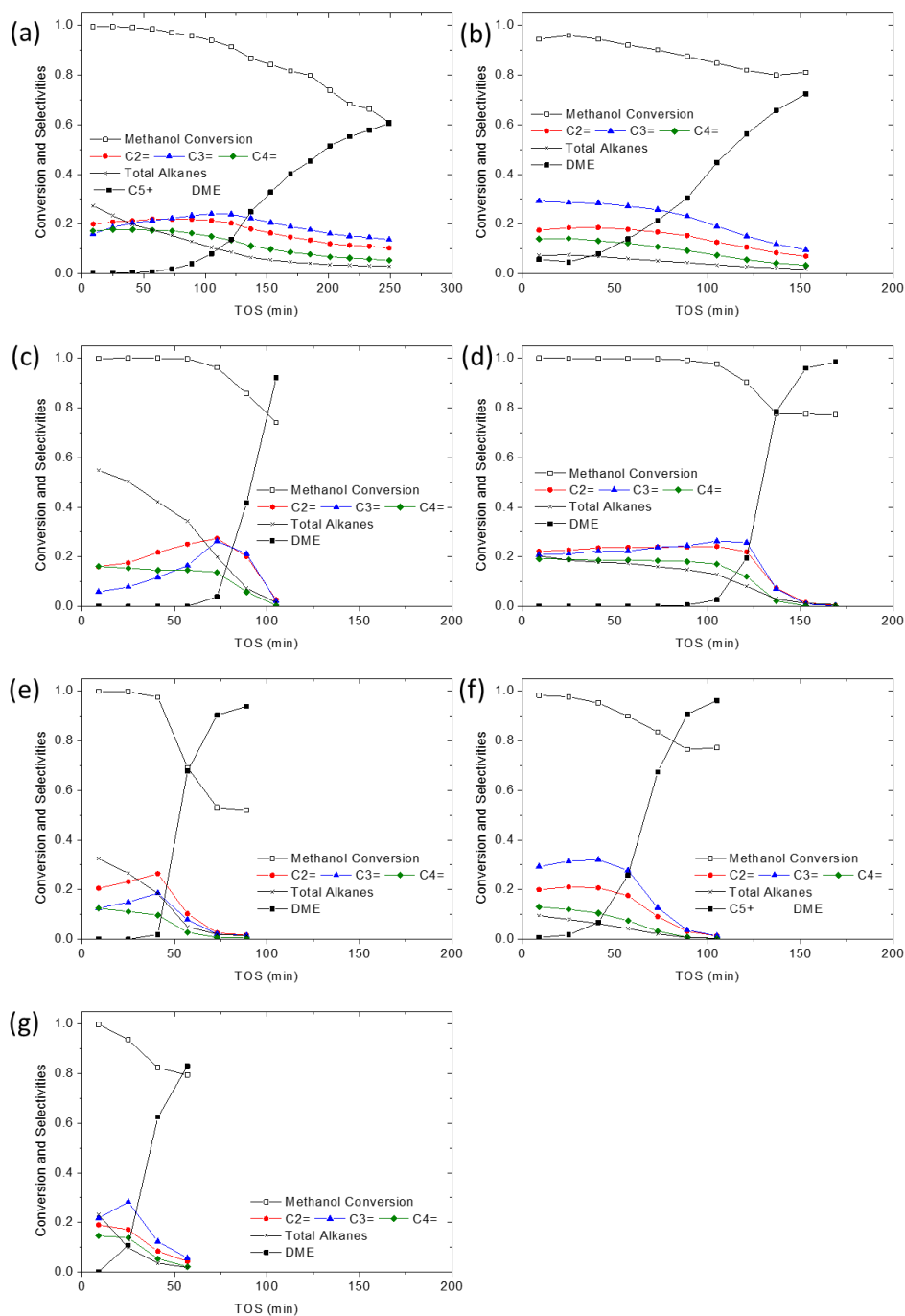


Figure 2.18. MTO-reaction time-on-stream profiles of (a) Zeolite LTA, (b) SAPO-42, (c) Zeolite RHO, (d) DNL-6, (e) Zeolite KFI, (f) STA-14, and (g) UZM-5.

2.4. Summary

In this chapter, the synthesis procedures of molecular sieves studied in this work and OSDAs used to prepare those molecular sieves were provided. The prepared molecular sieves were characterized based on PXRD, SEM and EDS to investigate their crystallinities, morphologies and elemental compositions. The MTO reaction data of the 30 molecular sieves were acquired, and the time-on-stream charts showing transient behaviors of MTO product selectivities were demonstrated. Regardless of elemental compositions, molecular sieves having the same topology showed very similar patterns of selectivities. Some topologies generated more propylene than ethylene, and some others showed ethylene-dominant selectivity patterns. Topologies like CHA, AFX, and SFW gave ethylene selectivities similar to propylene selectivities. Catalysts having LTA cages as their major cages showed very complex patterns of MTO product distributions. Also, catalysts having high concentrations of heteroatom (acid sites) showed high initial propane selectivities.

On the basis of the observation that the topology is more influential to the MTO product distributions than is the element composition, the studied topologies could be classified into four groups: ethylene similar to propylene, higher ethylene, higher propylene, and high butylenes. In the next chapter, the details of this categorization will be dealt with, and a new geometric factor which can correlate the cage geometry to the product distribution will be finally introduced.

Chapter 3

Categorization of Topologies based on Product Distributions and Cage-Defining Rings

In this chapter, the discussion part (investigation of the obtained product distributions, correlation to the cage topologies, introduction of a new geometric concept, cage-defining ring) of Part I of my thesis is presented. This chapter is a combined reconstitution of two of my publications: J. H. Kang et al., *ChemPhysChem* 2018, 19, 412 and J. H. Kang et al., *ACS Catal.* 2019, DOI: 10.1021/acscatal.9b00746. The majority of this chapter is adapted from the Result and Discussions part of my ACS Catalysis paper, but further augmented with the contents from my *ChemPhysChem* paper.

3.1. Introduction

The last chapter demonstrated the MTO time-of-stream data which show transient selectivity behaviors of 30 catalysts investigated in this work. A global pattern of the influence of topology on MTO product selectivity did exist. At a fixed temperature 400 °C, topologies could be grouped into 4 categories based on their product distributions. The first category gave almost one-to-one ethylene-to-propylene selectivity ratios. The second and third categories showed ethylene- and propylene-dominant product selectivity distribution patterns, respectively. The fourth category of topologies possessing the LTA cages in common yielded high butylene selectivities. This categorization of topologies was possible because those product distributions were primarily dependent on the cage topology rather than the elemental composition.

In this chapter, the MTO product distributions will be revisited on the basis of overall selectivities evaluated in the range of the maximum conversion of methanol (98–100%). The concept of cage-defining and its size which show a strong correlation to the four types of topologies will be introduced. A graphic abstract which summarizes the contents of this chapter is shown in Figure 3.1.

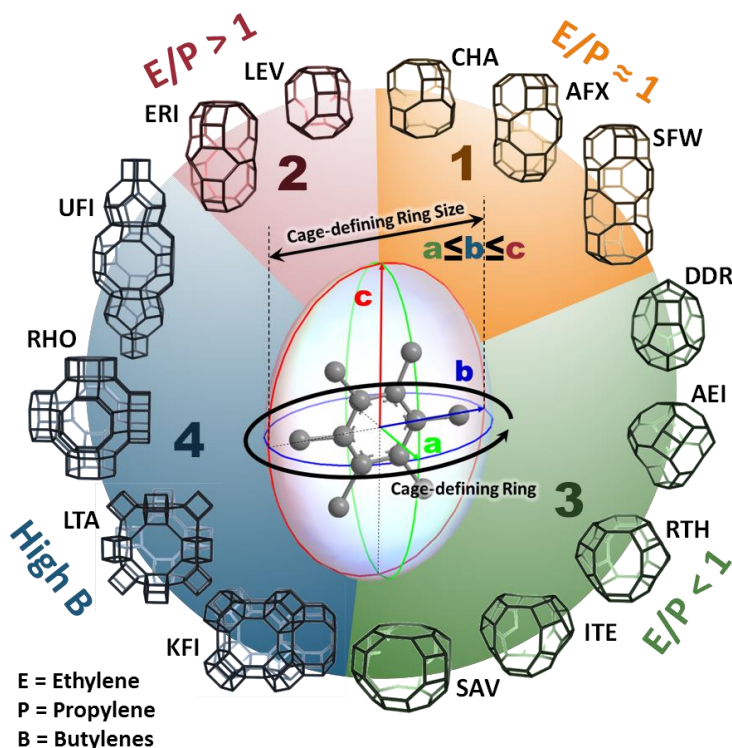


Figure 3.1. Schematic illustrations of 14 small-pore/cage topologies which were classified into four categories based on their olefin product distributions and the concept of the cage-defining ring.

3.2. Categorization of Topologies

On the basis of olefin selectivity distributions, the investigated topologies could be classified into the four groups as follows:

At the MTO reaction temperature of 400 °C,

- Category I: group of CHA, AFX, SFW, SSZ-99, and SSZ-104 which show even-balanced ethylene-to-propylene ratios close to unity. ($E/P \sim 1$)
- Category II: group of LEV, ERI, and SSZ-105 which show ethylene selectivities higher than propylene selectivities. ($E/P > 1$)
- Category III: group of DDR, AEI, RTH, ITE, and SAV which show propylene selectivities higher than ethylene selectivities. ($E/P < 1$)
- Category IV: group of LTA, RHO, KFI, and UFI which show no clear pattern of ethylene-to-propylene, but high butylenes selectivities with the LTA cages as their major cages in common.

3.2.1. Ethylene-to-Propylene Ratio

The product distributions from MTO reactions conducted at 400 °C were illustrated as bar charts in this chapter, as shown in Figures 3.2–3.5, and representing selectivity values were obtained by averaging selectivities of products in the range of 98–100% of methanol conversion.

Category I Figure 3.2. (a) shows the MTO product distributions of four CHA-type isostructural catalysts. Apparently, these CHA-type catalysts yielded strikingly similar product distributions despite completely different elemental compositions. The overall ethylene-to-propylene ratios were close to 1-to-1 at 400 °C. These results strongly support that the cage geometry plays the most important role in determining the resultant olefin

product ratio from MTO reaction. Also, these CHA-type catalysts showed the highest ethylene and propylene selectivities (85–90 %) among all tested topologies in this work and low butylenes selectivities (< 10 %), as mentioned in the previous chapter.

The only three frameworks that are built exclusively with parallel arrays of d6r composite building units are CHA, AFX, and SFW belonging to the ABC-6 family, as mentioned in the previous chapter.^{16, 91} In terms of the methanol-accessible regions within cages (see Figure A5), the cage length order is CHA (6.8 Å) < AFX (11.5 Å) < SFW (15.6 Å). In spite of this serious size difference, the ethylene-to-propylene ratios of these three types of cages were close to unity regardless of the elemental composition as shown in Figure 3.2(b). The AFX-type zeolite shown here is the high silica (Si/Al = 14.7) sample. The cage size order was the same to the total alkane selectivity (C₂₋₄) order and the initial propane selectivity order, regardless of elemental compositions. For the zeolite series, the total alkane selectivity order was 9.6 % for SSZ-13, 30.5 % for SSZ-16, and 48.8 % for SSZ-52, respectively. This sequence was the same to the case of SAPO-series (4.8 % for SAPO-34 < 13.1 % for SAPO-56 < 20.7 % for STA-18). The initial propane selectivity sequence of the zeolite series was 11.9 % for SSZ-13, 47.2 % for SSZ-16, and 71.5 % for SSZ-52, respectively. This order was the same to the total alkane order since the majority of produced alkane species was propane which is predominantly produced at the beginning stage of all reactions. The SAPO-series showed the same sequence (8.0 % for SAPO-34 < 14.8 % for SAPO-56 < 19.5 % for STA-18) for the initial propane selectivity.

The extension of the CHA-AFX-SFW series eventually reaches the GME framework. GME has straight 12-membered ring channels which is a topological result of its AABB stacking. (i.e., the 12-ring channel of GME can be seen as an extra-long cage having an infinite length.) However, large-pore zeolitic frameworks such as GME cannot hold the hydrogen pool intermediates of MTO reaction. And furthermore, thermally unstable GME zeolite undergo a phase transition to another 12-ring framework AFI at a high temperature

over ca. 280 °C.⁹² SSZ-99 and SSZ-104 are the CHA-GME intergrown zeolites.⁷⁵⁻⁷⁶ In these zeolites, CHA-portions form ‘end closures’ for intergrown GME portions, and the GME-to-AFI phase transformation was not observed. Also, there are still active CHA-type cages just like SSZ-13. Therefore, it is predictable that SSZ-99 and SSZ-104 will also show ethylene-to-propylene ratios close to one. Indeed, although their Si/Al ratios were low and lifetimes were short, these two zeolite yielded ethylene-to-propylene ratios close to unity as shown in Figure 3.2(c). High initial propane selectivities (63.6 % for SSZ-99 and 62.9 % for SSZ-104) were observed probably due to the high density of paired Al-sites originated from low Si/Al ratios of these zeolites.⁶⁴

Category II LEV and ERI form the second category of topology on the basis of ethylene-to-propylene ratios. As demonstrated in the previous chapter, most of the catalysts belonging to this category yielded transient ethylene selectivities higher than propylene except for SAPO-35. Figure 3.3 illustrates overall product selectivity distributions of all catalysts in this category. The MTO data of SAPO-17 performed at 375 °C and 425 °C were adapted from a work reported by Wilson and Barger in 1999.⁴⁴

Among all topologies demonstrated in this work, LEV has the smallest cages. There are several known topologies which have minor cages smaller than LEV-type cages. However, such cages are not capable of accommodating hydrogen pool intermediate species. Deimund et al. reported that ERS-7 (ESV), MCM-35 (MTF), SAPO-39 (ATN) and RUB-37 (CDO) showed very poor or almost no MTO activity at 400 °C and that no significant amount of occluded aromatic species was detected in the used catalysts.⁸⁷ Therefore, one can conclude that the LEV-cage is practically the lowest limit in size for the MTO reaction. The Liu group at the Dalian Institute of Chemical Physics (DICP) confirmed that no significant amount of fully-substituted hydrogen pool species was formed in LEV-type catalysts (SAPO-35 and RUB-50) on the basis of the *in situ* solid-state ¹³C NMR technique.³³⁻³⁴

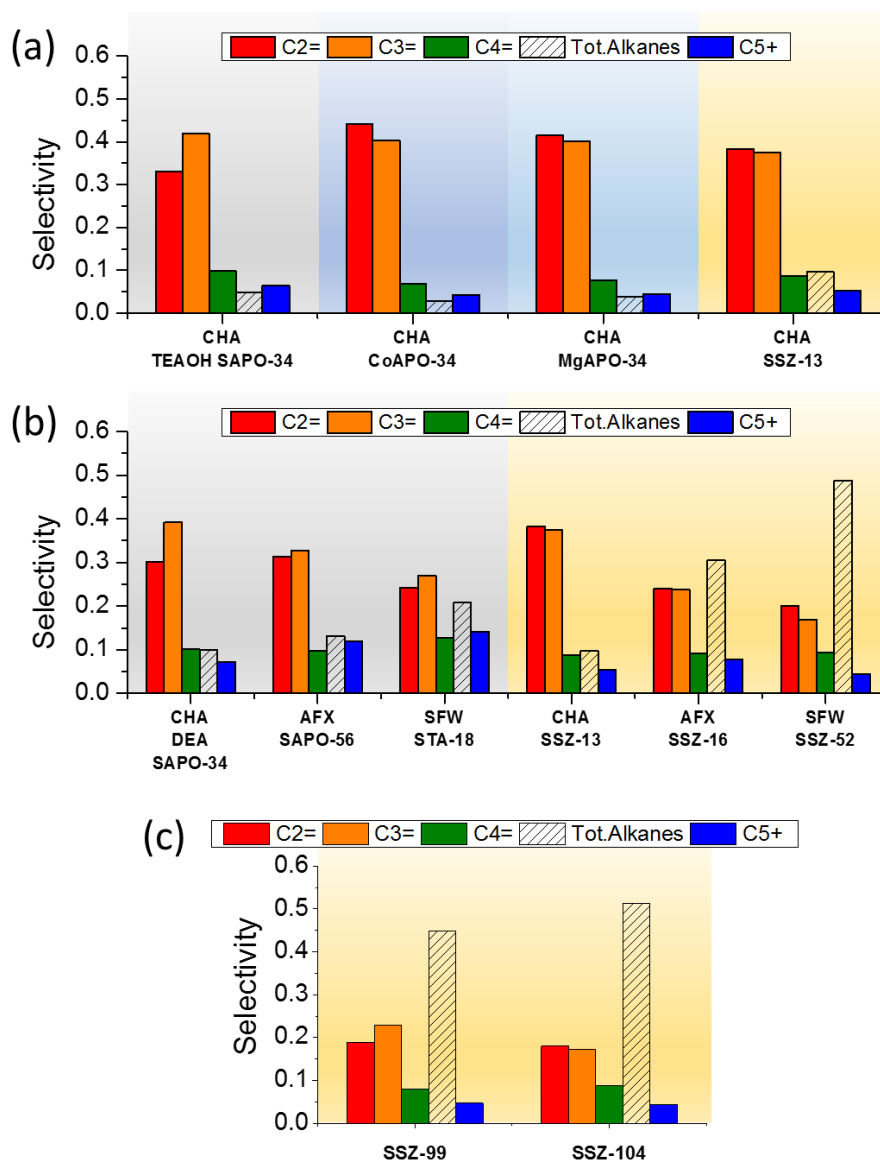


Figure 3.2. MTO product distributions when the methanol conversion is in the range of 98–100%: (a) four isostructural CHA-type molecular sieves, (b) two CHA-AFX-SFW series as SAPOs and zeolites, and (c) two CHA-related GME-intergrown ABC-6-type zeolites. The reactions are performed at $T = 400\text{ }^{\circ}\text{C}$ and $\text{WHSV}(\text{MeOH}) = 1.3\text{ h}^{-1}$.

Inasmuch as higher olefins are produced by aromatic intermediates having more and longer side chains,³⁷ it can be concluded that the confinement effect of small LEV cages is the main reason why ethylene and propylene are the main products of MTO reaction over LEV-type catalysts.

As demonstrated in the previous chapter, the two LEV zeolites synthesized from two different OSDAs having different Si/Al ratios produced more ethylene than propylene at all stages of reactions. It was reported that a LEV-type zeolite from another OSDA, 1-adamantylamine, also gave ethylene as the major MTO product.³² On the other hand, SAPO-35 showed a higher propylene selectivity than its ethylene selectivity despite the fact that SAPO-35 is a LEV-type molecular sieve. It is known that the ethylene-to-propylene ratios of SAPO-35 are depending on the Si-contents of the catalyst. Pinilla-Herrero et al. reported that the formation of islanded Si-sites is responsible for this trend and that SAPO-35 indeed produced more ethylene than propylene when Si/T ratio was higher than 0.140.³⁸ Interestingly, the transient ethylene-to-propylene ratio kept increasing with time of stream. As shown in Figure 2.15 in the previous chapter and Figure A9, the transient ethylene-to-propylene ratio was initially 0.80, but increased to 1.30 within an hour. However, the deactivation of SAPO-35 happened much earlier than that. This short lifetime of SAPO-35 is, as explained in the previous chapter, because of its large size of crystals (20–30 μm) and low-dimensional (2D) channel system. Most of MTO data of SAPO-35 in the literature show similarly short lifetimes of catalysts.^{38-39, 46, 93} As shown in Figure A9, the other LET and ERI-type catalysts also show sharply increasing transient ethylene-to-propylene ratios with time of stream, and deactivation occurs after the transient ratios became higher than unity. Also, this increasing trend of transient ethylene-to-propylene ratio was observed only from LEV and ERI-type catalysts. Other common MTO catalysts (CHA or AEI) did not show this type of rapidly increasing ethylene-to-propylene ratios, as illustrated in Figure A9. The origin of this behavior may be related to the transport (diffusion) processes within the porous

crystals,⁹⁴ but it is still not clear due to a lack of experimental evidence. Further investigation is required.

ERI is the other member of Category II. In terms of the methanol-accessible space (see Figure A6), an ERI cage (10.7 Å) is longer than a CHA cage (6.8 Å) and slightly shorter than an AFX cage (11.5 Å). But in terms of the diameter of the largest sphere that can be included, ERI (7.04 Å) is even narrower than LEV (7.10 Å). As shown in the previous chapter and Figure 2.15, SSZ-98 showed a very high overall ethylene-to-propylene ratio of 1.46 (transient maximum = 2.07). Other intergrown zeolites having ERI-type cages, such as ZSM-34 (ERI/OFF intergrowth)⁹⁵ or SSZ-105 (ERI/LEV intergrowth, this work) showed similarly high ethylene selectivities at 400 °C. These results strongly support the idea that the geometry of ERI-cage plays a crucial role to produce ethylene with high selectivity.

SAPO-17 is another ERI-type molecular sieve that gives very high ethylene selectivity. Wilson and Barger at UOP reported the ethylene-to-propylene ratios of 1.1 and 2.0 at 375 °C and 425 °C, respectively.⁴⁴ A similar result was reported by Nawaz et al. at 425 °C.⁵² Although these experiments were not conducted at 400 °C which is the standard temperature of this work, many works concluded that higher ethylene-to-propylene ratios can be achieved at higher reaction temperature within a temperature range of 350–450°C.^{32, 44, 46, 67, 88, 96} (Different reaction mechanisms undergo outside this temperature range.¹³) Therefore, on the basis of intrapolation, it can be deduced that, at 400 °C, the expected ethylene-to-propylene ratio from SAPO-17 will be approximately 1.4 to 1.5, which resembles the value from SSZ-98.

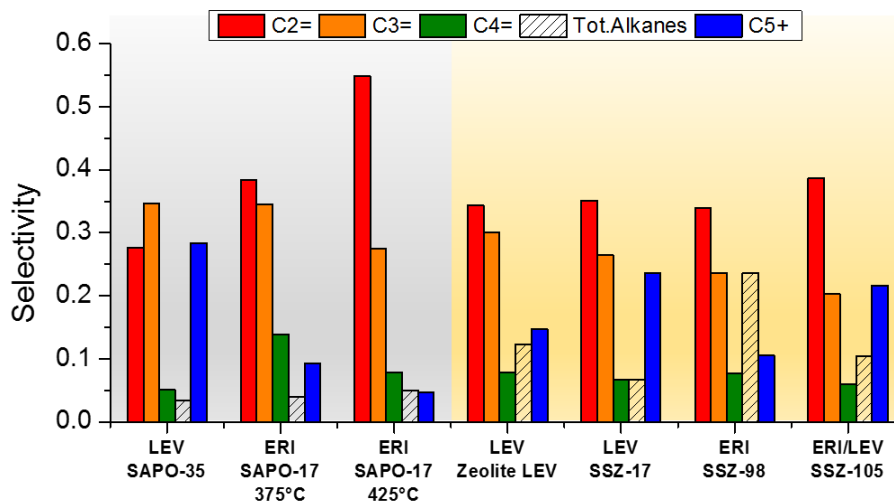


Figure 3.3. MTO product distributions when the methanol conversion is in the range of 98–100%. The selectivity data of SAPO-17 are reproductions of Wilson and Barger's work⁴⁴ and are obtained at $T = 375$ and 425 °C. The other reactions are performed at $T = 400$ °C and $WHSV(\text{MeOH}) = 1.3 \text{ h}^{-1}$.

Category III Four isostructural AEI-type catalysts (SSZ-39, SAPO-18, CoAPO-18, and MgAPO-18) were prepared and their MTO reactions were investigated at the same reaction conditions. The product distributions of the AEI-series catalysts were illustrated in Figure 3.4 (a). The observed product distributions were in coherence with previous reports in the literature.^{46, 67, 69, 88} Just like the CHA-series discussed above, the AEI-series also showed an impressive similarity regardless of elemental compositions. Again, these results solidly support the notion that it is the cage geometry that primarily determines the olefin product distributions. The overall alkane selectivity order (SAPO-18 < CoAPO-18 < MgAPO-18 < SSZ-39) can be results which were originated from differences among acid strength,^{67, 88-89, 97} but any conclusive statement could not be made here because the acid site density was not controlled. The SSZ-39 shown in this work was synthesized from a sodium-free gel, inspired by a related work on SSZ-13 where the paired-site density was controlled

by modifying gel Na/OSDA ratios.⁹⁸ However, no discernable difference between this sodium-free SSZ-39 and conventional SSZ-39 synthesized from gel containing sodium hydroxide⁶⁹ was observed.

MTO product distributions of three high-silica zeolites (DDR, RTH, and ITE) having 5-membered rings as their structural component were shown in Figure 3.4(b). As explained in the previous section, these three zeolites showed olefin product distributions with predominant propylene selectivities, which is consistent with the literature.^{32, 48, 99-100} The observed overall ethylene-to-propylene ratios of SSZ-28, zeolite RTH, and zeolite ITE were 0.62, 0.32, and 0.40, respectively. Corma et al. suggested that the RTH cage preferentially stabilizes fully substituted hydrogen pool intermediates which is responsible for its high propylene and butylene selectivity.⁹⁹ This is exactly opposite to the cases of SAPO-34 and LEV-type molecular sieves which prefer to possess partially substituted intermediates due to the spatial confinement effect.^{33-34, 99}

Two STA-7 molecular sieves with different Si/T ratios gave very similar ethylene-to-propylene ratios. The overall ethylene-to-propylene ratios of STA-7(1) and STA-7(2) were 0.58 and 0.59, respectively. The SAV frameworks actually have two distinct cage structures. Here, only the major cage was considered because the minor cage is too small to accommodate any hydrogen pool intermediates. In terms of the diameter of the largest sphere which can occlude the cage, the minor cage of SAV (6.33 Å) is much narrower than an LEV cage (7.10 Å) or an ERI cage (7.04 Å), and slightly larger than an MTF cage (6.25 Å) or an ESV cage (6.22 Å) which are not capable of harboring aromatic hydrogen pool intermediate species.⁸⁷ Considering the known kinetic diameters of partially substituted benzene (o-xylene, 6.8 Å) or fully substituted benzene (hexamethylbenzene, 7.1–8.0 Å),¹⁰¹ it is reasonable to assume that the minor cage of SAV plays a marginal role in hydrogen pool mechanism.

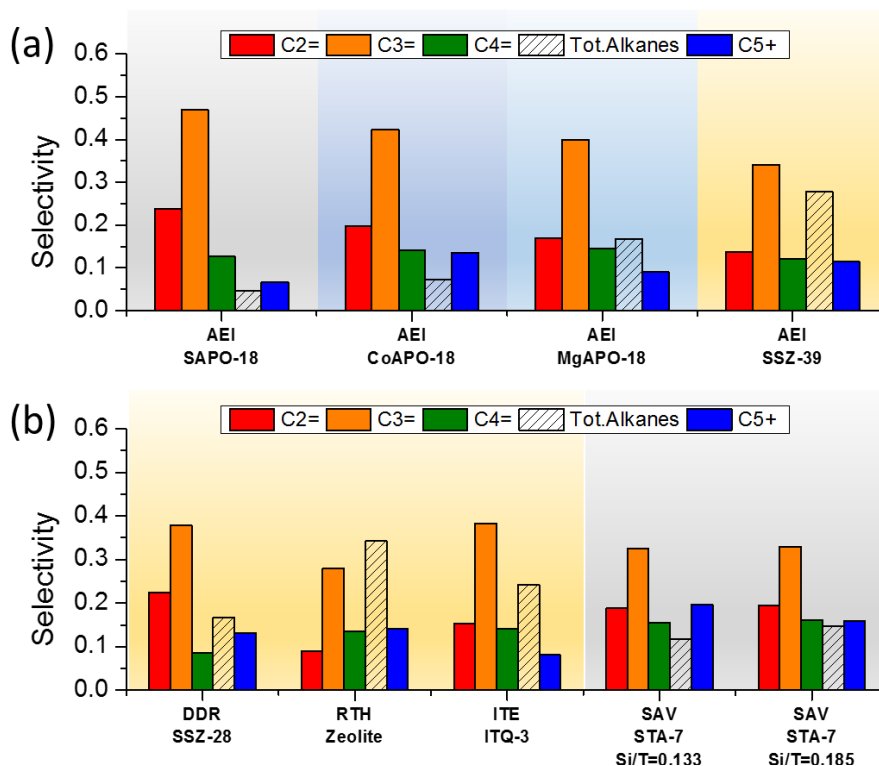


Figure 3.4. MTO product distributions when the methanol conversion is in the range of 98–100%: (a) four isostructural AEI-type molecular sieves, (b) three high-silica zeolites having DDR, RTH, and ITE-type topologies, and two SAPO materials having the SAV topology. The reactions are performed at $T = 400\text{ }^{\circ}\text{C}$ and $\text{WHSV}(\text{MeOH}) = 1.3\text{ h}^{-1}$.

Category IV The catalysts belonging to this category showed very complex patterns in terms of the ethylene-to-propylene ratio, as mentioned in the previous chapter. Unlike CHA, AFX, SFW, and AEI-type catalysts shown above, in this category, the influence of topology on ethylene-to-propylene ratios was weak. The high silica zeolite LTA gave an even-balanced ethylene-to-propylene ratio, while SAPO-42 clearly showed propylene-dominant product distribution patterns similar to those of SAV-type catalysts which belong to Category III. STA-14 gave a product distribution very similar to those of SAPO-42. The

similarity between STA-14 and SAPO-42 may be originated from their similar Si-distribution within frameworks caused by the use of the same OSDA (K222) for the formation of their LTA-cages. However, the KFI-type zeolite gave a very high ethylene-to-propylene ratio (1.59) which comes under Category II. Zeolite RHO also showed an ethylene-dominant product distribution, but the SAPO-material having RHO topology, DNL-6, showed a Category I-type ethylene-to-propylene ratio of 1.02. UZM-5 also showed an ethylene-to-propylene ratio (0.87) that is very close to unity.

The main cage structure of these four topologies is the same LTA cage having the same connectivity. But there are small differences among the cage sizes and 8-ring pore window dimensions due to the steric influence from secondary building units. In terms of the largest sphere that can be included in cavity, the size order is as follows: LTA (11.05 Å) > KFI (10.67 Å) > RHO (10.43 Å) > UFI (10.09 Å). The minor cages of UFI has a sphere diameter of 5.92 Å which is too small to contain hydrogen pool intermediate species. This size order has no correlation with the ethylene-to-propylene ratios. The sizes of these LTA cages are much larger than most of hydrogen pool intermediates such as hexamethylbenzene having a kinetic diameter of 7.1 Å.¹⁰¹ So these cages may have weak limiting abilities that can control the side-chain lengths of small aromatic intermediates. Li and co-workers calculated the stabilization energies of carbonium ions with different lengths of side-chains (methyl, ethyl, isopropyl, and isobutyl) within the SAPO-35 (LEV), SAPO-34 (CHA), and DNL-6 (RHO) topologies.³³ Unlike the LEV and CHA cages, the LTA cage showed similar stabilization energies of large negative values for all type of intermediates due to the lack of steric hindrance, which implies no preference in side-chain lengths.³³ Thus, for the topologies of Category IV, the final MTO product distributions may be dependent more on secondary factors such as the acid-site distributions of cage walls. More experimental investigation is required on this topic. Although the catalysts in this category did not exhibit coherent behaviors in terms of the ethylene-to-propylene ratios, all of them produced distinctly high butylenes selectivities, which will be discussed in the next section.

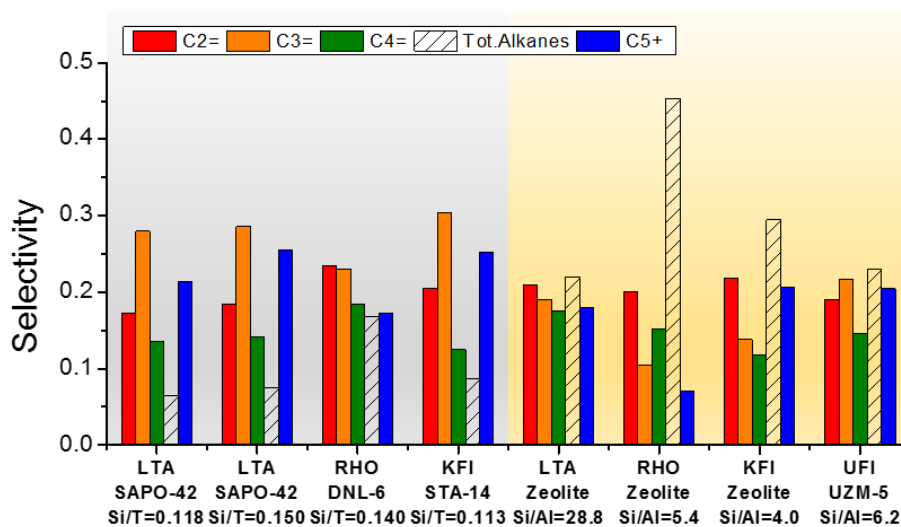


Figure 3.5. MTO product distributions of zeolites and SAPO-molecular sieves having LTA, RHO, KFI, and UFI-type topologies when the methanol conversion is in the range of 98–100%. The reactions are performed at $T = 400\text{ }^{\circ}\text{C}$ and $\text{WHSV}(\text{MeOH}) = 1.3\text{ h}^{-1}$.

3.2.2. Butylene Selectivity

Butylenes are another important products from the MTO reaction. There are many suggested pathways for the formation of butylenes (isomers of C_4 olefin). They can be formed from the pairing mechanism and/or side-chain mechanism in which hydrocarbon pool aromatics are involved.^{9, 13} Propylene can also be upgraded to butylenes by reacting with methanol and/or by cracking of higher olefins in the alkene cycle.⁸ The suggested mechanistic pathways that yield butylenes are illustrated in Figure 3.6. Though the elucidation of the origin of C_4 olefin formation mechanism is out of the scope of this work, the correlation between the cage structures and the observed butylenes selectivities could be established from the experimental results of this work.

On the GC-MS chromatograms (not shown) all four isomers of butylenes (1-butene, trans-2-butene, cis-2-butene, and isobutene) could be detected from the MTO reaction effluents. However, on chromatograms, peaks of these C₄ olefin isomers were partially overlapped with those of saturated C₄ paraffin isomers (n-butane and isobutane). For this practical reason, in this work, the integrated (sum) selectivity of all butylene isomers were evaluated. The contribution of overall butylene selectivity in final olefin product distributions was quantified on the basis of the ratio ($2S_B/(S_E+S_P)$) of overall butylene selectivities (S_B) to the average of ethylene and propylene selectivities ($(S_E+S_P)/2$). This ratio is denoted as *the butylene contribution ratio* here. The butylene contribution ratios of all MTO catalysis runs were displayed in Figure 3.7 together with the ethylene-to-propylene ratios.

As mentioned in the previous section, all four members (LTA, RHO, KFI, and UFI) of Category IV gave very high butylene selectivities. The butylene contribution ratios of these catalysts were similar to or higher than 0.5 regardless of their elemental compositions, as shown in Figure 3.7. Zeolite RHO (0.99), High-silica zeolite LTA (0.87), and DNL-6 (0.73) gave the highest butylene contribution ratio among all tested catalysts. Interestingly, the latter two catalysts showed almost even-balanced selectivity ratios across ethylene, propylene, and butylenes. (*i.e.*, ca. ethylene:propylene:butylene = 1:1:1) The lowest butylene contribution ratio among Category IV was observed from STA-14 (0.49). However, this value is still higher than most of the catalysts from the other categories, such as SAPO-34 (0.29) or SAPO-18 (0.36). Pinilla-Herrero et al.³⁹ and Li et al.³³ also previously reported high butylenes selectivities from SAPO-42 and DNL-6, respectively. Pinilla-Herrero and co-workers suggested that the high butylenes selectivity observed from SAPO-42 could be due to the wide pore of LTA ($4.1 \times 4.1 \text{ \AA}$).³⁹ However, this theory cannot explain the high butylene selectivities observed from the RHO-type catalysts that have pore openings ($3.6 \times 3.6 \text{ \AA}$) narrower than SAPO-34 ($3.8 \times 3.8 \text{ \AA}$).

Some of the catalysts from the other categories also gave high butylene selectivities. Based on the butylenes contribution ratio, the following topologies yielded high butylene selectivities other than the Category IV catalysts: AFX, SFW, SSZ-104, and all Category III catalysts except for DDR. One thing in common among these topologies is the sheer size of the cage. AFX and SFW have large and elongated cages. SSZ-104 has intergrown GME domains which can provide large spaces within its 12-ring large-pore channels. DDR has the smallest cage among the Category III catalysts. Unlike ethylene and propylene, it can be concluded that the butylene selectivity seems to have a relationship with the volume of cages. Wider cages may be able to provide extra spaces for other mechanisms of MTO reaction such as the alkene cycle, but it was not investigated in this work.

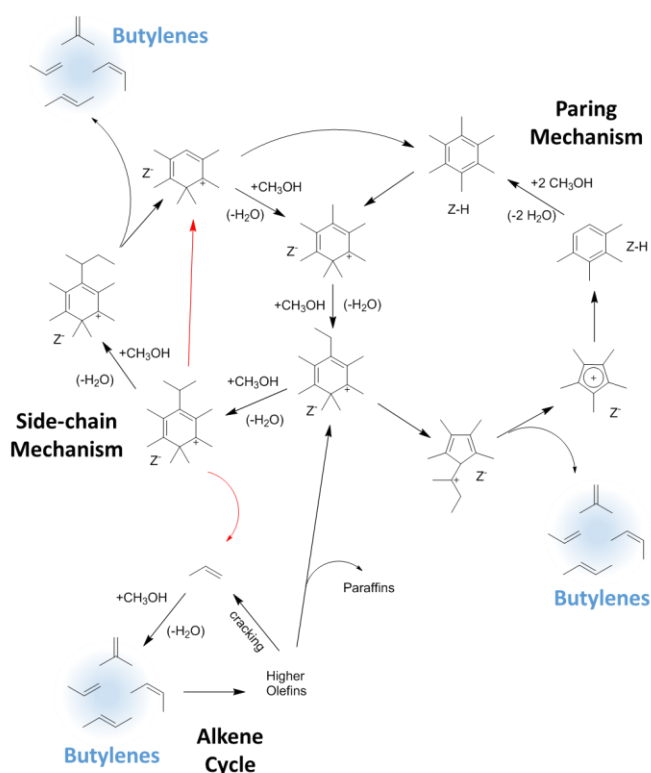


Figure 3.6. Suggested mechanistic pathways for the formation of butylenes. Z-H and Z⁻ refer to the zeolite Brønsted acid site and its conjugate base, respectively.

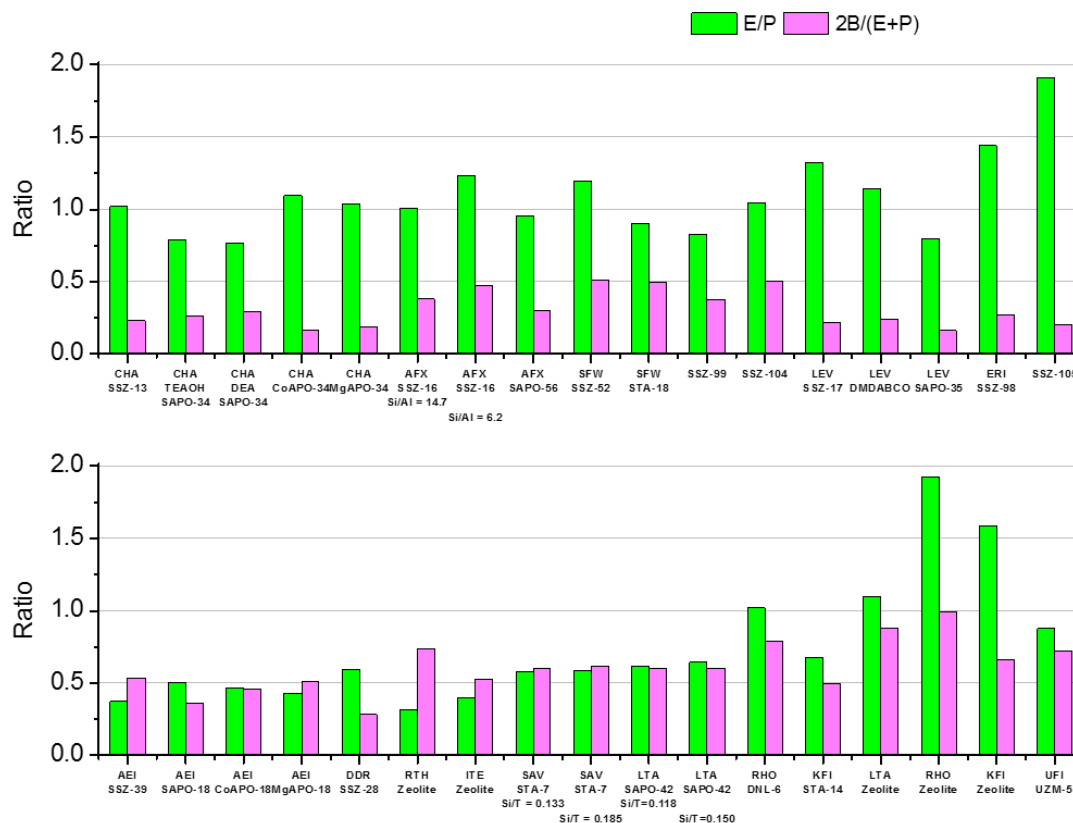


Figure 3.7. Ratios of light olefin selectivities (E; ethylene, P: propylene, B: butylenes) of all catalysts investigated in this work. All reactions are performed at 400 °C and $WHSV(\text{MeOH}) = 1.3 \text{ h}^{-1}$.

3.2.3. Initial Propane Selectivity

From the MTO reactions, not only light olefins but also small paraffins (ethane, propane, and butanes) are obtained as co-products. The majority of these alkane products is propane which takes up more than 80 % of total alkane selectivities. In the fixed-bed reactors, most of propane formed from the methanol conversion is observed at the very initial stage

(time on stream < 15 min, $g_{\text{MeOH}}/g_{\text{cat}} < 0.33$) of reaction. From the most of time of stream data shown in the previous chapter, particularly for zeolites, high total alkane selectivities (in fact, mostly propane) are observed in the initial stages of methanol injection. The formation of this ‘initial propane’ has been linked to the formation of polyaromatic species within cages.²⁷⁻²⁸ Later, it was found that the formation of alkanes is involved in the cyclization of higher olefins into aromatic hydrogen pool intermediates in the dual-cycle mechanism in ZSM-5.^{30, 102-103} The initial propane selectivity itself has a strong correlation with the acid strength and acid-site density.^{102, 104-105} Deimund et al. reported that there is a strong correlation between the acid site density in SSZ-13 and the initial propane selectivity,⁸⁷ and similar trends were also observed in this work from LEV- and AFX-type zeolites.

The observed initial propane selectivity values taken at the initial stage (TOS = 7–9 min) of the methanol injection from all zeolites and SAPO-based catalysts were plotted with respect to the heteroatom concentration (Figure 3.8). Apparently, zeolites generally yielded more initial propane than SAPO-based catalysts. The initial propane selectivity from various zeolites spanned even over 70 % depending on the topology and Si/Al ratio, while the highest propane selectivity for SAPOs was observed from STA-18 (19.5 %) having an SFW topology. Considering the fact that SAPO-based molecular sieves generally have milder acid sites than the isostructural zeolites, this result is consistent with the previous study which concluded that catalysts with stronger acid sites yield more initial propane.¹⁰⁵

Interestingly, the topology was another important factor that determines the initial propane selectivity. Generally, large and wider cages gave more initial propane. For zeolites, the initial propane order was SFW, AFX > AEI, RTH, LTA, RHO > CHA > LEV, ERI. The SAPO-based catalysts showed a roughly similar trend: SFW > RHO > AFX > SAV > CHA, KFI > LTA > LEV. In both zeolite and SAPO systems, SFW-type catalysts yielded the highest initial propane selectivities, and LEV-type catalysts gave the least amounts of initial propane regardless of elemental composition. Given that the SFW is one of the largest cages

among the tested topologies and that LEV is the smallest one, it can be concluded that the initial propane selectivity has a significant relation with the cage size.

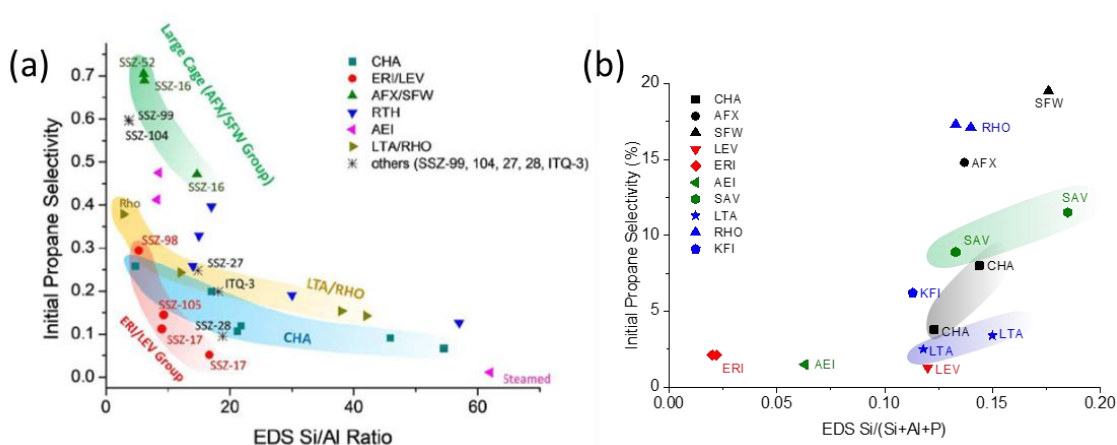


Figure 3.8. Effects of heteroatom concentration (Al in zeolites, and Si in SAPOs) and topology on the initial propane selectivities (time on stream = 7–10 min) of catalysts: (a) zeolites and (b) SAPOs. Some of the initial propane data points of SSZ-17 (Nu-3),⁴¹ zeolite RTH,⁴⁸ zeolite LTA,⁶² zeolite RHO,¹⁰⁶ SSZ-13,⁶⁴ and SSZ-39⁶⁹ are reproduced from articles previously published by our research group.

3.3. Concept of Cage-Defining Ring

3.3.1. Basic Idea and Development of Concept

A lesson from the large collection of data provided here is that the topology is the most important factor that primarily determines the final MTO product distributions at a fixed temperature. In this section, a new structural indicator that can be used to characterize these topologies will be introduced.

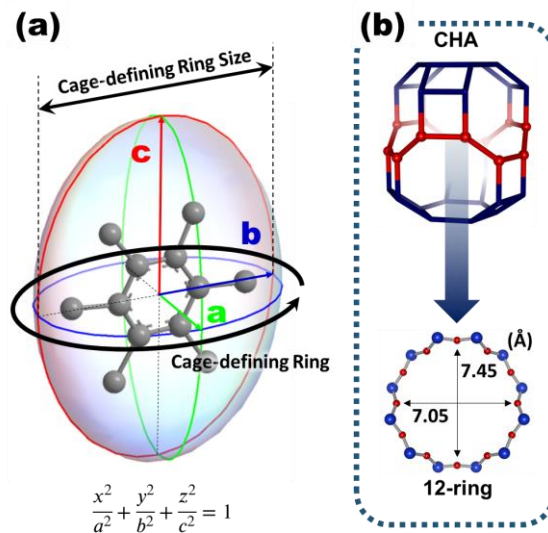


Figure 3.9. Determination of the cage-defining ring. (a) A hypothetical ellipsoidal model for the cage-defining ring and its size. (b) Selection of cage-defining ring from a CHA cage.

Unlike simple cylinders or ellipsoids, real zeolitic cages have very ‘non-linear’ shapes which cannot be easily explained by heights, widths, lengths, and volumes, as shown in Figures A1–A8. To find out the most important geometric parameter, a hypothetical model cage that has an ideal ellipsoidal shape with which is easy to deal is considered. An ellipsoid is defined by its three primary axes, a , b , and c where $a \leq b \leq c$. As a thought experiment, a planar aromatic molecule which represents a hydrogen pool intermediate (*e.g.*, hexamethylbenzene) is inserted in the ellipsoidal cage. The preferred orientation for the planar molecule will be being parallel to the bc plane and perpendicular to the a axis since it is the most energetically favorable orientation that maximizes the molecule-framework interaction. Figure 3.9(a) illustrates an aromatic molecule having such orientation within an ellipsoidal cage. One can easily notice that the limiting dimension for the size of the occluded

aromatic molecule is the second longest axis b . The shortest axis a and the longest axis c is less important in this view. In this model, the ellipse ab and the length of second-longest axis b were defined as *the cage-defining ring* and *the cage-defining ring size*. In the following section, how this concept can be applied to the real cages will be explained.

3.3.2. Selection of Cage-Defining Rings and Four Categories

Selecting cage-defining rings from real cages is essentially analogous to the procedure explained in the previous section for a hypothetical ellipsoidal cage, but is on the basis of the crystallographic data (*e.g.*, *.cif files) which can be obtained from the IZA database or elsewhere.¹⁶ For real cages, there are many choices for rings composed of tetrahedral atoms and oxygens. Among them, the smallest ring which is closest to the center of mass of the cage was selected. This is the cage-defining ring of the cage and corresponds to the ellipse ab of the ellipsoidal model shown in Figure 3.9(a) and explained in the previous section.

Figure 3.9(b) describes the case of a CHA cage as an actual example. In the case of CHA, the 12-membered ring that encircles the ‘waist’ of the cage which is perpendicular to the c axis is the cage-defined ring (red-colored ring in Figure 3.9.(b)). The dimension of this ring can be easily measured in the same matter as when measuring channel dimensions in zeolites. In this manner, the dimension of the selected 12-membered ring (cage-defining ring of CHA) is $7.45 \times 7.05 \text{ \AA}$. And finally, the longer axis of this ring (7.45 \AA) is what we denote as the cage-defining ring. Tetrahedral atoms and oxygen atoms are assumed as hard spheres having a diameter of 2.7 \AA in accordance with the IZA convention.¹⁶ The same selection procedures were undergone, and the results were summarized and visualized in Table 3.1 and Figures A1–A4.

Finally, the correlation between the cage-defining ring sizes and the four categories of topologies (on the basis of olefin product distributions) was illustrated in Figure 3.10. Firstly, the three frameworks of the Category I (CHA, AFX, SFW) have 12-membered cage-defining rings, and their cage-defining ring sizes are almost equal (7.45 Å). This is because these topologies are members of the AABBC-6 family that is closely related to the GME framework. In the previous section, it was shown that the ethylene-to-propylene ratios from the MTO reactions of CHA, AFX, and SFW-type catalysts were close to unity regardless of cage lengths and elemental compositions. The two Category II topologies (LEV and ERI) also have 12-membered cage-defining rings, but their sizes are smaller than 7.45 Å. Catalysts of Category II yielded high ethylene selectivities. The members of Category III have 14-membered cage-defining rings except for DDR which is only one exception. Catalysts having Category III topologies gave propylene-dominant product distributions without exception as shown in the previous section. DDR have a 12-membered cage-defining ring like Category I and II materials, but yielded higher propylene selectivities than ethylene. This is because of the fact that the cage-defining ring had to be selected away from the center of mass of the cage due to the positions of pore openings of a DDR cage. A DDR cage is actually wider than a CHA cage on the basis of the maximum included sphere diameter (DDR: 7.66 Å; CHA: 7.37 Å) and the tree-ring plot shown in Figure A7. Lastly, all four topologies belonging to Category IV have 16-membered cage-defining rings since all of them have LTA-cages of the same connectivity. The cage-defining ring sizes of these cages were larger than 10 Å. Again, as illustrated in Figure 3.10, the cage-defining ring sizes and the four categories based on olefin product distributions show an exceptionally strong correlation.

Table 3.1. Topological information of small-pore frameworks investigated in this work.

Framework	Channel Dimension	Framework Density (nm ⁻³)	Maximum Sphere (Å) [†]	Pore Window (Å)	Diffusing Max. Sphere (Å)	Cage-Defining Ring Size (Å)
CHA	3	15.1	7.37	3.8 × 3.8	3.72	7.45
AFX	3	15.1	7.76	3.6 × 3.4	3.73	7.44
SFW	3	15.1	7.78	4.1 × 4.1	3.65	7.45
LEV	2	15.9	7.10	4.8 × 3.6	3.53	7.15
ERI	3	16.1	7.04	5.1 × 3.6	3.42	6.76
DDR	2	17.9	7.66	4.4 × 3.6	3.65	7.07
AEI	3	15.1	7.33	3.8 × 3.8	3.84	8.52
RTH	2	16.1	8.18	4.1 × 3.8 5.6 × 2.5	4.14	9.00
ITE	2	15.7	8.30	4.3 × 3.8 5.8 × 2.7	4.21	9.11
SAV [†]	3	14.6	8.82	3.9 × 3.9 3.8 × 3.8	4.10	9.60
LTA	3	14.2	11.05	4.1 × 4.1	4.21	10.44
RHO	3	14.5	10.43	3.6 × 3.6	4.06	11.41
KFI [†]	3	15.0	10.67	3.9 × 3.9	4.04	10.16
UFI [†]	2	15.2	10.09	4.4 × 3.6 3.3 × 3.3	3.89	10.45

[†] For topologies having two or more cage structures (SAV, KFI and UFI), only the major cage (largest cage) was considered. All crystallographic data were obtained from the IZA database.¹⁶

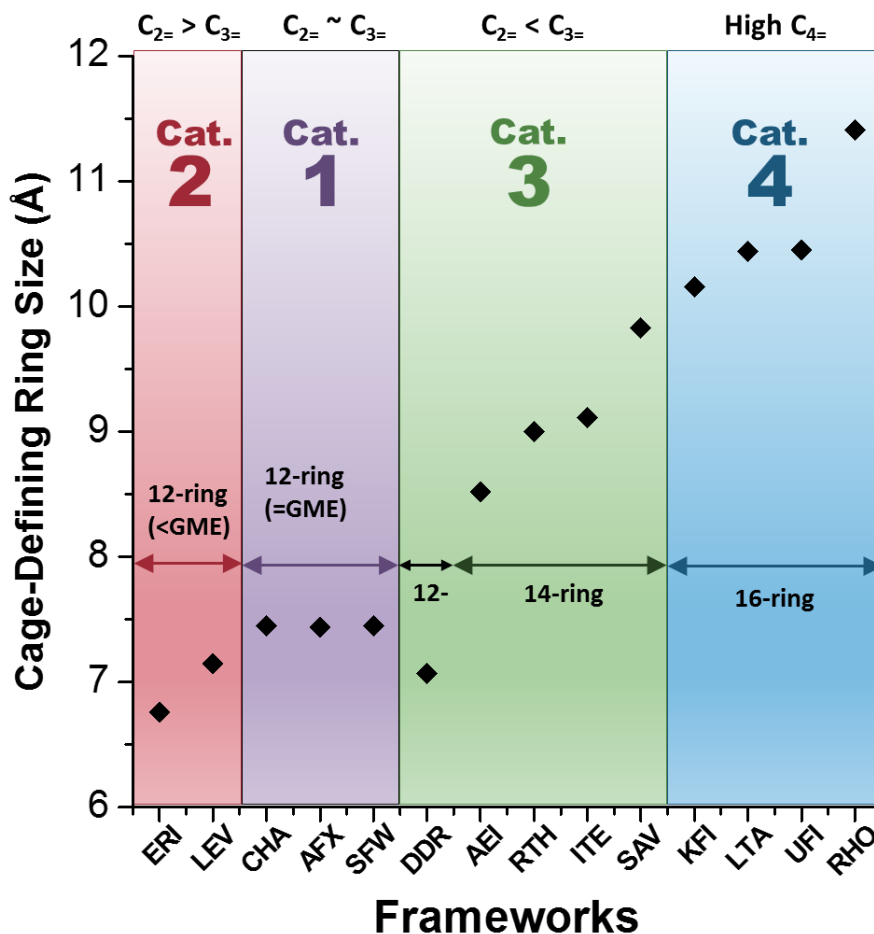


Figure 3.10. Correlation diagram between four categories of topologies and cage-defining ring sizes.

3.4. Summary

The MTO product distributions from 30 MTO catalysts from 14 different topologies were investigated in respect of overall product selectivity patterns in the range of full methanol conversion. This may be the most extensive collection of MTO reaction data from different topologies and elemental compositions which has ever been reported up to date.

The notion that it is the topology that primarily dictates the final olefin product distributions was confirmed. Based on a simple model of hypothetical ellipsoidal cage, the concepts of cage-defining ring and cage-defining ring size were established. The cage-defining ring size showed a strong correlation with the four categories of topologies. Finally, the descriptions of the four categories based on the MTO product selectivity distributions could be augmented with the concept of cage-defining ring, as follows:

At the MTO reaction temperature of 400 °C,

- Category I: group of CHA, AFX, SFW, SSZ-99, and SSZ-104 which show even-balanced ethylene-to-propylene ratios close to unity ($E/P \sim 1$). Members of this category had 12-membered cage-defining rings. Their cage-defining ring sizes were similar to the dimension of the 12-membered main channel of GME ($\sim 7.45 \text{ \AA}$).
- Category II: group of LEV, ERI, and SSZ-105 which show ethylene selectivities higher than propylene selectivities ($E/P > 1$). Members of this category had 12-membered cage-defining rings. Their cage-defining ring sizes were narrower than those of Category I ($< 7.45 \text{ \AA}$).
- Category III: group of DDR, AEI, RTH, ITE, and SAV which show propylene selectivities higher than ethylene selectivities ($E/P < 1$). Members of this category had 14-membered cage-defining rings except for DDR having a 12-membered cage defining ring. Their cage-defining ring sizes were narrower than those of Category I ($> 7.45 \text{ \AA}$).
- Category IV: group of LTA, RHO, KFI, and UFI which show no clear pattern of ethylene-to-propylene, but high butylenes selectivities with the LTA cages as their major cages in common. Members of this category had common 16-membered cage-defining rings. Their cage-defining ring sizes were the widest ($> 10 \text{ \AA}$).

Relevant supplementary visualizations which helps readers to ‘get the feel of’ real sizes of cages were provided in Appendix A. The cage-defining ring is a reliable metric that

connects the cage structures to the final product distributions. This geometric indicator based on the intermediate shape selectivity can be directly obtained from the most of common types of crystallographic information of topologies such as the *.cif files. Even from a novel structure having a small-pore/cage-type topology which has never been tested before, the final MTO product distributions can be predicted only based on the crystallographic information without performing sophisticated computations. I believe that this concept of cage-defining ring will provide guidance for further investigation of MTO reactions regarding the shape selectivity of cage structures.

Chapter 4

Summary and Future Work for Part I

The experimental results shown in the previous chapters of Part I will be summarized in this chapter. Lastly, several suggestions about future research directions to deepening the understanding of MTO reaction are made on the basis of my experimental results.

4.1. Overall Summary and Conclusion

Ethylene and propylene are the two most important hydrocarbon products which support the entire chemical industry and, by extension, the modern civilization. The MTO process using non-petroleum feeds is a promising technology that can cope with high oil prices and expected gaps between olefin demand and capacity. The commercialized catalyst SAPO-34 can produce ethylene and propylene with high selectivity over 80 % in continuous fluidized-bed reactors equipped with co-operating catalyst regeneration units. The MTO process is completely commercialized nowadays, and many plants are under construction or on stream including the Shenhua Baotou coal-to-olefin process which started operation in 2010, located in Inner Mongolia of China.

Tremendous efforts have been made to elucidate the fundamental mechanism of MTO reaction. The hydrocarbon pool mechanism suggested by Dahl and Kolboe in the early 1990s is the most widely accepted by the scientific community. The hydrocarbon pool mechanism consists of a wide array of polymethyl aromatic intermediates. The sizes and numbers of methyl groups of aromatic carbenium intermediates which governs the final

product distribution are restricted by cage geometries. Many previous works tried to deduce the shape selectivity in the MTO reaction. However, the global structure-property relation between the topology and olefin product distribution on the basis of reliable metrics has yet to be reported.

To establish the general rule about the shape selectivity in MTO reaction, among 245 molecular sieve topologies which have been ever reported, 14 topologies having cage structures limited by pore windows consisting of 8 tetrahedral atoms were selected. 30 molecular sieves (17 zeolites and 13 AlPO₄-based) having those topologies were prepared. The crystal structures, morphologies, and elemental compositions were characterized on the basis of PXRD, SEM, and EDS, respectively. The MTO behaviors of all of these catalysts were investigated. All MTO reactions were conducted at the same reaction condition ($T = 400\text{ }^{\circ}\text{C}$, $\text{WHSV}(\text{MeOH}) = 1.3\text{ h}^{-1}$) to make a valid comparison.

First, it was experimentally confirmed that the topology primarily determines the olefin selectivity distribution. Two topologies—CHA and AEI—were prepared as zeolites, SAPOs, CoAPOs, and MgAPOs. Impressive similarities in olefin selectivity distributions were observed among isostructural groups of catalysts. Several other topologies (AFX, SFW, LEV, LTA, RHO, and KFI) were prepared as both zeolites and SAPOs. Zeolite-based catalysts showed MTO behaviors similar to those of their SAPO-based counterparts. Regardless of elemental compositions, AFX and SFW showed transient ethylene-to-propylene ratios close to unity at all stages of reaction. SAPO-35 and Nu-3 sharing the same LEV topology showed sharply increasing transient ethylene-to-propylene ratios over time on stream. All LTA-, RHO-, and KFI-type molecular sieves showed very high butylene contribution ratios similar to or higher than 0.5.

Second, given that it is not the elemental composition, but the topology that dictates the final olefin selectivity distributions, the studied topologies were classified into 4 groups, and named as Category I, II, III, and IV. Category I consists of CHA, AFX, SFW, and other

GME-related topologies. These topologies gave ethylene-to-propylene ratios which are approximately one. The Category II topologies are ERI, LEV, and intergrowth of these two frameworks. These types of catalysts showed sharply increasing transient ethylene-to-propylene ratios and/or completely ethylene-dominating product distributions. The members of Category III are DDR, AEI, ITE, RTH, and SAV. Category III-type molecular sieves showed propylene selectivities which are almost twice higher than ethylene selectivities without exception. Topologies having LTA-type cages (LTA, RHO, KFI, and UFI) were grouped into Category IV which is characterized by their high butylenes selectivities.

Third, a geometric indicator that can correlate the cage structures to the four categories of catalytic results was suggested. On the basis of a thought experiment on a hypothetical cage having an ideally ellipsoidal shape, the most important metric that actually limits the size of hydrocarbon pool intermediates was extracted. Among three principal axes of an ellipsoidal cage, the ellipse defined by the shortest and second shortest principal axes was named the cage-defining ring, and the length of the second shortest axis was defined as the cage-defining ring size. Analogous procedures were applied to real cages based on the crystallographic data disclosed on the IZA database. The cage-defining rings and their sizes were determined for 14 topologies studied in this work. A strong correlation found between the cage-defining ring sizes and the categories of olefin product distributions.

This work may be the most extensive experimental study regarding the shape selectivity in the MTO reaction up to date. I believe that the concept of cage-defining ring will provide researchers a reliable way to estimate the product distributions from the crystal structures.

4.2. Proposed Future Work

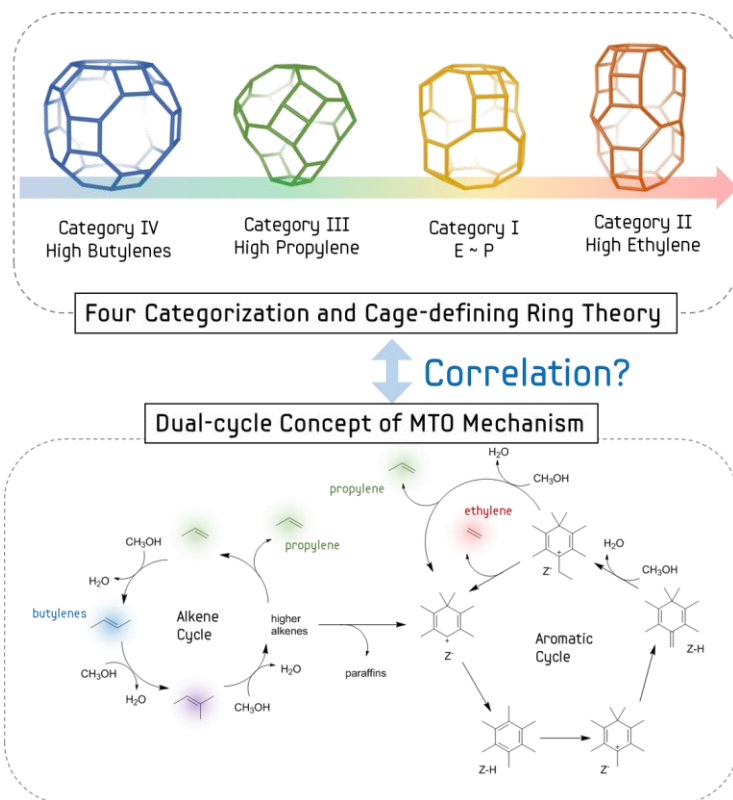


Figure 4.1. Possible correlation between the dual-cycle mechanistic concept and the cage-defining ring theory.

As mentioned in Chapter I, recent trends of mechanistic studies about the MTO reaction are toward the dual-cycle concept,^{8, 23} and the identification of carbenium intermediates formed within various types of cage topologies.^{13, 33, 35, 46} According to the dual-cycle concept, the alkene cycle generates propylene with high selectivity from the cracking of higher olefins, and the aromatic cycle produces both ethylene and propylene.²⁹⁻
³⁰ In Part I, it was experimentally demonstrated that ethylene-to-propylene ratios are

primarily dictated by the cage topology. Considering the result that ethylene is almost exclusively formed from the aromatic cycle,²⁹ the shape selectivity of cages can be eventually accomplished by the confinement effect on this dual-cycle mechanism. For example, it was shown that SSZ-98 zeolite having an ERI topology gave a very high ethylene selectivity. Combined with the recent mechanistic studies, a hypothesis such as “*the ERI topology may prefer the aromatic cycle and/or suppress the alkene cycle*” can be established. Analogous hypotheses can be considered for all other topologies and/or categories of topologies.

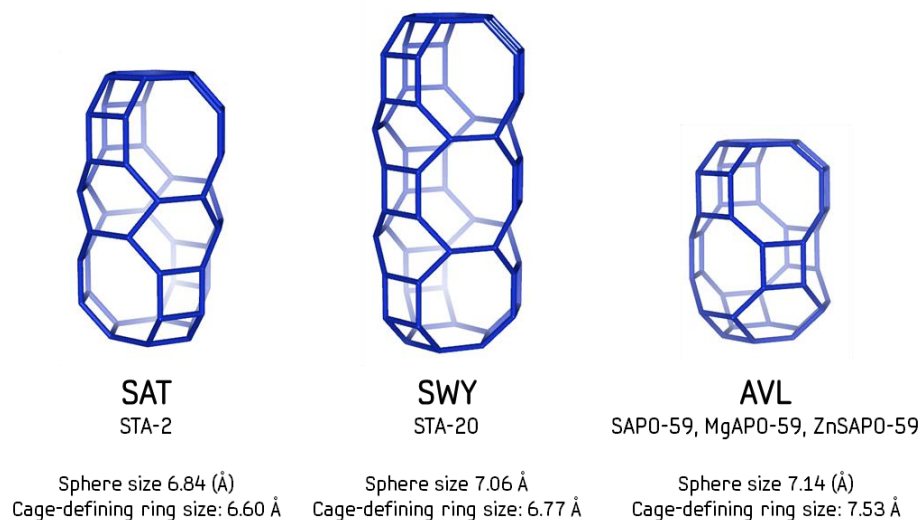


Figure 4.2. Cage structures, maximum sizes of sphere that can fit within cages, and cage-defining ring sizes of topologies SAT, SWY, and AVL.

There are several remaining topologies which should be tested in respect of the cage-defining ring concept. I suggest three topologies (SAT, SWY and AVL shown in Figure 4.2) for future work. The framework SAT is a very interesting topology since it is expected to show a high ethylene-to-propylene selectivity because it belongs to Category II. Its cage-

defining ring size (6.60 Å) is smaller than that of ERI (6.76 Å). This framework was first reported as a MgAPO-based molecular sieve STA-2,¹⁰⁷ and later, a pure SAT-type AlPO₄-based molecular sieve was reported.¹⁰⁸ But this framework has not yet been synthesized as a pure SAPO form, and SAPO-56 (AFX) was always observed as an impurity phase in the SAPO system. I successfully synthesized pure CoAPO-based SAT phases, but no complete conversion of methanol was observed in the MTO reaction. It is also possible that this SAT cage is too narrow to possess the aromatic intermediates of MTO reaction.

The framework SWY is another cage-based topology which is expected to belong to Category II. Its cage-defining ring size (6.77 Å) is almost the same to that of ERI (6.76 Å). The only SWY-type molecular sieve which has ever been reported is a SAPO-based molecular sieve STA-20.¹⁰⁹ I synthesized several STA-20 samples, but they showed very high selectivities of heavy hydrocarbons (C₅, C₆, etc.) presumably due to the presence of impurity phases. Optimization of synthesis recipes is required.

The framework AVL is a 2-dimensional framework whose cage structure is essentially a hybrid of CHA and LEV.⁵⁶ The MTO behaviors of SAPO-59 were already reported in the literature,⁴⁰ but the data were collected at a different reaction temperature (350 °C). The cage-defining ring size of AVL (7.53 Å) is very close to those of Category I (7.45 Å). But at the same time, the diameter of maximum sphere that can be included in the cage is 7.14 Å which is smaller than that of CHA (7.37 Å). I expect that SAPO-59 having an AVL topology will show product distributions similar to that of SAPO-34 at 400 °C. But due to its low channel dimensionality, I also expect that it will show a much shorter lifetime than SAPO-34, just like SAPO-35.

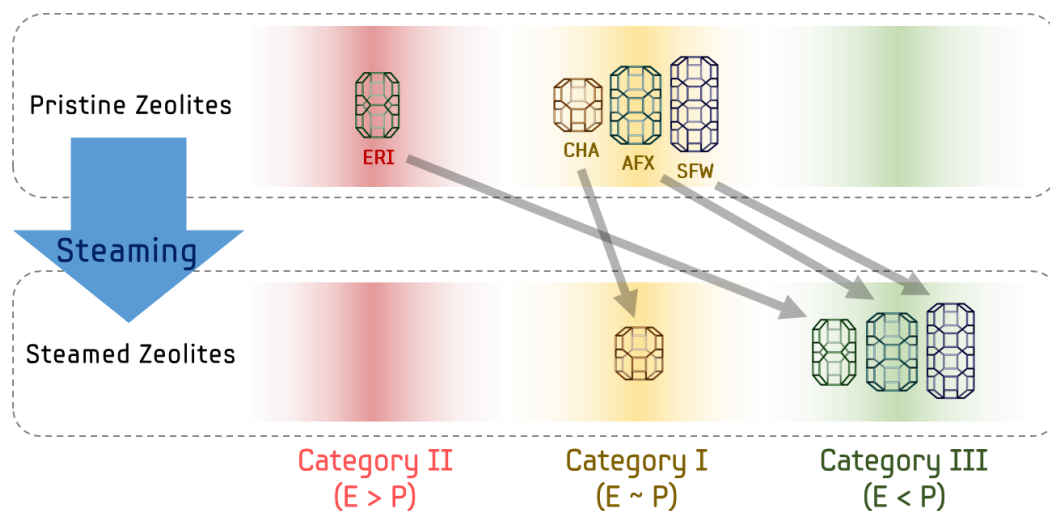


Figure 4.3. Inter-categorical transition induced by streaming of zeolites.

Steaming of zeolites is another interesting topic from the point of view of the MTO product distributions. There is a scientific agreement that the steaming process dealuminates zeolites, particularly from paired aluminum sites.¹¹⁰ The Davis lab has made many efforts to investigate the effects of zeolite steaming having different topology types on the resultant MTO behaviors.^{48, 69, 106, 111} Low-silica CHA,¹¹¹ RHO, and KFI zeolites¹⁰⁶ synthesized without use of OSDAs and an AEI-type zeolite SSZ-39⁶⁹ were steam-treated at high temperatures (> 600 °C) and their MTO behaviors were investigated. For most of these zeolites, there was no significant change in olefin product distributions, but their lifetimes were significantly improved due to the suppression of coke formation from paired aluminum sites.⁶⁴

I investigated the MTO behaviors of steamed SSZ-13 (CHA), SSZ-16 (AFX), SSZ-52 (SFW) and SSZ-98 (ERI) at the same reaction condition (steaming condition: 750 °C for 8 hours with a bubbler temperature of 80 °C; MTO reaction: 400 °C). The changes of MTO behaviors of steamed AFX-, SFW-, and ERI-type zeolites have not been reported in the

literature. The frameworks were preserved after steaming without degradation (Figure A10). The ^{29}Si NMR spectra of these zeolites before and after steaming shown in Figure A11 support that the framework Si/Al_T ratios were significantly increased due to dealumination. After steaming, the amounts of penta-coordinated and octahedral extra-framework aluminum species were substantially increased. (Figure A12) The formation of extra-framework aluminum is commonly observed in other steamed zeolites.^{106, 111}

Finally, the MTO time-on-stream charts of these selected zeolites (before and after steaming) were demonstrated in Figure A13. After steaming, SSZ-13 retained its even-balanced ethylene-to-propylene ratio (~ 1). But interestingly, SSZ-98 of Category II and SSZ-16/SSZ-52 of Category I showed propylene-dominant product distributions which are corresponding to Category III-type topologies. These inter-categorical transitions were graphically summarized in Figure 4.3. I believe that this inter-categorical transition induced by steaming has something to do with the presence of secondary minor cages of ERI, AFX, and SFW frameworks; AFX and SFW have GME cages as minor cages, and ERI has smaller CAN cages. My hypothesis is that the steaming process of zeolites having minor cages results in an effective increase in cage-defining ring size. Extra-framework aluminum species can retreat into such small cages that are not MTO-active. The frameworks show no inter-categorical transitions such as CHA and AEI have no secondary cage-like units. I believe that further investigation of this inter-categorical transitions induced by steaming will deepen the understanding of the nature of the steaming process regarding the shape selectivity of the MTO reactions.

**Part II. Synthesis and Topotactic Transformation of
Germanosilicate CIT-13**

Chapter 5

Introduction to Part II: Extra-large-pore Molecular Sieves and Germanosilicates

In this chapter, the topic of Part II of my thesis is introduced. First, a brief history of extra-large-pore zeolites is provided. Next, I describe why they are an important class of molecular sieves. The pros and cons of germanosilicates are discussed, and how the drawbacks related to the use of germanium may be overcome. I close with my motivations and objectives for this part of my thesis work.

5.1. Background

Zeolites and molecular sieves are one of the most frequently used heterogeneous catalysts in modern chemical industry.¹¹²⁻¹¹⁵ Their merits as catalysts encompasses many advantageous properties such as well-defined pore structures, high thermal stability and environmental tolerance, excellent accessibility of catalytic sites and high catalytic activities, a wide array of elemental compositions, etc.¹¹⁶⁻¹²⁰ These beneficial properties of zeolites and molecular sieves have a very close relation with their structural architectures.^{112, 121} In this regard, discovery of new frameworks and modification of porosity are very important in the field of zeolite science.¹²²⁻¹²³ Thus, the scientific community has spared no effort in finding new structures of molecular sieves which can be used for many high-value-added industrial purposes. One of the hottest research topics is extra-large-pore frameworks.¹¹⁵

5.1.1. Extra-large-pore Molecular Sieves

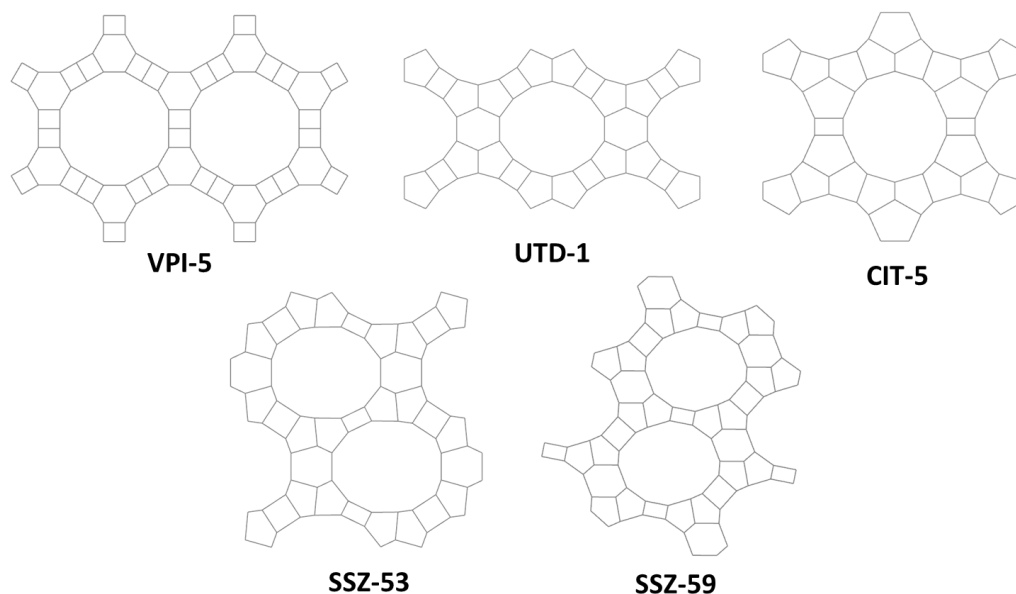


Figure 5.1. Examples of extra-large-pore frameworks.

Zeolitic frameworks having pore systems which are delimited by rings consisting of 8, 10, and 12 tetrahedral atoms (T-atoms) are called small-pore, medium-pore, and large-pore frameworks, as introduced in Chapter 1, Part I. While small-pore and medium-pore molecular sieves which have relatively narrow dimensions of cavities and/or channels (3–6 Å) are of interest due to their prominent shape selectivity (e.g., the topic of Part I of my thesis), larger-pore topologies are gathering attention thanks to their ability to process larger reactant molecules. *Extra-large-pore frameworks* are molecular-sieve structures having pore windows delimited by more than 12 T-atoms.¹¹⁴ These frameworks have ca. 1-nm-sized pore windows which are wider than most of commercial large-pore zeolites such as zeolite Y or Beta. Figure 5.1. shows several representative examples of extra-large-pore frameworks.

The first extra-large-pore molecular sieve is the aluminophosphates-based VPI-5 (VFI) and was discovered by Prof. Mark E. Davis and co-workers.¹²⁴⁻¹²⁵ VPI-5 has one-dimensional 18-ring channels with a 12.7 Å-wide pore dimension.¹²⁶ Interestingly, at elevated temperature ($T > 100^{\circ}\text{C}$) with the presence of sorbed moisture, VPI-5 could be transformed to $\text{AlPO}_4\text{-8}$ (AEI) which is another extra-large-pore molecular sieve having 14-ring channels.¹²⁷⁻¹²⁸ This captivating property of VPI-5 gathered tremendous scientific interest and ignited efforts in exploring new phosphate-based extra-large-pore molecular sieves. A 20-ring gallophosphate-based Cloverite (-CLO) is one example of accomplishments made in those days.¹²⁹

The late 1990's was the era of 14-ring aluminosilicates and borosilicates. 14-membered ring high silica zeolites UTD-1 (DON), CIT-5 (CFI), SSZ-53 (SFH), and SSZ-59 (SFN) were discovered one after the other.¹³⁰⁻¹³³ These aluminosilicate and borosilicate zeolites opened the field of catalysis of extra-large-pore molecular sieves in earnest.¹¹⁴ Many examples of catalytic reactions over extra-large-pore zeolites were developed such as cracking of 1,3-diisopropylbenzene, 1,3,5-triisopropylbenzene, gasoil, disproportionation of ethylbenzene, alkylation of biphenyl, etc.¹³⁴⁻¹³⁶

The number of extra-large-pore frameworks started to explosively increase as germanium was introduced within the frameworks by Corma et al.¹¹⁴ Examples include 2-dimensional 14/12-ring IM-12/ITQ-15 (UTL),^{116, 137} 3-dimensional 18/10/10-ring ITQ-33 (ITT, Figure 5.2.),¹³⁸⁻¹³⁹ 3-dimensional 30-ring mesoporous ITQ-37 (-ITV),¹⁴⁰ 3-dimensional 16/15-ring ITQ-40 (-IRY),¹⁴¹ and 2-dimensional 14/10-ring CIT-13 (*CTH)⁶³ which is the main topic of Part II of my thesis. Although germanosilicates only have a limited Lewis acidity as a heteroatom within the zeolite framework,¹⁴² their rich chemistry opened an entirely new field of zeolite science—*topotactic transformation*.

1.1.2. Germanosilicates

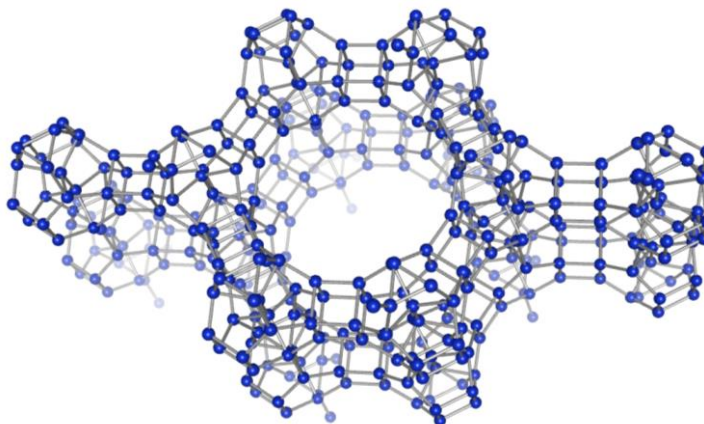


Figure 5.2. Extra-large-pore germanosilicate ITQ-33 (ITT) possessing a 3-dimensional 18/10/10-ring channel system.

It was computationally predicted that the presence of small-rings can decrease the framework density, thereby enabling frameworks to have higher probability to possess extra-large pores.¹⁴³ However, it is inevitable for small-ring building units such as 3-membered ring (3), double-3-ring (*d3r*) or double-4-ring (*d4r*) to have very small T-O-T angles ($< 145^\circ$) which are not energetically favored. Inclusion of germanium can solve this problem since Ge-O-T (T = Si, Ge) bonds can stabilize such units.^{116, 144} Indeed, many frameworks realized as germanosilicates possess *d4r* units.^{116, 137, 140, 145} All frameworks enumerated in the previous section as examples of extra-large-pore germanosilicates—UTL, ITT, -ITV, -IRY, *CTH—do have *d4r* units or even *d3r* units. The *d4r* units are also frequently found in other germanosilicates ITQ-22 (IWW), ITQ-13 (ITH), beta polymorph C (BEC), and ITQ-27 (IWW) which are not extra-large-pore frameworks.¹⁴⁶⁻¹⁴⁹

There are several drawbacks of inclusion of germanium within the frameworks. One is the cost of element. It is possible to collect leached germanium after postsynthetic stabilization,¹¹⁴ but the cost of the separation and purification processes must be also considered. Also, germanosilicates can be used as crystallization seeds for germanium-free zeolites. Cantin et al. reported that pure borosilicate ITQ-24 could be obtained on the basis of seeding strategy.¹⁵⁰

The other obstacle is the limited catalytic activity of the germanium sites.¹⁴² Isomorphous substitution can overcome this issue by incorporating second heteroatoms in the germanosilicate system. For example, IWR-type aluminogermanosilicate,¹⁵¹ B, Al, Ga-containing germanosilicates ITH,¹⁵² B, Al, Ga, Fe, In-incorporated germanosilicate UTL¹⁵³ were reported.

The most important drawback of germanosilicate is its weak hydrothermal stability.^{151, 154-157} This is simply because Ge-O-Ge bonds and Ge-O-Si bonds can be easily dissociated by hydrolysis.¹⁵⁷⁻¹⁵⁸ It is known that many germanosilicates having a very low Si/Ge ratio (< 2–3) can be immediately degraded into amorphous materials upon exposure to water.¹⁵⁴ Postsynthetic stabilization is one way to enhance the hydrothermal stability of germanosilicates by substituting germanium T-atoms within the frameworks with other stable T-atoms such as Al, Si, or Sn, etc. Many cases of postsynthetic modifications of germanosilicates have been reported in the literature.¹⁵⁸⁻¹⁶⁰ This postsynthetic modification of germanosilicate not only improves the stability of the frameworks, but also provides catalytic activity by introducing Brønsted or Lewis acid sites.¹⁵⁷

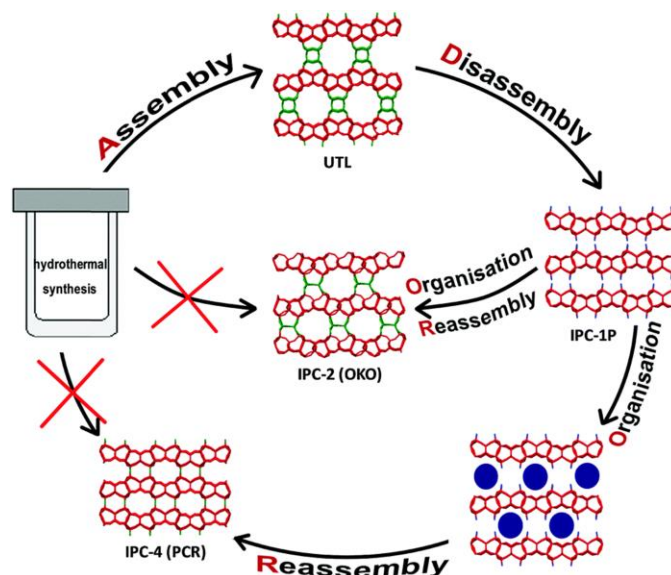


Figure 5.3. The ADOR process of UTL-type germanosilicate producing two structurally related frameworks OKO and PCR. Reproduced with Permission from Ref [50]. Copyright 2014 Royal Society of Chemistry.

It is also possible to make use of the chemical lability of framework germanium.¹⁴⁵ In the early 2010's, two milestone progresses were reported. One is the delamination of UTL-type germanosilicate IM-12,¹⁶¹ and the other is the inverse sigma transformation of the same molecular sieve.¹¹⁸ These two structural transformations of germanosilicates made use of the fact that germanium T-atoms regioselectively occupy the $d4r$ sites. The delaminated layered material IPC-1P was further transformed into many unseen frameworks such as IPC-2 and IPC-4,¹²² and later, IPC-9 and IPC-10¹⁶² by alkoxylation and/or condensation. This concept is called the ADOR (assembly-disassembly-organization-reassembly) strategy, and these types of transformations are called *topotactic transformations*. The topotactic transformation is structural transformation of crystalline materials where the crystal lattices of the parent phase and the product phase are closely related to one another on the basis of one or more crystallographically equivalent symmetry elements.¹⁶³ In the case of the

transformation of UTL into OKO and PCR, all three frameworks belong to the same space group $C2/m$. Thus the ADOR transition of UTL is a good example of topotactic transformation.

5.2. Motivation

In 2016, our group reported a new germanosilicate framework CIT-13.⁶³ CIT-13 was discovered in the course of studying the structure-directing ability of many imidazolium-based organic structure-directing agents (OSDAs). The structure of CIT-13 revealed on the basis of the rotational electron diffraction (RED) technique strikingly resembled that of UTL. UTL consists of *fer*-type layers connected with bridging *d4r* units while CIT-13 is composed of *cfi*-type layers similarly connected with *d4r* units. Therefore, it is easily expected that CIT-13 can undergo various transformations analogous to those of UTL.

Indeed, the discovery of CIT-13 immediately attracted interest of many research groups. Although CIT-13 was registered as the type material of framework *CTH, germanosilicates NUD-2¹⁶⁴ and SAZ-1¹⁶⁵ which are essentially isostructural to CIT-13 were reported one after the other. These germanosilicates were synthesized using similar imidazolium-based OSDAs. While we disclosed the transformation of CIT-13 into two novel frameworks CIT-14 and CIT-15,¹⁶⁶ IPC-16¹⁶⁵ (isostructural to CIT-14) and IPC-15¹⁶⁵ and ECNU-21¹⁶⁷ (isostructural to CIT-15) were reported. However, the full network of transformations in which CIT-13 is involved, and its rich chemistry has yet to be reported.

Furthermore, in December 2016, I discovered that calcined CIT-13 samples had been slowly transformed into another extra-large-pore CFI-type germanosilicates which I named Ge-CIT-5. This spontaneous transformation was completely reproducible. To the best of my knowledge, this is the first inter-germanosilicate transformation occurring at room

temperatures. The only pathway to obtaining the CFI-type molecular sieves had been the original protocol for CIT-5 using sparteine-derived OSDA which is hard to obtain and expensive. The introduction of Ge-CIT-5 will immensely widen the tunability of chemical and structural properties of CFI-type molecular sieves.

5.3. Objectives

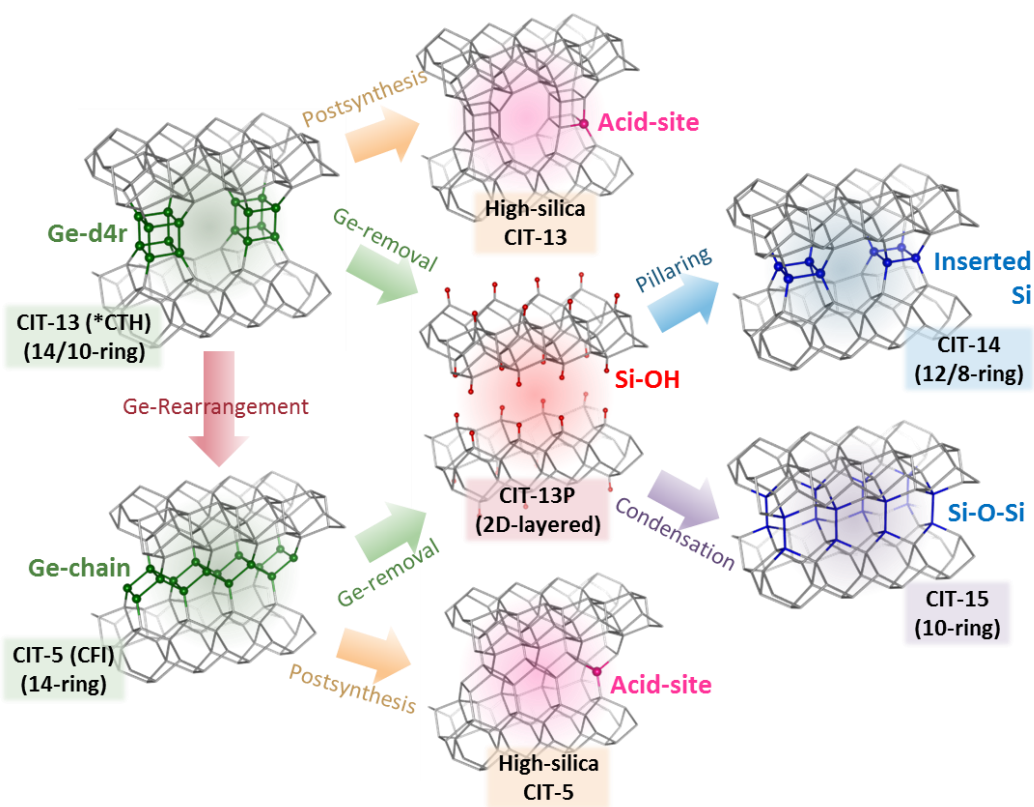


Figure 5.4. Schematic illustration of the full network of transformations of Ge-CIT-13 which will be discussed in Part II of my thesis.

The main purpose of Part II of my thesis is to elucidate the full transformation and postsynthesis network of germanosilicate CIT-13. For each of the structural and chemical modification steps shown in Figure 5.4, the most important synthetic parameters will be deduced and the preparation conditions will be optimized.

In Chapter 6, the synthesis, characterization and properties of Ge-CIT-13 will be presented. Many synthetic procedures to yield CIT-13-type molecular sieves will be illustrated, and the synthesis-property relationships will be discussed. In Chapter 7, the transformation of Ge-CIT-13 into Ge-CIT-5 will be presented, where the role of moisture is extensively investigated. In Chapter 8, various topotactic transformation and postsynthesis pathways are outlined and discussed. Lastly, in Chapter 9 the overall summary and future outlook will be provided.

Chapter 6

Synthesis and Characterization of CIT-13

Contents of this chapter were obtained in collaboration with Dr. Dan Xie and Dr. Stacey I. Zones from Chevron Energy Technology Company, Dr. Stef Smeets and Prof. Lynne B. McCusker from ETH Zurich and Stockholm University. Dr. Smeets and Prof. McCusker collected synchrotron XRD data and refined the structure of CIT-13. A part of the results and discussions of this chapter was published on August 18th, 2016: J. H. Kang et al., *Chem. Mater.* 2016, **28**, 6250, DOI: 10.1021/acs.chemmater.6b02468.

6.1. Introduction

The synthesis of a zeolite is one of the most complicated chemical assemblies, and involves control of various synthetic parameters such as pH, water content, structures of OSDA, types of alkali cations, mineralizing agents, aging time, etc.^{131, 168} Zeolite synthesis has traditionally been regarded as a delicate art which inevitably entails a number of trials and errors.^{117, 169} Synthesis of extra-large-pore molecular sieves is particularly challenging due to the low framework density of the desired structures. Corma et al. suggested several strategies to obtain extra-large-pore molecular sieves such as the use of rigid three-dimensional OSDAs, the use of fluorides which helps to lower the framework density, the use of high-throughput gel-composition screening systems, etc.¹¹⁴ Although there is no proven road to the discovery of novel extra-large-pore frameworks, inclusion of germanium in the system together with fluoride as the mineralizing agent can be a good starting point

since both germanium and fluoride favor the formation of composite building units such as *d4r* units consisting of small-rings which is beneficial to lower the framework density.^{116, 149}

One of the classes of OSDAs having rigid structures is the imidazolium-derived cations. Imidazole-based OSDAs are potential candidates that can probably yield extra-large-pore frameworks thanks to their rigid structures and ability to have the π - π interactions.¹¹⁴ In the course of testing various methylbenzylimidazolium-derivatives in the germanosilicate system with fluoride, our group discovered a new extra-large-pore germanosilicate named CIT-13.⁶³ The structure of CIT-13, solved on the basis of RED technique, showed an impressive resemblance to an UTL-type germanosilicate IM-12 which has been extensively studied in terms of its ability to undergo topotactic transformations.

In this chapter, the optimized synthesis condition for germanosilicate CIT-13 will be provided by testing the influences of each synthetic parameters such as types of OSDAs, germanium content, water content, crystallization temperature, etc. Also, several other synthetic protocols such as the hydroxide-mediated synthesis and the isomorphous substitution of aluminum in germanosilicate synthesis will be introduced. On the basis of the refined structure solution of CIT-13, the nature of possible disorders in the framework will be discussed. Lastly, the physicochemical properties of resultant molecular sieves will be characterized and discussed.

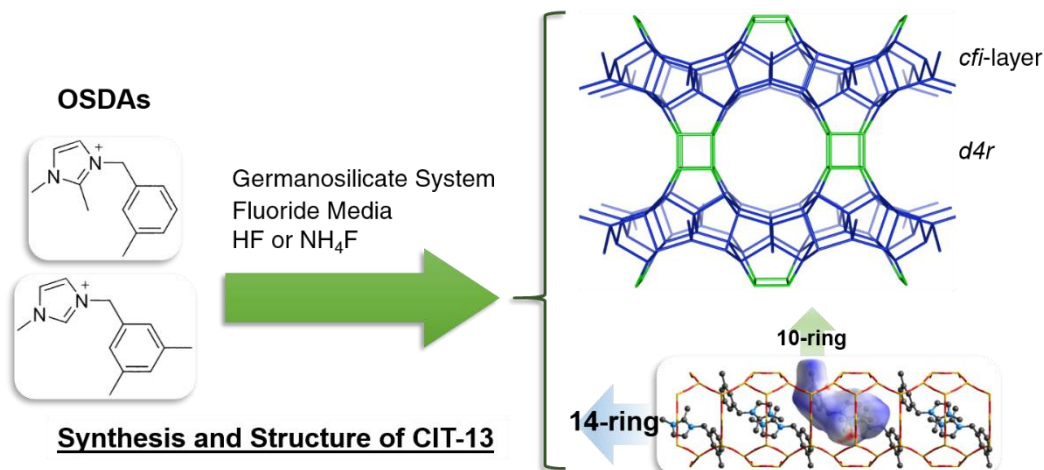


Figure 6.1. Brief graphic description of synthesis and structure of germanosilicate CIT-13. Reproduced with Permission from Ref [170]. Copyright 2014 American Chemical Society.

6.2. Experimental

6.2.1. Synthesis of OSDAs

All OSDAs used in this work were prepared from the cross-S_N2 reactions between two imidazole-derivatives and two methylbenzyl or dimethylbenzyl halides. 1,2-dimethylimidazole (98%), 1-methylimidazole (98%), 3-methylbenzyl chloride (98%) were purchased from Sigma-Aldrich. 3,5-dimethylbenzyl bromide (98%) was purchased from Alfa Aesar. All chemicals were used without further purification steps. In this chapter, the following four organic cation OSDAs were used to synthesize CIT-13: **(1)** 1,2-dimethyl-3-(3-methylbenzyl)imidazolium, **(2)** 1,2-dimethyl-3-(3,5-dimethylbenzyl)imidazolium, **(3)** 1-methyl-3-(3-methylbenzyl)imidazolium, **(4)** 1-methyl-3-(3,5-dimethylbenzyl)imidazolium. The schemes for the preparations of these OSDAs were illustrated in Figure 6.2.

150 mmol of imidazole-derivative (i or ii) was firstly dissolved in 500 ml of toluene. Then, an equimolar amount of benzyl halide-derivative (iii or iv) was added slowly. In the

case of the addition of 3,5-dimethylbenzyl bromide, the reaction which is exothermic underwent quickly even at room temperature due to the good ability of bromide as the leaving group of the substitution reaction. Therefore, the addition of 3,5-dimethylbenzyl bromide should be performed gradually in an ice bath. The reaction mixture was heated up to 105 °C and stirred for 1 day. Since the product salt is insoluble in toluene, the mixture became cloudy after several hours and the sedimentation of the powdery product phase was observed after 24 hours. The batch was cooled down, and this solid product was recovered by filtration. The product was washed using a copious amount of diethyl ether repeatedly and dried overnight in a vacuum at room temperature. One more OSDA denoted as “Ortho” in Table B4 is 1,2-dimethyl-3-(2-methylbenzyl)imidazolium which is the ortho-isomer of OSDA 1. This OSDA was synthesized in an analogous way.

Another OSDA, (6R,10S)-6,10-dimethyl-5-azaspiro[4.5]decanium (Figure 6.3.) was also synthesized to prepare IM-12 germanosilicates which was compared to CIT-13.¹¹⁶ 1 M NaOH aqueous solution (160 ml) was mixed with 150 mmol of 1,4-dibromobutane in a 500-ml double-neck round-bottom flask. The mixture was heated up to the reflux under vigorous stirring. 150 mmol of cis-2,6-dimethylpiperidine was added gradually for 45 min to eliminate the possibility of dimer formation. The reaction mixture was refluxed overnight. Using a dry-ice bath, the batch was cooled down. A portion of concentrated NaOH solution (50 wt.% in H₂O) was added until a floating brownish second phase appeared. An extended cooling made this oil phase solidify. This solid phase was filtered, and extracted with 200 ml of chloroform three times. The extracted chloroform phase can be dark and murky due to the presence of moisture. This mixture was dried with anhydrous magnesium sulfate. The clear solution was separated by filtration. Excess chloroform was removed by evaporation using a rotary evaporator. The solid was recovered and recrystallized with a small portion of chloroform (100 ml) and diethyl ether. This solid product was recovered by filtration. The product was washed using a copious amount of diethyl ether repeatedly and dried overnight in a vacuum at room temperature.

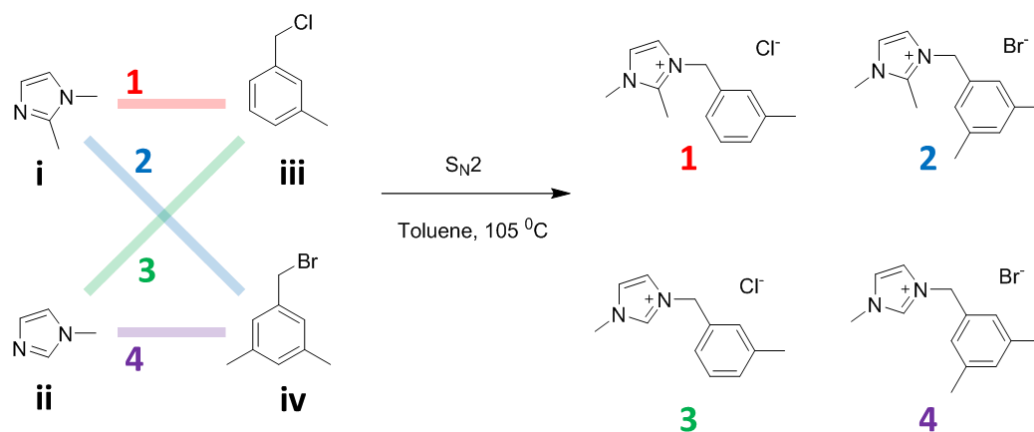


Figure 6.2. Reactions schemes for the syntheses of the OSDAs used in this work and the structures of them: i. 1,2-dimethylimidazole, ii. 1-methylimidazole, iii. 3-methylbenzyl chloride, iv. 3,5-dimethylbenzyl bromide, 1. 1,2-dimethyl-3-(3-methylbenzyl)imidazolium, 2. 1,2-dimethyl-3-(3,5-dimethylbenzyl)imidazolium, 3. 1-methyl-3-(3-methylbenzyl)imidazolium, 4. 1-methyl-3-(3,5-dimethylbenzyl)imidazolium

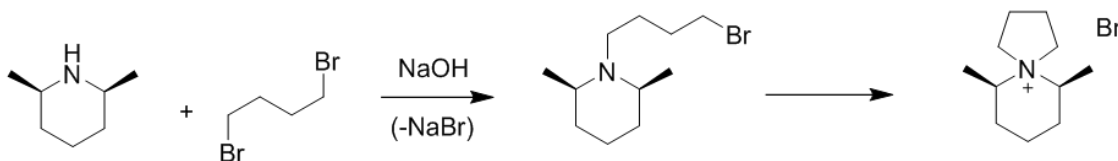


Figure 6.3. Reaction scheme for the synthesis of (6R,10S)-6,10-dimethyl-5-azaspiro[4.5]decanium.

To prepare OSDA hydroxide aqueous solutions which were used to prepare germanosilicate gels, ion-exchange steps were conducted. The product organic salts were dissolved in distilled water first (ratio: 500 ml of water per 100 mmol of product). Next, ion-

exchange resin (Dowex™ Monosphere™ 550A Hydroxide Form, Dow Chemical) was added to the solution (ratio: 300 ml (in volume) of ion-exchange resin per 100 mmol of product). The ion-exchange mixture was stirred at room temperature for 1 day. The solution phase was recovered by filtering out the resin. The same amount of resin was added again to the solution, and an exchange step was repeated for an extra day. After that, the solution phase was concentrated using a rotary evaporator until the solution volume became 100 to 200 ml. The concentration of the final OSDA hydroxide solution was characterized based on acid-base titration using a Mettler Toledo DL22 titrator. The desired concentration of the final solutions was 0.2–2 mmol OH⁻ per gram of solution.

6.2.2. Synthesis of Germanosilicates

All germanosilicate molecular sieves were synthesized by hydrothermal reactions. For a typical CIT-13 synthesis in fluoride media, the gel composition was $x/(1+x) \text{ SiO}_2 : 1/(1+x) \text{ GeO}_2 : y \text{ ROH} : y \text{ HF (or NH}_4\text{F)} : z \text{ H}_2\text{O}$, where x is essentially the Si/Ge molar ratio of the gel, and ROH is the desired imidazolium-derivative OSDA hydroxide. The values of x , y and z and synthesis results attempted in this work are provided in Table B1. First, a desired amount of germanium dioxide (GeO₂, 99.999%, Strem chemical) was dissolved in OSDA solution in a 23-ml PTFE liner for a Parr steel autoclave. Then, a desired amount of tetraethyl orthosilicate (TEOS, 98%, Alfa Aesar) was added to the mixture and stirred overnight to fully hydrolyze TEOS. Using an air flow, the gel was dried until it became thick and viscous. After that, concentrated hydrogen fluoride (HF, Sigma-Aldrich, 48% in H₂O) was added dropwise. (*Caution: Hydrogen fluoride is a dangerous substance that can cause fatal burns and irreversible damages to human skin, tissue, and bone. It must be handled with appropriate PPE including a lab coat, a respirator, a full-face shield, an acid-apron, a pair of long-sleeve nitrile gloves, etc. with a proper ventilation in a fume hood.*) The addition of HF turns clear viscous gel into a powdery phase. If ammonium fluoride (NH₄F) was used as the fluoride source, it was added with germanium dioxide. The gel was dried for an extra

couple of days to evaporate the remaining water and ethanol. As the final gel preparation step, a desired amount of water was added to meet the target gel composition. If necessary, the batch was seeded with as-made CIT-13 (5 wt. % with respect to $\text{SiO}_2 + \text{GeO}_2$ in the gel). The liner was tightly sealed with a Parr steel autoclave and placed in a 160 °C static oven. An oven designed to agitate the batches by rotating them at 70 rpm was also used. Aliquoting was performed weekly in order to monitor the crystallization progress.

Aluminogermanosilicate CIT-13s were synthesized similarly to the cases of pure germanosilicate CIT-13 described above. For aluminum source, aluminum isopropoxide (98%, Sigma-Aldrich) was used. The ternary gel composition was $x \text{ SiO}_2 : y \text{ AlO}_{3/2} : z \text{ GeO}_2 : 0.5 \text{ ROH} : 0.5 \text{ HF} : 10 \text{ H}_2\text{O}$ where $x + y + z = 1$. The detailed compositions (x, y, z) are shown in the ternary gel composition diagram illustrated in Figure 6.7(a) shown in the following section. The crystallization was performed in the range of 150–175 °C for 1–4 weeks. Aliquoting was also performed on a weekly basis to monitor the crystallization progress. CIT-13-type aluminogermanosilicates prepared from this protocol were denoted Al/Ge-CIT-13.

The CIT-13 syntheses were also attempted without use of fluoride mineralizers. For a typical CIT-13 synthesis in hydroxide media, the gel composition was $x/(1+x) \text{ SiO}_2 : 1/(1+x) \text{ GeO}_2 : 0.5 \text{ ROH} : y \text{ H}_2\text{O}$, where x is the Si/Ge molar ratio of the gel, and ROH is the desired imidazolium-derivative OSDA hydroxide. The values of x and y and crystallization conditions attempted in this work are provided in Table B4 with the results. For silicon sources, TEOS and fumed silica (ACROS, Cab-O-Sil[®]) were used. The general procedure for hydroxide-mediated synthesis was analogous to the cases of fluoride syntheses explained above, except that the addition of HF or NH_4F is omitted. Excess water and ethanol were evaporated using an air flow. During the drying step, the gel weights must be measured very carefully to reliably estimate the water contents. The final gels having desired compositions

were generally translucent and had very sticky textures. It is recommendable to measure the weights of PTFE liners and stirring bars before starting this procedure.

For a typical IM-12 synthesis,¹¹⁶ a germanosilicate gel having a composition $0.667 \text{ SiO}_2 : 0.333 \text{ GeO}_2 : 0.25 \text{ ROH} : 30 \text{ H}_2\text{O}$ was prepared, where ROH is (6R,10S)-6,10-dimethyl-5-azaspiro[4.5]decanium hydroxide. Firstly, a desired amount of fumed silica and germanium dioxide were dispersed in the OSDA solution and homogenized by stirring overnight. After that, a desired amount of water was added or evaporated to make the final gel have the target composition. The mixture was sealed in a Parr autoclave and placed in a 175 °C static oven for 14 days. Similarly, aliquots were taken periodically to monitor the crystallization.

6.2.3. Characterization

Powder X-ray diffraction (PXRD) patterns were acquired using a Rigaku MiniFlex II benchtop diffractometer using Cu K α radiation ($\lambda = 1.54184 \text{ \AA}$) to assess the crystal structure and crystallinity of the products. The refined structure of as-prepared CIT-13 was obtained from synchrotron X-ray diffraction data performed at the MS-Powder beamline at the Swiss Light Source in Villigen, Switzerland.

Morphology and elemental composition (Si/Ge molar ratios of germanosilicates) were studied using a Zeiss 1550VP field-emission scanning electron microscope (FE-SEM) equipped with an Oxford X-Max SDD X-ray energy dispersive spectrometer. Pore volumes and pore-size information of microporous materials were studied based on Ar adsorption isotherms obtained using a Quantachrome Autosorb iQ at 87.45 K. Thermogravimetric analyses (TGA) profiles were performed to quantify weight fractions of occluded organic molecules in as-prepared CIT-13s using a PerkinElmer STA 6000 instrument.

^1H and ^{13}C nuclear magnetic resonance (NMR) spectra of OSDAs were acquired using a Varian 500 MHz spectrometer with carrier frequencies of 499.843 and 125.686 MHz, respectively. ^1H , ^{13}C , ^{27}Al and ^{29}Si magic-angle spinning (MAS) solid-state NMR spectra of samples were obtained using a Bruker Avance 500 MHz spectrometer with carrier frequencies of 499.843, 125.686, 130.287 and 99.305 MHz, respectively. A 4-mm zirconia rotor with a Kel-F cap was charged with 50–100 mg of as-made or freshly calcined germanosilicate. The MAS rate was 8 kHz both for ^1H - ^{13}C cross-polarization (CP) and normal bloch-decay ^{29}Si experiments, and 12 kHz for ^{27}Al experiments.

6.3. Results and Discussion

6.3.1. Effects of Synthetic Parameters

6.3.1.1. Germanosilicate System in Fluoride Media

The crystallization of germanosilicate CIT-13 was affected by many synthetic parameters. In this work, effects of gel Si/Ge ratios, water contents, OSDA and fluoride contents, type of fluoride source, and crystallization temperatures were systematically studied. Also, the structure-directing abilities of the four OSDAs were investigated. The batch of a gel composition 0.8 SiO_2 : 0.2 GeO_2 : 0.5 ROH : 0.5 HF : 10 H_2O (OSDA = 1) crystallized in an 160 °C static oven for 2–3 weeks was designated as *the reference condition*. From this reference condition, pure phase CIT-13 was reproducibly obtained. Each synthetic parameter was studied by varying only that parameter from the reference condition. The results of synthesis trials are summarized in Table B1, and the PXRD profiles from several selected successful synthesis conditions are displayed in Figure 6.4. No remaining GeO_2 phase was observed in any conditions.

The Si/Ge ratio of gels made a crucial impact on the formation of CIT-13. Gel Si/Ge ratios within a range from 2 to 16 were studied for OSDA **1**. From gel compositions of Si/Ge ratios 2, 3, and 4 (reference) gave pure CIT-13 phases having crystal Si/Ge ratios 3.84 ± 0.59 , 4.72 ± 0.55 , and 5.73 ± 0.89 , respectively. Si/Ge ratios of resultant CIT-13 crystals were higher than those of mother germanosilicate gels. The correlation of gel Si/Ge ratios to crystal Si/Ge ratio is illustrated in Figure B1. Also, the higher Ge content a gel had, the faster the crystallization of CIT-13 was. When gel Si/Ge ratios were 2 and 3, the crystallization was completed within 2 weeks. The gel having Si/Ge ratio = 4 crystallized after 3 weeks. When Si/Ge > 8, one or more impurity phases started to appear. The PXRD profiles of relevant batches from which aliquots were taken with an interval of 1 week are displayed in Figure B2.

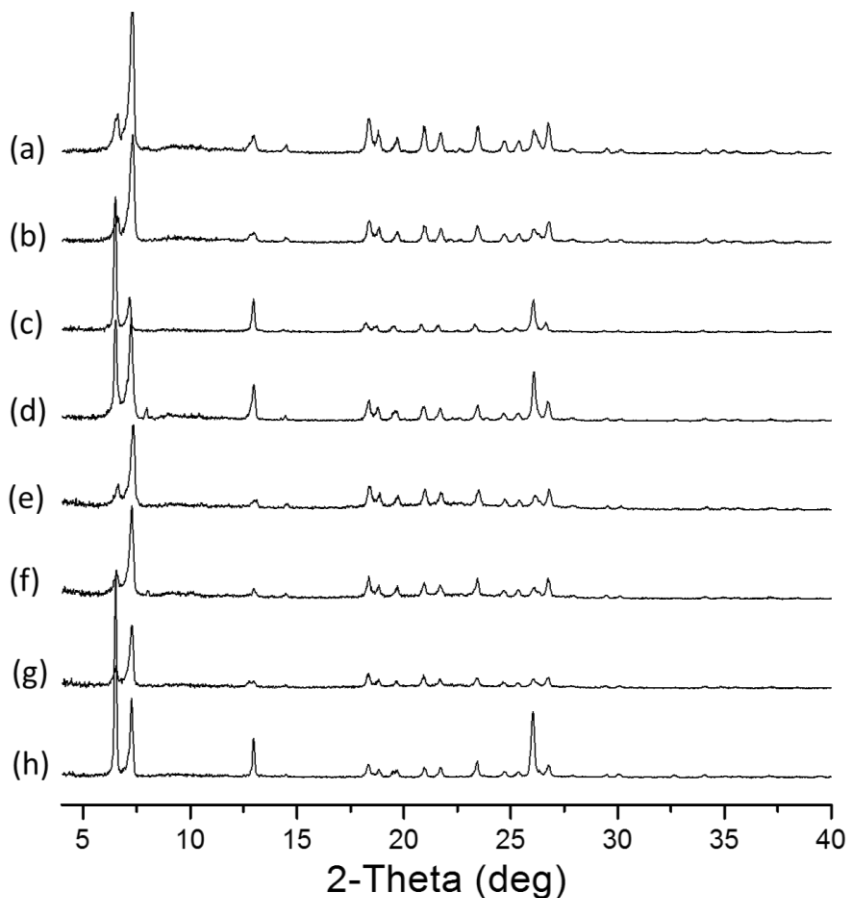


Figure 6.4. PXRD profiles of selected crystallization conditions which gave high-purity CIT-13: (a) reference condition, (b) Si/Ge = 3, (c) seeded, (d) $H_2O/T = 7.5$ where $T = Si + Ge$, (e) crystallization temperature 140 °C, (f) 150 °C, (g) 175 °C, and (h) OSDA **4**.

Water content and OSDA/F content were other factors that seriously influenced the crystallization and kinetics of CIT-13. For water content, in this work, gel H_2O/T ratios from 7.5 to 15 were tested. Within the studied range of the water content, only CIT-13 phases were crystallized. Water content was closely related to the rate of formation. When the batches were not seeded, crystallization of CIT-13 was faster in gels with less amounts of water. The

summary and PXRD patterns are shown in Table B1 and Figure B3. The $\text{H}_2\text{O}/\text{T} = 7.5$ gel crystallized pure CIT-13 within 2 weeks, while the $\text{H}_2\text{O}/\text{T} = 15$ gel required 5 weeks to yield the product. Seeding the batches with as-make CIT-13 shortened the crystallization time by ca. 1 week, but did not affect the overall tendency. The concentration of OSDA^+F^- ion-pair in gels was studied within a range of $0.50 < \text{OSDA}^+\text{F}^-/\text{T} < 0.75$. As shown in Figure B4, pure CIT-13 phases were obtained when $\text{OSDA}^+\text{F}^-/\text{T} < 0.625$. But further increase in OSDA concentration resulted in a formation of unknown impurity. The presence of seeds did not make a substantial influence on the rate of formation of CIT-13 in this series.

Temperature and types of ovens were parameters that affected the crystallization other than variables of gel compositions. Hydrothermal syntheses were conducted with four batches having the same reference gel composition at four different temperature (140, 150, 160, 175 °C) to investigate the influences of the crystallization temperatures. The PXRD profiles and SEM images of aliquots and final products from these trials are shown in Figures B5 and B6, respectively. The higher temperature the crystallization temperature was, the faster CIT-13 was formed. At 175 °C, pure CIT-13 was crystallized within a just week even without seeds; however, it took at least 4 weeks at a temperature below 150 °C. Also, the crystallization temperature influenced the size of product crystals. As shown in Figure B6, when a static-type oven was used, an increase in the crystallization temperature resulted in an increase in the crystal size. Agitation by using a rotary oven instead of a static oven also significantly influenced the crystal morphology (see Figure B7). From a static oven, large ($> 20 \mu\text{m}$) and apparently polycrystalline crystallites were obtained. When the batch was continuously agitated in the course of the crystallization, the size of crystallites was much smaller ($\sim 2\text{--}5 \mu\text{m}$), and the crystallites had a single-sheet-like morphology. This difference is because the agitation of the batch influenced both nucleation and diffusion in the system by attenuating the concentration gradients of gel species and generating transport flows in gels, respectively.

The structure of the OSDA is a crucial variable that determines the resultant frameworks.¹¹⁴ The Davis group reported the crystallization of germanosilicates using a series of imidazolium-derivative OSDAs having ortho-, meta-, and para-methylbenzyl pendant groups.⁶³ The OSDA having a methyl group on the ortho-position of the benzyl group crystallized an IWS-type germanosilicate when the Si/Ge ratio of gels was low (Si/Ge < 2), whereas the use of para-substituted benzylimidazolium derivative resulted in LTA-type germanosilicates, aluminosilicates, and pure-silica LTA.⁶²⁻⁶³ Only the methyl-substituted configurational isomer (1,2-dimethyl-3-(3-methylbenzyl)imidazolium) yielded pure CIT-13 phases in a wide range of Si/Ge ratios.⁶³ In this work, four related imidazolium-derivative cations (**1**, **2**, **3**, and **4**) having one or two methyl groups on the meta- site of their benzyl rings are tested in the germanosilicate system of Si/Ge ratios from 2 to 16. The structures are shown in Figure 6.2, and the resultant XRD profiles taken every week are provided in the Appendix B (Table B1, Figures B8, B9, and B10).

The diffraction peaks corresponding to CIT-13 are observed in batches containing any of the four OSDAs when Si/Ge < 16. However, only OSDA **1** and OSDA **4** successfully crystallized pure CIT-13 phases within a reasonably wide range of Si/Ge ratios. In batches of OSDA **2**, an MFI impurity phase was observed, and this impurity MFI phase dominated the product mixture when the Si/Ge ratio is high (Figure B8). Several previous works described the inclusion of Ge within the MFI framework,^{171, 192} but it was unclear whether Ge was incorporated in the MFI impurity phase observed in this work. OSDA **3** also yielded CIT-13 but one or more unidentified impurity phases were observed at all gel Si/Ge ratios (Figure B9).

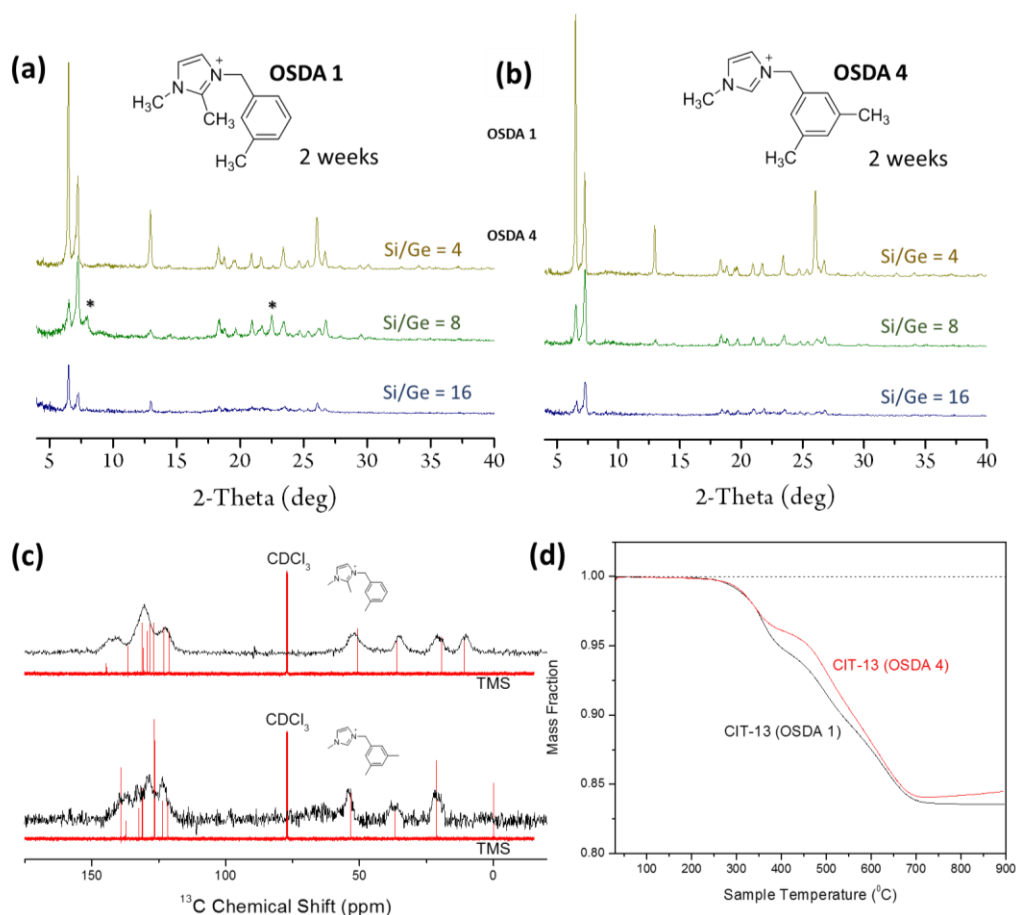


Figure 6.5. PXRD profiles of the samples crystallized from different Si/Ge ratios in the gel with (a) OSDA 1 and (b) OSDA 4 for gel compositions $x/(1+x)$ SiO_2 : $1/(1+x)$ GeO_2 : 0.5 ROH : 0.5 HF : 10 H_2O . (x is the Si/Ge ratio of gels; Asterisks * denote impurity peaks.) (c) ^{13}C solid-state 8 k MAS NMR spectra (black) of as-made CIT-13 from OSDA 1 and OSDA 4, overlapped with the ^{13}C solution (in CDCl_3) NMR spectra (red) of the corresponding OSDAs. (d) TGA profiles of as-made CIT-13 samples from OSDA 1 and OSDA 4.

OSDA **1** and OSDA **4** yielded high-purity CIT-13 germanosilicates with little impurity within 2 weeks at gel Si/Ge = 4, 8, and 16. Figure 6.5(a) and 6.5(b) show the PXRD patterns of products after 2 weeks of crystallization with OSDA **1** and OSDA **4**. For both OSDAs, the crystallinities were better when gel Si/Ge ratios were low. Also, the OSDA molecules were occluded within the pore systems of CIT-13 without degradation. The ^1H -decoupled ^{13}C solid-state 8 k MAS NMR spectra of as-prepared CIT-13 from the two OSDAs matched well with the ^{13}C solution NMR spectra of the two OSDAs in CDCl_3 . (Figure 6.5(c)) From the TGA profiles of as-prepared CIT-13, the weight fractions of OSDA molecules in as-prepared molecular sieves can be estimated. From the weight losses of TGA profiles shown in Figure 6.5(d), it was calculated that OSDA **1** and OSDA **4** occupied 16.5% and 15.6% of as-prepared CIT-13, respectively. If a unit cell of as-prepared CIT-13 had contained 4 OSDA molecules, the weight loss of TGA should have been 18%. However, the estimated values were lower than that. The structure refinement based on the synchrotron X-ray diffraction of as-prepared CIT-13 revealed that the OSDA occupancy was less than unity (ca. 0.8), which is corresponding to a weight loss of 15%. This incomplete OSDA occupancy is probably a result of the disorder in the $d4r$ unit arrangement in the CIT-13 framework. Similar types of reduced occupancy were also observed in the case of SSZ-55 (ATS) and SSZ-59 (SFN).¹⁷²

CIT-13 could be synthesized using NH_4F instead of concentrated HF solution. Replacing HF with NH_4F is important in terms of scaled-up industrial production since it provides a way to avoid the use of volatile and dangerous HF. It was proven that equimolar amounts of NH_4F can replace HF successfully, yielding identical CIT-13 products. Two CIT-13 samples, one from the reference condition using HF and the other from a protocol that used an equimolar amount of NH_4F instead of HF, were prepared in an 160 °C static oven and compared with PXRD, SEM, EDS, TGA, and Ar-adsorption at 87.45 K. The PXRD profiles agreed to each other without impurity peaks (Figure 6.6(a)). The SEM micrographs shown in Figure 6.6(b) and 6.6(c) demonstrate that the two CIT-13 have very similar

morphology. From the TGA profiles given in Figure 6.6(d), it was found that the two as-prepared CIT-13 samples possessed very similar amounts (16.5 wt. % for CIT-13/HF and 16.1 wt.% for CIT-13/NH₄F) of occluded organic molecules. Finally, the Ar adsorption isotherms from freshly calcined versions of the two CIT-13 well matched each other (Figure 6.6(e)). The micropore volumes of CIT-13/NH₄F characterized based on the t-plot model and the Saito-Foley (SF) model¹⁷³ were 0.191 cm³ g⁻¹ and 0.215 cm³ g⁻¹, respectively. These values are very close to the values obtained from CIT-13/HF (0.182 cm³ g⁻¹ from the t-plot method and 0.222 cm³ g⁻¹ for the SF model).

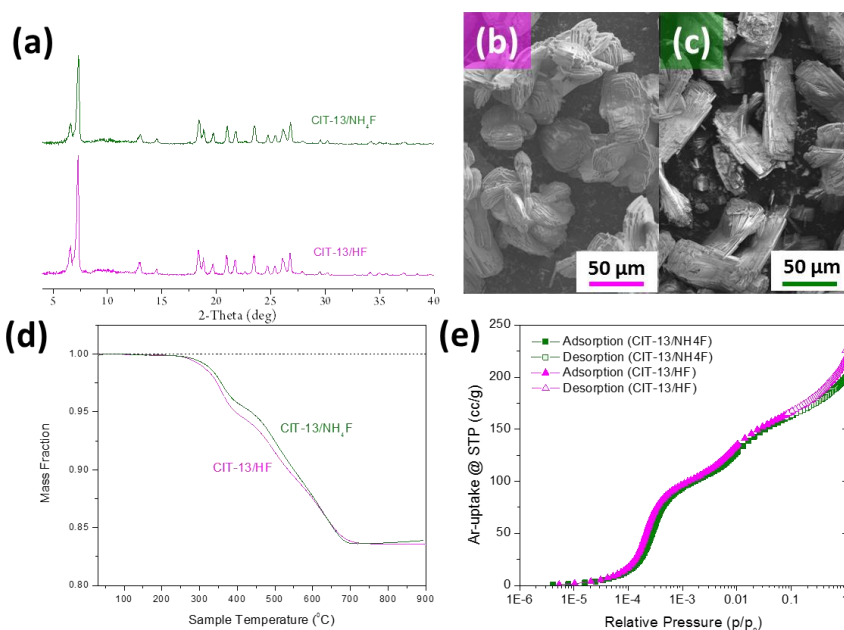


Figure 6.6. (a) PXRD profiles of as-prepared CIT-13 using NH₄F (green) and HF (magenta) as the mineralizing fluoride sources. SEM images of CIT-13 resulting from the (b) HF and (c) NH₄F protocols. (d) TGA profiles of as-prepared CIT-13 using NH₄F (green) and HF (magenta). (e) Ar adsorption and desorption isotherms (log-scale, 87.45 K) of calcined CIT-13 from NH₄F- (green) and HF-protocol (magenta).

6.3.1.2. Aluminogermanosilicate System in Fluoride Media

The incorporation of aluminum is investigated on the basis of aluminogermanosilicate ternary elemental compositions. Although it is known that germanium incorporated in germanosilicate framework shows a weak Lewis acidity,^{142, 156} it is desirable to incorporate elements having an oxidation state of +3 (*e.g.*, B, Al, Ge, Fe, In, etc.) with a tetrahedral coordination in frameworks to let resultant molecular sieves have decent strength of Brønsted and Lewis acidities.^{153, 173} Generally, there are two ways to incorporate these elements within germanosilicate frameworks: direct incorporation in hydrothermal synthesis and postsynthetic modification. In this section, the method of direct incorporation of aluminum in CIT-13 hydrothermal synthesis will be discussed. The postsynthetic method will be discussed in Chapter VIII.

The ternary gel elemental composition diagram and resultant phases are illustrated in Figure 6.7(a). Pure CIT-13 phases were obtained only when the Al-composition of gel was low (gel Si/Al < 20). A PXRD pattern of Al/Ge-CIT-13 obtained from a gel having a Si/Al ratio of 30 is compared with that of pure germanosilicate CIT-13 in Figure 6.7(b). With high aluminum contents (Gel Si/Al < 20) in gels, LTA phases were primarily obtained. This narrow tolerance for aluminum contents in the Si-Al-Ge CIT-13 ternary system resembled the Si-B-Ge and Si-Al-Ge UTL ternary systems in which STT or STF phases appeared with high boron or aluminum contents.^{153, 1617} Inclusion of aluminum also resulted in smaller crystal sizes (SEM: Figure 6.7(e)) and longer crystallization times. This observation was also in consistent with an analogous study on UTL.¹⁵³

The ²⁹Si NMR of obtained Al/Ge-CIT-13 (Figure 6.7(c)) showed a broad peak in the range of -100 to -120 ppm. There are seven crystallographically different T-sites in the unit cell of CIT-13, and two heteroatoms (Al, Ge) which shift silicon signal toward downfield. Furthermore, the high bond strain of *d4r* units contribute to overlapping of peaks. The ²⁷Al NMR spectrum of Al/Ge-CIT-13 is shown in Figure 6.7(d). Only one broad signal at 50.5

ppm, which corresponds to tetrahedral aluminum sites, was observed. This absence of octahedral aluminum species is also seen in the direct incorporation of aluminum in UTL.¹⁵³

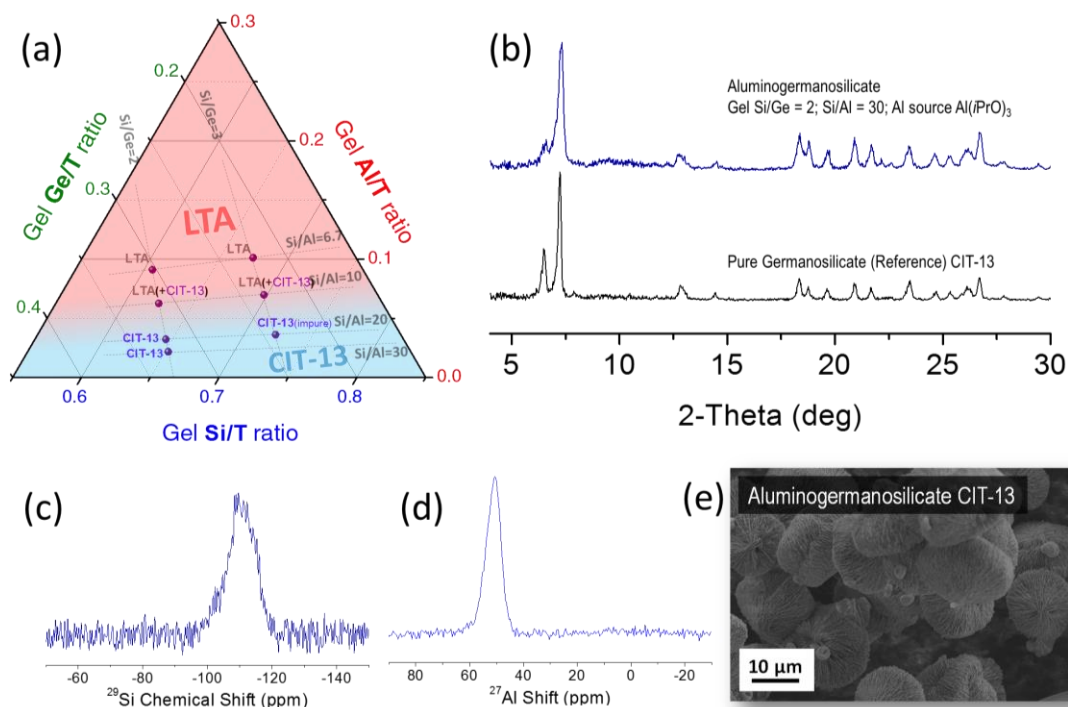


Figure 6.7. Material characterization results of Al/Ge CIT-13. (a) The resultant phases of hydrothermal products ($T = 150\text{--}175\text{ }^{\circ}\text{C}$, for 1–4 weeks) denoted on a Si–Al–Ge ternary gel composition diagram. (b) PXRD pattern of Al/Ge-CIT-13. (c) 8 kHz MAS solid-state ²⁹Si NMR spectrum of Al/Ge-CIT-13. (d) 12 kHz MAS solid-state ²⁷Al NMR spectrum of Al/Ge-CIT-13. (e) SEM image of obtained Al/Ge-CIT-13 crystallites.

6.3.1.3. Germanosilicate System in Hydroxide Media

Ge-CIT-13 could be prepared without use of fluoride. Some other *d4r*-type germanosilicates such as ITQ-13 and ITQ-22 can be prepared from both fluoride-based and hydroxide-based recipes.^{146, 175–176} IM-12 is also prepared without any fluoride media.¹¹⁶

The gel compositions for hydroxide-based CIT-13 syntheses trials are shown in Table B4. In this work, CIT-13 samples synthesized in hydroxide media were denoted as CIT-13/OH(#) where # is the sample number shown in Table B4. Also, only in contexts where comparisons between fluoride- and hydroxide-media were made, CIT-13 samples from fluoride media were denoted as CIT-13/F.

Figure 6.8 shows PXRD profiles, SEM images, ^{29}Si NMR spectra, and argon adsorption isotherms (87.45 K) of several selected CIT-13/OH samples. PXRD patterns shown in Figure 6.8(a) are comparable to typical CIT-13/F PXRD patterns. The ortho-isomer (denoted “Ortho” in Table B4) of OSDA **1** which yields IWS-type germanosilicates in fluoride media⁸ was also able to crystallize pure CIT-13 in hydroxide media. In this work, OSDA **1** was generally used to prepare CIT-13/OH samples.

The hydroxide-mineralized crystallization generally took longer than the cases of fluoride-based recipes. Although CIT-13/OH showed planar crystal morphologies similar to CIT-13/F, as shown in Figure 6.8(b) and (c), CIT-13/OH crystals were generally smaller than CIT-13/F crystals despite longer crystallization times. Example ^{29}Si NMR spectra of CIT-13/OH and CIT-13/F are compared in Figure 6.8(d). Shapes of ^{29}Si resonance patterns were very similar to each other. This result implies that the natures Si-sites in the CIT-13 framework were very similar regardless of type of mineralizers used. Further deconvolution of ^{29}Si NMR spectra was not performed. An argon adsorption isotherm of CIT-13/OH was also obtained and compared to that of CIT-13/F. The CIT-13/OH isotherm also shows two-step adsorption at $p/p_0 = 5 \times 10^{-4}$ and 0.01 just like other CIT-13/F samples as shown in Figure 6.8(e). This two-step adsorption behavior will be discussed in detail in Section 6.3.3. The micropore volumes of CIT-13/OH estimated based on the t-plod method and the Saito-Foley (SF) model were 0.171 cc g^{-1} and 0.202 cc g^{-1} , respectively.

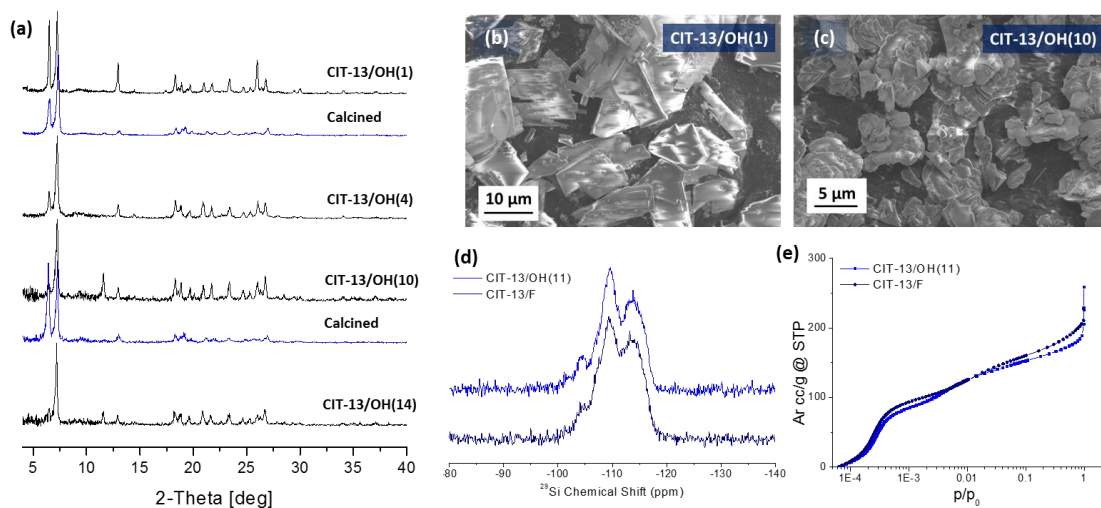


Figure 6.8. (a) Examples of PXRD patterns of CIT-13/OH samples. (b) SEM images of selected CIT-13/OH samples. (d) 8 kHz MAS ^{29}Si solid-state NMR spectra of CIT-13/OH(11) compared to that of CIT-13/F. (e) Argon adsorption isotherms (87.45 K) of CIT-13/OH(11) and a typical CIT-13/F.

6.3.2. Structural Disorder within CIT-13

An in-depth structural study on as-prepared CIT-13 was performed in collaboration with Dr. Stef Smeets from Stockholm University, Sweden (now at TU Delft, the Netherlands) and Dr. Lynne B. McCusker from ETH Zürich, Switzerland.

The Rietveld refinement of as-prepared CIT-13 was performed based on the PXRD using a synchrotron beamline. The observed and calculated 1-dimensional patterns are shown in Figure 6.9. The crystallographic information calculated from the refined model is given in Appendix B. Due to the presence of OSDA molecules filling up the channel system, the refinement was performed at a lower symmetry $P\bar{1}$. (The original model determined based on the rotational electron diffraction (RED) experiment of calcined CIT-13 belongs to

the space group $Cmmm$.⁶³) The main difference between the observed and calculated diffraction profiles (Figure 6.9.) is presumably due to the asymmetric peak shapes of the observed profile. A complete interpretation for this asymmetric peak shape was not made. The Si/Ge ratio of the refined model was 5.63 which matches well with the value observed using EDS (5.73 ± 0.89). Also, most Ge atoms were located in the $d4r$ units. The estimated occupancy of OSDA was 3.26 molecules per unit cell which is 81.5% of the full occupancy (4 molecules per unit cell). This incomplete occupancy also agrees well with the observed weight loss from the TGA experiment which is smaller than the expected value (*vide supra*). The positions of fluoride anions were located at the center of the $d4r$ units, similarly to other germanosilicate frameworks possessing the $d4r$ units synthesized from fluoride media.²¹

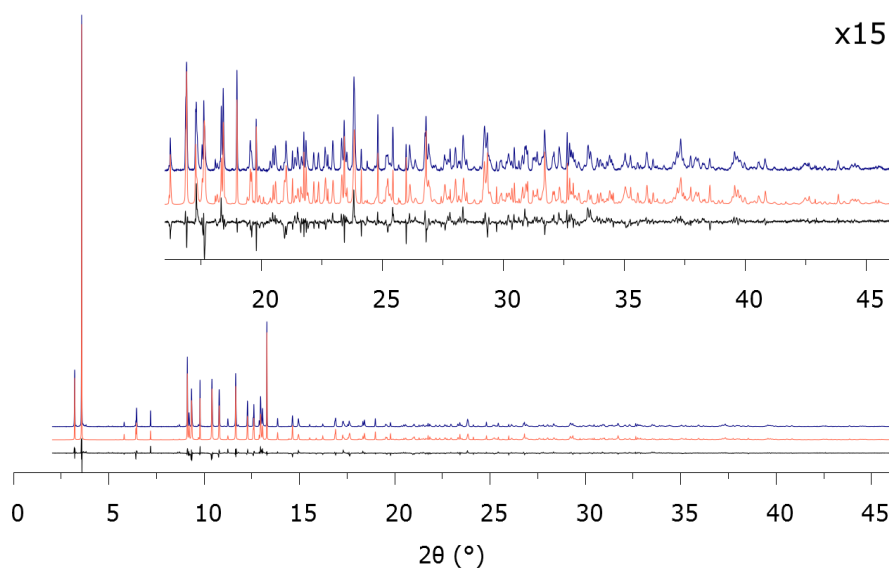


Figure 6.9. The observed diffraction profile (blue), calculated profile (red), and difference between the two (black) for the Rietveld refinement of as-prepared CIT-13.

The disorder in CIT-13 is originated from multiple number of possible arrangements of the $d4r$ units in the framework. As previously mentioned, the CIT-13 framework is composed of the cfi -layers and the 2-dimensional arrays of $d4r$ units connecting neighboring layers. There are two different ways to stack the cfi -layers: ABAB and AAAA as shown in Figure 6.10(a) and 10(b). The presence of this stacking disorder in CIT-13 is also suggested based on the high annular dark field scanning transmission electron microscopy (HADDF STEM).¹⁶⁵ No line broadening due to this type of disorder was observed in the powder diffraction pattern. This result suggests that CIT-13 consists of 10–20-unit-cell sized domains of either ABAB or AAAA along the x-axis.

Figures 6.10.(c) and (d) illustrate the other type of disorder which is related to the arrangements of $d4r$ units *within* the interlayer region. One possible arrangement shown in Figure 6.10(c) generates straight 10-ring channels, while the other displayed in Figure 6.10(d) makes the 10-ring channels sinusoidal. However, the staggered arrangement of $d4r$ units (Figure 6.10(d)) makes the OSDA molecules arranged within the channel system of CIT-13 very unfavorable; the intermolecular distances among OSDA molecules are too close to or too far from their neighboring molecules, and the distances between the framework wall and molecules are also too close. Thus, it can be concluded that the staggered arrangement is less likely than the parallel arrangement shown in Figure 6.10(c).

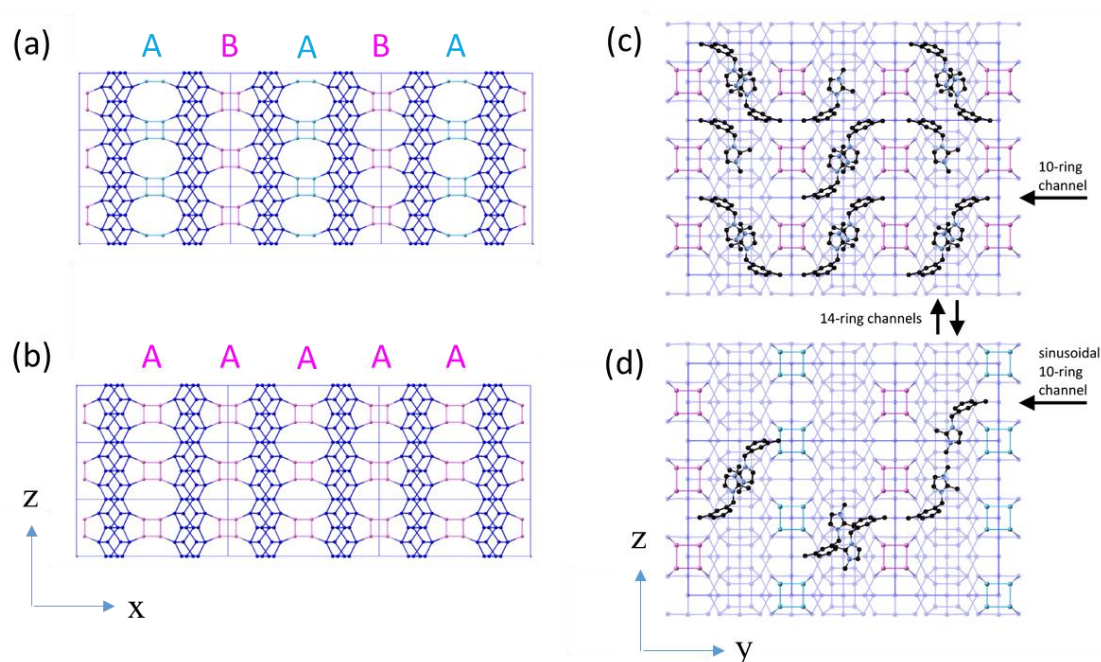


Figure 6.10. Schematic illustrations of possible disordered models for CIT-13. (a–b) Views along the y-axis showing two possibilities of the *cfi*-layers stacking mode: (a) ABAB and (b) AAAA. (c–d) Projections along the x-axis showing two possibilities of the *d4r* unit arrangements together with OSDA molecules within the interlayer region making (c) straight 10-ring channels and (d) tortuous 10-ring channels.

6.3.3. Comparison to Relative Germanosilicates

The UTL-type germanosilicate is another framework that is composed of Si-rich dense layers and 2-dimensional arrays of Ge-rich *d4r* units, belonging to a monoclinic space group $C2/m$. The *fer*-layers are interconnected with the *d4r* units and an extra-large pore channel system consists of perpendicularly intersecting 14-ring and 12-ring straight channels are present within the interlayer region. Due to the structural difference between *fer*-type layers and *cfi*-type layers, the UTL framework has no disorder within the interlayer region

that is the case for CIT-13. The schematic illustrations which demonstrate similarities and differences between UTL and CIT-13 are provided in Figure 6.11.

A high-Ge extra-large pore molecular sieve IM-12 having a UTL topology was prepared and compared to CIT-13. IM-12 was synthesized using a spiro-type ammonium OSDA, (6R,10S)-6,10-dimethyl-5-azaspiro[4.5]decanium, in hydroxide medium according to the protocol reported previously in literature.¹¹⁶ The PXRD profile and SEM image of the resultant as-prepared IM-12 is shown in Appendix (Figure B11). The Si/Ge ratio of the IM-12 was 4.5 which is lower than that of the compared CIT-13 (Si/Ge = 5.0).

The ²⁹Si solid-state NMR spectra of freshly calcined two germanosilicates are shown in Figure 6.12(a). Signals were almost absent in the region -100 to -105 ppm. Thus, these two germanosilicates had almost no significant Q³ silanol groups and could be regarded as complete *tecto*-germanosilicates. For both germanosilicates, multiple peaks which significantly overlap with one another were observed in the region -105 to -120 ppm. IM-12 showed more peaks than CIT-13, probably because the framework UTL has more crystallographically unique T-atoms (twelve) than CIT-13 (seven). The signals within the region -110 to -120 ppm are contributed by high silica Q⁴-Si atoms residing in *fer*- or *cfi*-layers.¹¹⁸ Small shoulder signals observed in the region -105 to -110 ppm must be either Q⁴-Si atoms in the *d4r* units^{154, 177} or Si atoms neighboring with one or more Ge atoms,^{153, 178} but conclusive peak assignments were not made here.

The micropore volumes of IM-12 and CIT-13 were obtained based on Ar adsorption isotherms at 87.45 K. Based on the t-plot method and the Saito-Foley model, the estimated micropore volumes of IM-12 were 0.177 cm³ g⁻¹ and 0.205 cm³ g⁻¹. The acquired isotherms described in linear scale and logarithmic scale are demonstrated in Figure 6.12.(b) and (c). Unlike IM-12, CIT-13 showed a characteristic two distinct steps of pore filling phenomena which is apparent in the log-scale chart shown in Figure 6.12.(c). The first pore filling occurred at $p/p_0 \sim 10^{-4} - 10^{-3}$ and the second pore filling appeared at $p/p_0 \sim 10^{-2}$. The former

may be contributed to pore-filling of the narrow and eccentric 10-ring channels and the latter may be from pore-filling of remaining space within the wide 14-ring channels. The pore-size distribution derived from the isotherm of CIT-13 based on the cylindrical Saito-Foley model¹⁷³ is shown in Figure B12(a). Unlike IM-12, CIT-13 apparently shows a two-step pore-filling behavior. The reason why IM-12 did not show such behavior may be that the 12-ring channel of IM-12 has no high eccentricity and a size close to that of the 14-ring main channel of UTL. Argon isotherms of zeolite A (LTA) and Y (FAU) are provided in Figures B12(b) and (c) for clearer comparison.

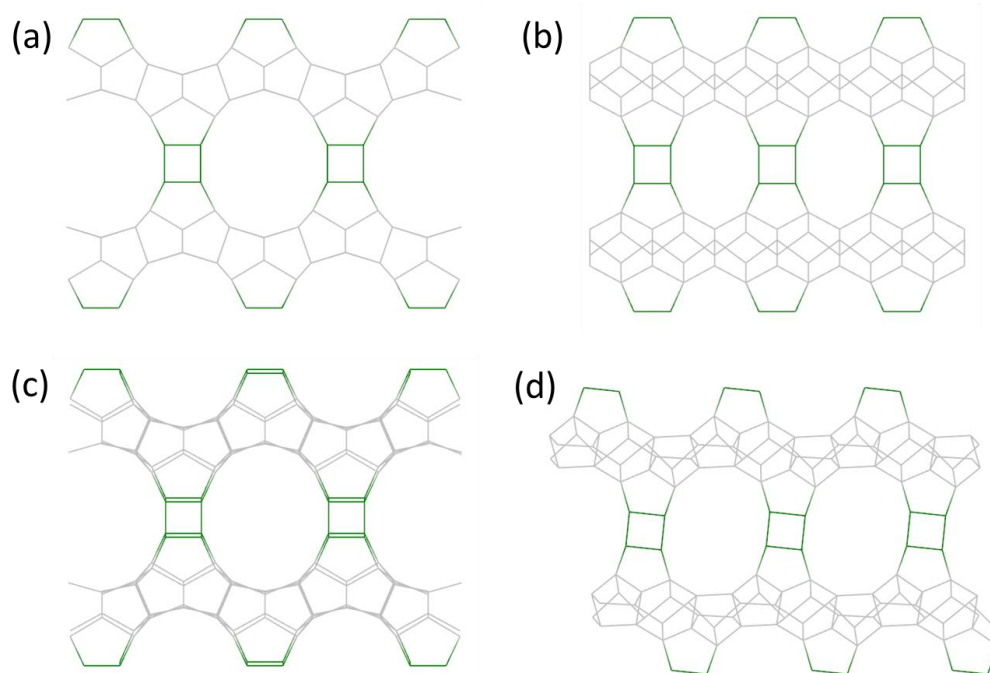


Figure 6.11. Comparison between the crystal structures of CIT-13 and IM-12. (a) CIT-13 viewed along the [001] direction showing the 14-ring pore, and (b) along the [010] direction showing the 10-ring pore. (c) IM-12 viewed along the [001] direction showing the 14-ring pore, and (d) along the [010] direction showing the 12-ring pore.

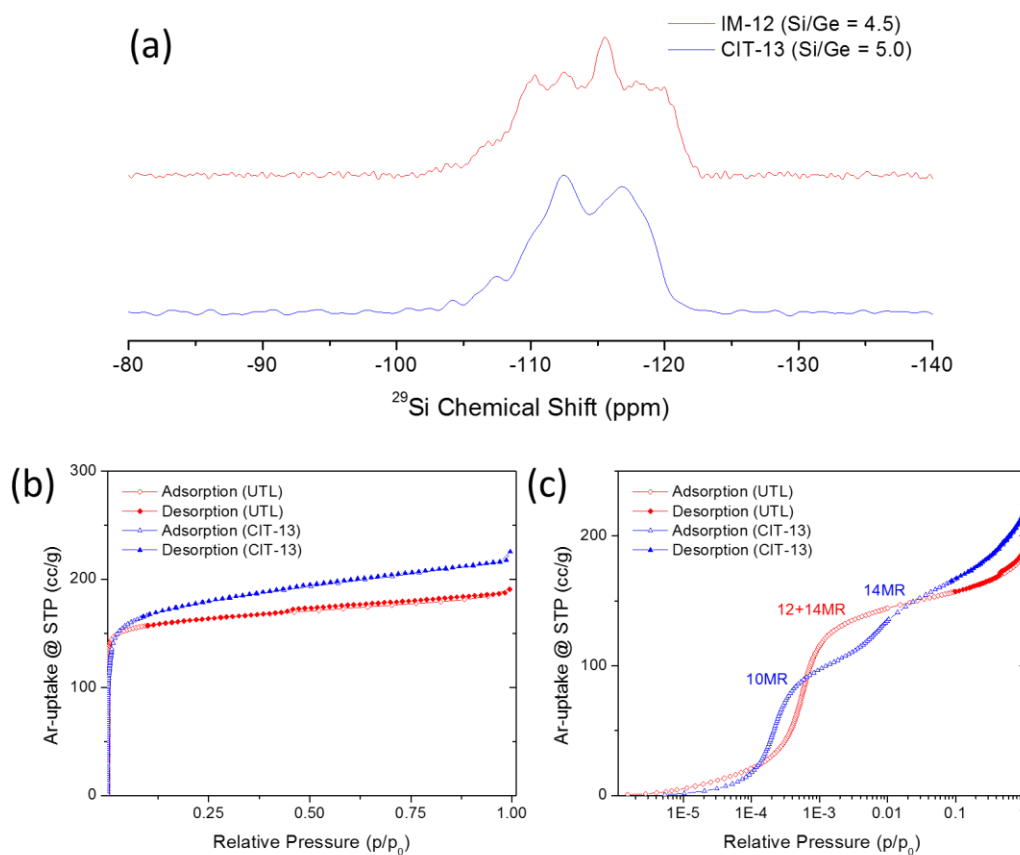


Figure 6.12. Material characterization results of IM-12 and CIT-13. (a) ^1H -decoupled ^{29}Si solid-state 8 k NMR spectra of IM-12 and CIT-13. Ar adsorption and desorption isotherms at 87.45 K of IM-12 and CIT-13 in (b) linear and (c) log-scale.

6.4. Summary

In this chapter, the synthesis conditions for CIT-13 were optimized. The gel composition of 0.80 SiO_2 : 0.20 GeO_2 : 0.5 ROH : 0.5 HF : 10 H_2O was suggested as the optimized synthesis condition for CIT-13 in fluoride media. It was experimentally shown that HF can be replaced with the same molar amount of ammonium fluoride. For

isomorphous substitution synthesis, the ternary gel system of Al, Ge, and Si was studied. LTA phase appeared as the major impurity phase when the gel Si/Al ratio was low (Si/Al < 20). CIT-13 could be also synthesized without fluoride. The CIT-13 sample synthesized in hydroxide media showed properties similar to CIT-13 from fluoride-mediated syntheses. The nature of structural disorder was also studied on the basis of the Rietveld refinement result, focusing on the arrangement of $d4r$ units within the interlayer region. It was concluded that the staggered arrangement of $d4r$ units along the 10-ring direction is not favorable. Lastly, the properties of CIT-13 were compared to those of IM-12. CIT-13 showed a two-step argon adsorption behavior which may originate from the eccentricity of 10-ring pore which IM-12 does not have.

Chapter 7

Transformation from CIT-13 to CIT-5

In this chapter, the spontaneous transformation of Ge-CIT-13 into Ge-CIT-5 is discussed. The influence of the type of parent Ge-CIT-13 on the transformation rate and the role of moisture in the transformation are elucidated. The resultant Ge-CIT-5 is characterized and compared to CIT-5 synthesized using the methylsparteinium OSDA. Similar layered germanosilicates containing Ge-rich *d4r* units are also investigated in terms of transformability upon exposure to moisture in ambient air as a comparison to the Ge-CIT-13.

7.1. Introduction

CIT-5 (CFI) is an extra-large-pore high-silica zeolite having one-dimensional 14-ring channels.¹³¹ As mentioned in Chapter V, since its discovery, the catalysis over extra-large-pore zeolites has been extensively studied together with other 14-pore aluminosilicate and borosilicate such as UTD-1, SSZ-53, and SSZ-59.^{134-135, 139} Unfortunately, the only synthetic pathway for CIT-5 that has been reported was the recipe using N-methylsparteinium as the OSDA which is very expensive and hard to obtain. In 2017, the scientific community saw news regarding the sudden nationwide scarcity of sparteine in the market for an unknown reason.¹⁷⁹ Since the use of sparteine is the only way to obtain CIT-5, the market availability of CIT-5 automatically will be always open to questions unless any stable sources of sparteine are secured.

CIT-13 is structurally related not only to IM-12, but also to CIT-5. The two frameworks share the same *cfi*-layer structure and have 14-ring pores. In CIT-13 and CIT-5, the *cfi*-layers are connected via *d4r* units and double zigzag chains, respectively. Surprisingly, calcined germanosilicate CIT-13 slowly transformed into another germanosilicate having a CFI topology under a general lab atmosphere. This transformation was so slow that sometimes it took many months. There has been a consensus in the scientific community that exposing calcined germanosilicate to moisture in ambient atmosphere is not desirable in terms of preservation of structures.^{158, 180}

Intentionally exploiting the chemical lability of germanium T-sites in zeolitic frameworks has begotten many transformation and postsynthesis protocols, such as the ADOR method.¹⁸¹ However, in those procedures, germanosilicates should be submerged in liquid phases such as weak or strong acids.^{118, 161, 182} The transformation of Ge-CIT-13 into Ge-CIT-5 can be accomplished without such wet procedures. The key stage of the CIT-13-to-5 transformation was sorption of moisture from the atmosphere. In this regard, this transformation is like the moisture-mediated transformation of VPI-5 to $\text{AlPO}_4\text{-8}$ at elevated temperature.^{127, 183}

In this chapter, the role of sorbed water within the pore systems of germanosilicates will be discussed. The relationship between the rate of transformation and the nature of the parent Ge-CIT-13 will be also investigated. The resultant Ge-CIT-5 will be also compared to pure-silica CIT-5 synthesized from the original recipe. Also, the structure evolutions of other germanosilicates will be discussed.

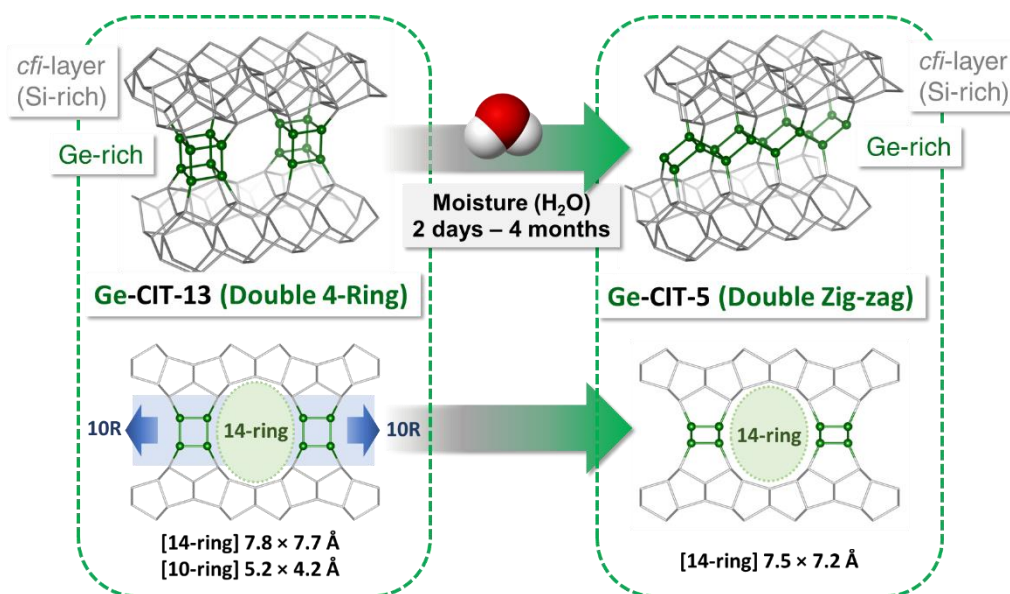


Figure 7.1. Transformation from Ge-CIT-13 to Ge-CIT-5

7.2. Experimental

7.2.1. Preparation of Parent Ge-CIT-13

Parent Ge-CIT-13 molecular sieves were synthesized according to the methods explained in the previous chapter. Ge-CIT-13 samples were prepared on the basis of the two protocols: the fluoride recipes and the hydroxide recipes. The gel compositions are given in the previous chapter. The target Si/Ge ratios of Ge-CIT-13 parent materials were in the range of 3.5–5.5. This range of Si/Ge ratios could be achieved by controlling the gel Si/Ge ratios in the range of 2.5–4.0. An empirical correlation between the gel Si/Ge ratio and the Si/Ge ratio of the resultant CIT-13 is given in Figure B1. Calcination was performed at 580 °C for 6 hours to remove occluded organics.

7.2.2. Transformation of Ge-CIT-13 to Ge-CIT-5

The transformation from Ge-CIT-13 to Ge-CIT-5 requires no specific procedure because it starts immediately after calcination. Just by leaving calcined Ge-CIT-13, the transformation was automatically achieved under an ambient condition (room temperature and relative humidity of 30 %). To keep the humidity constant, in this work, the transformation was conducted in a small chamber where the internal temperature and humidity were monitored and controlled (30 % relative humidity at 25 °C).

7.2.3. Preparation of Reference Sparteine-CIT-5

Pure-silica reference CIT-5 was prepared from hydrothermal synthesis using N-methylsparteinium hydroxide as the OSDA on the basis of protocols reported by our group.^{131-132, 184} First, 50 mmol of (-)-Sparteine (Aldrich) was dissolved in 150 ml of chloroform. The reaction mixture was cooled down in an ice bath, and 70 mmol of methyl iodide was added dropwise for 30 min. The reaction was undergone at room temperature for 72 hour under continuous stirring in the dark. The product was crystallized by adding excess diethyl ether, and collected by filtration. Recrystallization was performed using isopropanol and ethyl acetate. The final product was dried in vacuum at room temperature. The obtained bright yellow N-methylsparteinium iodide salt was converted to its hydroxide-form by a typical ion-exchange procedure using DOWEX™ Monosphere™ 550A ion-exchange resin (Dow Chemical). The detailed procedure for the ion-exchange was described in the previous chapter. If (-)-sparteine sulfate salt was provided as the starting material, free (-)-sparteine can be obtained by extraction using 3 M NaOH aqueous solution.¹⁸⁴

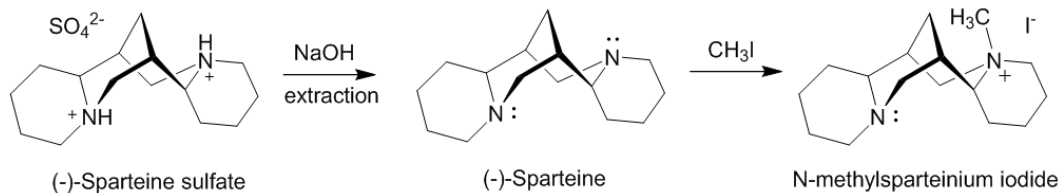


Figure 7.2. Reaction scheme for the preparation of N-methylsparteinium OSDA.

The gel composition used for the hydrothermal synthesis of pure-silica sparteine-CIT-5 was 1.0 SiO₂ : 0.10 LiOH : 0.24 MSpaOH : 40 H₂O where MSpaOH denotes N-methylsparteinium hydroxide. A desired amount of lithium hydroxide monohydrate (LiOH·H₂O, Sigma-Aldrich, 98.5–101.5 %) was dissolved in a desired amount of MSpaOH aqueous solution. Colloidal silica Ludox[®] HS-30 (Sigma-Aldrich) was added, and the mixture was stirred for 24 hours. Lastly, distilled water was added to the gel to achieve the desired gel composition. The final gel was charged into a 23-mL PTFE-lined Parr steel autoclave. The crystallization was performed at 175 °C for 7 days in a static oven. The resultant product was washed with distilled water and acetone, and dried at 100 °C. Calcination was performed at 580 °C for 6 hours under an air flow. For the rest of this work, this reference sample based on the original recipe of CIT-5 is referred to as Spa-CIT-5 to avoid confusion.

7.2.4. Preparation of IM-12, JLG-18, and ITQ-22

Germanosilicates IM-12 (UTL), JLG-18 (ITH), and ITQ-22 (IWW) were prepared on the basis of protocols reported in the literature.^{116, 146, 185} Detailed descriptions for the synthesis of IM-12 are provided in the previous chapter.

JLG-18 was synthesized using commercially available N,N,N',N'-tetramethyl-1,6-hexanediamine (TMDA) as the OSDA.¹⁸⁵ In a desired amount of distilled water, TMDA (Sigma-Aldrich, 99%), tetraethyl orthosilicate (TEOS, Alfa Aesar, 98%), and germanium

oxide (Strem, 99.999%) were added and homogenized for 24 hours. After that, a desired amount of ammonium fluoride (98%, Sigma-Aldrich) was added and stirred overnight. The final gel molar composition was $x/(x+1)$ SiO₂ : $1/(x+1)$ GeO₂ : 7.0 TMDA : 1.40 NH₄F : 44 H₂O where x ($0.75 < x < 1$) is the gel Si/Ge molar ratio. The mixture was sealed in a PTFE-lined steel autoclave (Parr Instrument) and crystallized in a rotating or static oven at 175 °C for 1 week. The resultant product was washed with distilled water and acetone, and dried in a convection oven at 100 °C.

ITQ-22 was prepared using 1,5-bis-(methylpyrrolidinium)-pentane dibromide (MPP²⁺Br₂⁻) which can be synthesized from the S_N2 reaction between N-methylpyrrolidine and 1,5-dibromopentane.^{146, 186} An excess amount of N-methylpyrrolidine (97%, Sigma-Aldrich, 25.5 g, 300 mmol) was dissolved in 350 ml of acetone in a round-bottom flask, and 23.0 g (100 mmol) of 1,5-dibromopentane (97%, Sigma-Aldrich) was added dropwise. The mixture was stirred under reflux for 48 hours and the solid product was collected by filtration. The product was washed with cool acetone and diethyl ether, and dried in a vacuum at room temperature. The ion-exchange and titration procedures were described in the previous chapter.

The gel composition used for the hydrothermal synthesis of ITQ-22 was 0.67 SiO₂ : 0.33 GeO₂ : 0.25 MPP²⁺(OH⁻)₂ : 7.0 H₂O. A desired amount of germanium oxide was dissolved in a desired amount of MPP²⁺(OH⁻)₂ aqueous solution. TEOS was added, and the mixture was stirred for 24 hours. Lastly, excess water was evaporated under an air flow. The final gel was charged into a 23-mL PTFE-lined Parr steel autoclave. The crystallization was performed at 175 °C for 7 days in a static oven. The resultant product was washed with distilled water and acetone, and dried at 100 °C. Calcination was performed at 580 °C for 6 hours under an air flow.

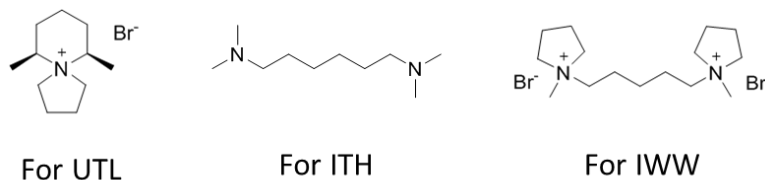


Figure 7.3. Structures of OSDA used to synthesize germanosilicates.

7.2.5. Characterization

PXRD patterns were acquired using a Rigaku MiniFlex II benchtop diffractometer using Cu K α radiation ($\lambda = 1.54184 \text{ \AA}$) to assess the crystal structure and crystallinity of the products. Thermogravimetric analysis (TGA) was performed using a PerkinElmer STA6000 instrument under a nitrogen flow of 20 mL min^{-1} . Morphology and elemental composition were studied using a Zeiss 1550VP FE-SEM equipped with an Oxford X-Max SDD X-ray EDS. Pore volumes and pore-size information of microporous materials were studied based on Ar adsorption isotherms obtained using a Quantachrome Autosorb iQ at 87.45 K . ^1H , ^{27}Al and ^{29}Si MAS solid-state NMR spectra of samples were obtained using a Bruker Avance 500 MHz spectrometer with carrier frequencies of 499.843, 130.287 and 99.305 MHz, respectively. A 4-mm zirconia rotor with a Kel-F cap was charged with 50–100 mg of as-made or freshly calcined sample. The MAS rates were 8 kHz both for ^1H - ^{29}Si CP and ^1H -decoupled ^{29}Si Bloch-decay experiments, and 12 kHz for ^{27}Al experiments.

7.3. Results and Discussion

7.3.1. Rate of Transformation

The transformation from Ge-CIT-13 to Ge-CIT-5 is a very slow process which typically takes several weeks or even several months. The rate of transformation depends on many factors. Among them, the two most important factors determining the rate of

transformation were the germanium content of the parent Ge-CIT-13 and the synthetic recipe of which the parent germanosilicate is based.

In this chapter, synthetic and material information of the parent Ge-CIT-13 is denoted as Ge-CIT-13/ x [y], where x is the mineralizer ($x = \text{F}$ or OH) used to synthesize the sample, and y denotes the EDS Si/Ge ratio of the sample. For example, Ge-CIT-13/F[4.5] means a Ge-CIT-13 sample of Si/Ge = 4.5 which was synthesized from the fluoride media.

The progress of transformation can be monitored on the basis of diffraction patterns. As a result of the transformation, the interlayer distance among the *cfi*-layers decreases. This interlayer contraction engenders a discernable shift of the (200) diffraction peak of PXRD pattern of transforming material. For Ge-CIT-13, the peak position of (200) diffraction is at $2\theta = 6.44^\circ$ ($d_{200} = 13.7 \text{ \AA}$). This interlayer diffraction peak of the parent material moves toward a higher angle until it reaches $2\theta = 6.9\text{--}7.0^\circ$ ($d_{200} = 12.6\text{--}12.8 \text{ \AA}$) which corresponds to the theoretical (200) diffraction peak position of the framework CFI which is at $2\theta = 6.93^\circ$ ($d_{200} = 12.7 \text{ \AA}$). The (110) diffraction peak also moves from 7.16° to 7.32° , and this shift of the (110) peak is crystallographically consistent with the shift of (200) peak.

The CFI framework shows its characteristic three diffraction peaks in the range of $2\theta = 12\text{--}15^\circ$; three peaks at 12.2° , 12.9° , and 13.9° are corresponding to the (301), (002), and (400) diffractions of the CFI framework.¹⁶ The initial framework *CTH also show the corresponding diffractions in the same region of 2θ at 11.6° , 12.8° , and 12.9° , but practically only one or two diffractions are observed because the (301) diffraction at 11.6° is often very weak and because the latter two peaks overlap one another at the same angle of 2θ .

Figure 7.4 illustrates this slow transformation of Ge-CIT-13/F[4.31] to Ge-CIT-5. The interlayer (200) diffraction of the freshly calcined Ge-CIT-13 moved slowly from $2\theta = 6.40^\circ$ to 7.02° during 85 days of exposure to the ambient air. Three diffraction peaks of (301), (002), and (400) also appeared in the range of $2\theta = 12\text{--}15^\circ$. This pattern showed no further

evolution for the next 700 days. The final diffraction pattern matched well with the PXRD diffraction pattern of the reference pure-silica Spa-CIT-5. To the best of my knowledge, this is the first inter-framework germanosilicate transition occurring at the room temperature. Ge-CIT-5, the final material, is also the first CFI-type extra-large-pore germanosilicate which is structurally stable under the ambient humidity. Some more examples of transformations of Ge-CIT-13/F[y] ($y = 4.11\text{--}4.65$) are provided in Figures B13–B16, Appendix B.

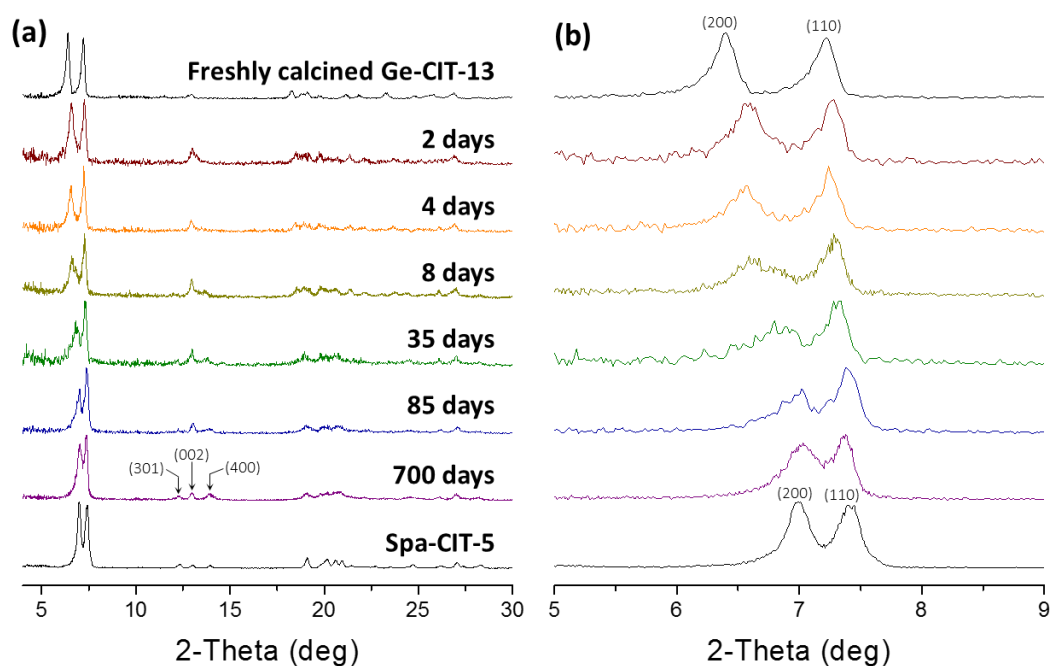


Figure 7.4. Transformation of Ge-CIT-13/F (Si/Ge = 4.31) to Ge-CIT-5 over time observed on the basis of PXRD patterns in 2-theta scanning ranges of (a) 4–30° and (b) 5–9°.

Increasing the germanium contents of parent Ge-CIT-13 greatly accelerated the rate of transformation. Figure 7.5 shows an analogous transformation of Ge-CIT-13/F[3.87] having more germanium in the framework than Ge-CIT-13/F[4.31]. This high-germanium

Ge-CIT-13 transformed just within 12 days, much faster than the Ge-CIT-13/F[4.31] which took 85 days. Interestingly, 3 days after calcination, Ge-CIT-13/F[3.87] showed two distinct peaks at 6.68° and 6.90° which may correspond to the (200) interlayer diffractions of intermediate stages. This observation clearly supports that there are two types of crystals in some transforming batches. The latter peak at 6.90° must be corresponding to the (200) peak of the CFI framework which is the final phase of the transformation. The former peak located between the (200) peaks of Ge-CIT-13 (6.44°) and Ge-CIT-5 (6.93°) is presumably the interlayer diffraction of hydrated Ge-CIT-13 phase. Similar behaviors were observed in the case of Ge-CIT-13/F[4.65] shown in Figure B16. The origin of this inhomogeneous transformation remains unknown to me. On the other hand, Ge-CIT-13 having Si/Ge ratios

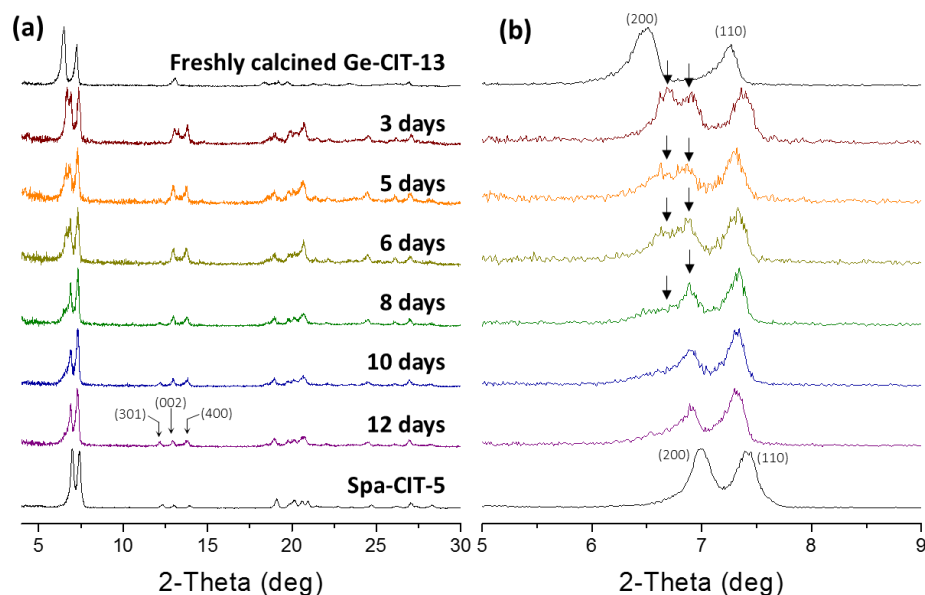


Figure 7.5. Transformation of Ge-CIT-13/F (Si/Ge = 3.87) to Ge-CIT-5 over time observed on the basis of PXRD patterns in 2-theta scanning ranges of (a) $4\text{--}30^\circ$ and (b) $5\text{--}9^\circ$.

higher than 6 showed an extremely slow rate of transformation. Figure 7.6. illustrates the structural change of Ge-CIT-13/F[6.38] on the basis of PXRD patterns. This Ge-CIT-13 was not transformed even after 895 days of exposure to ambient humidity. No significant change was observed during the last 140 days of transformation. This result provides further evidence that the Si/Ge ratio of parent Ge-CIT-13 is one of the most important factor that determines the rate of transformation.

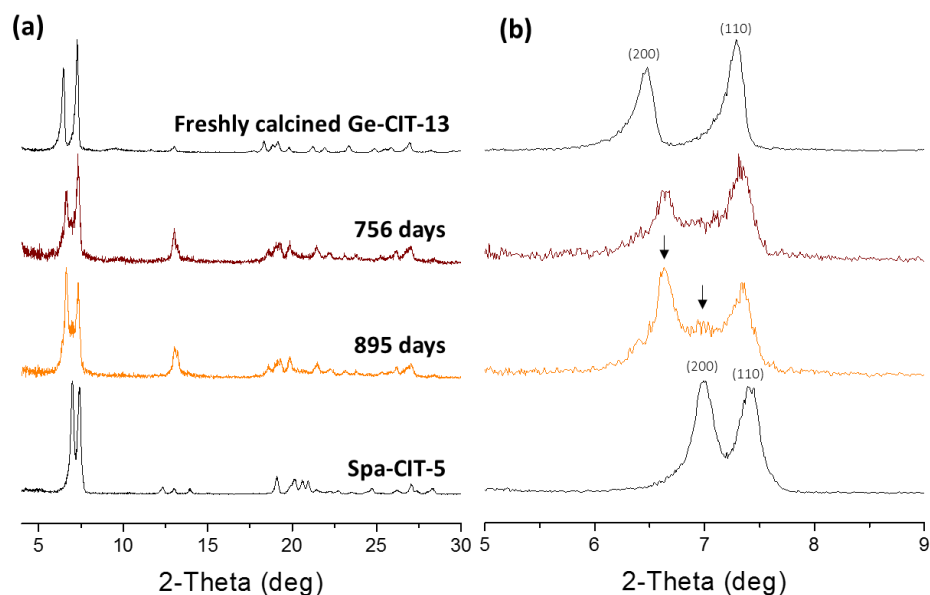


Figure 7.6. Transformation of Ge-CIT-13/F (Si/Ge = 6.38) to Ge-CIT-5 over time observed on the basis of PXRD patterns in 2-theta scanning ranges of (a) 4–30° and (b) 5–9°.

Ge-CIT-13/OH samples synthesized without use of fluoride showed a much faster transformation. While Ge-CIT-13/F[4.31] took 85 days (ca. 3 months) for the transformation as shown above, Ge-CIT-13/OH[4.33] having a similar germanium content was transformed into the corresponding Ge-CIT-5 within just 8 days under the same temperature and humidity, as shown in Figure 7.7. As expected, the combination of low Si/Ge ratio and hydroxide-based synthesis immensely accelerated the transformation. Figure 7.8 depicts the

transformation of Ge-CIT-13/OH[3.88] which is completed in 2 days. No sign of CIT-13 is left after the second day of the transformation, and all diffractions well matched those of the reference Spa-CIT-5.

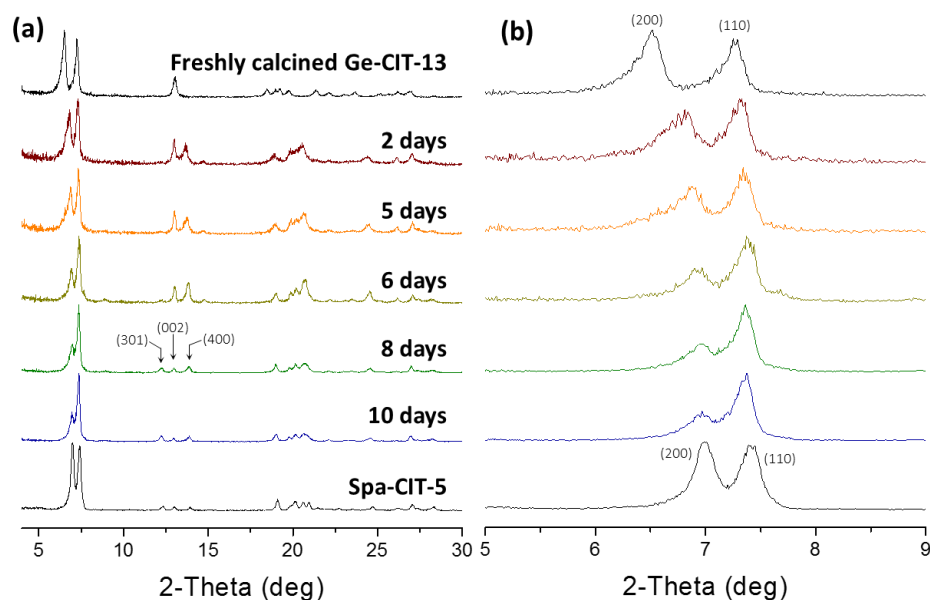


Figure 7.7 Transformation of Ge-CIT-13/OH (Si/Ge = 4.33) to Ge-CIT-5 over time observed on the basis of PXRD patterns in 2-theta scanning ranges of (a) 4–30° and (b) 5–9°.

I believe that this big difference in the rate of transformation in spite of similar Si/Ge ratios is related to the arrangement of germanium atoms within the *d4r* units of CIT-13 structure. It is known that fluoride anions can structure-direct the *d4r* units.^{129, 187} This structure-directing ability of fluoride is particularly important for pure-silica syntheses of *d4r*-containing molecular sieves such as STW¹⁸⁸ or LTA.⁶² But some *d4r*-containing germanosilicates (*e.g.*, ITH) can be prepared in both ways: with or without fluoride.^{146, 175-176}

Ge-CIT-13 is also one of these cases. The inverse sigma transformation from Ge-rich CIT-13/OH[y] ($y < 3.8$) to CIT-14 will be discussed in the next chapter. This type of transformability strongly suggests the presence of Ge-O-Ge bonds in the $d4r$ units.¹¹⁸ I believe that the absence of fluoride promotes the formation of Ge-O-Ge bonds which can be hydrolyzed easier than Si-O-Ge bonds and that this preferred formation of Ge-O-Ge bonds is the main reason for the difference between the transformation rates of Ge-CIT-13/OH and Ge-CIT-13/F.

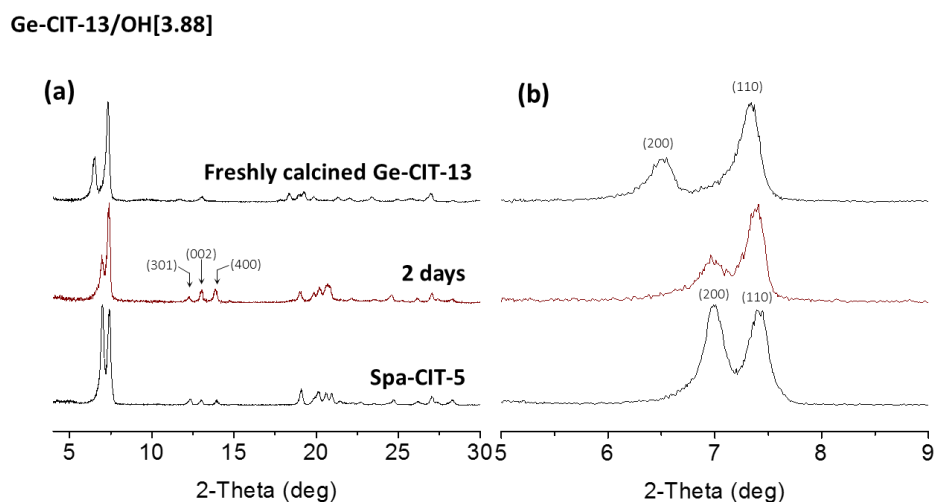


Figure 7.8. Transformation of Ge-CIT-13/OH (Si/Ge = 3.88) to Ge-CIT-5 over time observed on the basis of PXRD patterns in 2-theta scanning ranges of (a) 4–30° and (b) 5–9°.

7.3.2. Role of Sorbed Water within Pore System

The pith of the transformation from Ge-CIT-13 to Ge-CIT-5 is the formation of Ge-rich double-zigzag-chain (dzc) from arrays of $d4r$ units. To achieve this transformation,

dissociation and new formation of T-O-T bonds must occur. On the basis of the observations presented in the previous section, it can be deduced that the chemical lability of Ge-O bonds plays a crucial role in transformation. Ge-O bonds can be hydrolyzed very easily even by moisture in an ambient air. It has been pointed out many times that the low hydrothermal stability of most of the germanosilicate is originated from the hydrolysis of Ge-O bonds which significantly contribute to architectures of frameworks.^{151, 154, 157-158} However, the hydrolysis of Ge-O bonds by occluded water is an essential part of the CIT-13-to-5 transformation. Indeed, the final Ge-CIT-5 after 4 months of exposure to ambient humidity possessed approximately 4.2 wt. % of water (see Figure B17).

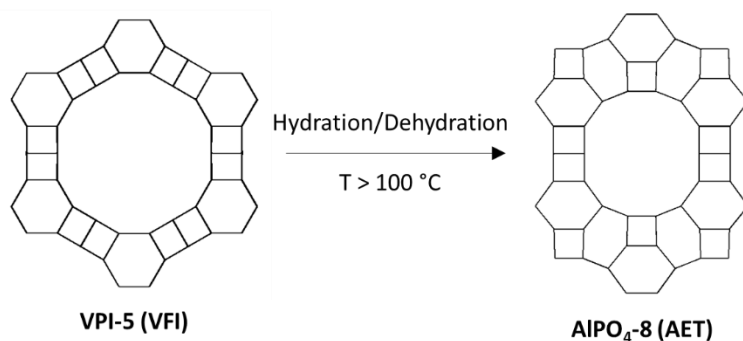


Figure 7.9. Transformation from VPI-5 to AlPO₄-8.

There is another inter-zeolitic transformation in which the role of sorbed water phase is essential: the transformation from VPI-5 (VFI) to AlPO₄-8 (AET). (see Figure 7.9) VPI-5 is the first synthetic extra-large-pore aluminophosphates-based molecular sieve discovered 32 years ago by Prof. Mark E. Davis who is my advisor.¹²⁴ VPI-5 transforms into AlPO₄-8 if moisture is present at an elevated temperature (> 100 °C).^{125, 127} The hydration-dehydration of VPI-5 is the key process driving the transformation. The case of the transformation from Ge-CIT-13 to Ge-CIT-5 resembles the transformation from VPI-5 to AlPO₄-8 in regard of

the necessity of moisture. One difference between these two inter-zeolitic transformations is temperature. Ge-CIT-13 transforms at room temperature.

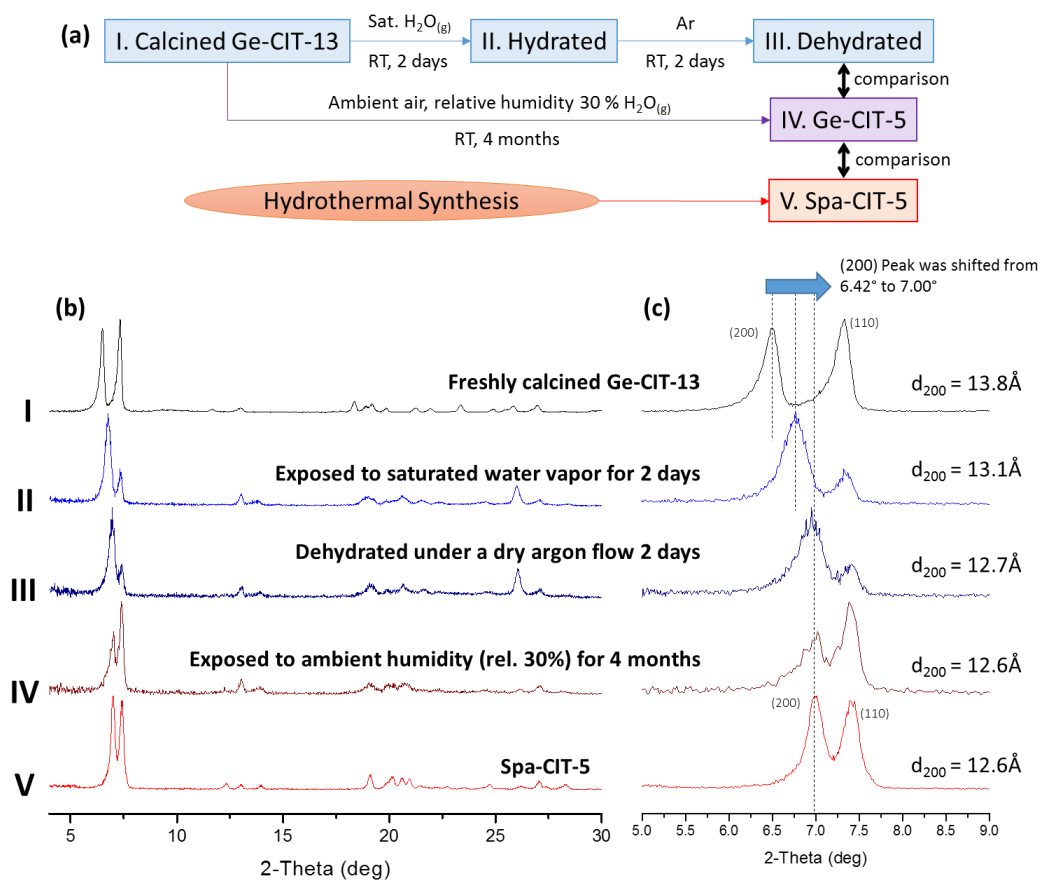


Figure 7.10. Accelerated transformation of Ge-CIT-13/F (Si/Ge = 4.31) to Ge-CIT-5: (a) design of experiment, (b) PXRD patterns in 2-theta scanning ranges of (b) 4–30° and (c) 5–9°.

To verify the role of sorbed water molecules within the pore system of CIT-13 in the transformation, a similar hydration/dehydration process was performed on Ge-CIT-13. Calcined Ge-CIT-13/F[4.31] was hydrated by exposing it to saturated water vapor for 2 days and subsequently dehydrated under a dry argon flow for another 2 days. This

hydration/dehydration process was performed at room temperature. PXRD patterns were acquired at each stage to investigate structural evolution. The design of this experiment and related PXRD patterns are shown in Figure 7.10. Clearly, the interlayer distance of Ge-CIT-13/F[4.31] was decreased to 12.7 Å which corresponds to that of CIT-5. Extended hydration did not further decrease the interlayer distance of the germanosilicate (see Figure B17, Appendix B). However, the resultant material obtained in this way showed very low crystallinity, presumably due to disorder caused by larger amounts of sorbed water than in a usual ambient condition. The weak relative intensities of the (110) diffraction of PXRD profiles II and III indicate that a significant level of degree of disorder is generated along the b-axis (the direction perpendicular to the direction of the 14-ring main channel within the interlayer region).

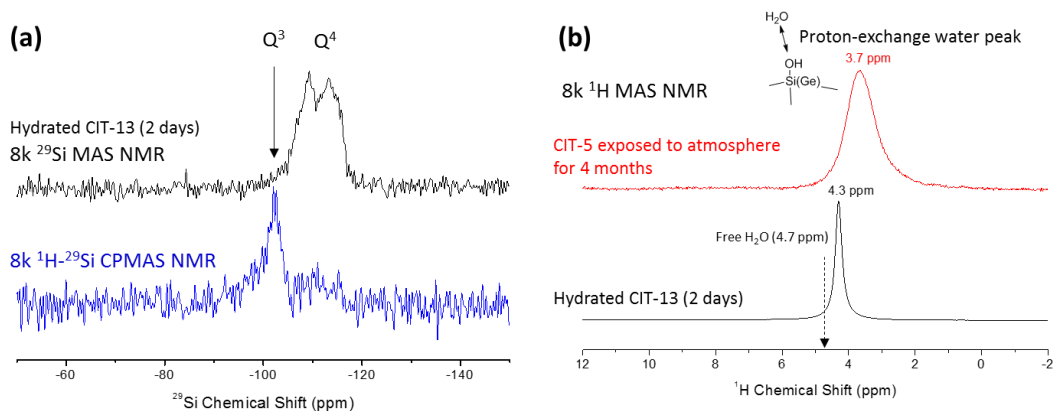


Figure 7.11. NMR spectra of hydrated Ge-CIT-13. (a) 8 kHz MAS ^1H -decoupled ^{29}Si solid-state NMR spectrum and ^1H - ^{29}Si CP-MAS solid-state NMR spectrum of hydrated Ge-CIT-13/F[4.31] (II of Figure 7.10) and (b) 8 kHz MAS ^1H solid-state NMR spectra of sorbed water within Ge-CIT-5 produced by exposing Ge-CIT-13/F[4.31] to ambient humidity for 4 months (red, IV of Figure 7.10) and saturated water vapor for 2 days (black, II of Figure 7.10).

The hydrated germanosilicate (III of Figure 7.10) and sorbed water phase within its pore system were further studied on the basis of the solid-state ^1H and ^{29}Si NMR spectroscopy. The acquired spectra are illustrated in Figure 7.11. The ^{29}Si Bloch-decay NMR spectra (blue, Figure 7.11(a)) of hydrated Ge-CIT-13/F[4.31] give a pattern very similar to that of typical calcined Ge-CIT-13 shown in the previous chapter. But the Q^3 -silanol (Si-OH) signal that appeared at -102.6 ppm in the ^1H - ^{29}Si CP-MAS spectrum supports the presence of a small amount of hydrolyzed Si-O-Ge bonds.

It was also found that there is a continuous proton exchange between sorbed water phase and surface silanol groups in Ge-CIT-5 and hydrated Ge-CIT-13/F[4.31] on the basis of ^1H NMR spectra. The proton exchange between sorbed water phase and surface silanol groups can be evidenced by the upfield-shift of water signal in the proton NMR spectra.¹⁸⁹ Bulk pure water and silanol group shows their proton signal at 4.7 ppm and 1.9 ppm, respectively. For Ge-CIT-5 and hydrated Ge-CIT-13/F[4.31], the resonances of sorbed water within the pore systems of germanosilicates were detected at 3.7 ppm and 4.3 ppm, respectively. The line broadening of 3.7 ppm peak of the ^1H spectrum of Ge-CIT-5 from Ge-CIT-13/F[4.31] may be due to the strong dipole-dipole interaction among surface protons which could not be removed by MAS.¹⁸⁹ These signals which were broadened and shifted toward upper field support that the sorbed water phase and the surface silanol groups exchange protons.

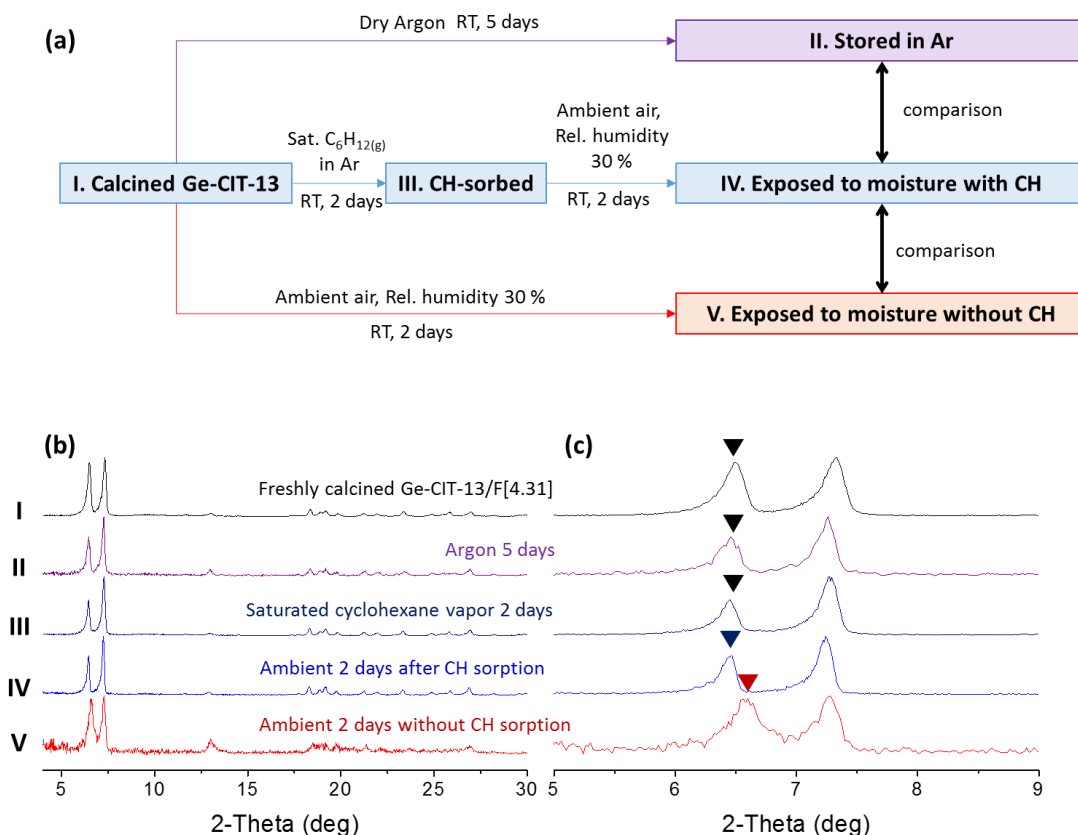


Figure 7.12. Inhibited transformation of Ge-CIT-13/F (Si/Ge = 4.31) to Ge-CIT-5 by excluding moisture from the system by argon and cyclohexane (CH): (a) design of experiment, and PXRD patterns in 2-theta scanning ranges of (a) 4–30° and (b) 5–9°.

On the other hand, isolating calcined Ge-CIT-13 from moisture inhibited or substantially decelerated the transformation. The design of experiment is illustrated in Figure 7.12(a). Firstly, freshly calcined dry Ge-CIT-13/F[4.31] was exposed to a dry argon (99.999%) flow for 5 days and a diffraction pattern was acquired, and compared to the case of ambient air exposure. No sign of structural evolution or degradation was found in the sample exposed to dry argon (II of Figure 7.12). However, the sample exposed to ambient

air (30 % relative humidity) showed a noticeable decrease in the interlayer distance from 13.7 Å ($2\theta = 6.46^\circ$) to 13.4 Å ($2\theta = 6.6^\circ$) within just 2 days. (V of Figure 7.4)

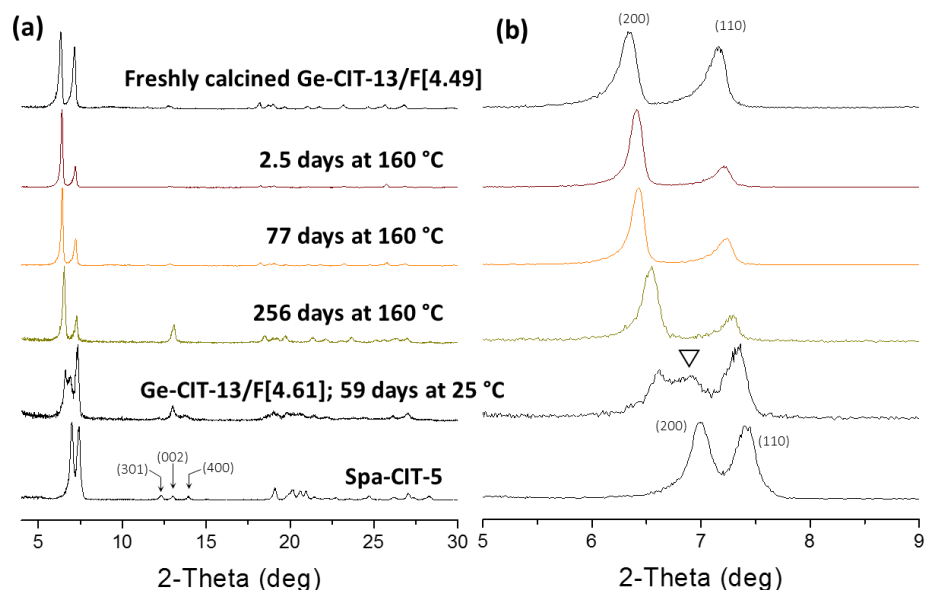


Figure 7.13. Structural change of Ge-CIT-13/F (Si/Ge = 4.49) at an elevated temperature (160 °C) over time observed on the basis of PXRD patterns in 2-theta scanning ranges of (a) 4–30° and (b) 5–9°.

Another portion of the same calcined Ge-CIT-13/F[4.31] was exposed to the saturated vapor of cyclohexane in dry argon at room temperature for 2 days. The vapor pressure of cyclohexane at 25 °C is 97.6 torr,¹⁹⁰ and the cyclohexane uptake of Ge-CIT-13 characterized by TGA was 7.5 wt. %. (TGA: not shown) Also, this cyclohexane-sorption did not cause any structural evolution of Ge-CIT-13. (III of Figure 7.12) After that, this Ge-CIT-13 having occluded cyclohexane in its pore system is exposed to ambient air of 30 % relative humidity for another 2 days. The PXRD pattern IV of Figure 7.12 clearly indicate that Ge-CIT-13 occluded with cyclohexane did not transform at all. The ^1H - ^{13}C CP-MAS NMR and ^1H NMR spectra of cyclohexane-occluded Ge-CIT-13 (not shown) revealed that sorbed

cyclohexane is still the majority species in Ge-CIT-13 and that sorption of water that can cause the transformation is substantially suppressed by the presence of hydrophobic cyclohexane. A barely visible and broad water signal was observed at 2.9 ppm which further shifted from 3.7 ppm of Ge-CIT-13 exposed to ambient humidity without cyclohexane. This inhibition experiment further evidences that moisture drives the transformation of Ge-CIT-13 to -5.

Lastly, the transformation was attempted at an elevated temperature higher than the boiling point of water. Calcined Ge-CIT-13/F[4.49] was placed in a convection oven at 160 °C, and its structural change was investigated for 256 days of high-temperature storage. PXRD patterns are shown in Figure 7.13. Ge-CIT-13/F[4.49] was barely transformed even after 256 days at 160 °C. Considering the fact that Ge-CIT-13/F[4.61] having higher Si/Ge ratio showed a sign of transformation after 59 days of ambient moisture exposure at room temperature, Ge-CIT-13/F[4.49] richer in germanium should have transformed faster than that—but it did not. The relative humidity of 30 % at room temperature (25 °C) is corresponding to the water vapor pressure of 7.1 torr.¹⁹⁰ The same air was circulated into the convection oven. Since the saturation vapor pressure of water at 160 °C is 4640 torr,¹⁹⁰ 7.1 torr is corresponding to a low relative humidity of 0.15 % at 160 °C at which liquid-phase water does not exist under a standard pressure (752 torr). So it can be again concluded that prevention of sorption of water within germanosilicate Ge-CIT-13 certainly inhibits the transformation.

7.3.3. Characterization of Resultant Ge-CIT-5

The physicochemical properties of the resultant Ge-CIT-5 obtained from the transformation of Ge-CIT-13 were further studied on the basis of the ²⁹Si solid-state NMR spectroscopy, argon adsorption isotherms (87.45 K), and computational chemistry.

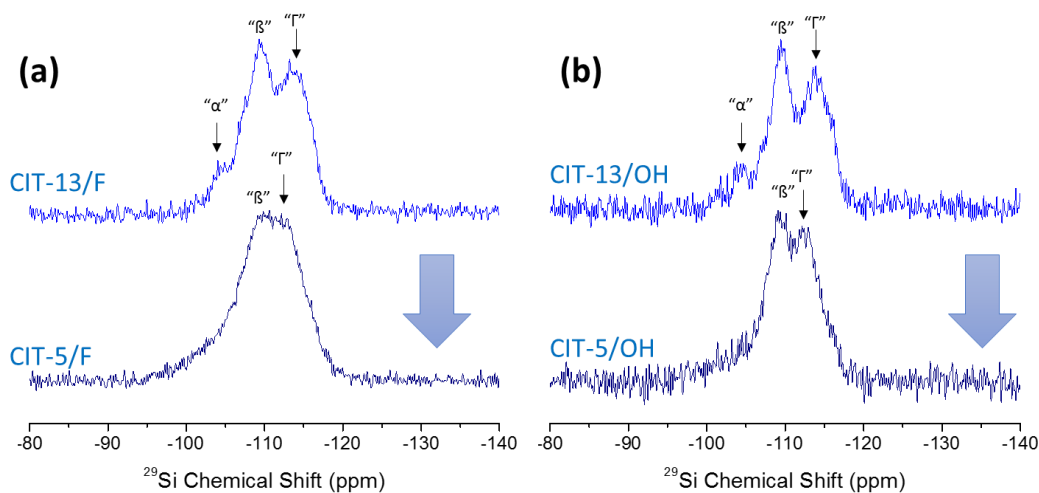


Figure 7.14. Transformation from (a) Ge-CIT-13/F[4.28] and (b) Ge-CIT-13/OH[3.87] and the resultant Ge-CIT-5's on the basis of 8 kHz MAS ^1H -decoupled ^{29}Si solid-state NMR spectra.

The ^{29}Si solid-state NMR spectra of freshly calcined Ge-CIT-13/F[4.28] and Ge-CIT-13/OH[3.87] and the resultant Ge-CIT-5 products from the two parent Ge-CIT-13 samples are illustrated in Figure 7.14. The studied germanosilicates were thoroughly dehydrated to eliminate possible influences of sorbed moisture and Q^3 -silanol groups on ^{29}Si Bloch-decay NMR spectra by treating them under a dry air flow at 580 °C for 12 hours. The completeness of dehydration was confirmed by the absence of any peaks in the ^1H NMR and ^1H - ^{29}Si CP-MAS NMR spectra (not shown). Deconvolution of ^{29}Si NMR spectra of typical extra-large-pore germanosilicates having many T-atoms such as CIT-13 is generally very complicated due to the presence of germanium and high-strain composite building units such as $d4r$ units. These factors often make ^{29}Si NMR spectra of germanosilicates difficult to interpret in the range from -100 ppm to -120 ppm.^{170, 191-192} But as one can see in Figure 7.14., calcined Ge-CIT-13 always shows three groups of peaks (denoted as “ α ”, “ β ”, and “ γ ”) at approximately -104 ppm, -109 ppm, and -114 ppm

regardless of the type of mineralizers used to synthesize and Si/Ge ratios. There is a consensus that the most downfield peak α typically seen in the range from -102 ppm to -110 ppm originates from the Q⁴-silicon in Ge-rich *d4r* units.^{118, 178, 193} The other two groups β and γ are assigned as the Q⁴-silicon in Si-rich *cfi*-layers. After the transformation, group α peaks seemingly disappear since it is actually mixed with group β peaks as a result of an upfield shift. This is a reasonable observation since the core part of the transformation from CIT-13 to CIT-5 is the disassembly-reassembly process from arrays of *d4r* units to double zigzag chains. Peak group “ β ” showed no chemical shift change after the transformation. However, peak group γ slightly moved toward downfield from -114 ppm to -112 ppm after the transformation. These downfield-shifts were observed in the transformations of both Ge-CIT-13/F[4.28] and Ge-CIT-13/OH[3.87].

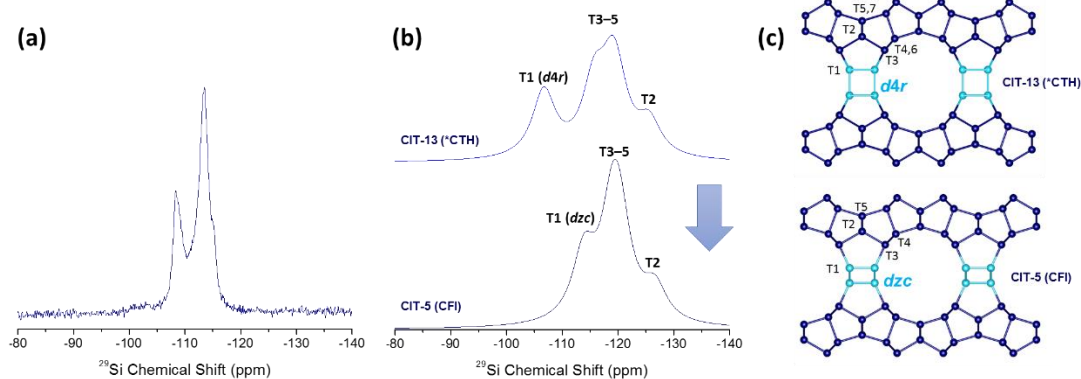


Figure 7.15. NMR spectroscopy and transformation. (a) 8 kHz MAS ¹H-decoupled ²⁹Si solid-state NMR spectrum of the reference Spa-CIT-5. (b) Calculated ²⁹Si NMR spectra of theoretical pure-silica molecular sieves having CIT-13 and CIT-5 topologies. (100% Lorentzian, width = 5.08 ppm) (c) Frameworks of CIT-13 and CIT-5 seen from the 14-ring channel direction with T-atom labels.

To further study the origins of these peak groups, estimated signal positions of each T-atom in the two frameworks were calculated based on a theoretical model. Thomas and Klinowski et al. suggested the following empirical linear equation to estimate the chemical shifts of silicon atoms within pure silica tectosilicate frameworks: δ_{Si} (ppm) = -25.44 - 0.5793 $\times\theta_{\text{T-O-T(avg)}}$ ($^{\circ}$) where δ_{Si} is the estimated chemical shift of a framework Si from TMS (0 ppm) and $\theta_{\text{T-O-T(avg)}}$ is the average of four T-O-T angles surrounding that Si atom.¹⁹⁴ For CIT-13, a structure solution based on the rotational electron diffraction (RED) experiment conducted by Dr. Dan Xie at Chevron was used. This solution was acquired from one of the first Ge-CIT-13 samples made in 2016.⁶³ For CIT-5, the structure refinement based on the synchrotron PXRD data published by the Davis group in 1998 was used.¹³² All frameworks were assumed to be pure-silica. Estimated values of chemical shifts were also provided in Table B5.

The calculated ^{29}Si NMR spectra of hypothetical pure-silica *CTH and CFI-type zeolites are illustrated in Figure 7.15(b). The actual ^{29}Si NMR spectrum of pure-silica Spa-CIT-5 is also acquired and provided in Figure 7.15(a) for comparison. The obtained ^{29}Si spectrum of Spa-CIT-5 was within experimental error of the reported spectrum.¹³² It also was found that the empirical equation by Thomas et al.¹⁹⁴ apparently overestimates the magnitude of magnetic shielding in these extra-large-pore molecular sieves. In the calculated spectra, it can be easily noticed that there are also three groups of T-atoms in the frameworks of CIT-13 and CIT-5, as observed in those of germanosilicates shown in Figure 7.14, even though the presence of Ge-O-Si bonds broadens and moves ^{29}Si signals toward further downfield.¹⁹² The first groups are groups of T-atoms involved in layer-connecting composite building units which are the *d4r* and *dzc* units in CIT-13 and CIT-5 frameworks, respectively. There is only one crystallographically distinguishable T-atom site (denoted as T1 in Figure 7.15(c)) in each of frameworks in the first group. The estimated positions of the first group T-atoms in ^{29}Si NMR spectra were -106.7 ppm (*d4r* in CIT-13) and -113.9 ppm (*dzc* in CIT-5). As expected, this explains the “disappearance” of the peak group α in Figure 7.14 (a) and (b).

The second group is a group of T-atoms which are not directly exposed to pores (denoted as T2). Four oxide ions which are directly connected to this T2-site, are not exposed to the channel system either. This T-site appeared at the most upfield positions (-125.6 ppm for CIT-13, -126.7 ppm for CIT-5) in the theoretical spectra due to its high T-O-T angles. But, these estimated positions fail to explain the downfield shift of the peak group γ in the actual spectra. The last group is a group of T-atoms (T3-5 for CIT-5, and T3-7 for CIT-13) forming the rest of 14-ring channel walls of CIT-13 and CIT-5. This third group of T-atoms can be assigned as the group β peaks in the actual spectra based on their unmoved positions. In conclusion, the downfield shift of the peak group γ could not be explained on the basis of the Thomas empirical equation. I believe that there must be some influences of neighboring germanium atoms which are not considered in this model.

The microporosity of the related germanosilicates were studied based on the argon adsorption isotherms acquired at 87.45 K. The isotherms of as-calcined Ge-CIT-13/F[4.22], the resultant Ge-CIT-5, and the reference pure-silica Spa-CIT-5 are illustrated in Figure 7.16 in (a) linear scale and (b) log scale. As a result of the transformation, the estimated micropore volume was decreased from 0.169 cc g⁻¹ (Ge-CIT-13) to 0.079 cc g⁻¹ (Ge-CIT-5). On the other hand, the micropore volume of the reference Spa-CIT-5 was 0.091 cc g⁻¹ which is 15 % higher than the isostructural Ge-CIT-5. The difference between the unit cell formula weight of Ge-CIT-5 and that of Spa-CIT-5 explains this micropore volume difference; the unit cell formula weight of Ge-CIT-5 having a Si/Ge ratio 4.22 (2.20 kg mol⁻¹, Si_{25.9}Ge_{6.1}O₆₄) is approximately 14 % heavier than that of pure silica CIT-5 (1.92 kg mol⁻¹, Si₃₂O₆₄). The unit-cell specific micropore volumes of Ge-CIT-5 and Spa-CIT-5 were 173 cc (mol of UC)⁻¹ and 175 cc (mol of UC)⁻¹, respectively, which are almost identical to each other.

In the log scale plot, a low-pressure adsorption behavior of Ge-CIT-5 was observed. Ge-CIT-13/F[4.22] and Spa-CIT-5, which are molecular sieves prepared directly from hydrothermal syntheses, started to adsorb argon at ca. $p/p_0 \sim 10^{-4}$. But Ge-CIT-5, which is a

resultant material of transformation, started its argon uptake at ca. $p/p_0 \sim 10^{-5}$. As shown in Figure B12, the smaller-pore frameworks with higher-curvature surfaces uptake gas at lower partial pressures. It can be also concluded that this lower-pressure adsorption indicates the presence of higher-curvature surfaces which are presumably due to structural disorder caused during the transformation.

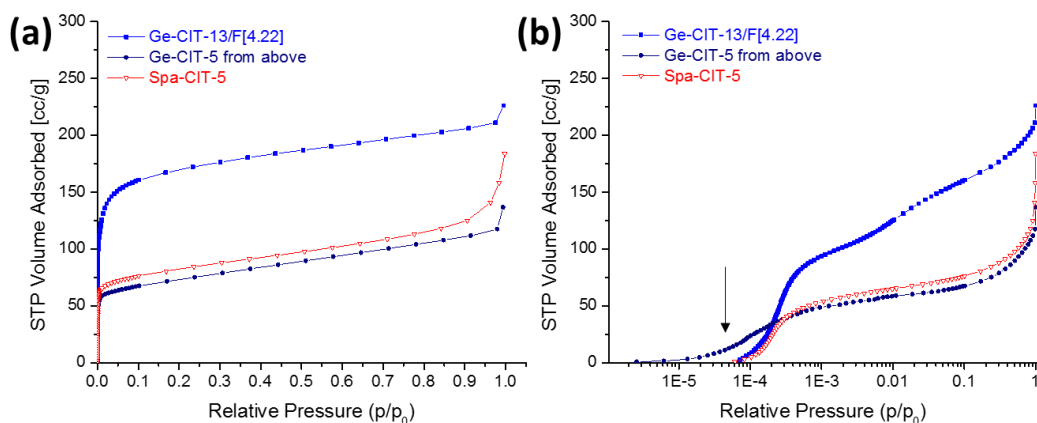


Figure 7.16. Argon adsorption isotherms (87.45 K) of Ge-CIT-13/F[4.22] and the resultant Ge-CIT-5 compared to the reference Spa-CIT-5. (“↓” denotes the low-pressure adsorption of Ge-CIT-5)

Lastly, the transformation was computationally investigated in terms of the lattice energy. It is reasonable to think that the major driving force of the transformation must be the high framework energy of CIT-13, particularly due to the high strain caused by the presence of $d4r$ units. The lattice energies of CIT-13 and CIT-5 frameworks were calculated in the pure-silica and germanosilicate (Si/Ge = 3) systems. The models are shown in Figure 7.17. The computation was performed by Dr. Dan Xie at Chevron. For the pure-silica and

germanosilicate computation, the GULP algorithm with the Catlow parameters and the FORCITE program with the COMPASS forcefield parameters were adopted, respectively, because the Catlow library used in the former module had no parameter relevant to germanosilicates. In the pure-silica system, the lattice energies of SiO₂-CIT-13 and SiO₂-CIT-5 relative to the α -quartz phase were +16.90 kJ mol⁻¹ and +13.34 kJ mol⁻¹ per Si-atom, respectively. The SiO₂-CIT-5 lattice model was more stable than that of SiO₂-CIT-13 by $\Delta U = -3.56$ kJ mol⁻¹ per Si-atom mostly due to the high steric energy caused by *d4r* units.

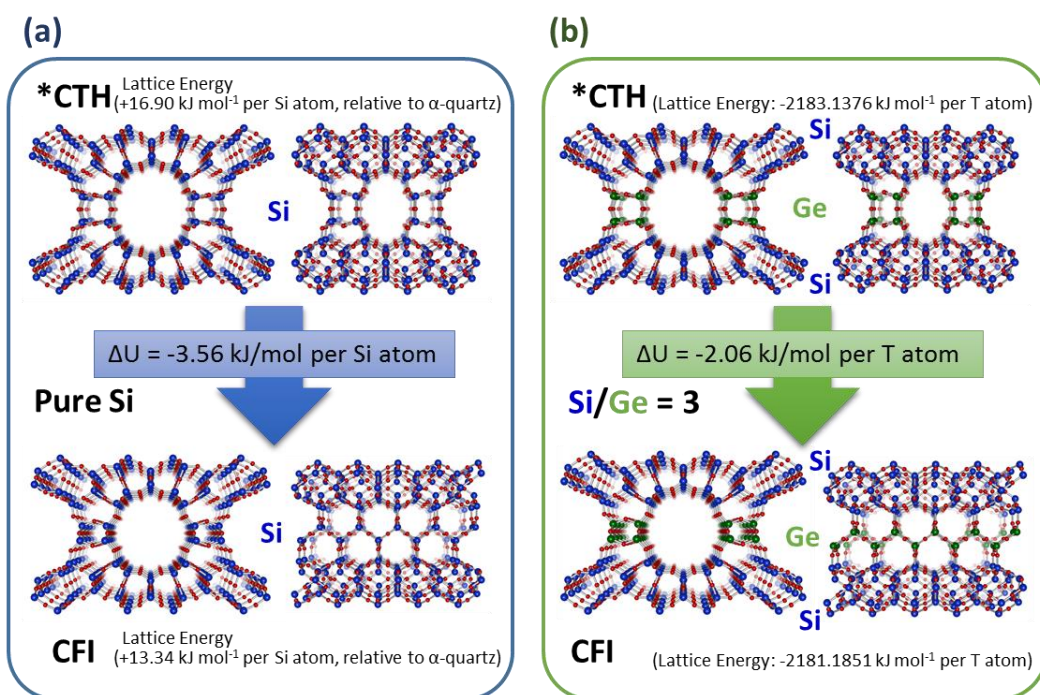


Figure 7.17. The lattice models used to calculate lattice energies: (a) pure-silica *CTH and CFI, and (b) hypothetical germanosilicate (Si/Ge = 3) crystal models of *CTH and CFI whose *cfi*-layers are exclusively composed of pure silica and whose connecting units—*d4r* and *dzc*—are completely composed of germanium oxide.

For the case of germanosilicates, two hypothetical germanosilicate Ge-CIT-13 and Ge-CIT-5 consisting of pure-silica *cfi*-layers and pure-germania *d4r* and *dzc* units (Si/Ge = 3 for both), respectively, were investigated. (Figure 7.17(b)) The calculated lattice energy difference between Ge-CIT-13 and Ge-CIT-5 was $\Delta U = -2.06 \text{ kJ mol}^{-1}$ per T-atom. Although detailed information about intermediate stages (i.e., activation energy, etc.) of this transformation are not clear yet, these computational results support that the transformation from CIT-13 to CIT-5 is energetically favorable and that it can be spontaneous if a proper condition is provided.

7.3.4. Comparison to Related Germanosilicate

Germanosilicates consisting of chemically stable silicate layers pillared with Ge-rich *d4r* units have attracted tremendous interest from the scientific society due to their ability to be transformed into novel structures. The most extensively studied framework is UTL.^{117, 119} A number of novel microporous frameworks were prepared on the basis of transformation of UTL-type germanosilicates.^{118, 122-123, 161-162} This family of frameworks includes IWW, ITH, ITR, IWR, and UOV.¹⁹⁵

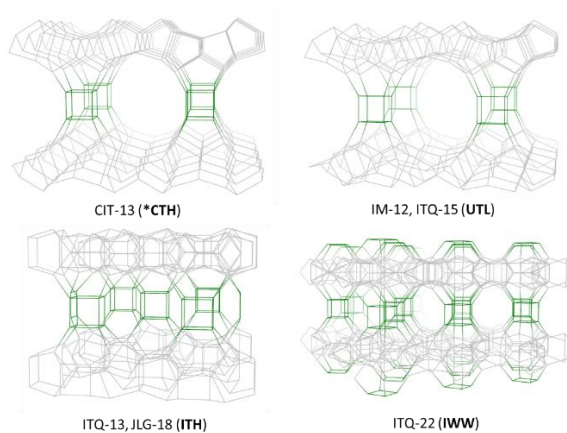


Figure 7.18. Structures of germanosilicates consisting of Ge-rich *d4r* units and Si-rich layers.

In this section, how structures of these germanosilicates evolve upon exposure to moisture in ambient air is discussed. Among the frameworks enumerated above, the three most frequently studied frameworks—UTL, ITH, and IWW—were selected and investigated. Figure 7.18 demonstrates the structures of these topologies together with CIT-13. UTL is a “sister” framework of CIT-13 whose two dimensional channel system is defined by 14- and 12-ring. ITH is a medium-pore germanosilicate that has a staggered arrangement of $d4r$ units in the interlayer region.¹⁴⁹ IWW has a very interesting 3-dimensional channel system consisting of perpendicularly intersecting 12-, 10-, and 8-ring pores.¹⁴⁶ For all of these frameworks, efforts have been made to hydrothermally stabilize these germanosilicates on the basis of many postsynthetic treatments.^{154, 158-159, 196}

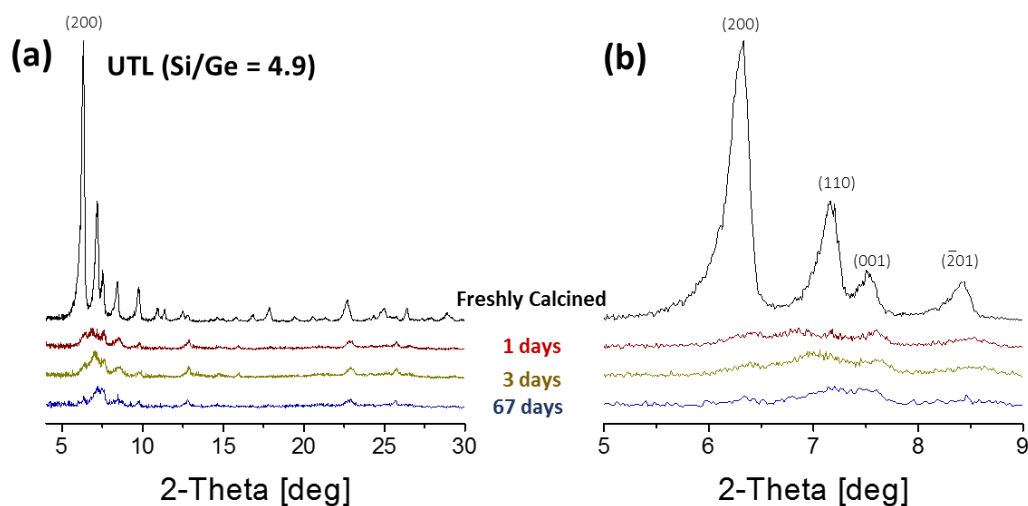


Figure 7.19. Structural change of IM-12/OH (Si/Ge = 4.9) over time observed on the basis of PXRD patterns in 2-theta scanning ranges of (a) 4–30° and (b) 5–9°.

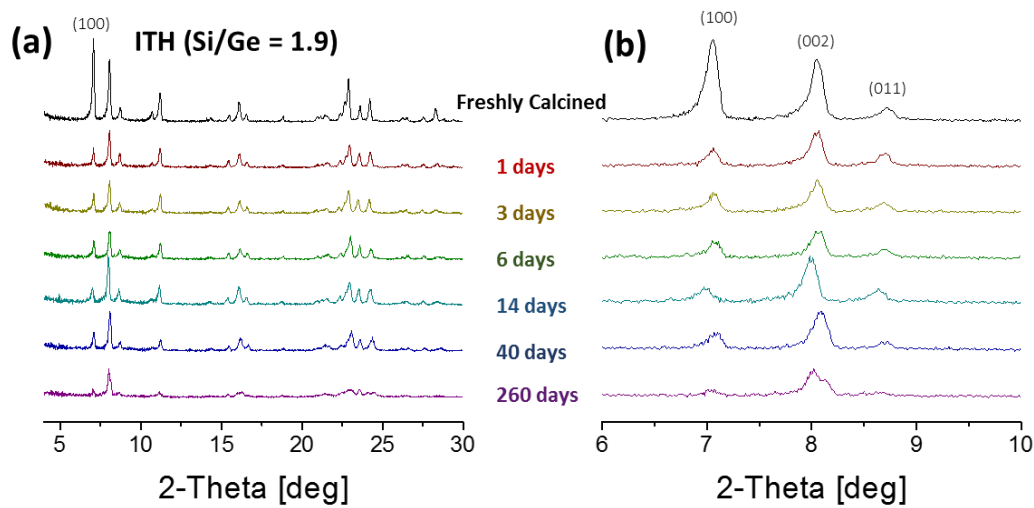


Figure 7.20. Structural change of JLG-18/F (Si/Ge = 1.9) over time observed on the basis of PXRD patterns in 2-theta scanning ranges of (a) 4–30° and (b) 6–10°.

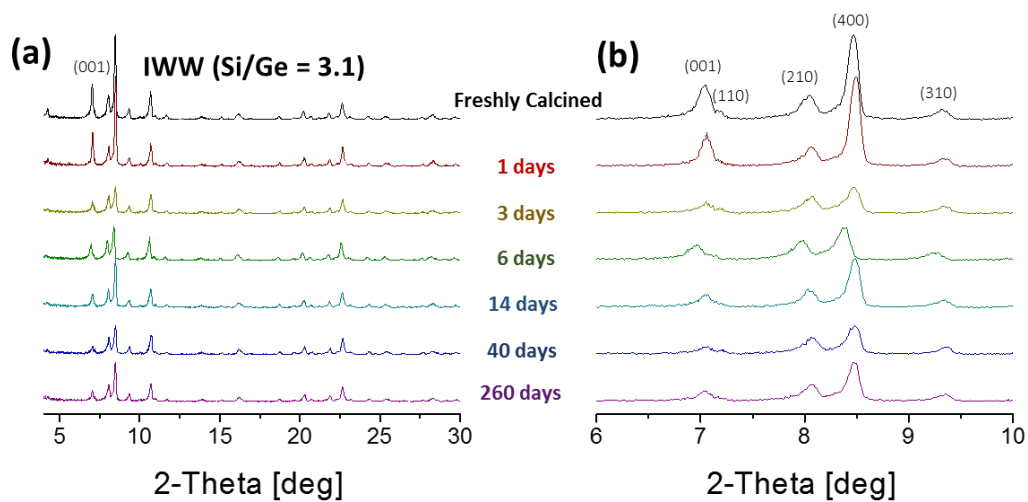


Figure 7.21. Structural change of ITQ-22/OH (Si/Ge = 3.1) over time observed on the basis of PXRD patterns in 2-theta scanning ranges of (a) 4–30° and (b) 6–10°.

In this work, IM-12,¹¹⁶ JLG-18,¹⁸⁵ and ITQ-22¹⁴⁶ germanosilicates having UTL, ITH, and IWW frameworks, respectively, were prepared. Following the same nomenclature used for a series of parent CIT-13 samples in the previous sections of this chapter, each sample was also named as “*material name*”/*mineralizer*[*Si/Ge ratio*]. For example, ITQ-22/OH[3.5] denotes an ITQ-22 germanosilicate sample having a Si/Ge ratio of 3.5 which was synthesized from hydroxide media.

Instead of being transformed into another frameworks, IM-12/OH[4.9] simply lost its crystallinity rapidly as shown in Figure 7.19. After 1-day exposure to ambient humidity, the initial UTL structure completely disappeared. No further structural change was observed in this collapsed structure during the following 67 days of extended observation. Contrary to the case of UTL, JLG-18/F[1.9] and ITQ-22/OH[3.1] showed almost no structural change. (Figures 7.20. and 7.21) These structures were stable despite their low Si/Ge ratios. After 260 days of exposure, JLG-18/F[1.9] lost most of its crystallinity, but still retained its original framework. ITQ-22/OH[3.1] showed no significant structural degradation even after 260 days of exposure to moisture.

The fragility of UTL germanosilicates can be explained by its most opened structure and unique arrangement of germanium atoms in its *d4r* units. UTL has the lowest framework density (15.6 T-atoms nm⁻³) and largest pore opening (14×12) among all studied frameworks in this chapter. Water molecules from the atmosphere may have rapidly reached the deepest part of the UTL framework and hydrolyzed Ge-O bonds which are well exposed to the surrounding large- and extra-large-pore channel system. The distance between neighboring two *d4r* units is too far to achieve the CIT-13-like transformation by forming new Ge-O-T bonds. The 2-dimensional arrangements of *d4r* units within the interlayer region of germanosilicates are illustrated in Figure B18. The closest distance between two neighboring *d4r* units in UTL is 6.04 Å which is much longer than that of CIT-13 (3.63 Å). Instead, UTL-type germanosilicates could undergo a novel type of transformation based on the shift of

layers by half the unit-cell vector along the 14-ring channel direction thanks to this geometry, yielding two new topologies, IPC-9 and IPC-10 having 2-dimensional 10/7-ring and 12/9-ring channel systems, respectively.¹⁶²

The unique arrangement of germanium T-atoms within *d4r* units may be another reason for the hydrothermal instability of UTL. UTL had been the only germanosilicate that can undergo the inverse sigma transformation¹¹⁸ before I discovered that Ge-CIT-13/OH has the same ability (shown in the next chapter) to transform. The existence of single-4-ring (*s4r*) configuration of germanium T-atoms within the *d4r* units is an indispensable condition for this type of direct transformation.^{118, 176} The presence of Ge-O-Ge bonds within *d4r* units may have seriously weakened the framework in terms of hydrolysis by sorbed moisture.

ITH also have a long distance (5.53 Å) between parallel pairs of neighboring *d4r* units, and IWW has no parallel pair of neighboring *d4r* units as shown in Figure B18. The high hydrothermal stability of ITQ-22 was reported many times.¹⁷⁶ Delamination and reassembly of Ge-rich ITQ-22 resulted in the restoration of initial IWW framework.¹⁹⁷ Xu et al. reported that, even after complete removal of germanium from germanosilicate ITQ-22 by soaking the material in strong acid, the IWW framework was retained.¹⁵⁴ On the basis of delamination and relevant NMR studies, Kasian et al. concluded that the high stability of ITQ-13 (ITH) and ITQ-22 is due to their arrangements of Ge and Si T-atoms within *d4r* units which is vastly different to that of UTL.¹⁷⁶

7.4. Summary

The kinetics of the transformation from Ge-CIT-13 to Ge-CIT-5 was closely related to the nature of the parent Ge-CIT-13. Apparently, Ge-CIT-13 with a higher germanium content was transformed faster than Ge-CIT-13 with a lower germanium content.

Interestingly, it was found that the type of mineralizer which was used to synthesize the parent CIT-13 immensely influenced the rate of transformation. Ge-CIT-13 synthesized from the fluoride-free recipe was transformed into Ge-CIT-5 much faster than Ge-CIT-13 crystallized in fluoride media. A Ge-CIT-13 sample synthesized in hydroxide media having a low Si/Ge ratio of 3.88 was completely transformed into Ge-CIT-5 within a couple of days.

Isolating Ge-CIT-13 from the presence of moisture inhibited the transformation. All measures which excludes sorption of water within the pore system of Ge-CIT-13 including dry argon mood, hydrophobic cyclohexane adsorption, and storage temperature higher than the boiling point of water significantly decelerated the transformation. These observations strongly evidence that the presence of sorbed water is indispensable for the transformation of Ge-CIT-13 to Ge-CIT-5.

The properties of resultant Ge-CIT-5 were investigated. In argon adsorption, a small degree of disorder was observed in the low pressure region presumably formed during the transformation. However, the overall microporosity matched well with pure-silica CIT-5. In the ^{29}Si NMR spectra, disappearance of $d4r$ signals was observed. But other evolutions in the ^{29}Si NMR spectra could not fully be explained with the currently available experimental results. The structural changes of other germanosilicates having $d4r$ units were also investigated. While UTL completely collapsed within a day, ITH and IWW retained their original structures relatively well. No significant diffraction shift was observed in these materials. Ge-CIT-13 remained as the only germanosilicate to date which undergoes this type of transformation.

Chapter 8

Topotactic Transformation and Postsynthetic Modification of CIT-13 and CIT-5

In this chapter, investigations involving the transformation of Ge-CIT-13 and Ge-CIT-5 into two novel structures CIT-14 and CIT-15 is presented. Also, the postsynthetic alumination of Ge-CIT-13 and Ge-CIT-5 yielding hydrothermally stable high-silica Al-CIT-13 and Al-CIT-5 is discussed.

8.1. Introduction

The topotactic transformations of UTL-type germanosilicate have attracted significant interest during the last decade.^{118, 122-123, 145, 162, 181, 195} Unlike other *d4r*-germanosilicates such as IWW or ITH, it was found that UTL has a unique arrangement of germanium T-atoms within its *d4r* units on the basis of the extended X-ray absorption fine structure (EXAFS) spectroscopy and solid-state NMR spectroscopy.^{118, 176} Starting with the 2D layered *fer*-type silicate IPC-1P which is the delamination product from IM-12,¹⁶¹ a number of novel frameworks were obtained such as IPC-2, IPC-4,¹²² IPC-6, IPC-7,¹²³ IPC-9, and IPC-10.¹⁶² Also, the inverse sigma transformation directly from IM-12 to COK-14 was demonstrated.¹¹⁸

It was already pointed out that Ge-CIT-13 can be transformed into two novel frameworks, large-pore CIT-14 and medium-pore CIT-15, via transformations analogous to the case of UTL. There are a couple of reports regarding the topotactic transformation of

CIT-13-type molecular sieves,^{165, 167} but the full picture of its rich chemistry has never been reported. In this chapter, the transformations from CIT-13 to CIT-14 and CIT-15 are discussed, focusing on the delamination time. Also, the inverse sigma transformation of Ge-CIT-13 is demonstrated for the first time. Furthermore, another set of transformations starting from Ge-CIT-5 are also discussed. Lastly, the postsynthetic aluminations processes of Ge-CIT-13 and Ge-CIT-5 are demonstrated. Figure 8.1. graphically summarizes the scope of what is presented in this chapter.

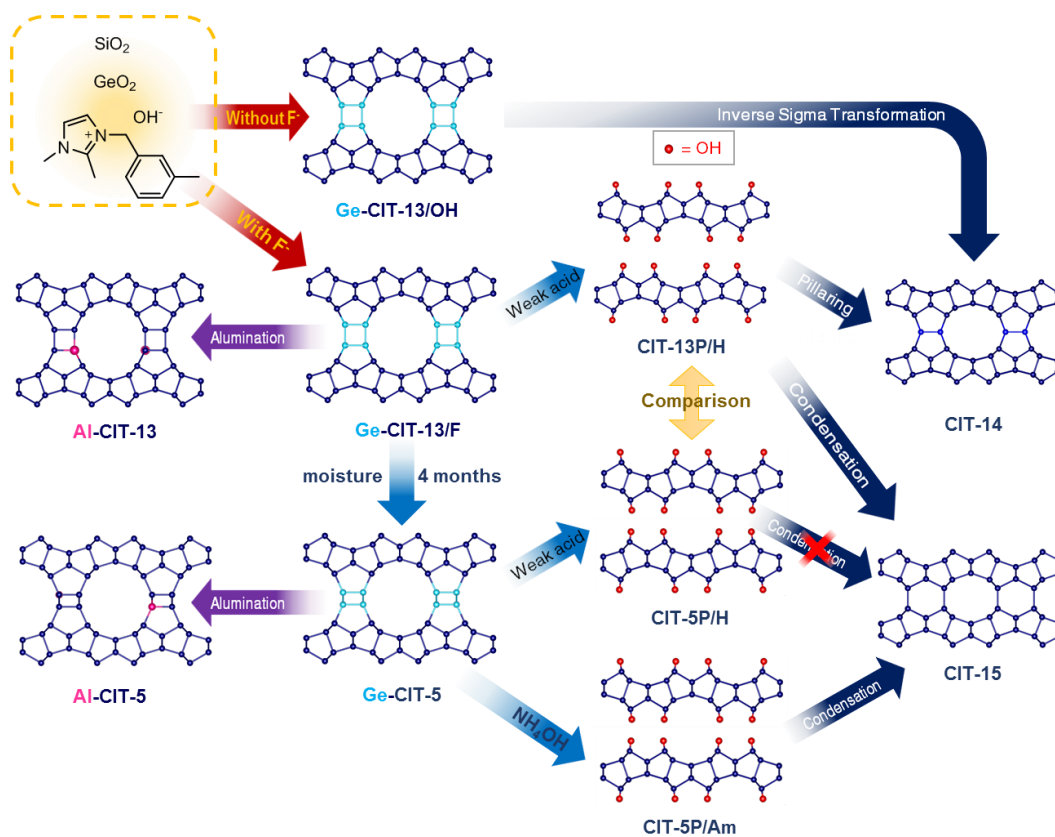


Figure 8.1. Overview of the network of topotactic transformations and postsynthetic modification pathways discussed in this chapter.

8.2. Experimental

8.2.1. Preparation of Parent Materials

Parent Ge-CIT-13 samples were prepared according to the protocol described in Chapter 6. Parent Ge-CIT-5 samples were prepared from the transformation from Ge-CIT-13 as described in Chapter 7.

8.2.2. Hydrolytic Delamination of Weak Acid and Base

Delamination of Ge-CIT-13 and Ge-CIT-5 was conducted using 0.1 M HCl solution at 99 °C or 1–3% NH₄OH solution at room temperature.^{161, 167} Freshly calcined germanosilicate was dispersed in a desired concentration of weak acid or base solution in a solid : liquid ratio of 1 mg : 1 mL. The mixture was stirred continuously during the delamination. The resultant solid was collected using a centrifuge, and washed with distilled water and acetone. Drying was conducted at room temperature in a vacuum desiccator overnight.

8.2.3. Alkoxysilylational Pillaring

Alkoxysilylational pillaring of layered CIT-13P was performed as a procedure previously reported in the literature.¹²² Specifically, in a 23-mL PTFT-lined autoclave, layered CIT-13P was mixed with diethoxydimethylsilane (DEDMS) and 1 M nitric acid solution. The weight ratio CIT-13P : DEDMS : acid solution was 5 : 1 : 100. The mixture was sealed and heat-treated at 170 °C for 16 hours. The resultant solid was collected using a centrifuge, and washed with distilled water. The dried solid was calcined at 580°C for 6 hours.

8.2.4. Inverse Sigma Transformation

The inverse sigma transformation protocol for the transformation from Ge-CIT-13 to CIT-14 was performed on the basis of the original procedure reported by Verheyen et al.¹¹⁸ Freshly calcined Ge-CIT-13 was dispersed in 12 M HCl (37 wt. % in H₂O) in a PTFE-lined autoclave. The solid : acid weight ratio was 1 : 50. This suspension was tumbled in a rotating oven at 95 °C for 48 hours. The resultant solid was collected by centrifuge. This intermediate product (-CIT-14) was washed with distilled water and acetone, and dried at room temperature in vacuum for 24 hours. Finally, under an air flow, the dried -CIT-14 was calcined at 550 °C for 6 hours.

8.2.5. Direct Condensation of CIT-13P

The formation of CIT-15 was achieved by calcining CIT-13P samples prepared according to the procedure described in Section 8.2.2. The calcination was conducted at 580 °C for 6 hours under an air flow.

8.2.6. Degermanation and Alumination

Postsynthetic alumination was performed using 1 M aluminum nitrate solution.^{158, 160} Here, 1 N nitric acid was used together to control the acidity of treating solutions.¹⁵⁴ The compositions of acidic aluminum nitrate solutions were given in Table 8.1. Freshly calcined Ge-CIT-13 (or Ge-CIT-5) samples were dispersed in the desired amount of treating solutions. The solid-to-solution ratio was 100 mL of solution per a gram of solid. The mixture was charged in a 23-mL PTFE-lined Parr autoclave and placed in a rotating oven at 175 °C (CIT-13) or 185 °C (CIT-5). The treatment was performed for 24 hours. The resulting solid was separated by centrifuge, and repeatedly washed twice with 0.01 M HNO₃ and twice with distilled water. The final Al-CIT-13 (or Al-CIT-5) samples were dried at room temperature in a vacuum chamber.

8.2.7. Characterization

PXRD patterns were acquired using a Rigaku MiniFlex II benchtop diffractometer using Cu K α radiation ($\lambda = 1.54184 \text{ \AA}$) to assess the crystal structure and crystallinity of the products. Morphology and elemental composition were studied using a Zeiss 1550VP FE-SEM equipped with an Oxford X-Max SDD X-ray EDS. Pore volumes and pore-size information of microporous materials were studied based on Ar adsorption isotherms obtained using a Quantachrome Autosorb iQ at 87.45 K.

^1H , ^{27}Al and ^{29}Si MAS solid-state NMR spectra of samples were obtained using a Bruker Avance 500 MHz spectrometer with carrier frequencies of 499.843, 130.287 and 99.305 MHz, respectively. A 4-mm zirconia rotor with a Kel-F cap was charged with 50–100 mg of as-made or freshly calcined sample. The MAS rates were 8 kHz both for ^1H - ^{29}Si CP and ^1H -decoupled ^{29}Si Bloch-decay experiments, and 12 kHz for ^{27}Al experiments.

8.3. Results and Discussion

8.3.1. Effects of Initial Germanosilicate Structure on Delamination

The first step of the topotactic transformations of Ge-CIT-13 and Ge-CIT-5 is the delamination that creates *cfi*-layers by removing Ge-rich *d4r* units connecting adjacent layers. In this chapter, the kinetics of the delamination process and physicochemical properties of layered CIT-13P/CIT-5P are discussed in terms of initial germanosilicate structures and delamination process parameters.

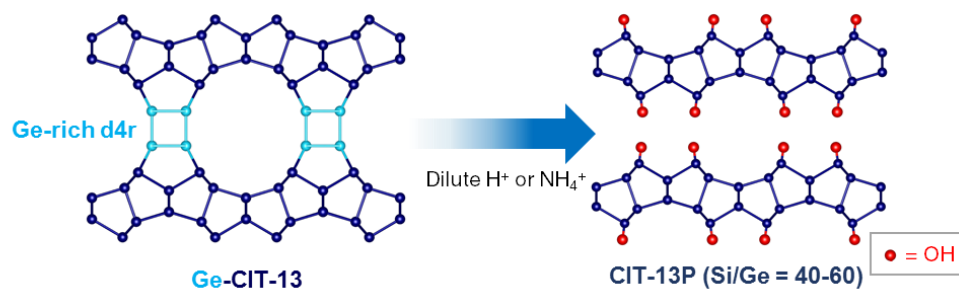


Figure 8.2. Schematic illustration of the acid- or ammonium-delamination of Ge-CIT-13 resulting in CIT-13P.

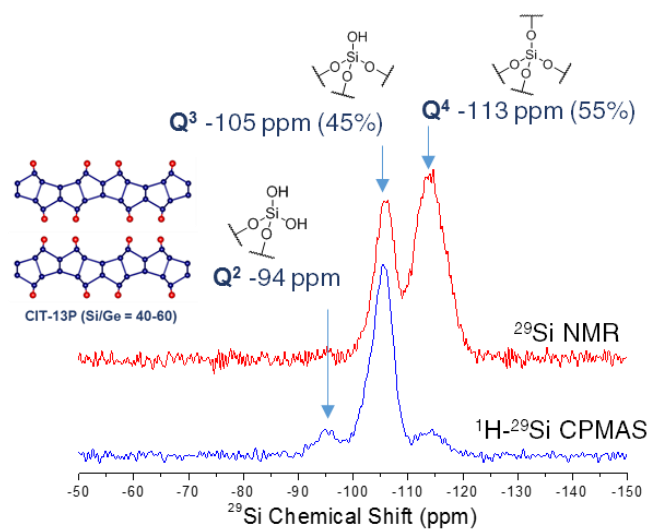


Figure 8.3. Typical ^{29}Si solid-state NMR spectra of CIT-13P.

Figure 8.2 briefly illustrates the delamination transformation of Ge-CIT-13 to CIT-13P. A layered 2D-silicate CIT-13P is produced by removing the bridging Ge-rich *d4r* units which is hydrothermally labile. The delamination can be accomplished using weak acid,^{122, 161, 181} weak base,¹⁶⁷ or even distilled water.¹⁷⁶ The resultant CIT-13P possesses surface silanol groups (Si-OH) as a result of removal of *d4r* units. In a typical ^{29}Si NMR spectra

(Figure 8.3), CIT-13P shows 2–3 peaks within the range from -90 ppm to -120 ppm. Unlike tectosilicates such as the parent CIT-13 or CIT-5, phyllosilicate CIT-13P shows a prominent peak at -105 ppm which is assigned to Q³-silanol (Si(OH)(OT)₃) silicon T-atoms having one disconnected –OH group. The majority of the Si T-atoms in CIT-13P are still completely connected Q⁴ Si-sites. The theoretically ideal CIT-13P in which no *d4r* remnants are present and with no defects within the remaining *cfi*-layers will show a Q³-site proportion of 33.3%. But, typically the actual CIT-13P samples show Q³-contributions much higher than 33% due to the presence of layer defects possibly generated by the degermanation directly from the *cfi*-layers. The example shown in Figure 8.3 shows a 45% of Q³-contribution. In the ¹H-²⁹Si CP-MAS spectrum of CIT-13P, Q²-silanediol (Si(OH)₂(OT)₂) T-sites could be also detected due to the Hartmann-Hahn amplification by proton nuclei. But those Q²-sites are typically few in number.

Ge-CIT-5 is produced from Ge-CIT-13 by the transformation of arrays of *d4r* units into double-zigzag chain (*dzc*) units. Thus, it can be easily deduced that the bridging *dzc* units in a Ge-CIT-5 framework are also consisting of Ge-rich T-sites which can be hydrolyzed by weak acid. The kinetics of delamination processes of Ge-CIT-13/F[4.33] and Ge-CIT-5 transformed from the former parent Ge-CIT-13 were studied. The design of this experiment is shown in Figure 8.4(a). The two parent germanosilicates were delaminated by 0.1 M HCl solution at 99 °C for controlled durations. In this work, the delamination product of Ge-CIT-5 is named as CIT-5P, following the same nomenclature. Figure 8.4(b–e) are the PXRD patterns of the parent materials (Ge-CIT-13 and Ge-CIT-5) and delaminated layered products (CIT-13P and CIT-5P). The calculated interlayer distances and Si/Ge ratios characterized on the basis of EDS are illustrated in Figure 8.5.

Clearly, the interlayer diffraction peaks of the CIT-13P products were shifted toward higher diffraction angles as the delamination time extended as shown in Figure 8.4(d). The interlayer distance which had been initially 13.7 Å (Ge-CIT-13) was decreased to 12.3 Å and

11.4 Å after 3 and 24 hours of delamination, respectively. However, the series of PXRD patterns of CIT-5P samples displayed in Figure 8.4(e) did not show any significant change in the interlayer distance in accordance with the extension of delamination time. All PXRD patterns of CIT-5P were overlapped at the same position. The calculated interlayer distance, which had been 12.6 Å (Ge-CIT-5) before delamination, was decreased to 12.2 Å after 3 hours of delamination and no further decrease was observed.

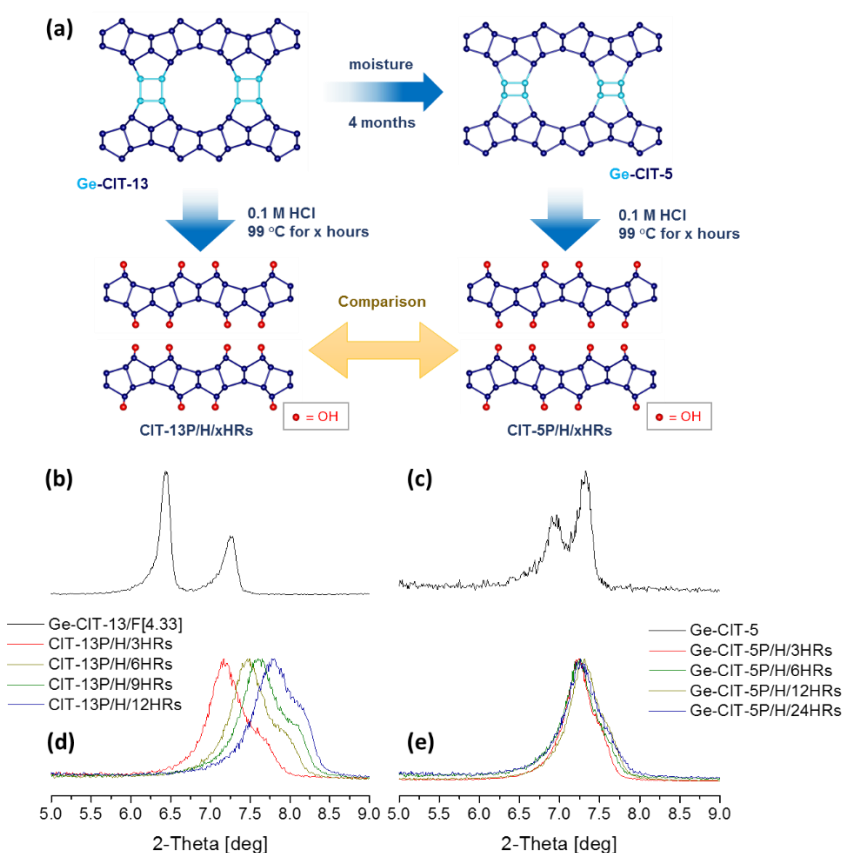


Figure 8.4. Kinetics of the acid-delamination of Ge-CIT-13 and Ge-CIT-5 (a) Design of experiment. PXRD patterns of (b) Parent Ge-CIT-13/F[4.33], (c) Ge-CIT-5, (d) a series of CIT-13P/H samples acid-delaminated for x hours. (e) a series of CIT-5P/H samples acid-delaminated for x hours. (x = 3, 6, 12, 24)

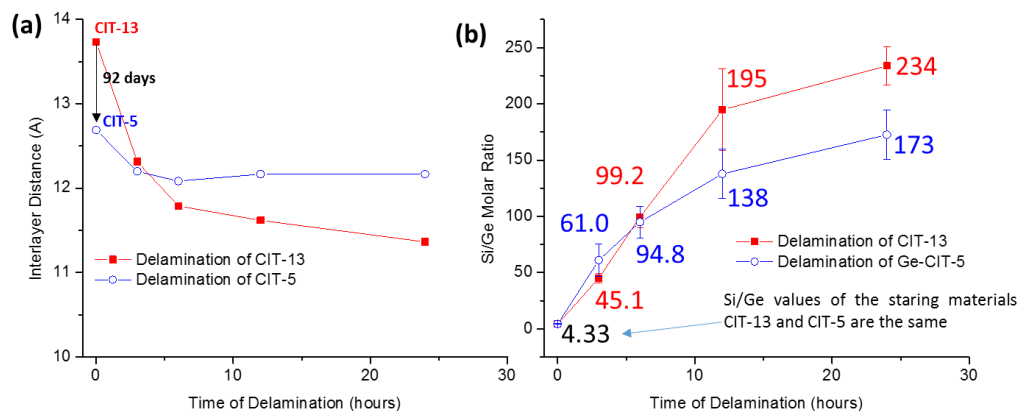


Figure 8.5. Time-dependent structural and compositional changes induced by acid-delamination. (a) Interlayer distances of CIT-13P/H/xHRs and CIT-5P/H/xHRs as functions of delamination time calculated from PXRD patterns shown in Figure 6.4(d–e). (b) Si/Ge molar ratios of CIT-13P/H/xHRs and CIT-5P/H/xHRs as functions of delamination time.

Curiously, germanium T-atoms were continuously being extracted in the course of delamination of both Ge-CIT-13 and Ge-CIT-5. In case of the CIT-13 delamination, the Si/Ge ratio was increased from 4.33 to 234 during 24 hours of delamination process. Although the interlayer distance was not changed after 3 hours of delamination, the Si/Ge ratio of CIT-5P kept increasing even after 3 hours of delamination with a rate slower than CIT-13 as illustrated in Figure 8.5(b). This observation suggests the presence of very refractory siliceous remnant moieties in CIT-5P. Since this trend was not observed in the series of CIT-13P, it can be concluded that the formation of these stable siliceous species are related to the CIT-13-to-5 transformation.

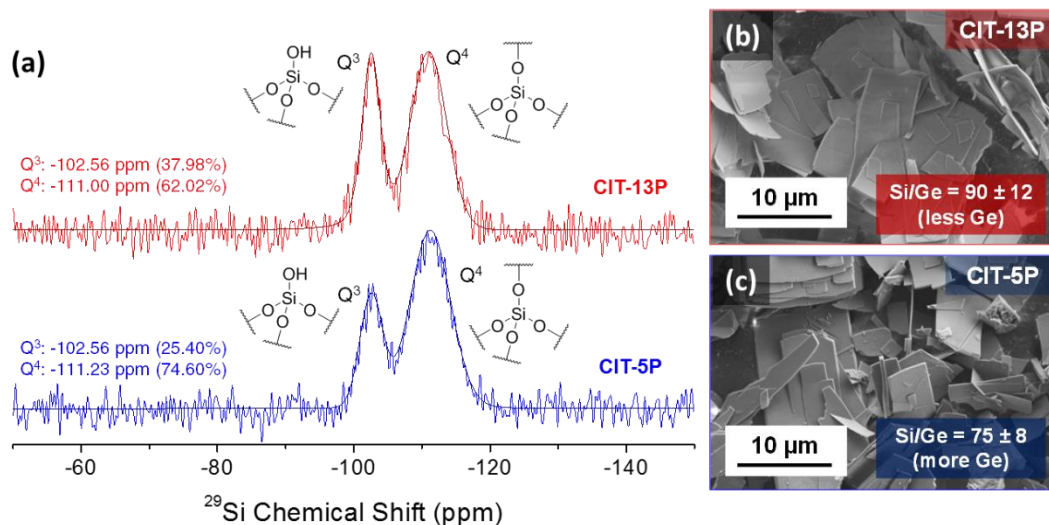


Figure 8.6. NMR spectra and morphologies of acid-delaminated germanosilicates. (a) ^{29}Si solid-state NMR spectra of CIT-13P and CIT-5 originated from the same parent Ge-CIT-13/F. SEM images of (b) CIT-13P and (c) CIT-5P.

A pair of CIT-13P and CIT-5P layered materials originating from the same parent Ge-CIT-13/F were subjected to the ^{29}Si solid-state NMR spectroscopy to acquire further information about the arrangements of Si and Ge T-sites. The NMR spectra and corresponding SEM and EDS results are provided in Figure 8.6. After the same delamination process, the resultant CIT-13P and CIT-5P had high Si/Ge ratios of 90 and 75 which correspond to 1.0 % and 1.3 % of T-site occupancies of germanium, respectively. So it can be assumed that the influence of remaining germanium would be negligible.

On the basis of ^{29}Si solid-state NMR spectra, proportions of Q^3 -silanol sites in CIT-13P and CIT-5P were of 38.0 % and 25.4 %, respectively. Considering the fact that the theoretically ideal CIT-13P will show a Q^3 -site contribution of 33.3%, CIT-5P is showing a too small of a Q^3 -contribution. The formation of new Si-O-Si bonds can be one explanation as a result of the formation of *dzc* units, but it is also hard to believe that silanol condensation

forming Si-O-Si bonds can extensively occur at room temperature. Although it will be discussed later, a complete delamination of CIT-5 is actually possible if ammonium hydroxide is used as a delaminating base instead of dilute acid. This result suggests that the interlayer siliceous species within CIT-5P which could not be removed by acid can be removed by basic solution. Further experimental evidence must be collected to elucidate the nature of this interlayer remnant siliceous species in CIT-5P.

8.3.2. CIT-14 Formation by Ethoxysilylational Pillaring and Inverse Sigma Transformation

8.3.2.1. Ethoxysilylational Pillaring

In 2013, two topotactic transformations of UTL-type germanosilicate IM-12, which is a related germanosilicate of CIT-13, resulted in two zeolites IPC-2 (OKO) and IPC-4 (PCR) having novel topologies.¹²² The OKO-type IPC-2 was prepared by a protocol called ethoxysilylational pillaring.¹⁴⁵ IM-12 was firstly delaminated into IPC-1P layered silicate using weak acid, and pillared with a pillaring agent diethoxydimethylsilane (DEDMS). This pathway yielded the large-pore, high-silica IPC-2.

The structural similarity between IM-12 and CIT-13 enables an analogous pathway toward another novel framework. In this section, the topotactic transformation of Ge-CIT-13 to CIT-14 via the ethoxysilylational pillaring of layered CIT-13P will be discussed. The schematic description of this transformation is shown in Figure 8.7(a) The first step of the process is the substitution reaction between CIT-13P silanol and alkylsilane bonds of pillaring agents such as DEDMS or 1,3-diethoxy-1,1,3,3-tetramethyldisiloxane (DETMDMS).¹⁸² This reaction forms diethoxysiloxane bridges between neighboring CIT-13P layers (Figure 8.7(c)). These diethoxysiloxane bridges are further condensed by calcination. The net overall change is the replacement of Ge-rich *d4r* units with pure-silica single-4-ring (*s4r*) units. The influences of the preceding delamination process will be also discussed.

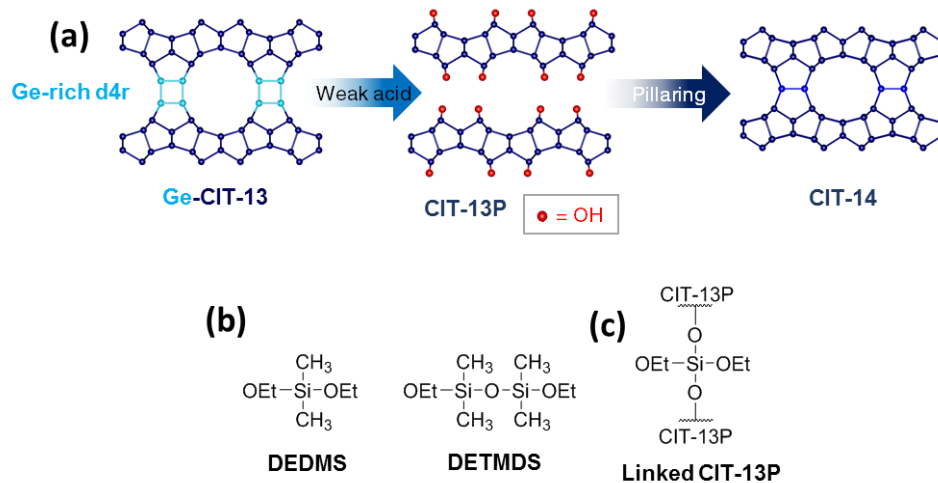


Figure 8.7. Pathway from CIT-13 to CIT-14 via the pillaring process. (a) Schematic illustration of the topotactic transformation from Ge-CIT-13 to CIT-14 by the ethoxysilylational pillaring. (b) Examples of alkoxyalkylsilane species which can be used as pillaring agents. (c) Intermediate stage of CIT-13 layers linked with bridging diethoxysilane.

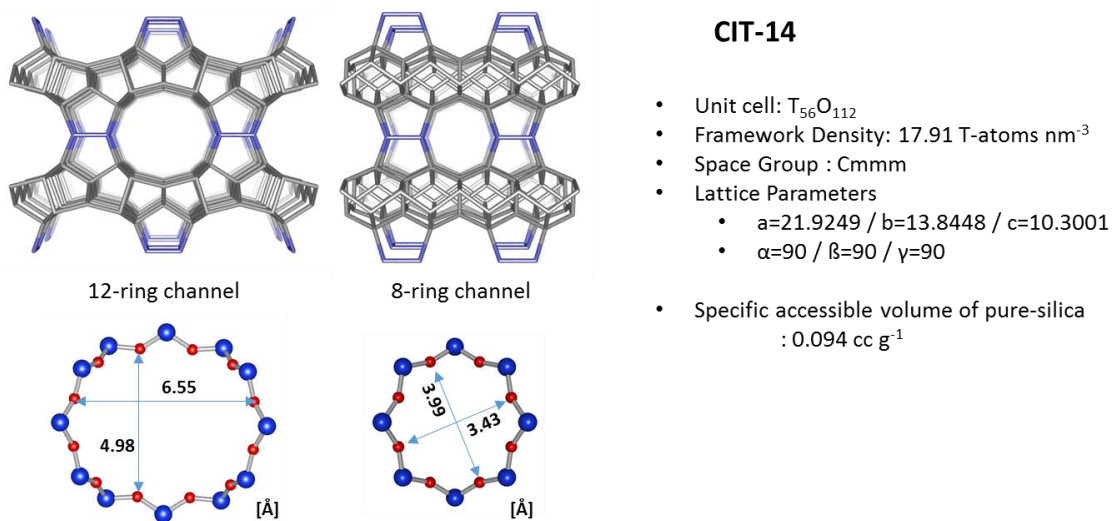


Figure 8.8. Structure, pore sizes, and expected topological information of CIT-14.

Most of the zeolite hydrothermal syntheses are still “black box” processes in which any reliable way to predict the structures of products *a priori* has yet to be established; however, in this case, the structure of desired framework can be exactly predicted. The predicted structure of CIT-14 was optimized using the GULP algorithm¹⁹⁸ with the Catlow parameters as a hypothetical pure-silica framework by Dr. Dan Xie at Chevron. The structure, pore sizes, and expected topological information calculated using a utility program for topological analysis of zeolite materials, TOTOPOL are provided in Figure 8.8.¹⁹⁹

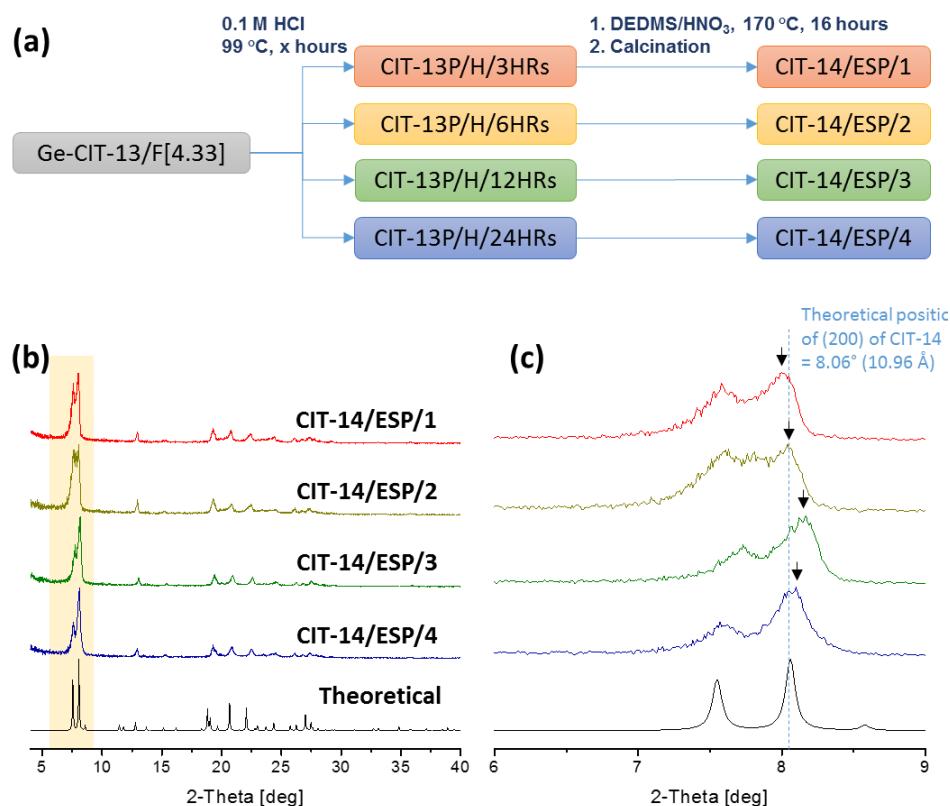


Figure 8.9. Influence of degree of delamination on the formation of CIT-14 (a) Design of experiment. PXRD patterns of the resultant CIT-14 samples in the range of (b) 4–40° and (d) 6–9°.

As the precursor material, Ge-CIT-13/F[4.33] was used. Calcined Ge-CIT-13 was delaminated in 0.1 M HCl solution at 99 °C for 3, 6, 12, and 24 hours, and four CIT-13P samples having different extents of delamination were obtained. These four CIT-13P samples are the same samples which were discussed in the previous section. Here, these samples are named as CIT-13P/H/ x HRs ($x = 3, 6, 12, 24$). This series of CIT-13P samples was pillared with DEDMS at the same reaction condition. As a result, four pillared materials which are named as CIT-14/ESD/ y ($y = 1, 2, 3, 4$), where ESD stands for ethoxysilylational pillaring, were produced. The design of this experiment and the resultant PXRD profiles are shown in Figure 8.9.

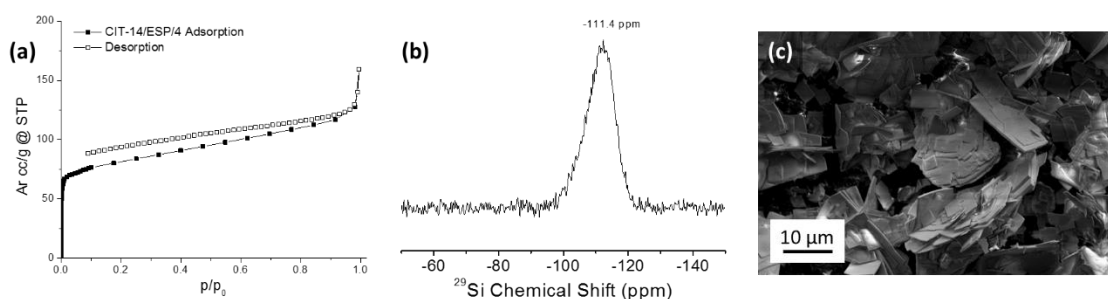


Figure 8.10. Material characterization of CIT-14/ESP. (a) Argon adsorption/desorption isotherm, (b) 8 kHz MAS ¹H-decoupled ²⁹Si solid-state NMR spectrum, and (c) SEM image of CIT-14/ESP/4.

All of the resultant materials showed their interlayer diffraction lines to be very close to the predicted position (8.06°) of the interlayer diffraction line of CIT-14. The peaks shown in the higher diffraction angle region ($20\text{--}30^\circ$) matched well with the theoretically predicted spectra. Interestingly, the interlayer distances of resultant CIT-14-type materials were barely influenced by the extent of delamination. Presumably, this observation is maybe because it is possible for the remnant T-atoms of Ge-rich $d4r$ units which survived the degermanation

by acid-delamination to constitute a part of new *s4r* units during the following ethoxysilylation step.

The obtained CIT-14 via the ethoxysilylational pillaring was further investigated on the basis of the argon adsorption/desorption isotherm, ^{29}Si solid-state NMR spectroscopy, SEM, and EDS elemental analysis. The results are shown in Figure 8.10. The micropore volumes of CIT-14/ESP/4 estimated from its argon adsorption isotherm were 0.065 cc g^{-1} and 0.102 cc g^{-1} based on the t-plot method and the Saito-Foley model, respectively. These values were close to or somewhat lower than the predicted accessible volume (0.094 cc g^{-1}) calculated using TOTOPOL.¹⁹⁹ From the desorption isotherm, a hysteresis was observed which indicates the presence of mesoporosity. A similar hysteresis was reported for the UTL-to-OKO ethoxysilylational transformation.¹²² This mesoporosity suggests the presence of defect sites and/or amorphous silica phase induced by the pillaring pathway.¹²² In the ^{29}Si NMR spectrum, CIT-14/ESP showed a broad signal across the range from -100 to -120 ppm. No deconvolution was attempted due to many T-sites (7) and possible presence of mesoporous impurities. No apparent change induced by the ethoxysilylational pillaring procedure was observed in the SEM image. The observed Si/Ge ratios of CIT-14/ESP/1, 2, 3, and 4 were 50.0, 92.6, 164, and 253. These values are very similar to the Si/Ge ratios of CIT-13P layered materials (45.1, 99.2, 195, and 234) used to prepare CIT-14 samples. Therefore, it can be concluded that no significant degermanation happened during the ethoxysilylational pillaring procedure.

8.3.2.2. *Inverse Sigma Transformation*

The inverse sigma transformation of IM-12 resulted in COK-14 which is the type material of the framework OKO that was reported by Verheyen et al. in 2012.¹¹⁸ The presence of pure- GeO_2 *s4r* parts occupying the one side of *d4r* units is essential for germanosilicates to undergo this type of transformation.¹⁷⁶ Such configuration of germanium T-atoms within *d4r* units was confirmed on the basis of the extended X-ray absorption fine

structure (EXAFS) spectroscopy in IM-12.¹¹⁸ However, up to this time, IM-12 was the only germanosilicate to have such transformability.

In this section, the inverse sigma transformation of Ge-CIT-13 will be discussed. Schematic illustration of the inverse sigma transformation of Ge-CIT-13 is shown in Figure 8.11. Calcined Ge-CIT-13 is treated with 37 wt. % HCl (12 M) at 95 °C for 48 hours. During this step, the pure-GeO₂ *s4r* parts are leached out of the *d4r* units by strong acid. After washing off leached germanium, an intermediate solid consisting of loosely connected *cfi*-layers remains. I named this intermediate -CIT-14 where (-) sign denotes the incompleteness of structure, following the notation of -COK-14.¹¹⁸ Calcining -CIT-14 results in a completely connected framework of CIT-14.

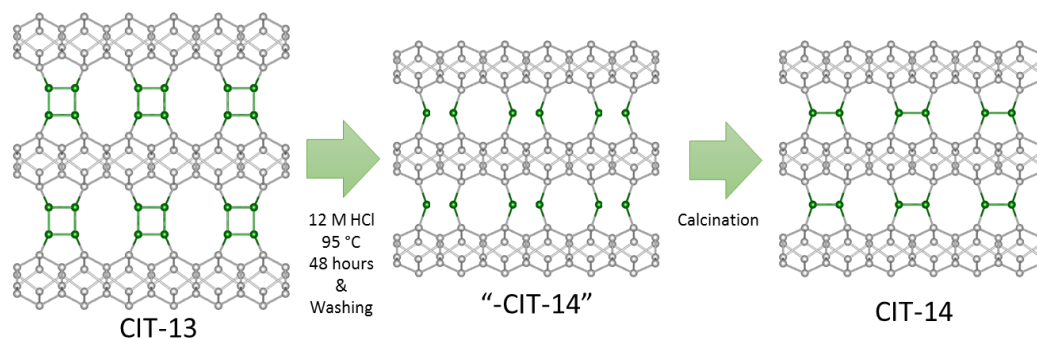


Figure 8.11. Schematic illustration of the inverse sigma transformation from CIT-13 to CIT-14.

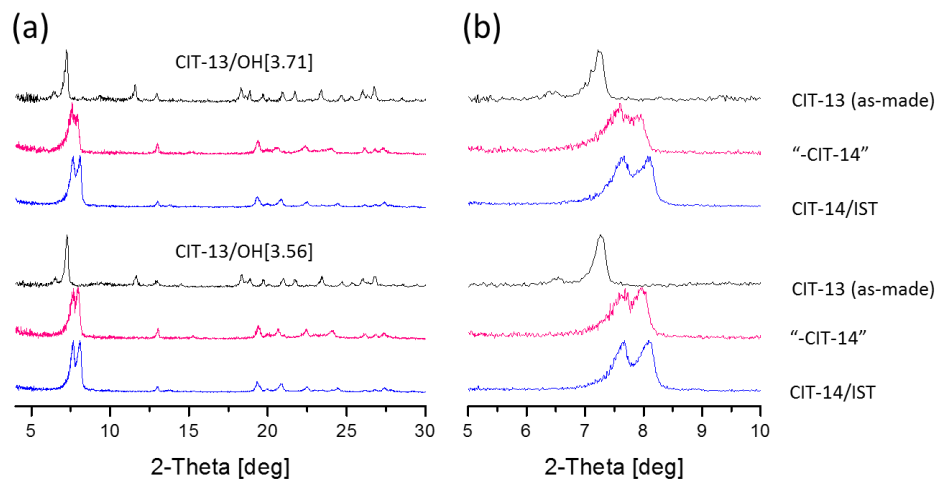


Figure 8.12. Examples of the inverse sigma transformation from CIT-13/OH to CIT-14 examined on the basis of PXRD patterns in the range of (a) 4–30° and (b) 5–10°.

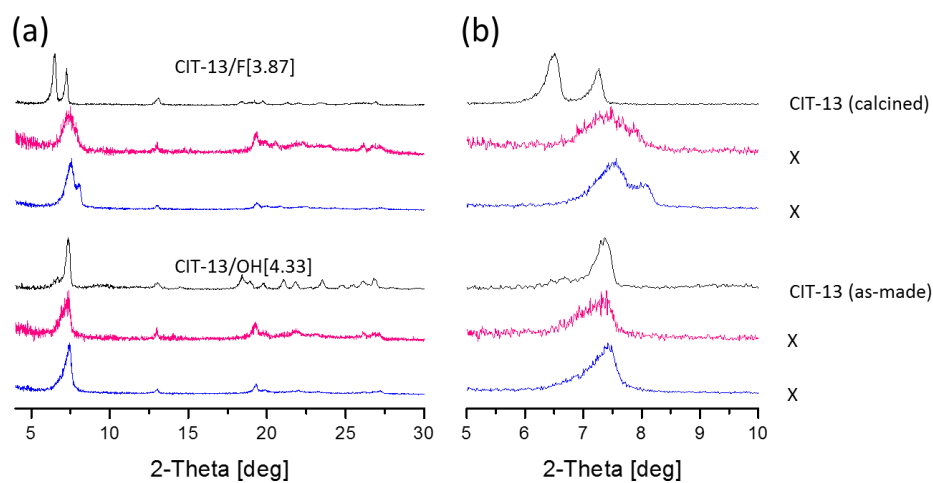


Figure 8.13. Trials of the inverse sigma transformation using a high-Ge CIT-13/F and a low-Ge CIT-13/OH examined on the basis of PXRD patterns in the range of (a) 4–30° and (b) 5–10°.

Interestingly, the inverse sigma transformation of Ge-CIT-13 was only possible for Ge-CIT-13/OH[y] ($y < 3.71$); i.e., only Ge-CIT-13 synthesized from *the hydroxide-media recipe having very high germanium content* underwent this type of transformation and yielded ordered CIT-14. Figure 8.12 shows the PXRD profiles of a couple of examples of inverse sigma transformation of parent Ge-CIT-13/OH samples yielding CIT-14 products. It is noteworthy that the intermediate -CIT-14 materials already showed PXRD patterns very similar to those of CIT-14 even before calcination. CIT-14 samples obtained by the inverse sigma transformation were referred to as CIT-14/IST where IST stands for inverse sigma transformation. Ge-CIT-13/F[3.87] synthesized in fluoride media and Ge-CIT-13/OH[4.33] having a high Si/Ge ratio resulted in disordered materials after acid-leaching of germanium followed by calcination (Figure 8.13).

It has been a long-standing question why only IM-12 could yield its inverse sigma transformation products. Kasian et al. investigated the germanium arrangement within the *d4r* units of UTL, ITH, and IWW frameworks in terms of ^{19}F MAS NMR and ^1H - ^{29}Si CP-MAS NMR spectroscopy.¹⁷⁶ Unlike ITH and IWW, as shown in Figure 8.14(a), UTL-type germanosilicate IM-12 showed no Q^2 signal in the ^1H - ^{29}Si CP-MAS NMR spectrum after complete degermanation using distilled water.¹⁷⁶ The absence of Q^1 and Q^2 signals in completely degermanated *d4r*-containing frameworks in the ^1H - ^{29}Si CP-MAS NMR spectra is possible only when one whole side of the *d4r* units consists only of germanium T-atoms.¹⁷⁶ Unlike UTL, ITH and IWW showed strong Q^2 signals.¹⁷⁶ They suggested this absence of Q^2 signal in the ^1H - ^{29}Si CP-MAS NMR spectrum of degermanated UTL as an indirect evidence that IM-12 has a unique arrangement of germanium T-atoms within the *d4r* units different to other germanosilicates.¹⁷⁶

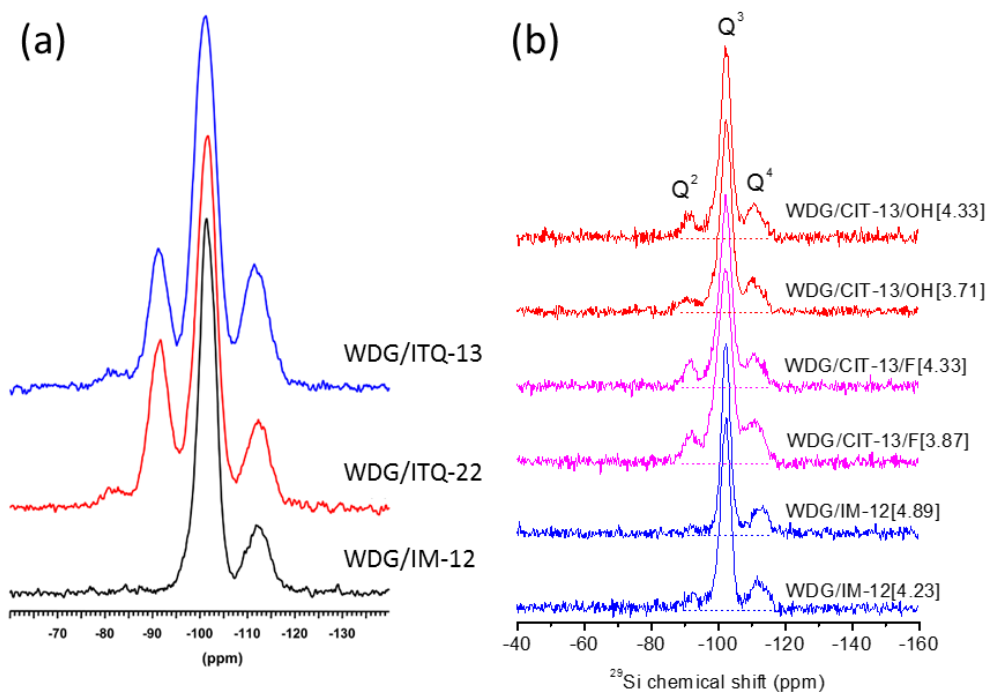


Figure 8.14. Silanol characterization after water-degermanation of germanosilicates. (a) ^1H - ^{29}Si CP-MAS NMR spectra of water-degermanated (WDG) ITQ-13, ITQ-22, and IM-12. Reproduced with Permission from Ref [176]. Copyright 2014 American Chemical Society. (b) ^1H - ^{29}Si CP-MAS NMR spectra of water-degermanated Ge-CIT-13/F, Ge-CIT-13/OH, and IM-12 samples having various Si/Ge ratios. WDG stands for ‘water-degermanated.’

Several CIT-13/OH, CIT-13/F, and IM-12/OH having various Si/Ge ratios were subjected to a similar degermanation experiment, and their ^1H - ^{29}Si CP-MAS NMR spectra were acquired (Figure 8.14 (b)). Just like in Kasian’s experiment, degermanated IM-12 samples showed very weak Q^2 signals. However, CIT-13/OH and CIT-13/F samples showed Q^2 signals of moderate and strong intensities. Interestingly, Ge-CIT-13/OH[3.71] showed the weakest Q^2 signal after degermanation among all degermanated CIT-13 samples. This

sample is the only Ge-CIT-13 which successfully underwent the inverse sigma transformation among all four Ge-CIT-13 samples subjected to this test. I believe that the arrangement of germanium T-atoms within the *d4r* units has a close relationship with the use of fluoride as the mineralizing agent. It is also known that fluorides can structure-direct the *d4r* units in high-silica gels and form a penta-coordinated germanium within the *d4r* units. Further experimental evidence must be obtained to elucidate the role of fluoride in the CIT-13 synthesis.

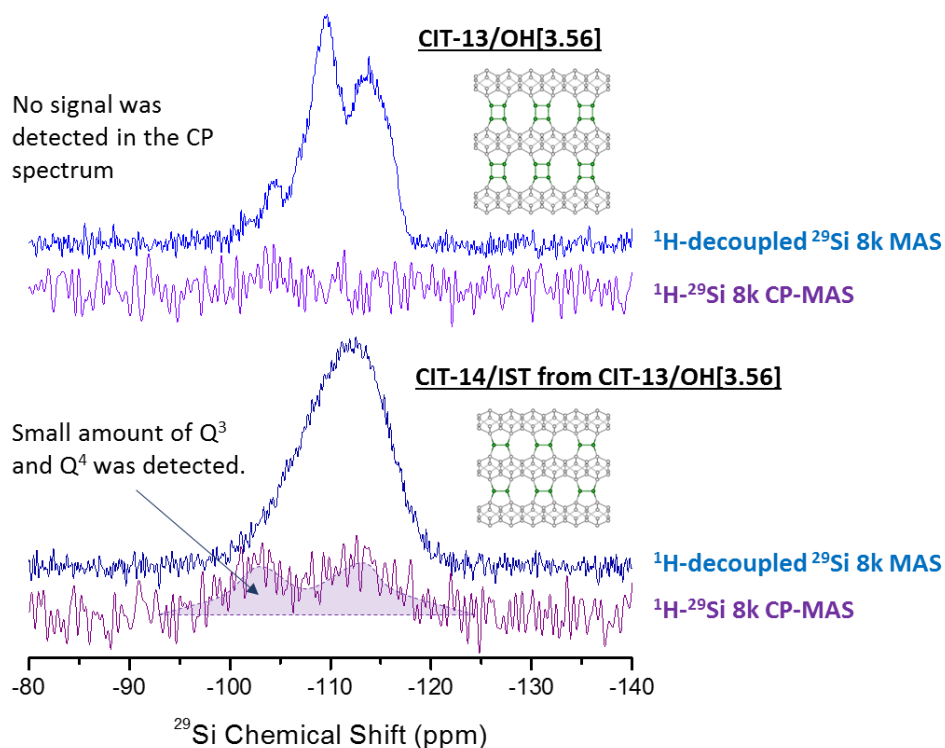


Figure 8.15. 8 kHz MAS ^{29}Si NMR spectra and ^1H - ^{29}Si CP-MAS NMR spectra of the parent CIT-13/OH and the resultant CIT-14 produced via the inverse sigma transformation.

Si/Ge ratios of CIT-14 samples obtained from Ge-CIT-13/OH[3.56] and Ge-CIT-13/OH[3.71] were 14.5 and 17.5, respectively, which are much lower than CIT-14/ESP samples discussed in the previous section. This suggests that the remaining parts of *d4r* units still have a significant amount of germanium T-atoms. ^{29}Si MAS and ^1H - ^{29}Si CP-MAS NMR spectra of the parent Ge-CIT-13/OH and the resultant CIT-14/IST were acquired. (Figure 8.15) The parent Ge-CIT-13/OH showed a typical “three-peak” shape of ^{29}Si spectrum of CIT-13 which was discussed in the previous chapter. CIT-14/IST showed a broad signal across the region from -100 to -120 ppm, which must be consisting of many signals originated from the combination of 7 T-sites of CIT-14 and the presence of germanium.

Lastly, argon adsorption isotherms of the parent CIT-13, CIT-14/IST and CIT-14/ESP (which were shown in the previous section) were compared and displayed in Figure 8.16. CIT-14/IST showed no mesoporosity-induced hysteresis and a micropore volume value (t-plot: 0.105 cc g^{-1} ; Saito-Foley: 0.141 cc g^{-1}) higher than that of CIT-14/ESP (t-plot: 0.065 cc g^{-1} ; Saito-Foley: 0.102 cc g^{-1}). This suggests that the inverse sigma transformation yields purer CIT-14 having better microporosity and crystallinity than the ethoxysilylational pillaring of layered CIT-13P method. The parent Ge-CIT-13/OH[3.56] showed a micropore volume of 0.202 cc g^{-1} on the basis of the Saito-Foley model (based on t-plot method, 0.141 cc g^{-1}). The ratio of the micropore volume of CIT-14/IST to that of Ge-CIT-13 is 0.698. The specific micropore volumes of CIT-14 and CIT-13 having Si/Ge ratios of 14.5 and 3.56 calculated using the TOTOPOL utility¹⁹⁹ are 0.088 cc g^{-1} and 0.126 cc g^{-1} , respectively. The ratio of these theoretical values is also 0.698 which is very close to the observed CIT-14/CIT-13 microporosity ratio.

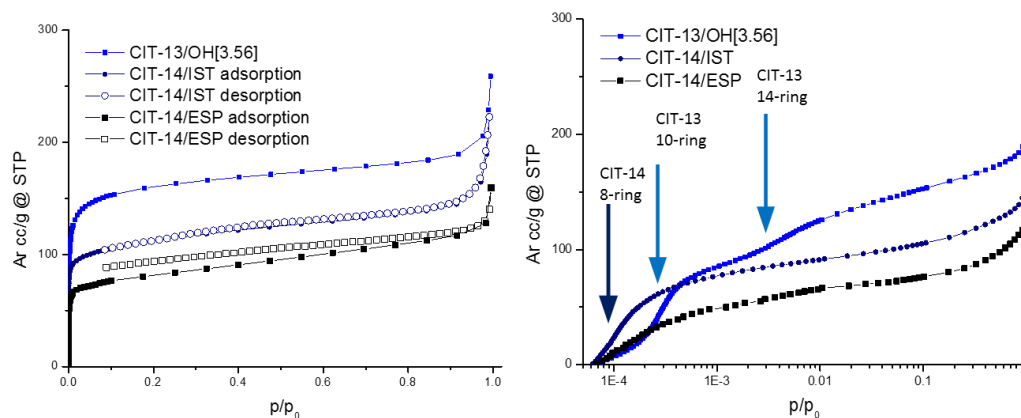


Figure 8.16. Argon adsorption isotherms (87.45 K) of the parent CIT-13/OH, two CIT-14 products from the inverse sigma transformation and the ethoxysilylational pillaring in (a) linear scale and (b) log scale.

8.3.3. CIT-15 Formation by Direct Condensation

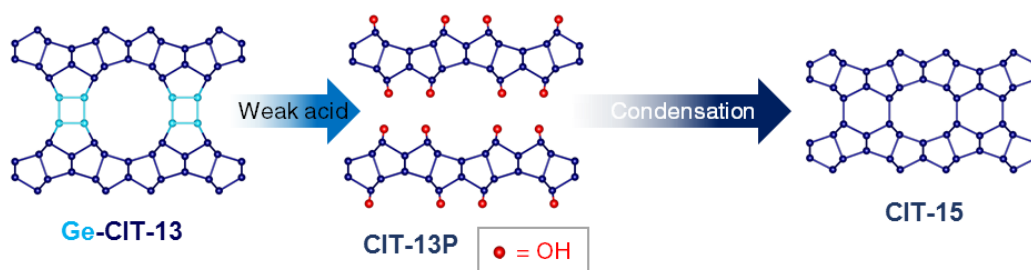


Figure 8.17. Schematic illustration of the topotactic transformation from Ge-CIT-13 to CIT-15 by the direct condensation of CIT-13P.

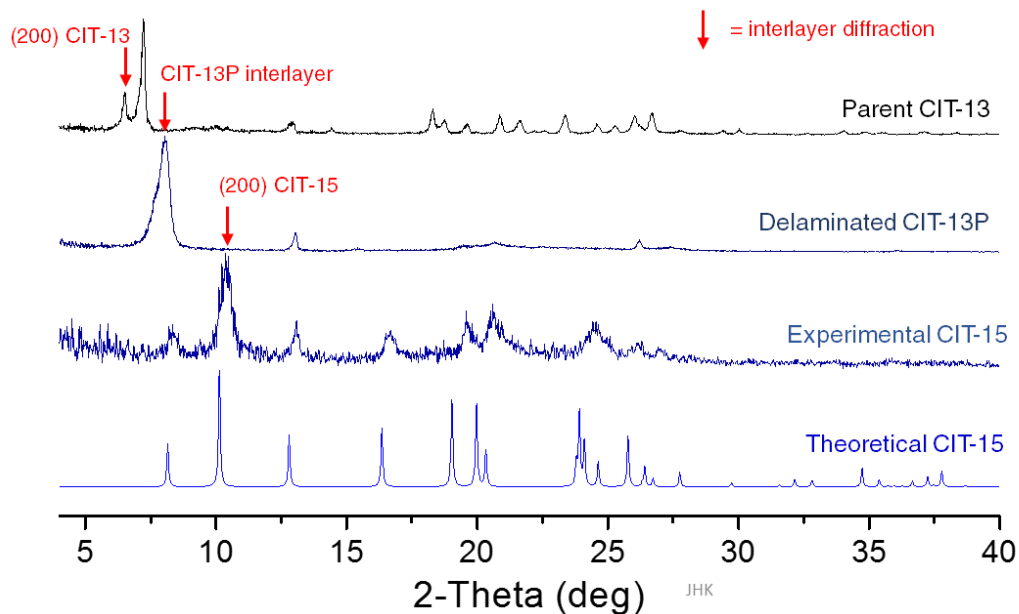
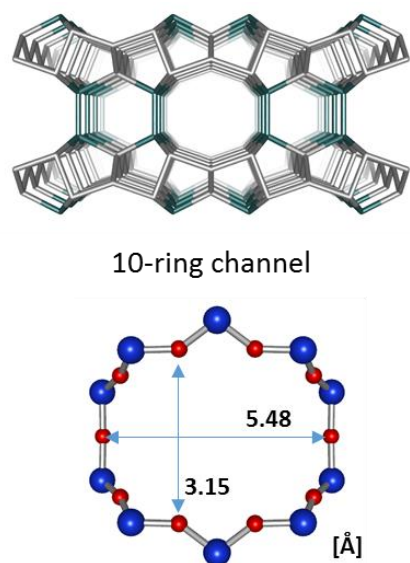


Figure 8.18. Experimentally demonstrated topotactic transformation from Ge-CIT-13 to CIT-15 investigated on the basis of PXRD patterns.

Another novel framework that can be derived from Ge-CIT-13 is CIT-15, a medium-pore framework having one-dimensional channel system. This transformation is an analogue of the topotactic transformation of UTL to PCR.¹²² In this transformation, layered CIT-13P is directly condensed by calcination. This process is schematically described in Figure 8.17. Figure 8.18 shows the involved steps of transformation in terms of PXRD patterns. The interlayer diffraction peaks are labelled with arrows (\downarrow). Initially, the parent Ge-CIT-13 had an interlayer distance of 13.6 Å which is a typical (200) interlayer distance of CIT-13. After acid-delamination, this interlayer distance was decreased down to 11.1 Å. As a result of condensation, the interlayer distance was decreased again to 8.6 Å, which is corresponding to the theoretically predicted position of interlayer diffraction of CIT-15 (8.7 Å) calculated on the basis of the GULP algorithm.¹⁹⁸



CIT-15

- Unit cell: $T_{56}O_{112}$
- Framework Density: $19.23 \text{ T-atoms nm}^{-3}$
- Space Group : Cmmm
- Lattice Parameters
 - $a=17.4686 / b=13.8271 / c=5.1665$
 - $\alpha=90 / \beta=90 / \gamma=90$
- Specific accessible volume of pure-silica : 0.056 cc g^{-1}

Figure 8.19. Structure, pore sizes, and expected topological information of CIT-15.

Just like the case of CIT-14, the structure and topological information of the product (CIT-15) of this topotactic transformation can be predicted on the basis of computational chemistry. Figure 8.19 shows the predicted structural and micropore information of CIT-15 calculated based on the TOTOPOL analysis.¹⁹⁹

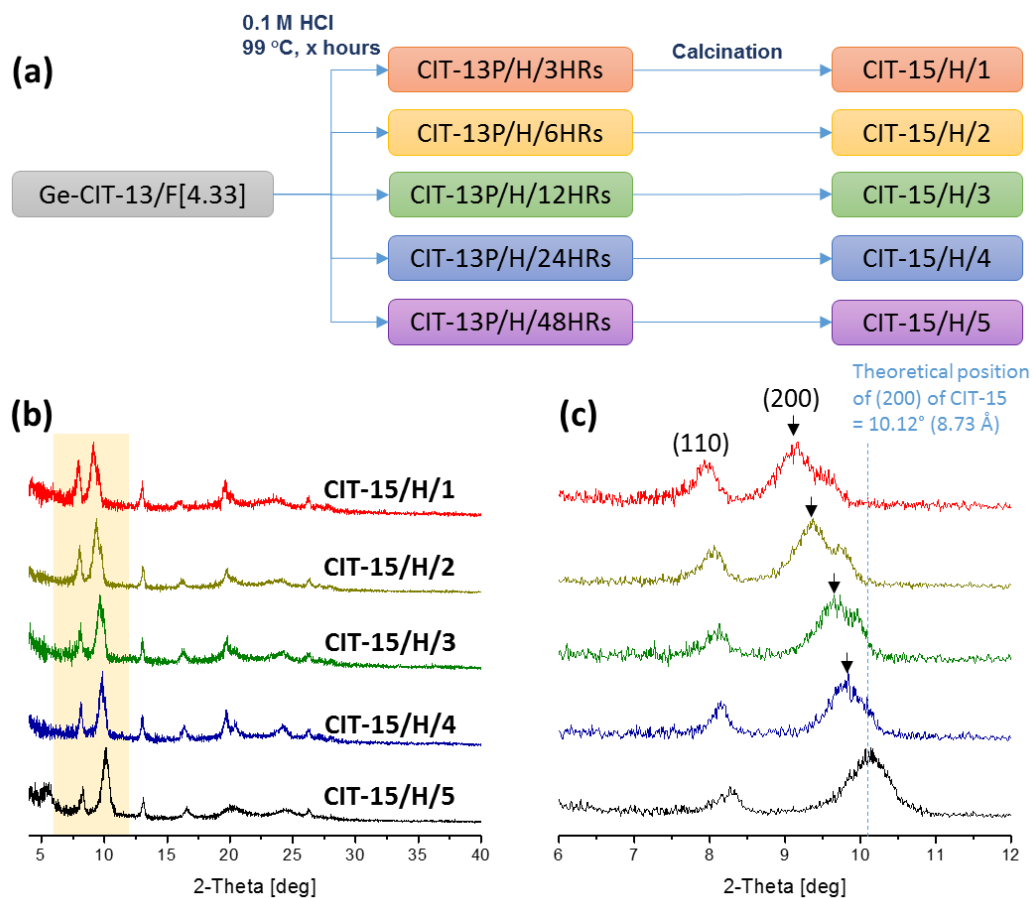


Figure 8.20. Influence of degree of delamination of Ge-CIT-13 on the formation of CIT-15 (a) Design of experiment. PXRD patterns of the resultant CIT-15 samples in the range of (b) 4–40° and (c) 6–12°.

To successfully achieve the transformation from CIT-13 to CIT-15, all T-atoms formerly constituting the *d4r* bridging units must be eliminated from the system during the delamination. This engenders a key difference between the transformations from CIT-13 to CIT-14 and CIT-15. In the transformation from CIT-13 to CIT-14, it was experimentally observed that the extent of acid-degermanation is not an important factor presumably because a small amount of remnant T-atoms which had been parts of *d4r* units still can constitute

newly formed silica *s4r* units together with foreign silicon sources. However, since the transformation from CIT-13 to CIT-15 requires direct connections between neighboring *cfi*-layers, ideally, no interlayer remnant T-atom is allowed. As shown in the PXRD patterns of Figure 8.20, unlike the case of CIT-14, the interlayer distance of condensed phases has a close relation with the extent of delamination of Ge-CIT-13. The successful formation of CIT-15 framework was determined on the basis of PXRD patterns and, particularly, the position of interlayer diffraction which is predicted to be at 10.12° in two-theta. As clearly seen from the diffraction patterns, 48 hours of acid-delamination was required to fully delaminate the parent Ge-CIT-13/F[4.33]. An issue with the resultant CIT-15 products is its poor crystallinity.

In case of the UTL-to-PCR transformation, octylamine was necessarily intercalated between neighboring IPC-1P layers as a layer-reassembling agent to obtain the resultant PCR-type IPC-4 with a high crystallinity.¹²² To enhance the crystallinity of CIT-15, several aliphatic amines (octylamine, heptylamine, and dipropylamine) were intercalated within the interlayer region of CIT-13P. However, none of these aliphatic amines successfully improved the poor crystallinity of CIT-15 formed. The PXRD patterns of the resultant CIT-15 from amine-intercalation were provided in Figure B19.

The direct condensation of CIT-5P layered materials from Ge-CIT-5 which is also the preceding transformation from Ge-CIT-13 was attempted. As expected, due to the presence of interlayer siliceous remnant of acid-delamination which was discussed in the previous section, none of CIT-5P samples successfully condensed into CIT-15-type materials (Figure B20). Their interlayer distance peaks were observed within the range between 9.0° and 9.3° which is far lower-angle than the predicted position of CIT-15 interlayer diffraction (10.12°). Even a CIT-5P obtained from one week of acid-delamination of Ge-CIT-5 did not produced a CIT-15-type product (not shown).

Instead of the acid-delamination using 0.1 M HCl solution which could not remove the delamination remnant of Ge-CIT-5, the base-delamination using ammonium hydroxide solution was tried in order to effectively remove the interlayer siliceous remnants which inhibited the direct connection between neighboring two *cfi*-layers of CIT-5P. Very recently, Liu and co-workers reported the formation of ECNU-21 which is essentially an isostructural framework of CIT-15 by delaminating Ge-CIT-13 with diluted ammonium hydroxide (1 % in H₂O) at room temperature.¹⁶⁷ In this work, the concentration of ammonium hydroxide was controlled. Ge-CIT-5[4.22] was dispersed in 1 wt. % and 3 wt. % of ammonium hydroxide solution and stirred for 24 hours at room temperature. The resultant CIT-5P/*x*% Am (*x* = 1, 3) was recovered by filtration and condensed by calcination.

The PXRD profiles of resultant materials are shown in Figure 8.21. The base-delamination using 1 % ammonium hydroxide could not fully delaminate Ge-CIT-5[4.33]. Although an interlayer diffraction close to the predicted position of CIT-15 was observed in the PXRD pattern of the condensed phase, the majority was still a disordered CIT-5-like phase in the PXRD pattern of CIT-5P/1% Am. On the other hand, 3 % ammonium hydroxide successfully delaminated Ge-CIT-5 leaving no remaining disordered parent phase. This CIT-5P/3% Am was condensed into a phase which shows a PXRD profile very similar to that of the theoretical CIT-15. The interlayer distance of the condensed CIT-5P/3% Am calculated from the peak position was 8.49 Å which is shorter than the theoretical value of 8.73 Å. This result suggests that the concentration of ammonium hydroxide is the key variable for the complete delamination of Ge-CIT-5 although materials can be “overly delaminated” if the concentration is too high.

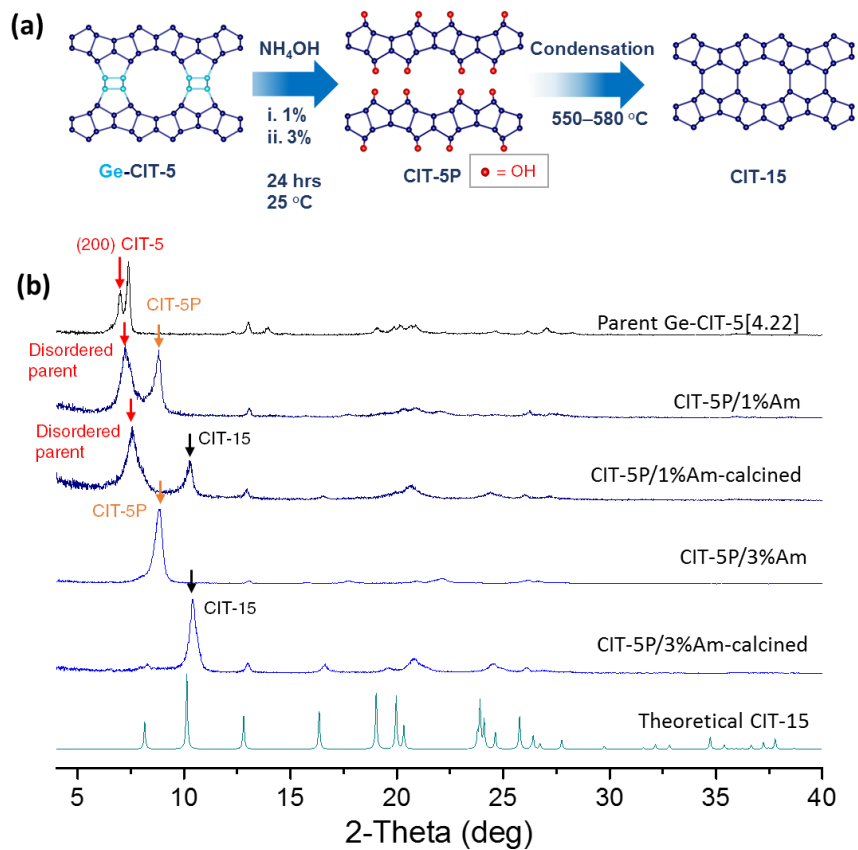


Figure 8.21. Pathway from CIT-13 to CIT-15 and characterizations. (a) Schematic illustration of transformation from Ge-CIT-5 to CIT-15 via ammonium delamination. (b) PXRD patterns of intermediate and resultant products.

8.3.4. Effects of Solution Acidity on Alumination

8.3.4.1. Postsynthetic Degermanation and Alumination of Ge-CIT-13

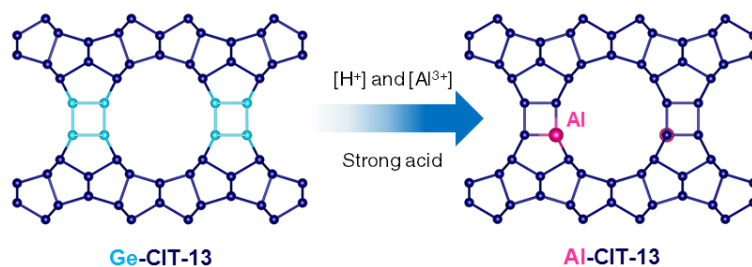


Figure 8.22. Schematic illustration of postsynthetic degermanation/alumination of Ge-CIT-13

Table 8.1. Summary of postsynthesis alumination of Ge-CIT-13

Sample	Parent Ge-CIT-13	Solution		Elemental Composition of Product	
		$[H^+]$ (M)	$[Al^{3+}]$ (M)	Si/Al ratio (Al/T %)	Si/Ge ratio (Ge/T %)
Al-CIT-13(1)	Si/Ge = 5.1 16% Ge/T	1	1	80 (1.2)	59 (1.6)
Al-CIT-13(2)		1	0.67	120 (0.81)	61 (1.6)
Al-CIT-13(3)		1	0.33	150 (0.66)	70 (1.4)
Al-CIT-13(4)		0.67	1	46 (2.1)	76 (1.3)
Al-CIT-13(5)		0.33	1	18 (5.2)	79 (1.2)
Al-CIT-13(6)		0	1	12 (7.7)	79 (1.2)
Al-CIT-13(7)	Si/Ge = 4.1	1	1	77 (1.3)	44 (2.2)
Al-CIT-13(8)	20% Ge/T	0	1	12 (7.8)	56 (1.6)

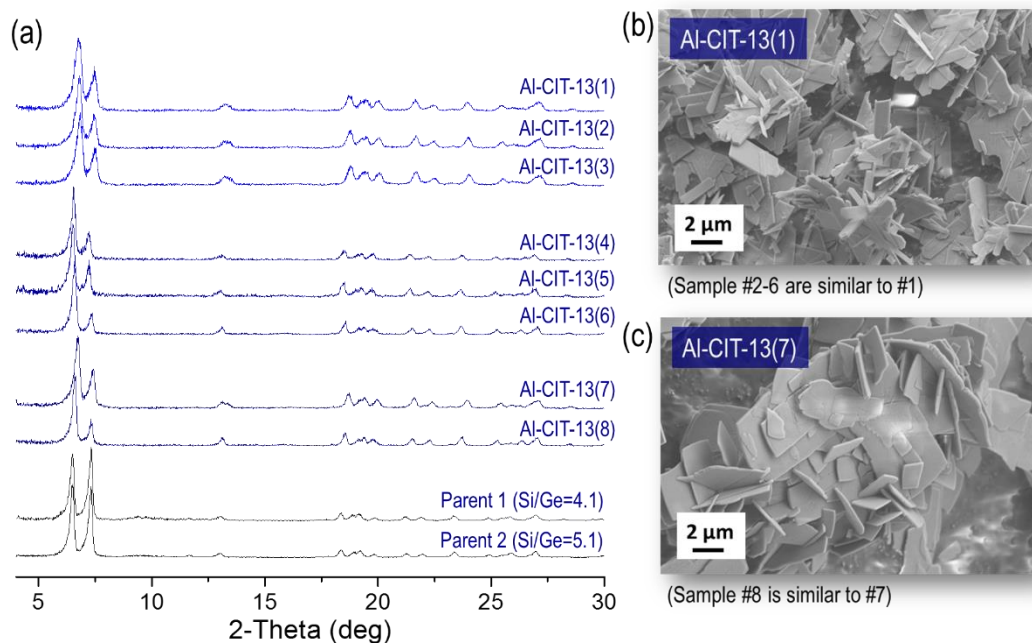


Figure 8.23. Material characterization of Al-CIT-13 samples. (a) PXRD profiles of aluminated Al-CIT-13 samples and those of the parent Ge-CIT-13s. SEM images of (b) Al-CIT-13(1) and (c) Al-CIT-13(7) samples.

No structural degradation was observed across all trials. For the sample series of Al-CIT-13(1), (2), and (3), the concentration of nitric acid were a fixed constant at $[H^+] = 1 \text{ M}$ and the concentrations of Al^{3+} were changed. The degree of alumination was almost proportional to the Al^{3+} concentration of acidic aluminum solution. The Si/Al ratios of the resultant Al-CIT-13 samples were in the range of 80–150. When the concentration of Al^{3+} was fixed, the lower the acidity was, the more Al was incorporated. The maximum Al-incorporation was achieved when pure 1 M $Al(NO_3)_3$ solution was used (Al-CIT-13(6)). It is known that the isoelectric point (pI) of silica surface is approximately 2.0 which is lower than the pH of pure 1 M $Al(NO_3)_3$ solution (2.45).²⁰⁰ The presence of aluminum in the solution phase can prevent the structure degradation by occupying the defect sites previously occupied by germanium.¹⁵⁸

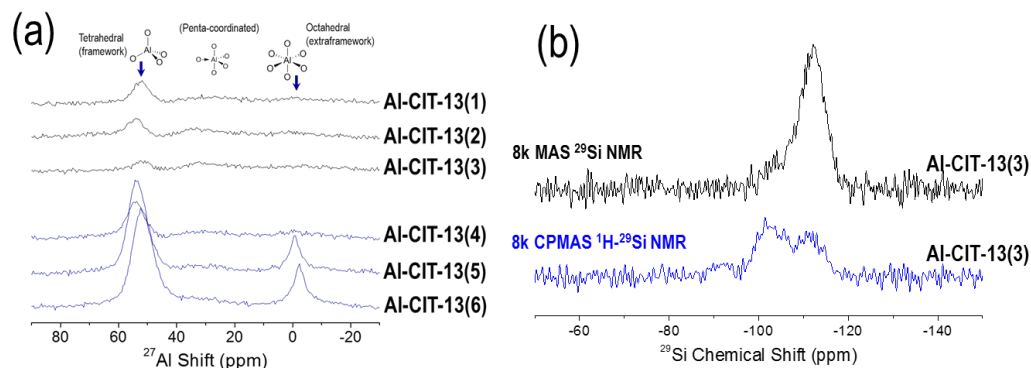


Figure 8.24. Al-site and defect characterizations of Al-CIT-13 samples. (a) 12 kHz MAS solid-state ^{27}Al NMR spectra of Al-CIT-13 samples. (b) 8 kHz MAS ^1H -decoupled solid-state ^{29}Si NMR spectrum and 8 kHz ^1H - ^{29}Si CP-MAS solid-state NMR spectrum of Al-CIT-13(3) sample.

However, a low acidity also resulted in the formation of extra-framework aluminum species as shown in the ^{27}Al NMR spectra in Figure 8.24(a). The resonances for tetrahedral and octahedral (extra-framework) aluminum species were observed at 50–55 ppm and 0 ppm, respectively. No penta-coordinated aluminum species was observed. In the two samples Al-CIT-13(5) and (6) which had the highest extents of Al-incorporation, significant amounts of octahedral aluminum species were detected. These two samples are ones treated with solutions of low acidity ($[\text{H}^+] < 0.33 \text{ M}$). Shamzhy et al. conducted a similar study using only 1 M $\text{Al}(\text{NO}_3)_3$ solution to aluminate germanosilicate ITH-type molecular sieves; octahedral aluminum species were observed in all of their samples regardless of the elemental composition of the parent germanosilicate and/or the treatment temperature.¹⁶⁰ However, no extra-framework aluminum was detected in the other Al-CIT-13 samples. Therefore, it can be concluded that low acidity results in octahedral aluminum species. It is desirable to control the pH of solution below 0.17 ($[\text{H}^+] = 0.67 \text{ M}$) to prevent the formation of extra-framework aluminum species within the channel systems.

Also, the ^{29}Si NMR spectrum and ^1H - ^{29}Si CP-MAS spectrum displayed in Figure 8.24(b) revealed that a majority of silicon atoms in Al-CIT-13(3) are not associated with silanol defects, showing mostly Q^4 -Si resonances. No deconvolution was attempted in this work. A small amount of Q^3 -silanols did exist in the samples. The observed extents of degermanation were almost the same across all samples. It can also be concluded that most of germanium atoms had presented within Ge-CIT-13 frameworks were replaced with framework silicon and aluminum atoms.

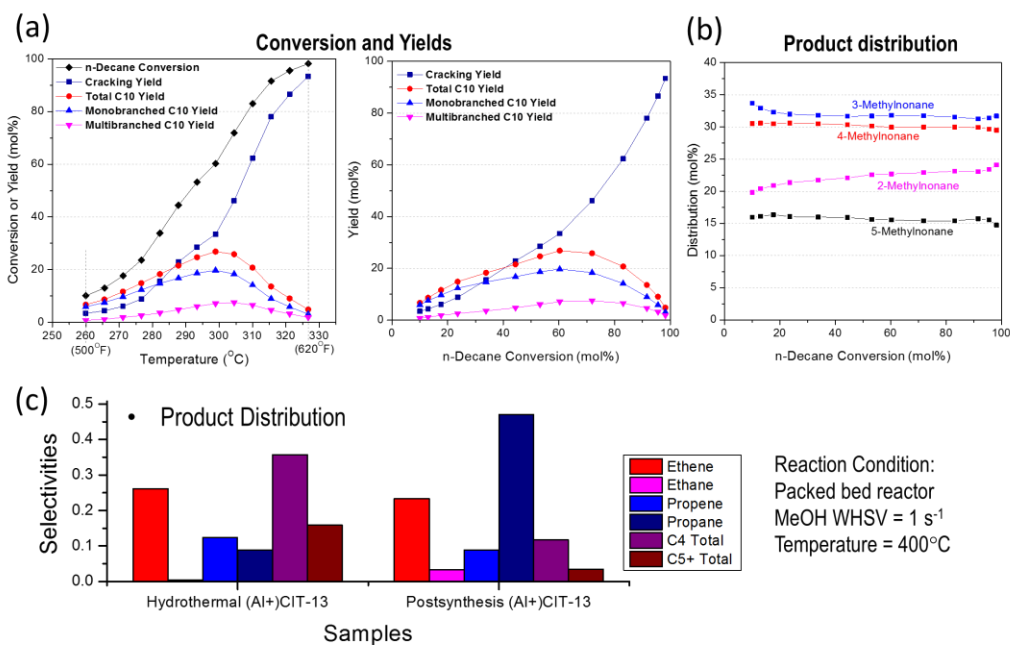


Figure 8.25. Catalysis of Al-CIT-13. (a) Conversions and yields of the decane hydrocracking/hydroisomerization reaction over Pt-CIT-13 catalyst by reaction temperatures. (b) Product distribution chart of the decane hydroisomerization of Pt-CIT-13. (c) Product distribution chart of the methanol to hydrocarbon reaction over Al-CIT-13 samples.

The hydrocracking/hydroisomerization reaction of decane over Pt-loaded Al-CIT-13 was performed by Dr. C. Y. Chen and collaborators from Chevron. (Figure 8.25(a) and (b)) *n*-decane in hydrogen flow (170 mL min^{-1}) was fed with a flow rate of $1 \text{ mL-liquid h}^{-1}$. The reaction pressure was 1.2 kpsi. Extra-large-pore CIT-13 required a higher temperature (ca. $300 \text{ }^\circ\text{C}$ for maximum isomerization; ca. $330 \text{ }^\circ\text{C}$ for 100% decane conversion) to isomerize *n*-decane into monomethyl nonanes than medium-pore Pt-ZSM-5 (ca. $185 \text{ }^\circ\text{C}$ for maximum isomerization; ca. $195 \text{ }^\circ\text{C}$ for 100% decane conversion),²⁰¹ but much lower than mesoporous Pt-MCM-41 which required higher than $400 \text{ }^\circ\text{C}$ for 100% decane conversion.²⁰² The decane isomerization product selectivity order from Pt-CIT-13 shown in Figure 8.25(b) was 3- > 4- > 2- > 5-methylnonane which was apparently different to that of Pt-ZSM-5 2- > 3- > 4- > 5-methylnonane.²⁰¹

The methanol conversion was also conducted to confirm the porosity and solid-acidity of Al-CIT-13, and the result was compared to that of Al/Ge-CIT-13 directly synthesized from one of ternary-composition gels shown in Chapter VI. The product selectivity distributions of two Al-containing CIT-13 are shown in Figure 8.25(c). Here, the resultant product distributions were not analyzed in detail since the 14-ring channel of CIT-13 is too wide to expect any shape selectivity. But this result sufficiently proves the surface acidity of Al-CIT-13 prepared on the basis of postsynthetic alumination.

8.3.4.2. Postsynthetic Degermanation and Alumination of Ge-CIT-5

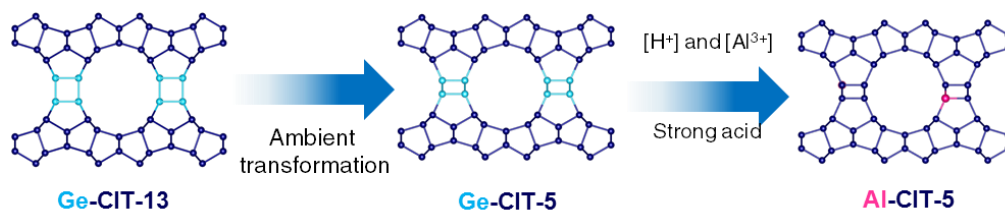


Figure 8.26. Schematic illustration of the CIT-13-to-5 transformation followed by the postsynthetic degermanation/alumination of Ge-CIT-13.

Similarly to the case of postsynthetic alumination of Ge-CIT-13 shown in the previous section, Ge-CIT-5 samples derived from Ge-CIT-13 were also subjected to the analogous postsynthetic alumination procedure. Here, Ge-CIT-5 having a Si/Ge ratio of 4.31 was treated with a series of mixtures of aluminum nitrate and nitric acid having varied concentrations. The treatment was performed at 185 °C for 24 hours. The concentrations of H^+ and Al^{3+} and the elemental compositions of the resultant materials were shown in Table 8.2. Here, the CFI-type molecular sieves prepared from this postsynthetic alumination of Ge-CIT-5 were denoted Al-CIT-5(#) where # is the sample number shown in Table 8.2. The postsynthesis resultant material treated without aluminum (acid only) was denoted Si-CIT-5.

Table 8.2. Summary of postsynthetic alumination of Ge-CIT-5

Sample	Parent Ge-CIT-5	Solution			Elemental Composition of Product	
		[H^+] (M)	[Al^{3+}] (M)	pH	Si/Al ratio (Al/T %)	Si/Ge ratio (Ge/T %)
Al-CIT-5(1)	Si/Ge = 4.31 16% Ge/T	0	1	2.45	13 (7.0)	56 (1.6)
Al-CIT-5(2)		0.1	0.5	0.30	39 (2.5)	47 (2.0)
Al-CIT-5(3)		0.5	0.1	0.05	170 (0.7)	38 (2.6)
Si-CIT-5		1	0	0	-	33 (3.0)

The overall process from Ge-CIT-13 to Al-CIT-5 is illustrated in Figure 8.27(a) with PXRD patterns of stages involved in the transformation. Similarly to the case of the postsynthetic alumination of Ge-CIT-5, the higher the concentration of aluminum of treating solution was, the higher aluminum content the resultant Al-CIT-5 had. It is noteworthy that the Si/Al ratio of Al-CIT-5(2) is much lower than that of aluminosilicate CIT-5 from a direct hydrothermal synthesis.¹³²

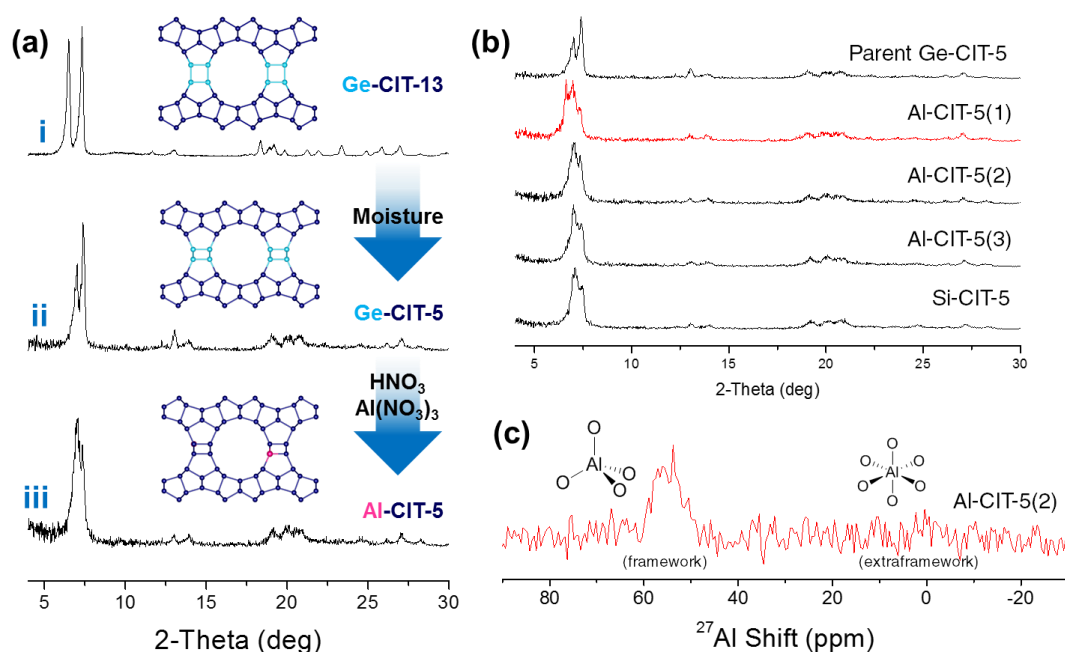


Figure 8.27. Material characterization of Al-CIT-5 samples. (a) a series of PXRD patterns showing the entire transformation sequence: Ge-CIT-13 \rightarrow Ge-CIT-5 \rightarrow Al-CIT-5. (b) PXRD patterns of resultant Al-CIT-5 samples and Si-CIT-5. (c) 12 kHz MAS solid-state ^{27}Al NMR spectrum of an Al-CIT-13 sample.

A disordered material (Al-CIT-5(1)) was produced when only aluminum nitrate was used. In the PXRD profile of Al-CIT-5(1) (the profile highlighted with red color in Figure 8.27(b)), an extra peak appeared at a diffraction angle (6.62°) lower than the typical (002) diffraction angle ($6.9\text{--}7.0^\circ$) of CIT-5. Although it cannot be clearly explained at this point due to a lack of further experimental evidence, some type of intercalation of T-atom might have happened at a low acidity, which resulted in an expansion of unit cell in the c -direction. The other Al-CIT-5 and Si-CIT-5 samples showed almost no structural degradation on the basis of PXRD patterns. Figure 8.27(c) shows the ^{27}Al NMR spectra of Al-CIT-5(2) in which

no extra-framework aluminum signal (ca. 0 ppm) is present. This result further supports the conclusion that increasing acidity of the solution phase prevents the formation of extra-framework aluminum species in postsynthetic aluminations processes.

8.4. Summary

In this chapter, various transformations and postsynthetic modifications of Ge-CIT-13 and Ge-CIT-5 were discussed. First, the acid-delamination of Ge-CIT-13 and Ge-CIT-5 was investigated in terms of delamination time. While the interlayer distances of delaminated CIT-13P kept decreasing as the acid-delamination proceeded, the delamination products from Ge-CIT-5 showed no further decrease in the interlayer distances after 3 hours of acid-treatment. The ^{29}Si solid-state NMR spectra suggested that the extent of acid-delamination of Ge-CIT-5 was poor.

Secondly, CIT-14 was prepared via two protocols. One was the ethoxysilylational pillaring and the other was the inverse sigma transformation. The ethoxysilylational pillaring was not seriously affected by the extent of delamination of CIT-13P. The inverse sigma transformation of CIT-13 into CIT-14 was only possible for low-Si/Ge (< 3.71) CIT-13 samples synthesized from hydroxide-mediated recipes. The microporosity of CIT-14 from the inverse sigma transformation was better than that of CIT-14 from the ethoxysilylational pillaring.

Thirdly, the condensation of CIT-13P/5P layered materials forming CIT-15 was investigated. Unlike the case of CIT-14, the extent of delamination was important in the preparation of CIT-15 because the condensation must be completely achieved directly between the neighboring CIT-13P/5P layers. It was impossible to obtain CIT-15 from the condensation of CIT-5P presumably due to the presence of delamination remnant species.

Instead, the base-delamination was performed for CIT-5P and a structure very close to CIT-15 was obtained.

Lastly, postsynthetic alumination of Ge-CIT-13 and Ge-CIT-5 yielding Al-CIT-13 and Al-CIT-5 was examined in terms of the acidity of the treating solutions. Increasing acidity resulted in lower degrees of aluminum incorporation and formation of octahedral aluminum species.

Chapter 9

Summary and Future Work for Part II

9.1. Overall Summary and Conclusion

In 2016, the Davis group reported an extra-large-pore germanosilicate CIT-13 which has a novel framework closely related to two other extra-large-pore frameworks UTL and CIT-5. From the library of methylbenzylimidazolium-derivative OSDAs, it was experimentally confirmed that several organic cations are able to crystallize CIT-13 in fluoride media. The use of hydrogen fluoride could be avoided by replacing it with an equimolar quantity of ammonium fluoride. It was also possible to synthesize CIT-13 without fluoride. CIT-13 synthesized in hydroxide media showed a unique property in terms of structural transformation. The isomorphous substitution technique was also confirmed as experimentally feasible. The structure and possible disorders in the CIT-13 framework were investigated on the basis of the synchrotron powder X-ray diffraction. The presence of disorders in the *d4r* arrangement was suggested. CIT-13 was registered as the type material of the 236th framework type *CTH in the International Zeolite Association Structure Database. Its microporosity was studied based on argon adsorption isotherms and compared to that of UTL.

The transformation of Ge-CIT-13 into Ge-CIT-5 was discovered. This transformation proceeded spontaneously at room temperature with the presence of moisture from ambient air. The kinetics of the transformation were investigated on the basis of the nature of the parent Ge-CIT-13. High Ge content and use of hydroxide as the mineralizing agent significantly increased the rate of transformation. The role of moisture was also studied. Under environments where water cannot be easily sorbed within the pore system of

CIT-13, such as high temperature, dry inert gas, presence of hydrophobic molecules, the rate of transformation was significantly decreased. Exposure to water-saturated vapor phase greatly accelerated the transformation.

The microporosity of Ge-CIT-5 well matched that from the pure silica CIT-5 synthesized from the sparteine-derivative OSDA. The moisture-derived structural evolutions of other *d4r*-containing germanosilicates, UTL, IWW, and ITH were also studied. UTL lost its structure within one day. IWW and ITH retained their structures for 256 days with minor structural degradations. It was suggested that the two hierarchical arrangements—the arrangement of *d4r* units within the interlayer region and the arrangement of germanium T-atoms within the *d4r* units—were the key factors of transformability. Up to now, Ge-CIT-13 is the first and only germanosilicate which can undergo this type of transformation.

Possible topotactic transformation pathways of Ge-CIT-13 and Ge-CIT-5 were investigated. These two germanosilicates showed very different delamination behaviors. Ge-CIT-13 was effectively delaminated into layered silicate CIT-13P by weak acid solution and transformed into CIT-14 and CIT-15. The extent of delamination was important for the achievement of CIT-15. It was also discovered that Ge-CIT-13 synthesized in hydroxide media can be transformed directly into CIT-14 via the inverse sigma transformation pathway. The resultant CIT-14 from this pathway showed excellent microporosity without any sign of mesoporosity. On the other hand, Ge-CIT-5 was not easily delaminated possibly due to the structural difference between bridging *d4r* units and double-zigzag-chain units. No CIT-15 structure could be successfully obtained via the acid-delamination of Ge-CIT-5. Instead, Ge-CIT-5 was effectively delaminated using ammonium hydroxide. Lastly, the postsynthetic alumination of Ge-CIT-13 and Ge-CIT-5 were performed, and high-silica aluminosilicate versions of Al-CIT-13 and Al-CIT-5 were obtained with no octahedral aluminum species.

This work demonstrates the versatile transformability of CIT-13. Many important discoveries are involved in regards of topotactic transformation of germanosilicates such as

the transformation of CIT-13 to CIT-5. Here, the most extensive network of inter-zeolitic transformations and modifications to date was established in this work. I believe this work may not only exhibit a new possibility of germanosilicate modification, but also provide a sound guideline for researchers who seek further utilities for their germanosilicates.

9.2. Proposed Future Work

Initially, the fluoride-mediated hydrothermal synthesis was the only synthetic route to obtain germanosilicate CIT-13. Now that I discovered a new pathway for CIT-13 synthesis in hydroxide media, it is important to optimize the synthesis recipe and to correlate the synthetic parameters to the properties of resultant materials. I believe that CIT-13 from the hydroxide media has a germanium T-atom arrangement within *d4r* units fundamentally different to that of CIT-13 from the fluoride media, given that fluoride anions can intervene in the formation of *d4r* units.¹¹⁶ In terms of the transformation of CIT-13 to CIT-5, in this work it was experimentally shown that CIT-13/OH and CIT-13/F having the same EDS Si/Ge ratio have immensely different rates of transformation. Furthermore, CIT-13/OH was successfully transformed directly into CIT-14 via the inverse sigma transformation whereas CIT-13/F was not.

Based on these observations, I suggest a future study on the arrangement of germanium atoms within *d4r* units. There are several methodologies to investigate this. One is the use of fluoride anion as a probe for the *d4r* units. It is reported that fluoride anions can be postsynthetically inserted into empty *d4r* units by treating as-made germanosilicates with ammonium fluoride at elevated temperatures.²⁰³⁻²⁰⁴ The inserted fluoride anions can be characterized with ¹⁹F solid-state NMR spectroscopy.^{176, 203} Also, there are other germanosilicates which can be prepared in both fluoride and hydroxide media such as ITH-

type germanosilicate ITQ-13.^{149, 175, 205} I believe that making comparisons between these germanosilicates to CIT-13 would provide new insights.

Another important topic which should be considered is to solve the structure of CIT-14 using a Rietveld refinement. The ADOR-type transformation of CIT-13 into CIT-14 was already suggested by another research group,¹⁶⁵ but no refinement was reported. I believe that CIT-14 prepared from the inverse sigma transformation route can be a good candidate for the following synchrotron XRD study.

REFERENCES

- (1)Plotkin, J. S. The Propylene Gap: How Can It Be Filled?, American Chemical Society. 2015.
- (2)Amghizar, I.; Vandewalle, L. A.; Van Geem, K. M.; Marin, G. B., New Trends in Olefin Production, *Engineering* **2017**, *3*, 171-178.
- (3)Plotkin, J. S. Beyond the Ethylene Steam Cracker, American Chemical Society. 2016.
- (4)Zimmermann, H.; Walzl, R., Ethylene. In *Ullmann's encyclopedia of industrial chemistry*, Wiley-VCH Verlag GmbH & Co. KGaA, Weinheim: 2009.
- (5)Bricker, J. In *History and State of the Art of Ethane/Propane Dehydrogenation Catalysis.*, The Changing Landscape of Hydrocarbon Feedstocks for Chemical Production: Implications for Catalysis, Proceedings of a Workshop, by Nat. Acad. Sci. Eng. and Med., Washington, DC, Washington, DC, 2016.
- (6)Annual Energy Review 2006, U.S. Energy Information Administration, Department of Energy. 2007.
- (7)Chang, C. D.; Silvestri, A. J., The conversion of methanol and other O-compounds to hydrocarbons over zeolite catalysts, *J. Catal.* **1977**, *47*, 249-259.
- (8)Olsbye, U.; Svelle, S.; Bjørgen, M.; Beato, P.; Janssens, T. V. W.; Joensen, F.; Bordiga, S.; Lillerud, K. P., Conversion of Methanol to Hydrocarbons: How Zeolite Cavity and Pore Size Controls Product Selectivity, *Angew. Chem. Int. Ed.* **2012**, *51*, 5810-5831.
- (9)Stöcker, M., Methanol-to-hydrocarbons: catalytic materials and their behavior, *Micropor. Mesopor. Mater.* **1999**, *29*, 3-48.
- (10)Maiden, C. J., The New Zealand Gas-to-Gasoline Project, *Stud. Surf. Sci. Catal.* **1988**, *36*, 1-16.
- (11)Lok, B. M.; Messina, C. A.; Patton, R. L.; Gajek, R. T.; Cannan, T. R.; Flanigen, E. M., Silicoaluminophosphate molecular sieves: another new class of microporous crystalline inorganic solids, *J. Am. Chem. Soc.* **1984**, *106*, 6092-6093.

(12)Vora, B. V.; Marker, T. L.; Barger, P. T.; Nilsen, H. R.; Kvisle, S.; Fuglerud, T., Economic route for natural gas conversion to ethylene and propylene, *Stud. Surf. Sci. Catal.* **1997**, *107*, 87-98.

(13)Tian, P.; Wei, Y.; Ye, M.; Liu, Z., Methanol to Olefins (MTO): From Fundamentals to Commercialization, *ACS Catal.* **2015**, *5*, 1922-1938.

(14)Szostak, R., *Molecular Sieves, Principles of Synthesis and Identification*. Van Nostrand Reinhold: New York, New York, the United States, 1989.

(15)Loewenstein, W., The distribution of aluminum in the tetrahedra of silicates and aluminates, *Am. Mineral.* **1954**, *39*, 92.

(16)International Zeolite Association Structure Database (<http://america.iza-structure.org/IZA-SC>).

(17)Miyamoto, M.; Nakatani, T.; Fujioka, Y.; Yogo, K., Verified synthesis of pure silica CHA-type zeolite in fluoride media, *Micropor. Mesopor. Mater.* **2015**, *206*, 67-74.

(18)Zones, S. I. Zeolite SSZ-13 and its method of preparation, US Patent 4,544,538. 1985.

(19)Marchese, L.; Frache, A.; Gianotti, E.; Martra, G.; Causà, M.; Coluccia, S., ALPO-34 and SAPO-34 synthesized by using morpholine as templating agent. FTIR and FT-Raman studies of the host-guest and guest-guest interactions within the zeolitic framework, *Micropor. Mesopor. Mater.* **1999**, *30*, 145-153.

(20)Ashtekar, S.; Prakash, A. M.; Chakrabarty, D. K.; Chilukuri, S. V. V., Small-pore aluminium phosphate molecular sieves with chabazite structure. Incorporation of magnesium in structures -34 and -44, *J. Chem. Soc. Faraday Trans.* **1996**, *92*, 2481-2486.

(21)Ashtekar, S.; Chilukuri, S. V. V.; Prakash, A. M.; Harendranath, C. S.; Chakrabarty, D. K., Small Pore Aluminum Phosphate Molecular Sieves with Chabazite Structure: Incorporation of Cobalt in the Structures -34 and -44, *J. Phys. Chem.* **1995**, *99*, 6937-6943.

(22)Wilson, S. T.; Lok, B. M.; Messina, C. A.; Cannan, T. R.; Flanigen, E. M., Aluminophosphate molecular sieves: a new class of microporous crystalline inorganic solids, *J. Am. Chem. Soc.* **1982**, *104*, 1146-1147.

(23)Yarulina, I.; Chowdhury, A. D.; Meirer, F.; Weckhuysen, B. M.; Gascon, J., Recent trends and fundamental insights in the methanol-to-hydrocarbons process, *Nat. Catal.* **2018**, *1*, 398-411.

(24)Olah, G. A.; Doggweiler, H.; Felberg, J. D.; Frohlich, S.; Grdina, M. J.; Karpeles, R.; Keumi, T.; Inaba, S.-i.; Ip, W. M.; Lammertsma, K.; Salem, G.; Tabor, D., Onium Ylide chemistry. 1. Bifunctional acid-base-catalyzed conversion of heterosubstituted methanes into ethylene and derived hydrocarbons. The onium ylide mechanism of the C1 to C2 conversion, *J. Am. Chem. Soc.* **1984**, *106*, 2143-2149.

(25)Chang, C. D.; Hellring, S. D.; Pearson, J. A., On the existence and role of free radicals in methanol conversion to hydrocarbons over HZSM-5: I. Inhibition by NO, *J. Catal.* **1989**, *115*, 282-285.

(26)Dahl, I. M.; Kolboe, S., On the reaction mechanism for propene formation in the MTO reaction over SAPO-34, *Catal. Lett.* **1993**, *20*, 329-336.

(27)Dahl, I. M.; Kolboe, S., On the Reaction Mechanism for Hydrocarbon Formation from Methanol over SAPO-34: I. Isotopic Labeling Studies of the Co-Reaction of Ethene and Methanol, *J. Catal.* **1994**, *149*, 458-464.

(28)Dahl, I. M.; Kolboe, S., On the Reaction Mechanism for Hydrocarbon Formation from Methanol over SAPO-34: 2. Isotopic Labeling Studies of the Co-reaction of Propene and Methanol, *J. Catal.* **1996**, *161*, 304-309.

(29)Svelle, S.; Joensen, F.; Nerlov, J.; Olsbye, U.; Lillerud, K.-P.; Kolboe, S.; Bjørgen, M., Conversion of Methanol into Hydrocarbons over Zeolite H-ZSM-5: Ethene Formation Is Mechanistically Separated from the Formation of Higher Alkenes, *J. Am. Chem. Soc.* **2006**, *128*, 14770-14771.

(30)Sun, X.; Mueller, S.; Shi, H.; Haller, G. L.; Sanchez-Sanchez, M.; van Veen, A. C.; Lercher, J. A., On the impact of co-feeding aromatics and olefins for the methanol-to-olefins reaction on HZSM-5, *J. Catal.* **2014**, *314*, 21-31.

(31)Lesthaeghe, D.; Horré, A.; Waroquier, M.; Marin, G. B.; Van Speybroeck, V., Theoretical Insights on Methylbenzene Side-Chain Growth in ZSM-5 Zeolites for Methanol-to-Olefin Conversion, *Chem. Eur. J.* **2009**, *15*, 10803-10808.

(32)Goetze, J.; Meirer, F.; Yarulina, I.; Gascon, J.; Kapteijn, F.; Ruiz-Martínez, J.; Weckhuysen, B. M., Insights into the Activity and Deactivation of the Methanol-to-Olefins Process over Different Small-Pore Zeolites As Studied with Operando UV-vis Spectroscopy, *ACS Catal.* **2017**, *7*, 4033-4046.

(33)Li, J.; Wei, Y.; Chen, J.; Xu, S.; Tian, P.; Yang, X.; Li, B.; Wang, J.; Liu, Z., Cavity Controls the Selectivity: Insights of Confinement Effects on MTO Reaction, *ACS Catal.* **2015**, *5*, 661-665.

(34)Zhang, W.; Chen, J.; Xu, S.; Chu, Y.; Wei, Y.; Zhi, Y.; Huang, J.; Zheng, A.; Wu, X.; Meng, X.; Xiao, F.; Deng, F.; Liu, Z., Methanol to Olefins Reaction over Cavity-type Zeolite: Cavity Controls the Critical Intermediates and Product Selectivity, *ACS Catal.* **2018**, *8*, 10950-10963.

(35)Xu, S.; Zheng, A.; Wei, Y.; Chen, J.; Li, J.; Chu, Y.; Zhang, M.; Wang, Q.; Zhou, Y.; Wang, J.; Deng, F.; Liu, Z., Direct Observation of Cyclic Carbenium Ions and Their Role in the Catalytic Cycle of the Methanol-to-Olefin Reaction over Chabazite Zeolites, *Angew. Chem. Int. Ed.* **2013**, *52*, 11564-11568.

(36)Li, J.; Wei, Y.; Xu, S.; Tian, P.; Chen, J.; Liu, Z., Heptamethylbenzenium cation formation and the correlated reaction pathway during methanol-to-olefins conversion over DNL-6, *Catal. Today* **2014**, *226*, 47-51.

(37)Haw, J. F.; Song, W.; Marcus, D. M.; Nicholas, J. B., The Mechanism of Methanol to Hydrocarbon Catalysis, *Acc. Chem. Res.* **2003**, *36*, 317-326.

(38)Pinilla-Herrero, I.; Márquez-Álvarez, C.; Sastre, E., Complex relationship between SAPO framework topology, content and distribution of Si and catalytic behaviour in the MTO reaction, *Catal. Sci. Technol.* **2017**, *7*, 3892-3901.

(39)Pinilla-Herrero, I.; Olsbye, U.; Márquez-Álvarez, C.; Sastre, E., Effect of framework topology of SAPO catalysts on selectivity and deactivation profile in the methanol-to-olefins reaction, *J. Catal.* **2017**, *352*, 191-207.

(40)Ahn, N. H.; Seo, S.; Hong, S. B., Small-pore molecular sieves SAPO-57 and SAPO-59: synthesis, characterization, and catalytic properties in methanol-to-olefins conversion, *Catal. Sci. Technol.* **2016**, *6*, 2725-2734.

(41)Bhawe, Y.; Moliner-Marín, M.; Lunn, J. D.; Liu, Y.; Malek, A.; Davis, M., Effect of Cage Size on the Selective Conversion of Methanol to Light Olefins, *ACS Catal.* **2012**, *2*, 2490-2495.

(42)Castro, M.; Warrender, S. J.; Wright, P. A.; Apperley, D. C.; Belmabkhout, Y.; Pirngruber, G.; Min, H.-K.; Park, M. B.; Hong, S. B., Silicoaluminophosphate Molecular Sieves STA-7 and STA-14 and Their Structure-Dependent Catalytic Performance in the Conversion of Methanol to Olefins, *J. Phys. Chem. C* **2009**, *113*, 15731-15741.

(43)Park, J. W.; Lee, J. Y.; Kim, K. S.; Hong, S. B.; Seo, G., Effects of cage shape and size of 8-membered ring molecular sieves on their deactivation in methanol-to-olefin (MTO) reactions, *Appl. Catal. A* **2008**, *339*, 36-44.

(44)Wilson, S.; Barger, P., The characteristics of SAPO-34 which influence the conversion of methanol to light olefins, *Micropor. Mesopor. Mater.* **1999**, *29*, 117-126.

(45)Chen, J.; Wright, P. A.; Natarajan, S.; Thomas, J. M., Understanding The Brønsted Acidity of Sapo-5, Sapo-17, Sapo-18 and SAPO-34 and Their Catalytic Performance for Methanol Conversion to Hydrocarbons, *Stud. Surf. Sci. Catal.* **1994**, *84*, 1731-1738.

(46)Chen, J.; Li, J.; Wei, Y.; Yuan, C.; Li, B.; Xu, S.; Zhou, Y.; Wang, J.; Zhang, M.; Liu, Z., Spatial confinement effects of cage-type SAPO molecular sieves on product

distribution and coke formation in methanol-to-olefin reaction, *Catal. Commun.* **2014**, *46*, 36-40.

(47)Yokoi, T.; Yoshioka, M.; Imai, H.; Tatsumi, T., Diversification of RTH-Type Zeolite and Its Catalytic Application, *Angew. Chem. Int. Ed.* **2009**, *48*, 9884-9887.

(48)Schmidt, J. E.; Xie, D.; Davis, M. E., Synthesis of the RTH-type layer: the first small-pore, two dimensional layered zeolite precursor, *Chem. Sci.* **2015**, *6*, 5955-5963.

(49)Xiang, D.; Yang, S.; Liu, X.; Mai, Z.; Qian, Y., Techno-economic performance of the coal-to-olefins process with CCS, *Chem. Eng. J.* **2014**, *240*, 45-54.

(50)Smit, B.; Maesen, T. L. M., Towards a molecular understanding of shape selectivity, *Nature* **2008**, *451*, 671.

(51)Lee, J. H.; Park, M. B.; Lee, J. K.; Min, H.-K.; Song, M. K.; Hong, S. B., Synthesis and Characterization of ERI-Type UZM-12 Zeolites and Their Methanol-to-Olefin Performance, *J. Am. Chem. Soc.* **2010**, *132*, 12971-12982.

(52)Nawaz, S.; Kolboe, S.; Stöcker, M., Conversion of Methanol to Light Olefins over Sapo-17 Molecular Sieve. In *Studies in Surface Science and Catalysis*, Curry-Hyde, H. E.; Howe, R. F., Eds. Elsevier: 1994; Vol. 81, pp 393-398.

(53)Effenberger, H.; Giester, G.; Krause, W.; Bernhardt, H. J., Tschörtnerite, a copper-bearing zeolite from the Bellberg volcano, Eifel, Germany, *Am. Mineral.* **1998**.

(54)Low, J. J.; Lewis, G. J. Synthetic crystalline aluminosilicate zeolite having the tschörtnerite framework topology and uses thereof, US Patent 6,534,034 B1. 2003.

(55)McGuire, N. K.; Bateman, C. A.; Scott Blackwell, C.; Wilson, S. T.; Kirchner, R. M., Structure refinement, electron microscopy, and solid-state magic angle spinning nuclear magnetic resonance characterization of AlPO₄-52: An aluminophosphate with a large cage, *Zeolites* **1995**, *15*, 460-469.

(56)Broach, R. W.; Greenlay, N.; Jakubczak, P.; Knight, L. M.; Miller, S. R.; Mowat, J. P. S.; Stanczyk, J.; Lewis, G. J., New ABC-6 net molecular sieves ZnAPO-57 and ZnAPO-59: Framework charge density-induced transition from two- to three-dimensional porosity, *Micropor. Mesopor. Mater.* **2014**, *189*, 49-63.

(57) Sedlmaier, S. J.; Döblinger, M.; Oeckler, O.; Weber, J.; Schmedt auf der Günne, J.; Schnick, W., Unprecedented Zeolite-Like Framework Topology Constructed from Cages with 3-Rings in a Barium Oxonitridophosphate, *J. Am. Chem. Soc.* **2011**, *133*, 12069-12078.

(58) Turrina, A.; Garcia, R.; Cox, P. A.; Casci, J. L.; Wright, P. A., Retrosynthetic Co-Templating Method for the Preparation of Silicoaluminophosphate Molecular Sieves, *Chem. Mater.* **2016**, *28*, 4998-5012.

(59) Zones, S. I.; Van Nordstrand, R. A., Further studies on the conversion of Cubic P zeolite to high silica organozeolites, *Zeolites* **1988**, *8*, 409-415.

(60) Xie, D. Method for Preparing Zeolite SSZ-98, US Patent 9,663,379B2. 2016.

(61) Xie, D. Synthesis of aluminosilicate LEV framework type zeolites, US Patent 9,708,193B2. 2017.

(62) Boal, B. W.; Schmidt, J. E.; Deimund, M. A.; Deem, M. W.; Henling, L. M.; Brand, S. K.; Zones, S. I.; Davis, M. E., Facile Synthesis and Catalysis of Pure-Silica and Heteroatom LTA, *Chem. Mater.* **2015**, *27*, 7774-7779.

(63) Boal, B. W.; Deem, M. W.; Xie, D.; Kang, J. H.; Davis, M. E.; Zones, S. I., Synthesis of Germanosilicate Molecular Sieves from Mono- and Di-Quaternary Ammonium OSDAs Constructed from Benzyl Imidazolium Derivatives: Stabilization of Large Micropore Volumes Including New Molecular Sieve CIT-13, *Chem. Mater.* **2016**, *28*, 2158-2164.

(64) Deimund, M. A.; Harrison, L.; Lunn, J. D.; Liu, Y.; Malek, A.; Shayib, R.; Davis, M. E., Effect of Heteroatom Concentration in SSZ-13 on the Methanol-to-Olefins Reaction, *ACS Catal.* **2016**, *6*, 542-550.

(65) Wilson, S. T.; Broach, R. W.; Blackwell, C. S.; Bateman, C. A.; McGuire, N. K.; Kirchner, R. M., Synthesis, characterization and structure of SAPO-56, a member of the ABC double-six-ring family of materials with stacking sequence AABBCB, *Micropor. Mesopor. Mater.* **1999**, *28*, 125-137.

(66) Corma, A.; Moliner, M.; Martínez, R. Synthesis of sa-po-18 and the catalytic applications thereof, US Patent Application 20170259253A1. 2017.

(67)Chen, J.; Thomas, J. M., MAPO-18 (M · Mg, Zn, Co): a new family of catalysts for the conversion of methanol to light olefins, *J. Chem. Soc. Chem. Commun.* **1994**, 603-604.

(68)Su, X.; Tian, P.; Li, J.; Zhang, Y.; Meng, S.; He, Y.; Fan, D.; Liu, Z., Synthesis and characterization of DNL-6, a new silicoaluminophosphate molecular sieve with the RHO framework, *Micropor. Mesopor. Mater.* **2011**, *144*, 113-119.

(69)Dusselier, M.; Deimund, M. A.; Schmidt, J. E.; Davis, M. E., Methanol-to-Olefins Catalysis with Hydrothermally Treated Zeolite SSZ-39, *ACS Catal.* **2015**, *5*, 6078-6085.

(70)Chatelain, T.; Patarin, J.; Fousson, E.; Soulard, M.; Guth, J. L.; Schulz, P., Synthesis and characterization of high-silica zeolite RHO prepared in the presence of 18-crown-6 ether as organic template, *Micropor. Mater.* **1995**, *4*, 231-238.

(71)Kim, J.; Cho, S. J.; Kim, D. H., Facile Synthesis of KFI-type Zeolite and Its Application to Selective Catalytic Reduction of NO_x with NH₃, *ACS Catal.* **2017**, *7*, 6070-6081.

(72)Archer, R. H.; Zones, S. I.; Davis, M. E., Imidazolium structure directing agents in zeolite synthesis: Exploring guest/host relationships in the synthesis of SSZ-70, *Micropor. Mesopor. Mater.* **2010**, *130*, 255-265.

(73)Xie, D.; McCusker, L. B.; Baerlocher, C.; Zones, S. I.; Wan, W.; Zou, X., SSZ-52, a Zeolite with an 18-Layer Aluminosilicate Framework Structure Related to That of the DeNO_x Catalyst Cu-SSZ-13, *J. Am. Chem. Soc.* **2013**, *135*, 10519-10524.

(74) Xie, D. Synthesis of molecular sieve SSZ-105, US Patent 9,663,377. 2017.

(75)Zones, S. I.; Xie, D.; Chen, C.-Y.; Liang, A. J.-B. Method for making molecular sieve SSZ-99, US Patent 9,193,600 B1. 2015.

(76)Davis, T. M. Molecular sieve SSZ-104, its synthesis and use, US Patent 9,725,328 B1. 2017.

(77)Zones, S. I.; Xie, D.; Saxton, R. J. Method for making molecular sieve SSZ-27, US Patent 9,586,830 B2. 2017.

(78)Zones, S. I.; Holtermann, D. L.; Innes, R. A. Zeolite SSZ-28, US Patent 5,200,377 A. 1993.

(79)Lee, G. S.; Zones, S. I., Polymethylated [4.1.1] Octanes Leading to Zeolite SSZ-50, *J. Solid State Chem.* **2002**, *167*, 289-298.

(80)Bereciartua, P. J.; Cantín, Á.; Corma, A.; Jordá, J. L.; Palomino, M.; Rey, F.; Valencia, S.; Corcoran, E. W.; Kortunov, P.; Ravikovitch, P. I.; Burton, A.; Yoon, C.; Wang, Y.; Paur, C.; Guzman, J.; Bishop, A. R.; Casty, G. L., Control of zeolite framework flexibility and pore topology for separation of ethane and ethylene, *Science* **2017**, *358*, 1068.

(81)Nishiyama, N.; Kawaguchi, M.; Hirota, Y.; Van Vu, D.; Egashira, Y.; Ueyama, K., Size control of SAPO-34 crystals and their catalyst lifetime in the methanol-to-olefin reaction, *Appl. Catal. A* **2009**, *362*, 193-199.

(82)Bakhtiar, S. u. H.; Ali, S.; Wang, X.; Yuan, F.; Li, Z.; Zhu, Y., Synthesis of sub-micrometric SAPO-34 by a morpholine assisted two-step hydrothermal route and its excellent MTO catalytic performance, *Dalton. Trans.* **2019**, *48*, 2606-2616.

(83)Yang, G.; Wei, Y.; Xu, S.; Chen, J.; Li, J.; Liu, Z.; Yu, J.; Xu, R., Nanosize-Enhanced Lifetime of SAPO-34 Catalysts in Methanol-to-Olefin Reactions, *J. Phys. Chem. C* **2013**, *117*, 8214-8222.

(84)Chen, J. Q.; Bozzano, A.; Glover, B.; Fuglerud, T.; Kvisle, S., Recent advancements in ethylene and propylene production using the UOP/Hydro MTO process, *Catal. Today* **2005**, *106*, 103-107.

(85)Borodina, E.; Meirer, F.; Lezcano-González, I.; Mokhtar, M.; Asiri, A. M.; Al-Thabaiti, S. A.; Basahel, S. N.; Ruiz-Martinez, J.; Weckhuysen, B. M., Influence of the Reaction Temperature on the Nature of the Active and Deactivating Species during Methanol to Olefins Conversion over H-SSZ-13, *ACS Catal.* **2015**, *5*, 992-1003.

(86)Wang, C.-M.; Wang, Y.-D.; Du, Y.-J.; Yang, G.; Xie, Z.-K., Similarities and differences between aromatic-based and olefin-based cycles in H-SAPO-34 and H-SSZ-13

for methanol-to-olefins conversion: insights from energetic span model, *Catal. Sci. Technol.* **2015**, *5*, 4354-4364.

(87)Deimund, M. A.; Schmidt, J. E.; Davis, M. E., Effect of Pore and Cage Size on the Formation of Aromatic Intermediates During the Methanol-to-Olefins Reaction, *Top. Catal.* **2015**, *58*, 416-423.

(88)Chen, J.; Wright, P. A.; Thomas, J. M.; Natarajan, S.; Marchese, L.; Bradley, S. M.; Sankar, G.; Catlow, C. R. A.; Gai-Boyes, P. L., SAPO-18 Catalysts and Their Brønsted Acid Sites, *J. Phys. Chem.* **1994**, *98*, 10216-10224.

(89)Wendelbo, R.; Akporiaye, D.; Andersen, A.; Dahl, I. M.; Mostad, H. B., Synthesis, characterization and catalytic testing of SAPO-18, MgAPO-18, and ZnAPO-18 in the MTO reaction, *Appl. Catal. A* **1996**, *142*, L197-L207.

(90)Chen, J.; Li, J.; Yuan, C.; Xu, S.; Wei, Y.; Wang, Q.; Zhou, Y.; Wang, J.; Zhang, M.; He, Y.; Xu, S.; Liu, Z., Elucidating the olefin formation mechanism in the methanol to olefin reaction over AlPO-18 and SAPO-18, *Catal. Sci. Technol.* **2014**, *4*, 3268-3277.

(91)Dusselier, M.; Davis, M. E., Small-Pore Zeolites: Synthesis and Catalysis, *Chem. Rev.* **2018**, *118*, 5265-5329.

(92)Dusselier, M.; Kang, J. H.; Xie, D.; Davis, M. E., CIT-9: A Fault-Free Gmelinite Zeolite, *Angew. Chem. Int. Ed.* **2017**, *56*, 13475-13478.

(93)Djeugoue, M.-A.; Prakash, A. M.; Kevan, L., Catalytic Study of Methanol-to-Olefins Conversion in Four Small-Pore Silicoaluminophosphate Molecular Sieves: Influence of the Structural Type, Nickel Incorporation, Nickel Location, and Nickel Concentration, *J. Phys. Chem. B* **2000**, *104*, 6452-6461.

(94)Hereijgers, B. P. C.; Bleken, F.; Nilsen, M. H.; Svelle, S.; Lillerud, K.-P.; Bjørgen, M.; Weckhuysen, B. M.; Olsbye, U., Product shape selectivity dominates the Methanol-to-Olefins (MTO) reaction over H-SAPO-34 catalysts, *J. Catal.* **2009**, *264*, 77-87.

(95)Zhou, F.; Tian, P.; Liu, Z.; Liu, G.; Chang, F.; Li, J., Synthesis of ZSM-34 and Its Catalytic Properties in Methanol-to-Olefins Reaction, *Chinese J. Catal.* **2007**, *28*, 817-822.

(96)Dubois, D. R.; Obrzut, D. L.; Liu, J.; Thundimadathil, J.; Adekkanattu, P. M.; Guin, J. A.; Punnoose, A.; Seehra, M. S., Conversion of methanol to olefins over cobalt-, manganese- and nickel-incorporated SAPO-34 molecular sieves, *Fuel Process. Technol.* **2003**, *83*, 203-218.

(97)Martín, N.; Li, Z.; Martínez-Triguero, J.; Yu, J.; Moliner, M.; Corma, A., Nanocrystalline SSZ-39 zeolite as an efficient catalyst for the methanol-to-olefin (MTO) process, *Chem. Commun.* **2016**, *52*, 6072-6075.

(98)Di Iorio, J. R.; Gounder, R., Controlling the Isolation and Pairing of Aluminum in Chabazite Zeolites Using Mixtures of Organic and Inorganic Structure-Directing Agents, *Chem. Mater.* **2016**, *28*, 2236-2247.

(99)Li, C.; Paris, C.; Martínez-Triguero, J.; Boronat, M.; Moliner, M.; Corma, A., Synthesis of reaction- adapted zeolites as methanol-to-olefins catalysts with mimics of reaction intermediates as organic structure- directing agents, *Nat. Catal.* **2018**, *1*, 547-554.

(100)Yarulina, I.; Goetze, J.; Gücüyener, C.; van Thiel, L.; Dikhtiarenko, A.; Ruiz-Martinez, J.; Weckhuysen, B. M.; Gascon, J.; Kapteijn, F., Methanol-to-olefins process over zeolite catalysts with DDR topology: effect of composition and structural defects on catalytic performance, *Catal. Sci. Technol.* **2016**, *6*, 2663-2678.

(101) Field, L. A. Two-step reforming process, US Patent 4,443,326. 1984.

(102)Pinilla-Herrero, I.; Borfecchia, E.; Holzinger, J.; Mentzel, U. V.; Joensen, F.; Lomachenko, K. A.; Bordiga, S.; Lamberti, C.; Berlier, G.; Olsbye, U.; Svelle, S.; Skibsted, J.; Beato, P., High Zn/Al ratios enhance dehydrogenation vs hydrogen transfer reactions of Zn-ZSM-5 catalytic systems in methanol conversion to aromatics, *J. Catal.* **2018**, *362*, 146-163.

(103)Müller, S.; Liu, Y.; Kirchberger, F. M.; Tonigold, M.; Sanchez-Sanchez, M.; Lercher, J. A., Hydrogen Transfer Pathways during Zeolite Catalyzed Methanol Conversion to Hydrocarbons, *J. Am. Chem. Soc.* **2016**, *138*, 15994-16003.

(104)Martínez-Espín, J. S.; De Wispelaere, K.; Janssens, T. V. W.; Svelle, S.; Lillerud, K. P.; Beato, P.; Van Speybroeck, V.; Olsbye, U., Hydrogen Transfer versus Methylation: On the Genesis of Aromatics Formation in the Methanol-To-Hydrocarbons Reaction over H-ZSM-5, *ACS Catal.* **2017**, *7*, 5773-5780.

(105)Li, J.; Liu, M.; Li, S.; Guo, X.; Song, C., Influence of Diffusion and Acid Properties on Methane and Propane Selectivity in Methanol-to-Olefins Reaction, *Ind. Eng. Chem. Res.* **2019**, *58*, 1896-1905.

(106)Ji, Y.; Birmingham, J.; Deimund, M. A.; Brand, S. K.; Davis, M. E., Steam-dealuminated, OSDA-free RHO and KFI-type zeolites as catalysts for the methanol-to-olefins reaction, *Micropor. Mesopor. Mater.* **2016**, *232*, 126-137.

(107)W. Noble, G.; A. Wright, P.; Kvick, Å., The templated synthesis and structure determination by synchrotron microcrystal diffraction of the novel small pore magnesium aluminophosphate STA-2†, *J. Chem. Soc. Dalton. Trans.* **1997**, 4485-4490.

(108)Castro, M.; Seymour, V. R.; Carnevale, D.; Griffin, J. M.; Ashbrook, S. E.; Wright, P. A.; Apperley, D. C.; Parker, J. E.; Thompson, S. P.; Fecant, A.; Bats, N., Molecular Modeling, Multinuclear NMR, and Diffraction Studies in the Templated Synthesis and Characterization of the Aluminophosphate Molecular Sieve STA-2, *J. Phys. Chem. C* **2010**, *114*, 12698-12710.

(109)Turrina, A.; Garcia, R.; Watts, A. E.; Greer, H. F.; Bradley, J.; Zhou, W.; Cox, P. A.; Shannon, M. D.; Mayoral, A.; Casci, J. L.; Wright, P. A., STA-20: An ABC-6 Zeotype Structure Prepared by Co-Templating and Solved via a Hypothetical Structure Database and STEM-ADF Imaging, *Chem. Mater.* **2017**, *29*, 2180-2190.

(110)Lago, R. M.; Haag, W. O.; Mikovsky, R. J.; Olson, D. H.; Hellring, S. D.; Schmitt, K. D.; Kerr, G. T., Proceedings of the 7th Annual International Zeolite Conference. Murakami, Y.; Ijima, A.; Ward, J. W., Eds. Elsevier: Amsterdam, 1986; Vol. 28, pp 677-684.

- (111) Ji, Y.; Deimund, M. A.; Bhawe, Y.; Davis, M. E., Organic-Free Synthesis of CHA-Type Zeolite Catalysts for the Methanol-to-Olefins Reaction, *ACS Catal.* **2015**, *5*, 4456-4465.
- (112) Davis, M. E., Ordered porous materials for emerging applications, *Nature* **2002**, *417*, 813-821.
- (113) Zones, S. I., Translating new materials discoveries in zeolite research to commercial manufacture, *Micropor. Mesopor. Mater.* **2011**, *144*, 1-8.
- (114) Jiang, J.; Yu, J.; Corma, A., Extra-Large-Pore Zeolites: Bridging the Gap between Micro and Mesoporous Structures, *Angew. Chem. Int. Ed.* **2010**, *49*, 3120-3145.
- (115) Li, Y.; Yu, J., New Stories of Zeolite Structures: Their Descriptions, Determinations, Predictions, and Evaluations, *Chem. Rev.* **2014**, *114*, 7268-7316.
- (116) Paillaud, J.-L.; Harbuzaru, B.; Patarin, J.; Bats, N., Extra-Large-Pore Zeolites with Two-Dimensional Channels Formed by 14 and 12 Rings, *Science* **2004**, *304*, 990.
- (117) Shvets, O. V.; Kasian, N.; Zukal, A.; Pinkas, J.; Čejka, J., The Role of Template Structure and Synergism between Inorganic and Organic Structure Directing Agents in the Synthesis of UTL Zeolite, *Chem. Mater.* **2010**, *22*, 3482-3495.
- (118) Verheyen, E.; Joos, L.; Van Havenbergh, K.; Breynaert, E.; Kasian, N.; Gobechiya, E.; Houthoofd, K.; Martineau, C.; Hinterstein, M.; Taulelle, F.; Van Speybroeck, V.; Waroquier, M.; Bals, S.; Van Tendeloo, G.; Kirschhock, C. E. A.; Martens, J. A., Design of zeolite by inverse sigma transformation, *Nat. Mater.* **2012**, *11*, 1059.
- (119) Shvets, O. V.; Zukal, A.; Kasian, N.; Žilková, N.; Čejka, J., The Role of Crystallization Parameters for the Synthesis of Germanosilicate with UTL Topology, *Chem. Eur. J.* **2008**, *14*, 10134-10140.
- (120) Maesen, T., Chapter 1 - The Zeolite Scene – An Overview, *Stud. Surf. Sci. Catal.* **2007**, *168*, 1-12.
- (121) Schmidt, J. E.; Xie, D.; Rea, T.; Davis, M. E., CIT-7, a crystalline, molecular sieve with pores bounded by 8 and 10-membered rings, *Chem. Sci.* **2015**, *6*, 1728-1734.

(122)Roth, W. J.; Nachtigall, P.; Morris, R. E.; Wheatley, P. S.; Seymour, V. R.; Ashbrook, S. E.; Chlubná, P.; Grajciar, L.; Položij, M.; Zukal, A.; Shvets, O.; Čejka, J., A family of zeolites with controlled pore size prepared using a top-down method, *Nat. Chem.* **2013**, *5*, 628.

(123)Wheatley, P. S.; Chlubná-Eliášová, P.; Greer, H.; Zhou, W.; Seymour, V. R.; Dawson, D. M.; Ashbrook, S. E.; Pinar, A. B.; McCusker, L. B.; Opanasenko, M.; Čejka, J.; Morris, R. E., Zeolites with Continuously Tuneable Porosity, *Angew. Chem. Int. Ed.* **2014**, *53*, 13210-13214.

(124)Davis, M. E.; Saldarriaga, C.; Montes, C.; Garces, J.; Crowder, C., VPI-5: The first molecular sieve with pores larger than 10 Ångstroms, *Zeolites* **1988**, *8*, 362-366.

(125)Davis, M. E.; Young, D., Further Studies on the Synthesis of VPI-5, *Stud. Surf. Sci. Catal.* **1991**, *60*, 53-62.

(126)Davis, M. E.; Saldarriaga, C.; Montes, C.; Garces, J.; Crowder, C., A molecular sieve with eighteen-membered rings, *Nature* **1988**, *331*, 698-699.

(127)Maistriau, L.; Gabelica, Z.; Derouane, E. G.; Vogt, E. T. C.; van Oene, J., Solid-state n.m.r. study of the transformation of VPI-5/MCM-9 into AIPO₄-8/SAPO-8, *Zeolites* **1991**, *11*, 583-592.

(128)Richardson, J. W.; Vogt, E. T. C., Structure determination and rietveld refinement of aluminophosphate molecular sieve AIPO₄-8, *Zeolites* **1992**, *12*, 13-19.

(129)Estermann, M.; McCusker, L. B.; Baerlocher, C.; Merrouche, A.; Kessler, H., A synthetic gallophosphate molecular sieve with a 20-tetrahedral-atom pore opening, *Nature* **1991**, *352*, 320-323.

(130)Freyhardt, C. C.; Tsapatsis, M.; Lobo, R. F.; Balkus, K. J.; Davis, M. E., A high-silica zeolite with a 14-tetrahedral-atom pore opening, *Nature* **1996**, *381*, 295-298.

(131)Wagner, P.; Yoshikawa, M.; Tsuji, K.; E. Davis, M.; Wagner, P.; Lovallo, M.; Taspatis, M., CIT-5: a high-silica zeolite with 14-ring pores, *Chem. Commun.* **1997**, 2179-2180.

(132)Yoshikawa, M.; Wagner, P.; Lovallo, M.; Tsuji, K.; Takewaki, T.; Chen, C.-Y.; Beck, L. W.; Jones, C.; Tsapatsis, M.; Zones, S. I.; Davis, M. E., Synthesis, Characterization, and Structure Solution of CIT-5, a New, High-Silica, Extra-Large-Pore Molecular Sieve, *J. Phys. Chem. B* **1998**, *102*, 7139-7147.

(133)Burton, A.; Elomari, S.; Chen, C.-Y.; Medrud, R. C.; Chan, I. Y.; Bull, L. M.; Kibby, C.; Harris, T. V.; Zones, S. I.; Vittoratos, E. S., SSZ-53 and SSZ-59: Two Novel Extra-Large Pore Zeolites, *Chem. Eur. J.* **2003**, *9*, 5737-5748.

(134)Martinez-Triguero, J.; Diaz-Cabañas, M. J.; Camblor, M. A.; Fornés, V.; Maesen, T. L. M.; Corma, A., The Catalytic Performance of 14-Membered Ring Zeolites, *J. Catal.* **1999**, *182*, 463-469.

(135)Sugi, Y.; Maekawa, H.; Mulla, S. A. R.; Ito, A.; Naitoh, C.; Nakagawa, K.; Komura, K.; Kubota, Y.; Kim, J.-H.; Seo, G., The Alkylation of Biphenyl over Fourteen-Membered Ring Zeolites. The Influence of Zeolite Structure and Alkylating Agent on the Selectivity for 4,4'-Dialkylbiphenyl, *Bull. Chem. Soc. Jpn.* **2007**, *80*, 1418-1428.

(136)Tontisirin, S.; Ernst, S., Zeolite SSZ-53: An Extra-Large-Pore Zeolite with Interesting Catalytic Properties, *Angew. Chem. Int. Ed.* **2007**, *46*, 7304-7306.

(137)Corma, A.; Díaz-Cabañas, M. J.; Rey, F.; Nicolopoulos, S.; Boulahya, K., ITQ-15: The first ultralarge pore zeolite with a bi-directional pore system formed by intersecting 14- and 12-ring channels, and its catalytic implications, *Chem. Commun.* **2004**, 1356-1357.

(138)Corma, A.; Díaz-Cabañas, M. J.; Jordá, J. L.; Martínez, C.; Moliner, M., High-throughput synthesis and catalytic properties of a molecular sieve with 18- and 10-member rings, *Nature* **2006**, *443*, 842-845.

(139)Moliner, M.; Díaz-Cabañas, M. J.; Fornés, V.; Martínez, C.; Corma, A., Synthesis methodology, stability, acidity, and catalytic behavior of the 18×10 member ring pores ITQ-33 zeolite, *J. Catal.* **2008**, *254*, 101-109.

(140)Sun, J.; Bonneau, C.; Cantín, Á.; Corma, A.; Díaz-Cabañas, M. J.; Moliner, M.; Zhang, D.; Li, M.; Zou, X., The ITQ-37 mesoporous chiral zeolite, *Nature* **2009**, *458*, 1154.

(141) Corma, A.; Díaz-Cabañas, M. J.; Jiang, J.; Afeworki, M.; Dorset, D. L.; Soled, S. L.; Strohmaier, K. G., Extra-large pore zeolite (ITQ-40) with the lowest framework density containing double four- and double three-rings, *Proc. Acad. Nat. Sci.* **2010**, *107*, 13997.

(142) Xu, H.; Jiang, J.; Yang, B.; Wu, H.; Wu, P., Effective Baeyer–Villiger oxidation of ketones over germanosilicates, *Catal. Commun.* **2014**, *55*, 83-86.

(143) Bnmner, G. O.; Meier, W. M., Framework density distribution of zeolite-type tetrahedral nets, *Nature* **1989**, *337*, 146-147.

(144) O'Keeffe, M.; Yaghi, O. M., Germanate Zeolites: Contrasting the Behavior of Germanate and Silicate Structures Built from Cubic T8O20 Units (T=Ge or Si), *Chem. Eur. J.* **1999**, *5*, 2796-2801.

(145) Morris, R. E.; Čejka, J., Exploiting chemically selective weakness in solids as a route to new porous materials, *Nat. Chem.* **2015**, *7*, 381.

(146) Corma, A.; Rey, F.; Valencia, S.; Jordá, J. L.; Rius, J., A zeolite with interconnected 8-, 10- and 12-ring pores and its unique catalytic selectivity, *Nat. Mater.* **2003**, *2*, 493-497.

(147) Corma, A.; Navarro, M. T.; Rey, F.; Rius, J.; Valencia, S., Pure Polymorph C of Zeolite Beta Synthesized by Using Framework Isomorphous Substitution as a Structure-Directing Mechanism, *Angew. Chem. Int. Ed.* **2001**, *40*, 2277-2280.

(148) Dorset, D. L.; Kennedy, G. J.; Strohmaier, K. G.; Diaz-Cabañas, M. J.; Rey, F.; Corma, A., P-Derived Organic Cations as Structure-Directing Agents: Synthesis of a High-Silica Zeolite (ITQ-27) with a Two-Dimensional 12-Ring Channel System, *J. Am. Chem. Soc.* **2006**, *128*, 8862-8867.

(149) Corma, A.; Puche, M.; Rey, F.; Sankar, G.; Teat, S. J., A Zeolite Structure (ITQ-13) with Three Sets of Medium-Pore Crossing Channels Formed by 9- and 10-Rings, *Angew. Chem. Int. Ed.* **2003**, *42*, 1156-1159.

(150)Cantín, A.; Corma, A.; Diaz-Cabanas, M. J.; Jordá, J. L.; Moliner, M., Rational Design and HT Techniques Allow the Synthesis of New IWR Zeolite Polymorphs, *J. Am. Chem. Soc.* **2006**, *128*, 4216-4217.

(151)Fu, W. H.; Yuan, Z.; Wang, Z.; Wang, Y.; Yang, W.; He, M.-Y., Direct synthesis of hydrothermally stable Ge-IWR zeolites, *Dalton. Trans.* **2017**, *46*, 6692-6699.

(152)Shamzhy, M. V.; Ochoa-Hernández, C.; Kasneryk, V. I.; Opanasenko, M. V.; Mazur, M., Direct incorporation of B, Al, and Ga into medium-pore ITH zeolite: Synthesis, acidic, and catalytic properties, *Catal. Today* **2016**, *277*, 37-47.

(153)Shamzhy, M. V.; Shvets, O. V.; Opanasenko, M. V.; Yaremov, P. S.; Sarkisyan, L. G.; Chlubná, P.; Zukal, A.; Marthala, V. R.; Hartmann, M.; Čejka, J., Synthesis of isomorphously substituted extra-large pore UTL zeolites, *J. Mater. Chem.* **2012**, *22*, 15793-15803.

(154)Xu, H.; Jiang, J.-g.; Yang, B.; Zhang, L.; He, M.; Wu, P., Post-Synthesis Treatment gives Highly Stable Siliceous Zeolites through the Isomorphous Substitution of Silicon for Germanium in Germanosilicates, *Angew. Chem. Int. Ed.* **2014**, *53*, 1355-1359.

(155)Shi, D.; Xu, L.; Chen, P.; Ma, T.; Lin, C.; Wang, X.; Xu, D.; Sun, J., Hydroxyl free radical route to the stable siliceous Ti-UTL with extra-large pores for oxidative desulfurization, *Chem. Commun.* **2019**, *55*, 1390-1393.

(156)Liu, X.; Xu, H.; Zhang, L.; Han, L.; Jiang, J.; Oleynikov, P.; Chen, L.; Wu, P., Isomorphous Incorporation of Tin Ions into Germanosilicate Framework Assisted by Local Structural Rearrangement, *ACS Catal.* **2016**, *6*, 8420-8431.

(157)Valtchev, V.; Majano, G.; Mintova, S.; Pérez-Ramírez, J., Tailored crystalline microporous materials by post-synthesis modification, *Chem. Soc. Rev.* **2013**, *42*, 263-290.

(158)Shamzhy, M. V.; Eliašová, P.; Vitvarová, D.; Opanasenko, M. V.; Firth, D. S.; Morris, R. E., Post-Synthesis Stabilization of Germanosilicate Zeolites ITH, IWW, and UTL by Substitution of Ge for Al, *Chem. Eur. J.* **2016**, *22*, 17377-17386.

(159)Gao, F.; Jaber, M.; Bozhilov, K.; Vicente, A.; Fernandez, C.; Valtchev, V., Framework Stabilization of Ge-Rich Zeolites via Postsynthesis Aluminations, *J. Am. Chem. Soc.* **2009**, *131*, 16580-16586.

(160)Shamzhy, M. V.; Opanasenko, M. V.; Ramos, F. S. d. O.; Brabec, L.; Horáček, M.; Navarro-Rojas, M.; Morris, R. E.; Pastore, H. d. O.; Čejka, J., Post-synthesis incorporation of Al into germanosilicate ITH zeolites: the influence of treatment conditions on the acidic properties and catalytic behavior in tetrahydropyranlation, *Catal. Sci. Technol.* **2015**, *5*, 2973-2984.

(161)Roth, W. J.; Shvets, O. V.; Shamzhy, M.; Chlubná, P.; Kubů, M.; Nachtigall, P.; Čejka, J., Postsynthesis Transformation of Three-Dimensional Framework into a Lamellar Zeolite with Modifiable Architecture, *J. Am. Chem. Soc.* **2011**, *133*, 6130-6133.

(162)Mazur, M.; Wheatley, P. S.; Navarro, M.; Roth, W. J.; Položij, M.; Mayoral, A.; Eliášová, P.; Nachtigall, P.; Čejka, J.; Morris, R. E., Synthesis of 'unfeasible' zeolites, *Nat. Chem.* **2015**, *8*, 58.

(163)IUPAC, *Compendium of Chemical Terminology, 2nd ed. (the "Gold Book")*. Blackwell Scientific Publication: 1997.

(164)Gao, Z.-H.; Chen, F.-J.; Xu, L.; Sun, L.; Xu, Y.; Du, H.-B., A Stable Extra-Large-Pore Zeolite with Intersecting 14- and 10-Membered-Ring Channels, *Chem. Eur. J.* **2016**, *22*, 14367-14372.

(165)Firth, D. S.; Morris, S. A.; Wheatley, P. S.; Russell, S. E.; Slawin, A. M. Z.; Dawson, D. M.; Mayoral, A.; Opanasenko, M.; Položij, M.; Čejka, J.; Nachtigall, P.; Morris, R. E., Assembly–Disassembly–Organization–Reassembly Synthesis of Zeolites Based on cfi-Type Layers, *Chem. Mater.* **2017**, *29*, 5605-5611.

(166)Schmidt, J.; Davis, M. E.; Boal, B. W.; Kang, J. H.; Xie, D. GERMANOSILICATE COMPOSITIONS AND METHODS OF PREPARING THE SAME, US Patent Application 20170252729. 2017.

(167)Liu, X.; Mao, W.; Jiang, J.; Lu, X.; Peng, M.; Xu, H.; Han, L.; Che, S.-a.; Wu, P., Topotactic Conversion of Alkali-Treated Intergrown Germanosilicate CIT-13 into

Single-Crystalline ECNU-21 Zeolite as Shape-Selective Catalyst for Ethylene Oxide Hydration, *Chem. Eur. J.* **2019**, *25*, 4520-4529.

(168)Lobo, R. F.; Tsapatsis, M.; Freyhardt, C. C.; Khodabandeh, S.; Wagner, P.; Chen, C.-Y.; Balkus, K. J.; Zones, S. I.; Davis, M. E., Characterization of the Extra-Large-Pore Zeolite UTD-1, *J. Am. Chem. Soc.* **1997**, *119*, 8474-8484.

(169)Davis, M. E.; Lobo, R. F., Zeolite and molecular sieve synthesis, *Chem. Mater.* **1992**, *4*, 756-768.

(170)Kang, J. H.; Xie, D.; Zones, S. I.; Smeets, S.; McCusker, L. B.; Davis, M. E., Synthesis and Characterization of CIT-13, a Germanosilicate Molecular Sieve with Extra-Large Pore Openings, *Chem. Mater.* **2016**, *28*, 6250-6259.

(171) van de Water, L. G. A.; van der Waal, J. C.; Jansen, J. C.; Cadoni, M.; Marchese, L.; Maschmeyer, T., Ge-ZSM-5: the Simultaneous Incorporation of Ge and Al into ZSM-5 Using a Parallel Synthesis Approach, *J. Phys. Chem. B* **2003**, *107*, 10423-10430.

(172)Smeets, S.; McCusker, L. B.; Baerlocher, C.; Elomari, S.; Xie, D.; Zones, S. I., Locating Organic Guests in Inorganic Host Materials from X-ray Powder Diffraction Data, *J. Am. Chem. Soc.* **2016**, *138*, 7099-7106.

(173)Saito, A.; Foley, H. C., Curvature and parametric sensitivity in models for adsorption in micropores, *AIChE J.* **1991**, *37*, 429-436.

(174)Shvets, O. V.; Shamzhy, M. V.; Yaremov, P. S.; Musilová, Z.; Procházková, D.; Čejka, J., Isomorphous Introduction of Boron in Germanosilicate Zeolites with UTL Topology, *Chem. Mater.* **2011**, *23*, 2573-2585.

(175)Vidal-Moya, J. A.; Blasco, T.; Rey, F.; Corma, A.; Puche, M., Distribution of Fluorine and Germanium in a New Zeolite Structure ITQ-13 Studied by ¹⁹F Nuclear Magnetic Resonance, *Chem. Mater.* **2003**, *15*, 3961-3963.

(176)Kasian, N.; Tuel, A.; Verheyen, E.; Kirschhock, C. E. A.; Taulelle, F.; Martens, J. A., NMR Evidence for Specific Germanium Siting in IM-12 Zeolite, *Chem. Mater.* **2014**, *26*, 5556-5565.

(177)Rojas, A.; Arteaga, O.; Kahr, B.; Cambor, M. A., Synthesis, Structure, and Optical Activity of HPM-1, a Pure Silica Chiral Zeolite, *J. Am. Chem. Soc.* **2013**, *135*, 11975-11984.

(178)Kasian, N.; Vanbutsele, G.; Houthoofd, K.; Koranyi, T. I.; Martens, J. A.; Kirschhock, C. E. A., Catalytic activity and extra-large pores of germanosilicate UTL zeolite demonstrated with decane test reaction, *Catal. Sci. Technol.* **2011**, *1*, 246-254.

(179)Ritter, S. K., Where has all the sparteine gone?, *Chemical Engineering News* **2017**, *95*, 18.

(180)Gao, F.; Jaber, M.; Bozhilov, K.; Vicente, A.; Fernandez, C.; Valtchev, V., Framework Stabilization of Ge-Rich Zeolites via Postsynthesis Alumination, *J. Am. Chem. Soc.* **2009**, *131*, 16580-16586.

(181)Eliášová, P.; Opanasenko, M.; Wheatley, P. S.; Shamzhy, M.; Mazur, M.; Nachtigall, P.; Roth, W. J.; Morris, R. E.; Čejka, J., The ADOR mechanism for the synthesis of new zeolites, *Chem. Soc. Rev.* **2015**, *44*, 7177-7206.

(182)Mazur, M.; Kubů, M.; Wheatley, P. S.; Eliášová, P., Germanosilicate UTL and its rich chemistry of solid-state transformations towards IPC-2 (OKO) zeolite, *Catal. Today* **2015**, *243*, 23-31.

(183)McCusker, L. B.; Baerlocher, C.; Jahn, E.; Bülow, M., The triple helix inside the large-pore aluminophosphate molecular sieve VPI-5, *Zeolites* **1991**, *11*, 308-313.

(184)Lobo, R. F.; Davis, M. E., Synthesis and characterization of pure-silica and boron-substituted SSZ-24 using N(16) methylsparteinium bromide as structure-directing agent, *Micropor. Mater.* **1994**, *3*, 61-69.

(185)Ren, X.; Liu, J.; Li, Y.; Yu, J.; Xu, R., Hydrothermal synthesis of an ITH-type germanosilicate zeolite in a non-concentrated gel system, *J. Porous Mater.* **2013**, *20*, 975-981.

(186)Corma, A.; Chica, A.; Guil, J. M.; Llopis, F. J.; Mabilon, G.; Perdigón-Melón, J. A.; Valencia, S., Determination of the Pore Topology of Zeolite IM-5 by Means of

Catalytic Test Reactions and Hydrocarbon Adsorption Measurements, *J. Catal.* **2000**, *189*, 382-394.

(187)Matijasic, A.; Paillaud, J.-L.; Patarin, J., Synthesis, characterization and structure determination of Mu-15: a new fluorogallophosphate with fluoride as a specific template of the D4R units, *J. Mater. Chem.* **2000**, *10*, 1345-1351.

(188)Schmidt, J. E.; Deem, M. W.; Davis, M. E., Synthesis of a Specified, Silica Molecular Sieve by Using Computationally Predicted Organic Structure-Directing Agents, *Angew. Chem. Int. Ed.* **2014**, *53*, 8372-8374.

(189)Grünberg, B.; Emmler, T.; Gedat, E.; Shenderovich, I.; Findenegg, G. H.; Limbach, H.-H.; Buntkowsky, G., Hydrogen Bonding of Water Confined in Mesoporous Silica MCM-41 and SBA-15 Studied by ¹H Solid-State NMR, *Chem. Eur. J.* **2004**, *10*, 5689-5696.

(190)NIST Chemistry WebBook, SRD 69, Thermophysical Properties of Fluid Systems (<https://webbook.nist.gov/chemistry/fluid/>).

(191)Lu, P.; Gómez-Hortigüela, L.; Xu, L.; Cambor, M. A., Synthesis of STW zeolites using imidazolium-based dications of varying length, *J. Mater. Chem. A* **2018**, *6*, 1485-1495.

(192)Kosslick, H.; Tuan, V. A.; Fricke, R.; Peuker, C.; Pilz, W.; Storek, W., Synthesis and characterization of Ge-ZSM-5 zeolites, *J. Phys. Chem.* **1993**, *97*, 5678-5684.

(193)Blasco, T.; Corma, A.; Díaz-Cabañas, M. J.; Rey, F.; Vidal-Moya, J. A.; Zicovich-Wilson, C. M., Preferential Location of Ge in the Double Four-Membered Ring Units of ITQ-7 Zeolite, *J. Phys. Chem. B* **2002**, *106*, 2634-2642.

(194)Thomas, J. M.; Klinowski, J.; Ramdas, S.; Hunter, B. K.; Tennakoon, D. T. B., The evaluation of non-equivalent tetrahedral sites from ²⁹Si NMR chemical shifts in zeolites and related aluminosilicates, *Chem. Phys. Lett.* **1983**, *102*, 158-162.

(195)Henkelis, S. E.; Mazur, M.; Rice, C. M.; Bignami, G. P. M.; Wheatley, P. S.; Ashbrook, S. E.; Čejka, J.; Morris, R. E., A procedure for identifying possible products in

the assembly–disassembly–organization–reassembly (ADOR) synthesis of zeolites, *Nat. Protoc.* **2019**, *14*, 781-794.

(196)Burel, L.; Kasian, N.; Tuel, A., Quasi All-Silica Zeolite Obtained by Isomorphous Degermanation of an As-Made Germanium-Containing Precursor, *Angew. Chem. Int. Ed.* **2014**, *53*, 1360-1363.

(197)Chlubná-Eliášová, P.; Tian, Y.; Pinar, A. B.; Kubů, M.; Čejka, J.; Morris, R. E., The Assembly-Disassembly-Organization-Reassembly Mechanism for 3D-2D-3D Transformation of Germanosilicate IWW Zeolite, *Angew. Chem. Int. Ed.* **2014**, *53*, 7048-7052.

(198)Gale, J. D., GULP: A computer program for the symmetry-adapted simulation of solids, *J. Chem. Soc. Faraday Trans.* **1997**, *93*, 629-637.

(199)Foster, M. D.; Rivin, I.; Treacy, M. M. J.; Delgado Friedrichs, O., A geometric solution to the largest-free-sphere problem in zeolite frameworks, *Micropor. Mesopor. Mater.* **2006**, *90*, 32-38.

(200)Shamzhy, M.; Opanasenko, M.; Tian, Y.; Konysheva, K.; Shvets, O.; Morris, R. E.; Čejka, J., Germanosilicate Precursors of ADORable Zeolites Obtained by Disassembly of ITH, ITR, and IWR Zeolites, *Chem. Mater.* **2014**, *26*, 5789-5798.

(201)Verheyen, E.; Jo, C.; Kurttepel, M.; Vanbutsele, G.; Gobechiya, E.; Korányi, T. I.; Bals, S.; Van Tendeloo, G.; Ryoo, R.; Kirschhock, C. E. A.; Martens, J. A., Molecular shape-selectivity of MFI zeolite nanosheets in n-decane isomerization and hydrocracking, *J. Catal.* **2013**, *300*, 70-80.

(202)Elangovan, S. P.; Hartmann, M., Evaluation of Pt/MCM-41//MgAPO-n composite catalysts for isomerization and hydrocracking of n-decane, *J. Catal.* **2003**, *217*, 388-395.

(203)Liu, X.; Ravon, U.; Bosselet, F.; Bergeret, G.; Tuel, A., Probing Ge Distribution in Zeolite Frameworks by Post-Synthesis Introduction of Fluoride in As-Made Materials, *Chem. Mater.* **2012**, *24*, 3016-3022.

(204)Liu, X.; Ravon, U.; Tuel, A., Evidence for F⁻/SiO⁻ Anion Exchange in the Framework of As-Synthesized All-Silica Zeolites, *Angew. Chem. Int. Ed.* **2011**, *50*, 5900-5903.

(205)Liu, X.; Chu, Y.; Wang, Q.; Wang, W.; Wang, C.; Xu, J.; Deng, F., Identification of double four-ring units in germanosilicate ITQ-13 zeolite by solid-state NMR spectroscopy, *Solid State NMR* **2017**, *87*, 1-9.

Appendix A. Supplementary Information for Part I

Crystallographic data which were used to generate the visualizations in this section were imported from the International Zeolite Association-Structure Committee (IZA-SC) Database. The visualizations were on the basis of the hard-sphere model, where the van der Waals radii of tetrahedral (silicon) and oxygen atoms are 1.35 Å, following the IZA tradition. The kinetic diameter of probe molecule used here is 3.60 Å which is the value commonly used for methanol molecules.

From the imported crystallographic data, the following scalar field was generated. (Ref: Nagy, T. F.; Mahanti, S. D.; Dye, J. L., *Zeolites* **1997**, *19*, 57-64.)

$$d(x, y, z) = \min \sqrt{(X_i - x)^2 + (Y_i - y)^2 + (Z_i - z)^2} - r_{\text{framework}} - r_{\text{probe}}$$

where (X_i, Y_i, Z_i) is the Cartesian coordination of the i -th framework atom. ($r_{\text{framework}} = 1.35$ Å, $r_{\text{probe}} = 3.60/2$ Å = 1.80 Å, as mentioned above.) $d(x,y,z)$ is the distance between the surface of the probe molecule at (x,y,z) and that of the closest framework atom. Where $d(x,y,z) = 0$, the probe molecule hard sphere contacts the framework. Therefore, the parametric visualization of $d(x,y,z) = 0$ will show the ‘real’ shape of accessible volume for methanol. The maximum sphere that can be included in a cage can also be found on the basis of the same equation by solving for the maximum of $d(x,y,z)$ when $r_{\text{probe}} = 0$.

The surface visualizations (Figure A1–A4) were drawn using Wolfram Mathematica 10.1 Student Edition with the Crystallica application developed by Bianca Eifert at Justus Liebig University Giessen, Germany. VESTA platform by Fujio Izumi at Quantum Beam Center, National Institute for Materials Science, Japan was used to generate cage structures. (Momma, K.; Izumi, F., *J. Appl. Crystallogr.* **2008**, *41*, 653-658.)

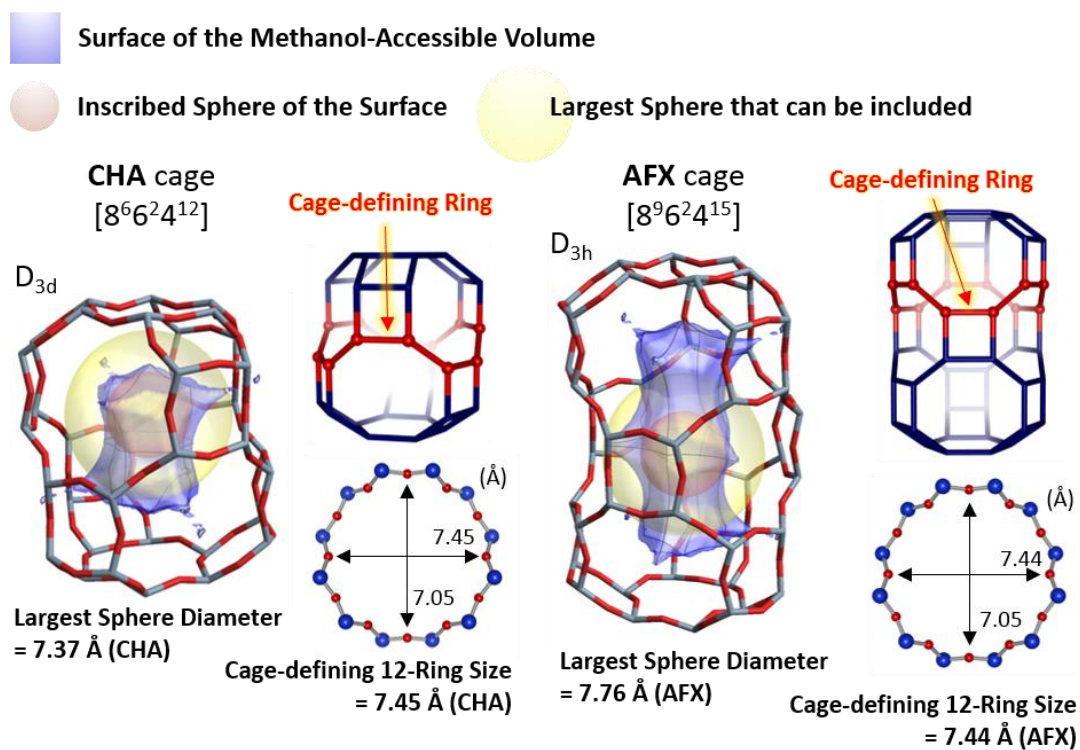


Figure A1. The cage visualizations, selection of the cage-defining rings, and their sizes for CHA and AFX.

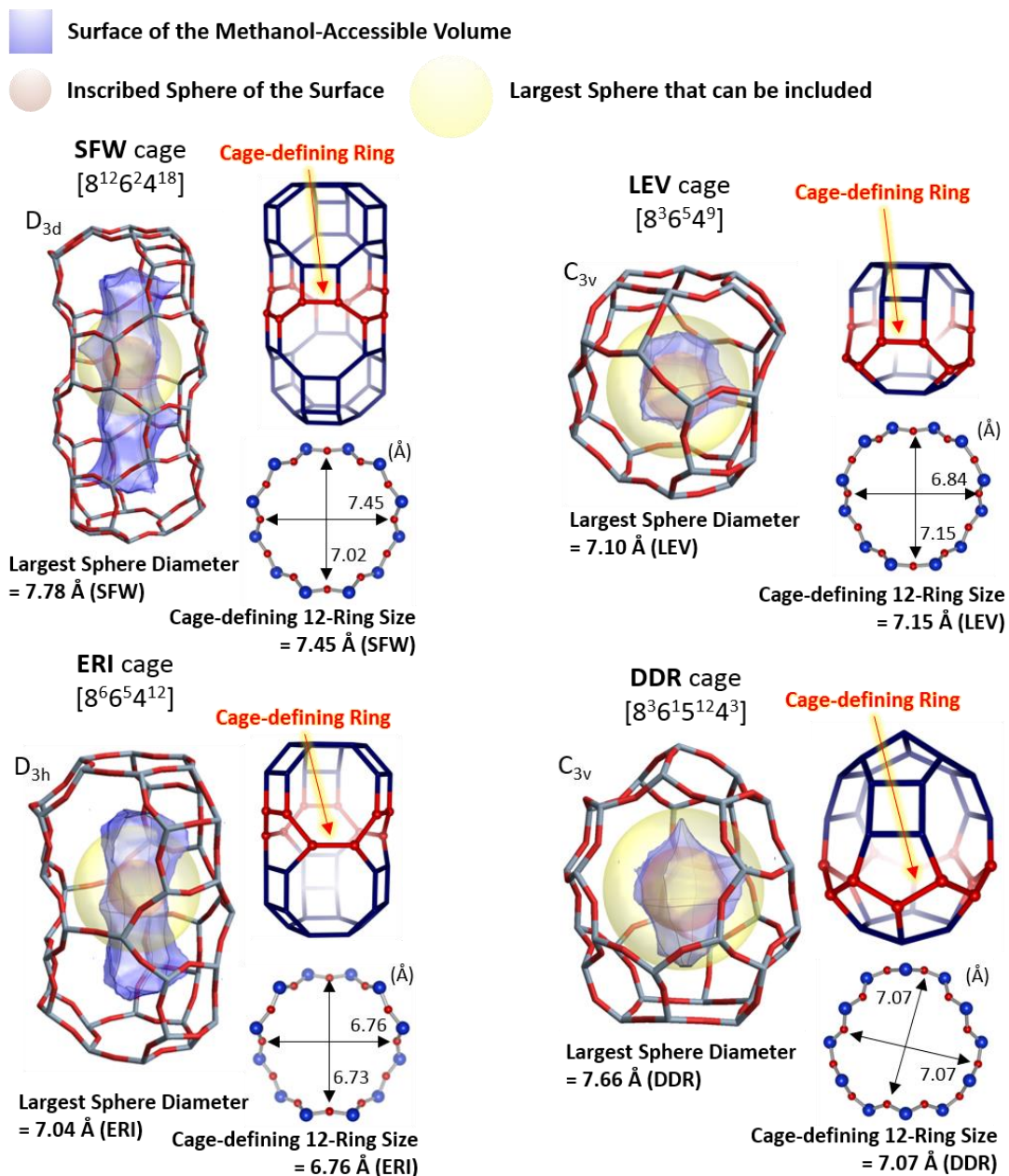


Figure A2. The cage visualizations, selection of the cage-defining rings, and their sizes for SFW, LEV, ERI, and DDR.

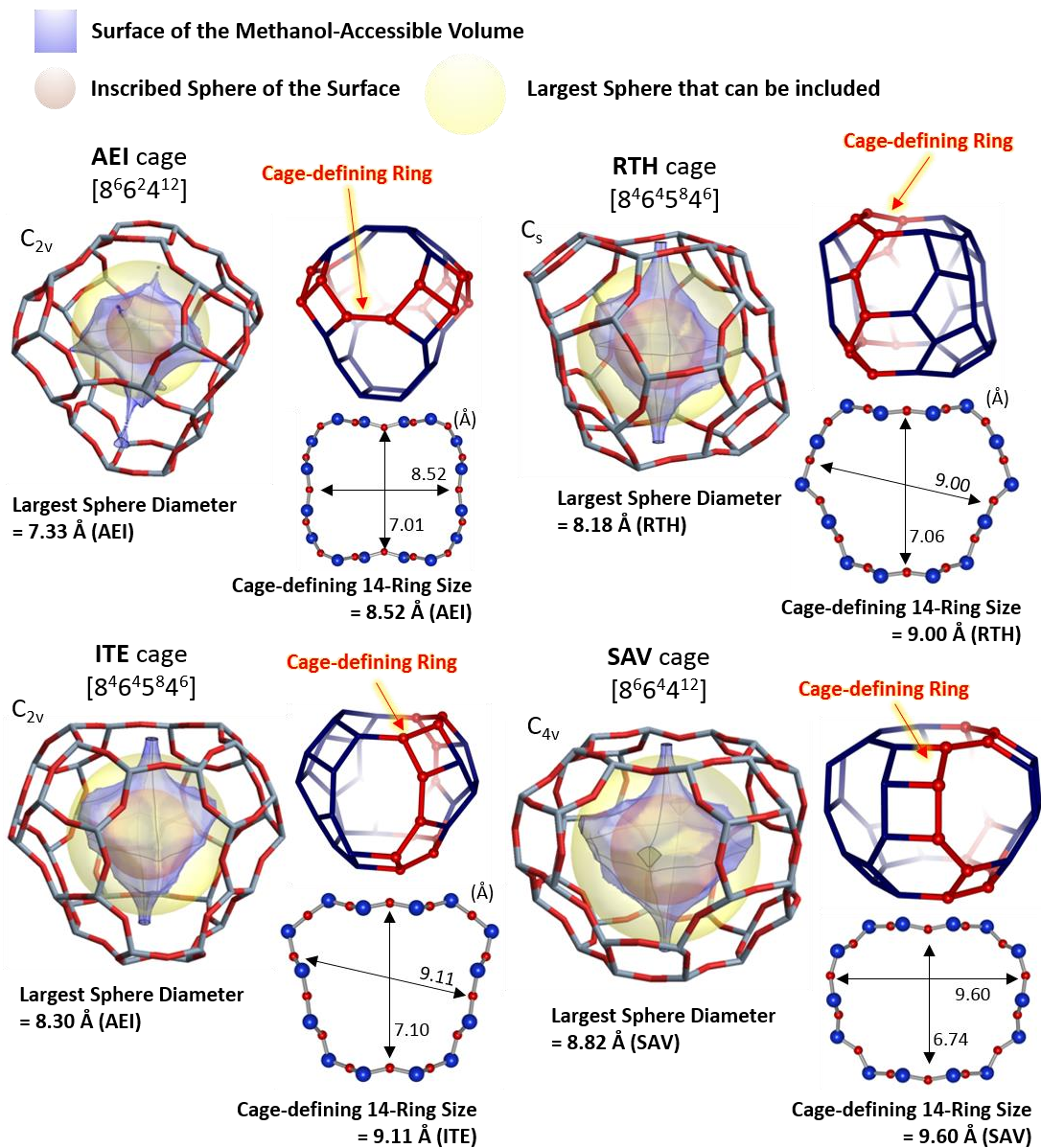


Figure A3. The cage visualizations, selection of the cage-defining rings, and their sizes for AEI, RTH, ITE, and SAV.

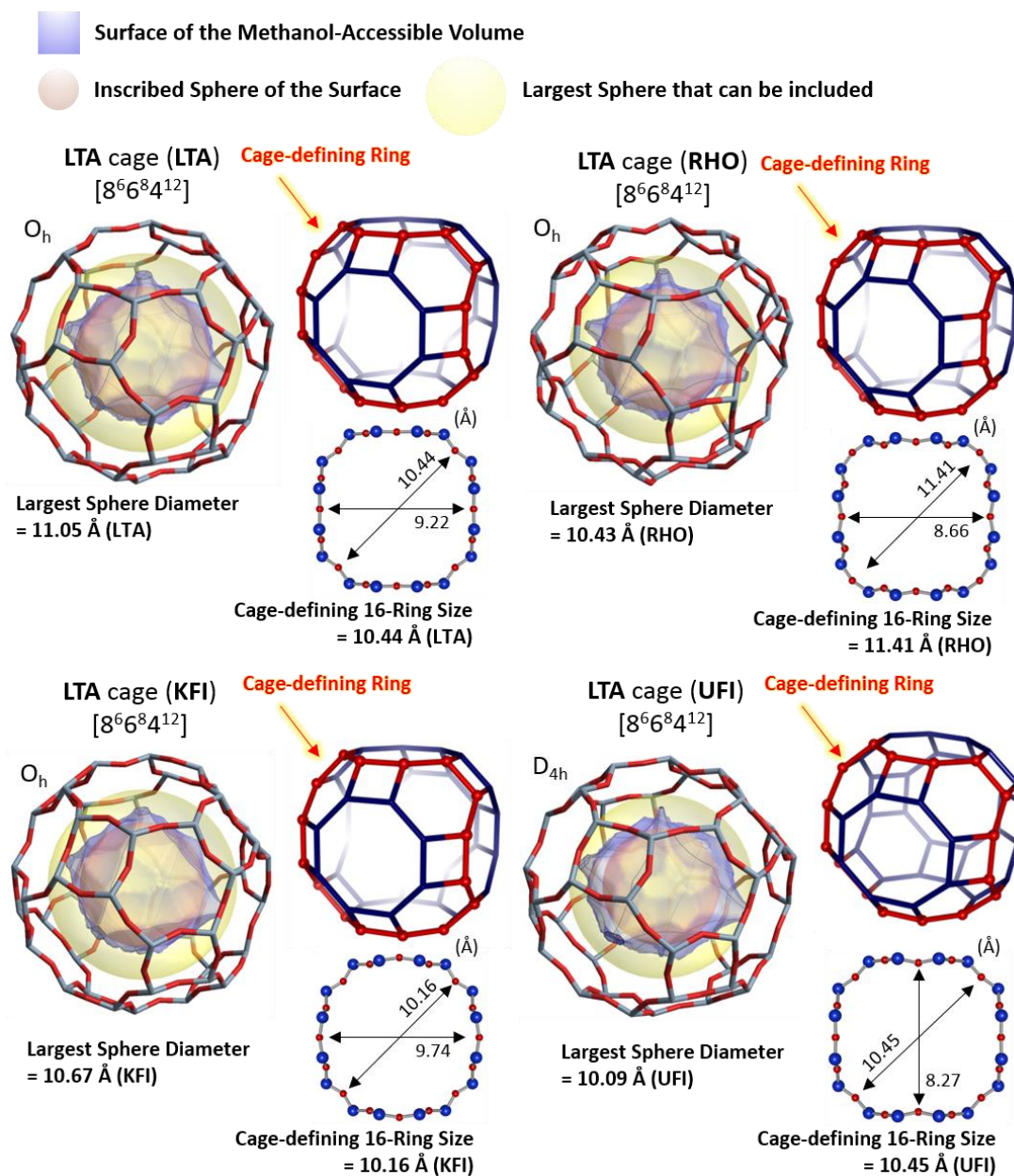


Figure A4. The cage visualizations, selection of the cage-defining rings, and their sizes for LTA, RHO, KFI, and UFI.

One can easily figure out how MTO-active cages actually look like on the basis of the visualizations shown in Figures A1–A4. However, it is hard to estimate how large molecules they can harbor based only on such 3-dimensional surface visualizations. Another way to quantitatively visualize accessible spaces within cages for foreign molecules is investigating the cross-sections of the accessible volumes visualized in Figures A1–A4. The cross-sections of accessible volumes within all cage structures along the three principle planes (xy, yz, and zx) are illustrated in the following figures (Figures A5–A8). The planes are selected to include the centers of mass of cages. Not only cross-sections of the accessible volumes for methanol ($r_{\text{probe}} = 1.80 \text{ \AA}$, outermost contours), but also contours for larger probe molecules ($r_{\text{probe}} = 2, 3, 4, \dots, n \text{ \AA}$) are illustrated together. I named such figures ‘*tree ring plots*’ because they resemble the annual growth rings of trees. The more rings those plots have, the larger molecules cages can accommodate. Although these tree ring plots are on the basis of the simplest, purely geometric hard-sphere model, I believe that this type of visualization will be helpful for those who want to understand how actually voluminous the cages are, how large molecules can be included, which part of the cage is the ‘deepest’, etc.

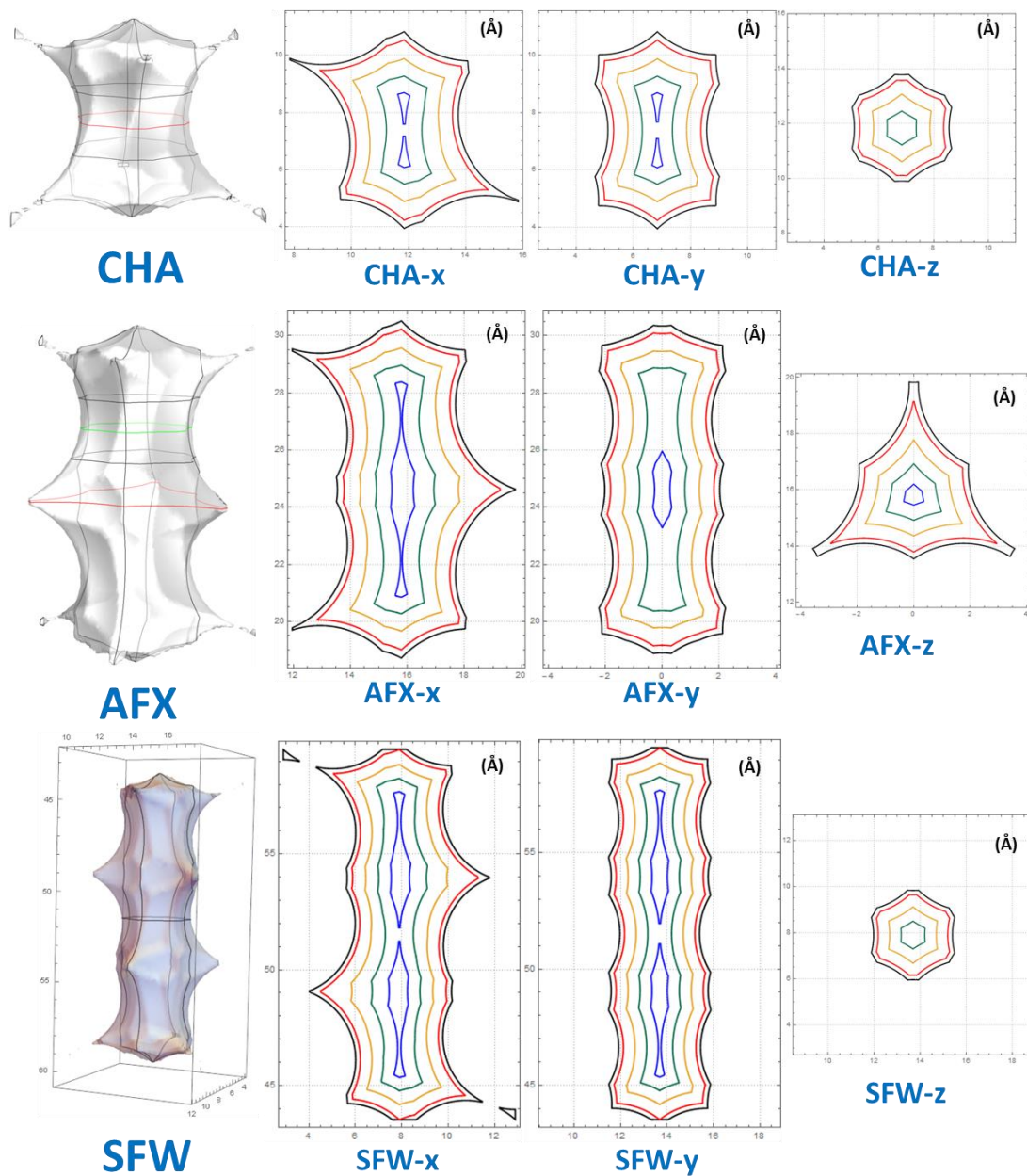


Figure A5. Cage visualizations and tree ring plots of CHA, AFX, and SFW cages. (probe molecule radius (r_{probe}): black (1.80 Å), red (2 Å), orange (3 Å), green (4 Å), blue (5 Å))

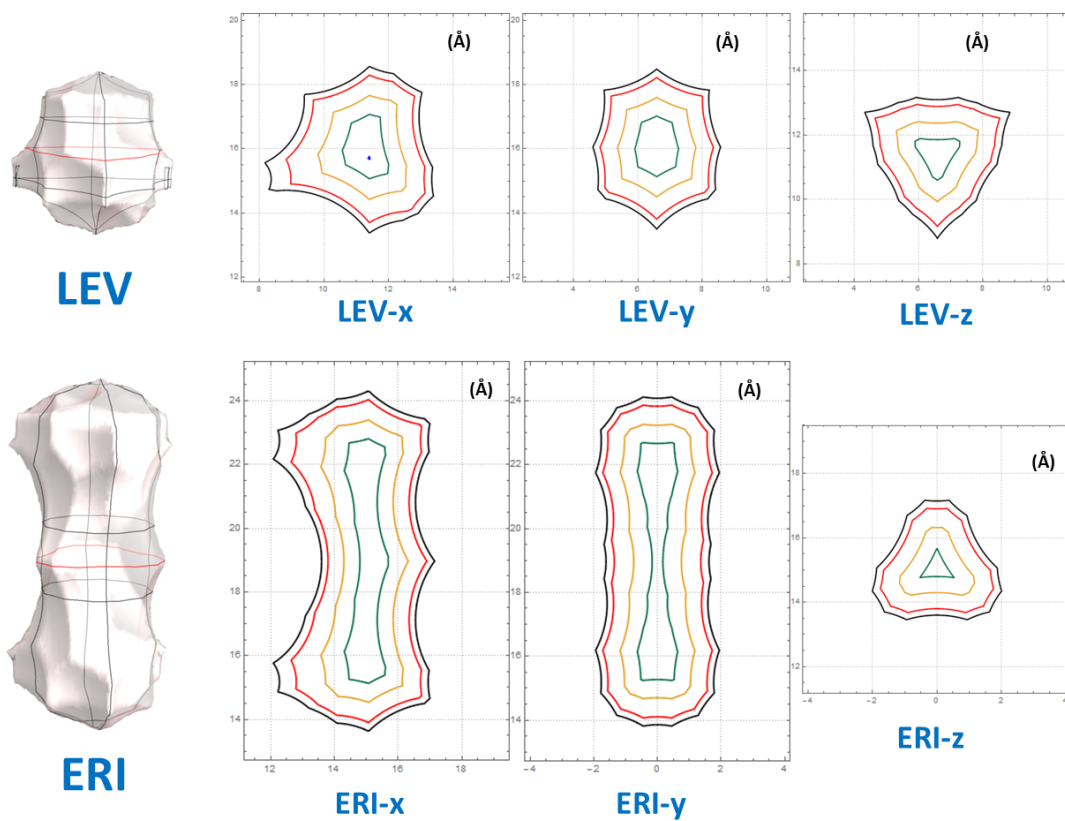


Figure A6. Cage visualizations and tree ring plots of LEV and ERI cages. (probe molecule radius (r_{probe}): black (1.80 Å), red (2 Å), orange (3 Å), green (4 Å))

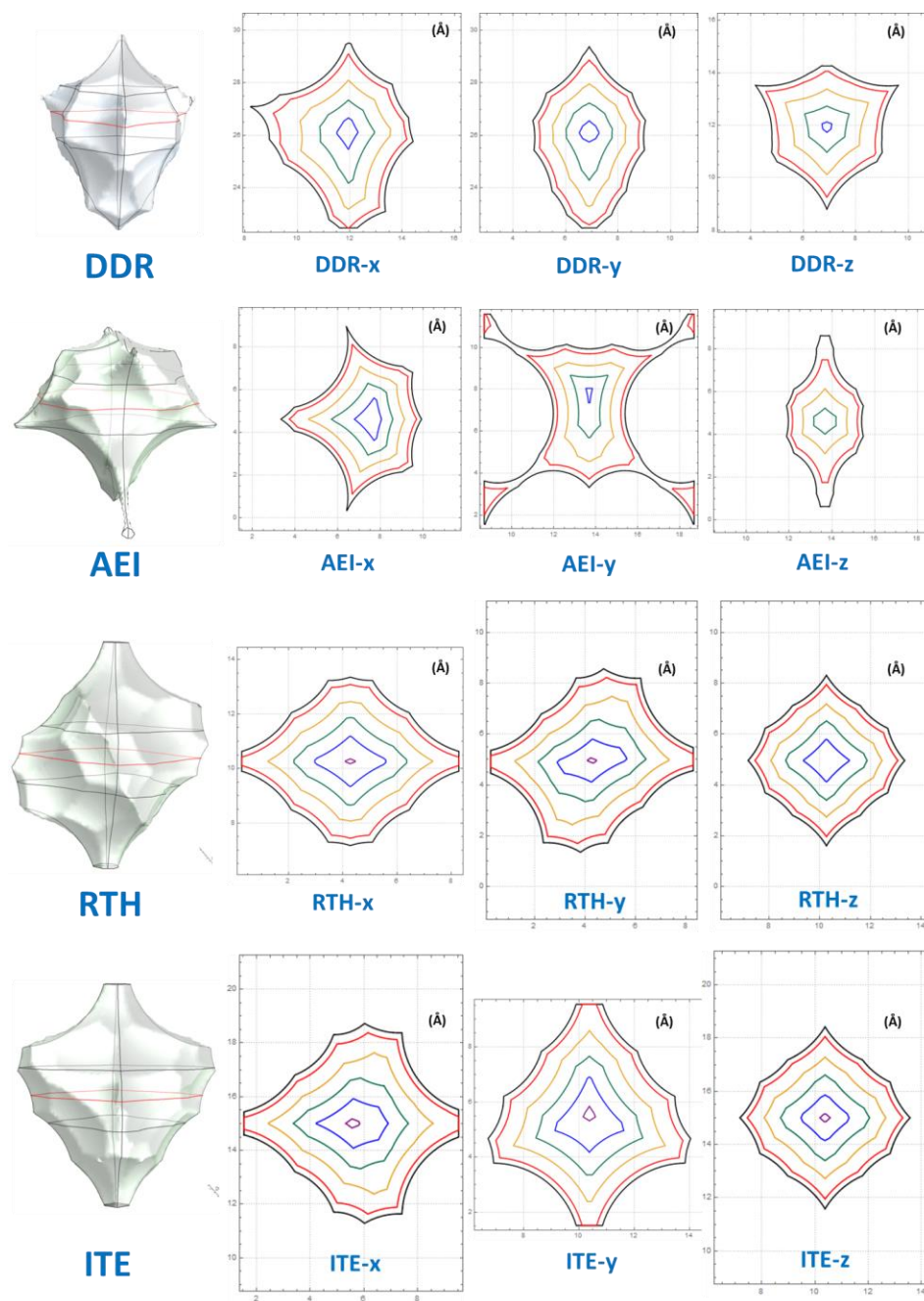


Figure A7. Cage visualizations and tree ring plots of DDR, AEI, RTH, and ITE cages. (probe molecule radius (r_{probe}): black (1.80 Å), red (2 Å), orange (3 Å), green (4 Å), blue (5 Å), purple (6 Å))

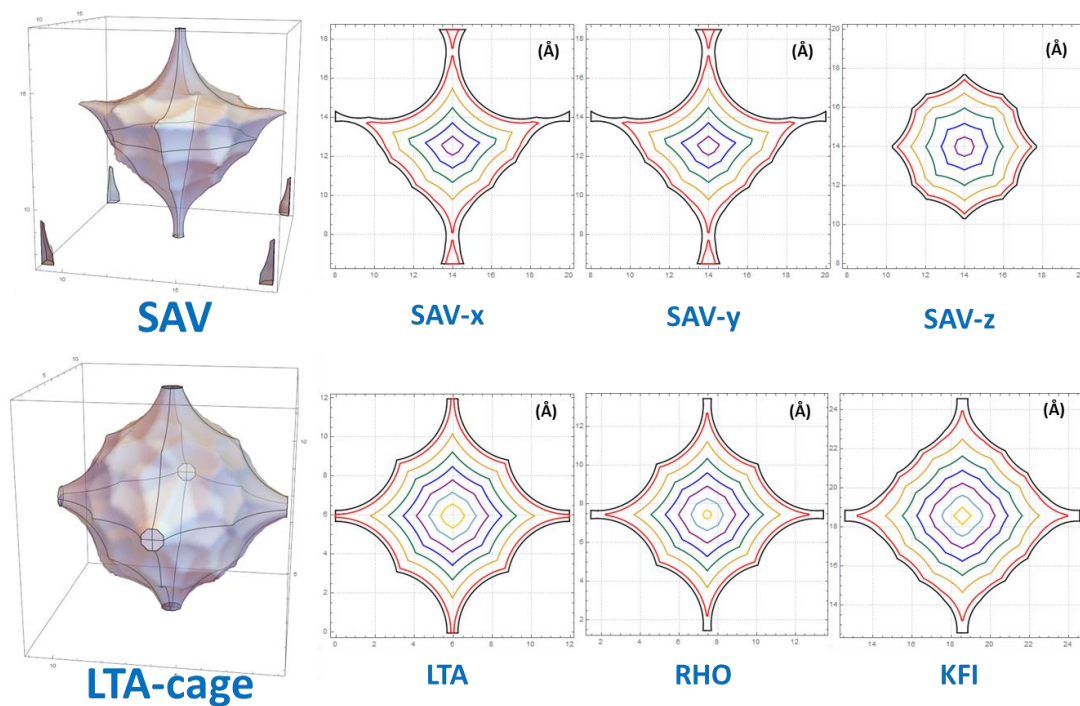


Figure A8. Cage visualizations and tree ring plots of SAV, and LTA cages of frameworks LTA, RHO and KFI. (probe molecule radius (r_{probe}): black (1.80 Å), red (2 Å), orange (3 Å), green (4 Å), blue (5 Å), purple (6 Å), cyan (7 Å), light-orange (8 Å))

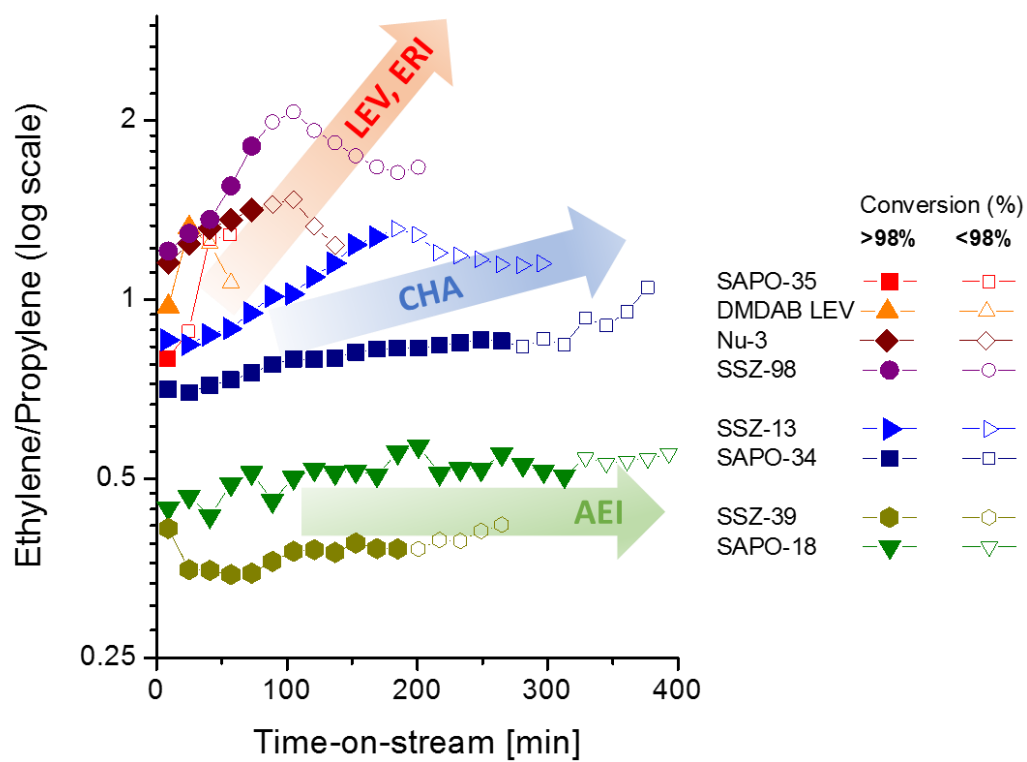


Figure A9. Time-dependent behaviors of ethylene-to-propylene ratios during the MTO reactions over selected catalysts.

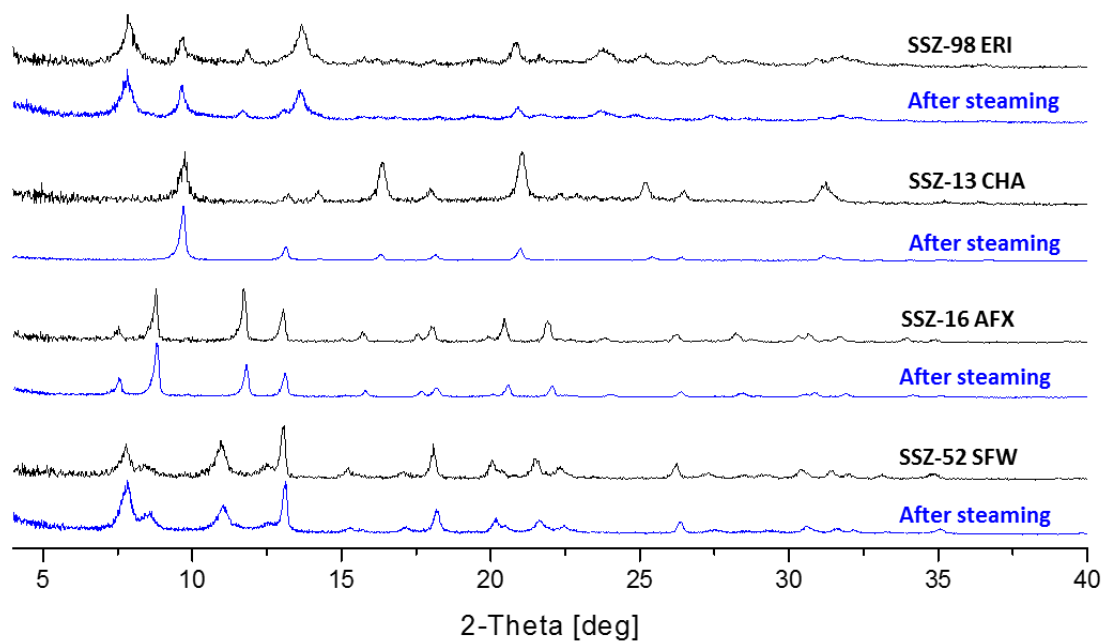


Figure A10. PXRD profiles of pristine and steamed zeolites having selected types of topologies.

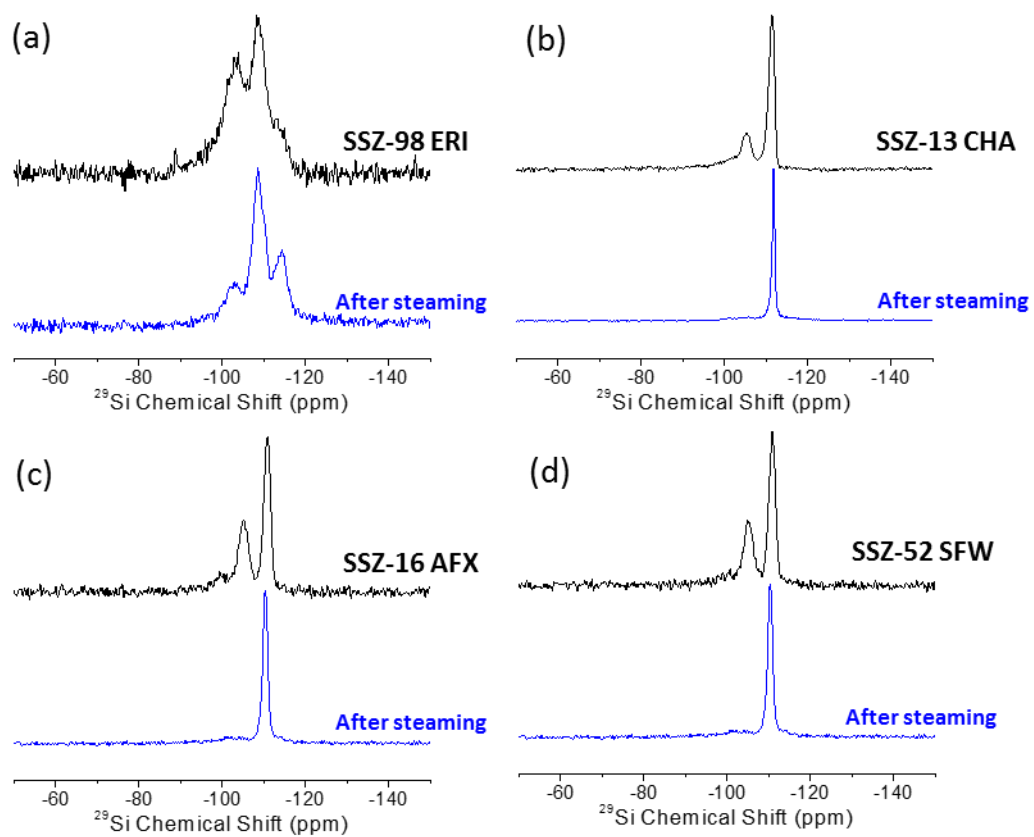


Figure A11. ^1H -decoupled ^{29}Si 8 k MAS solid-state NMR spectra of pristine and steamed zeolites having selected types of topologies.

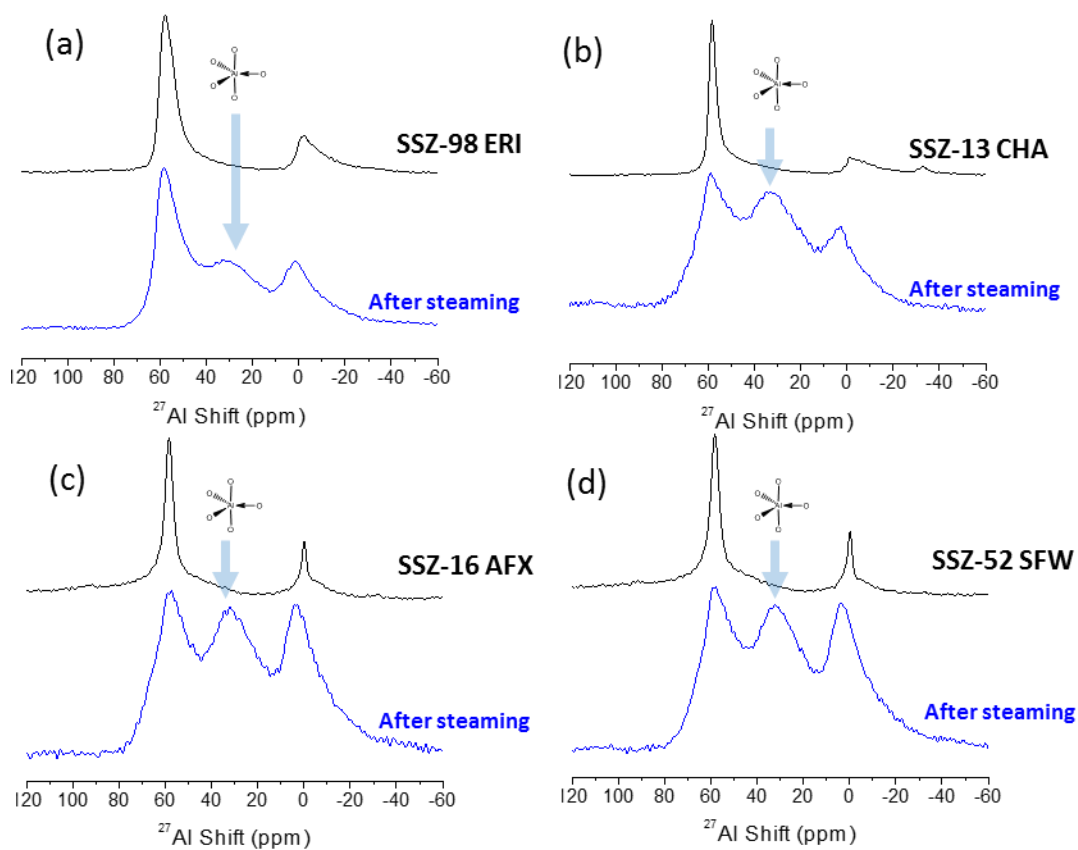


Figure A12. ^1H -decoupled ^{27}Al 10 k MAS solid-state NMR spectra of pristine and steamed zeolites having selected types of topologies.

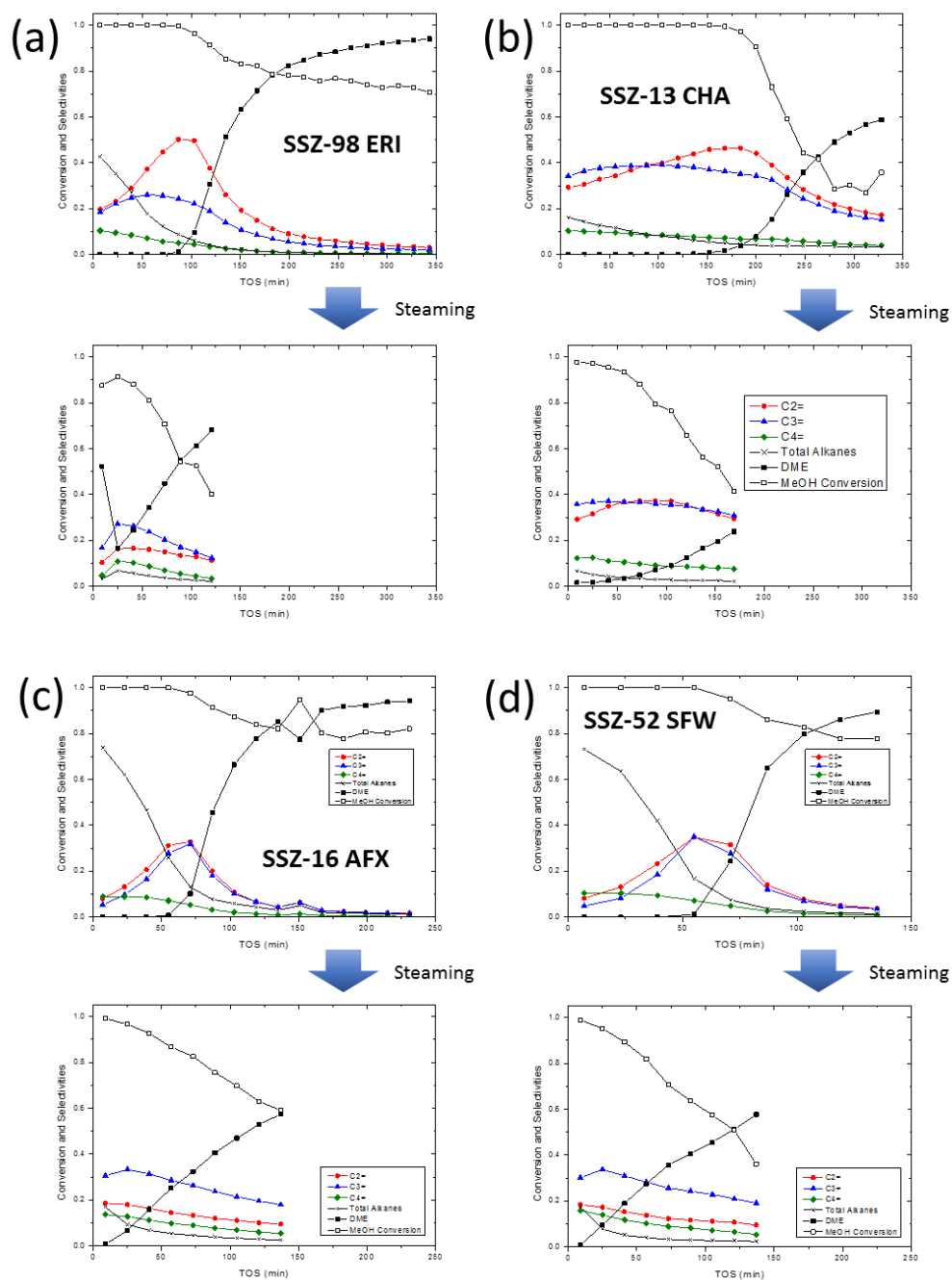


Figure A13. MTO time-on-stream selectivity chart of pristine and steamed zeolites having selected types of topologies.

Appendix B. Supplementary Information for Part II

Table B1. Summary of fluoride-based CIT-13 synthesis conditions and results.

OSDA	x	y	z	seeds	Temperature (°C)	Time (weeks)	Results
1	4	15	0.5	O	160	4	CIT-13 ^b
1	4	15	0.5	X	160	5	CIT-13 ^b
1	2	10	0.5	X	160	2	CIT-13 ^b
1	3	10	0.5	X	160	2	CIT-13 ^a
1	4	10	0.5	O	160	1	CIT-13 ^a
1	4	10	0.5	X	160	3	CIT-13 ^a
1	8	10	0.5	X	160	3	CIT-13 ^c
1	16	10	0.5	X	160	5	CIT-13 ^c
1	4	7.5	0.5	O	160	2	CIT-13 ^b
1	4	7.5	0.5	X	160	2	CIT-13 ^a
1	4	5	0.5	O	160	3	CIT-13 ^b
1	4	10	0.5	X	140	4	CIT-13 ^a
1	4	10	0.5	X	150	4	CIT-13 ^a
1	4	10	0.5	X	175	1	CIT-13 ^a
1	4	10	0.625	O	160	2	CIT-13 ^b
1	4	10	0.625	X	160	2	CIT-13 ^b
1	4	10	0.75	O	160	2	CIT-13 ^c
1	4	10	0.75	X	160	2	CIT-13 ^c

OSDA	x	y	z	seeds	Temperature (°C)	Time (weeks)	Results
2	2	10	0.5	X	160	2	CIT-13 ^c /MFI
2	4	10	0.5	X	160	2	CIT-13 ^c /MFI
2	8	10	0.5	X	160	2	MFI
2	16	10	0.5	X	160	4	MFI
2	50	10	0.5	X	160	4	MFI
3	2	10	0.5	X	160	3	CIT-13 ^c
3	4	10	0.5	X	160	3	CIT-13 ^c
3	8	10	0.5	X	160	3	CIT-13 ^c
3	16	10	0.5	X	160	8	CIT-13 ^c
3	50	10	0.5	X	160	8	amorphous
4	2	10	0.5	X	160	1	CIT-13 ^a
4	4	10	0.5	X	160	1	CIT-13 ^a
4	8	10	0.5	X	160	2	CIT-13 ^b
4	16	10	0.5	X	160	3	CIT-13 ^b
4	50	10	0.5	X	160	7	amorphous

CIT-13 purity index: ^a very pure, ^b acceptably pure, ^c CIT-13 was the major phase, but one of more unidentified impurity phase(s) were observed. The purity of the products were assessed based on the PXRD patterns.

Table B2. Crystallographic details for the structure refinement of as-synthesized CIT-13.

Sample	CIT-13
Chemical composition	$[(C_{13}N_2)_{3.30}F_2][Si_{54.34}Ge_{9.66}O_{128}]$
Space group	<i>Cmmm</i>
<i>a</i> (Å)	27.4374(5)
<i>b</i> (Å)	13.8000(2)
<i>c</i> (Å)	10.2910(2)
<i>V</i> (Å ³)	3896.6(1)
<i>Z</i>	8
ρ (g/cm ³)	2.144(2)
λ (Å)	0.776381(1)
2θ range (°)	2.0–46.0
<i>R</i> _i	0.0126
<i>R</i> _{wp}	0.0773
<i>R</i> _{exp}	0.0015
Observations	16899
Reflections	1241
Parameters	104
Geometric restraints	62 (zeolite) 38 (SDA)

Table B3. Selected bond lengths and angles (Å, °).

	T-O-T	O-T-O	T-O

13	CIT-	min	138.3	107.8	1.55
		max	180.0	113.8	1.63
		avg	156.6	109.6	1.59

Restraints used: T-O-T: $135 \pm 10^\circ$; O-T-O: $109.5 \pm 0.8^\circ$; T-O: $1.61 \pm 0.01 \text{ \AA}$; $w=1/\sigma^2$

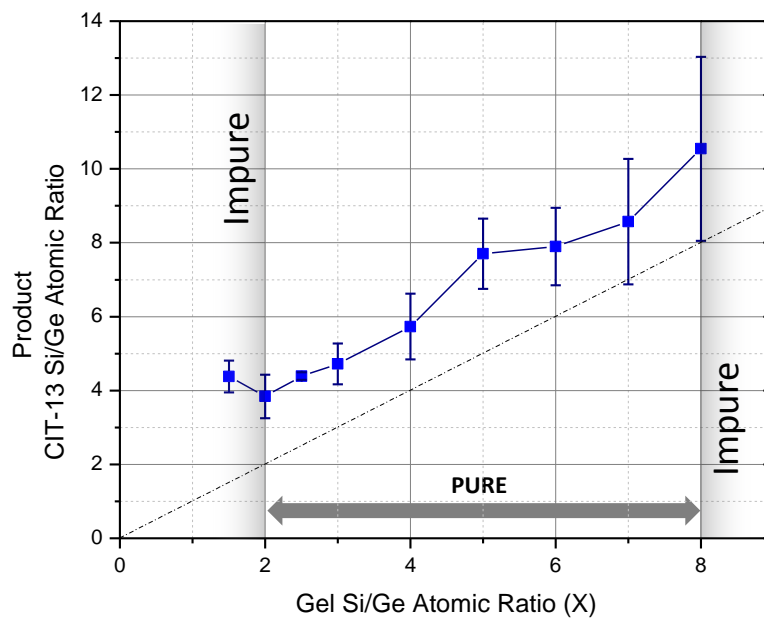


Figure B1. The relation between the gel Si/Ge ratios and the product CIT-13 Si/Ge ratios, characterized using the EDS.

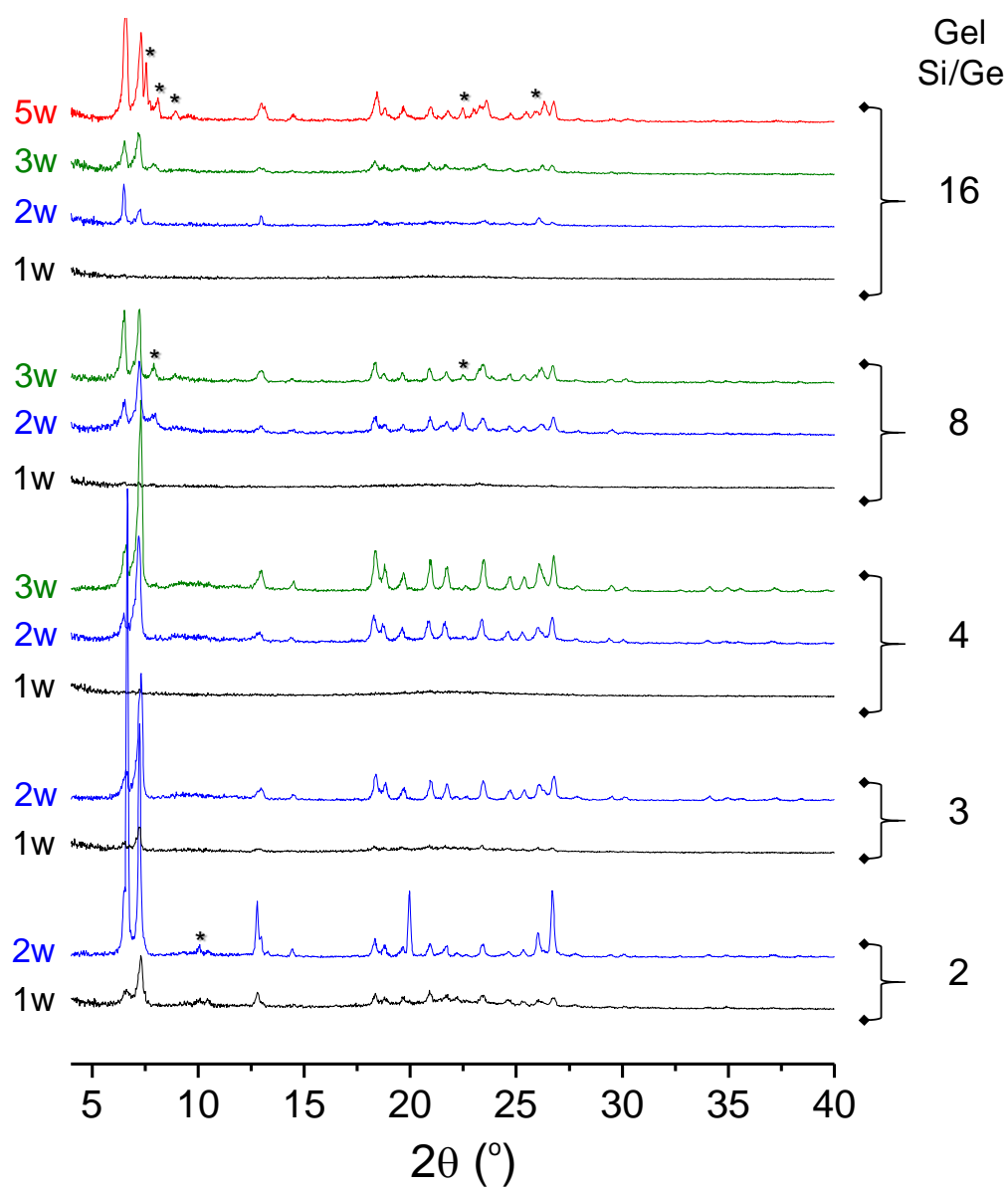


Figure B2. The effect of the Si/Ge ratio in the gel on the crystallization of CIT-13 (*: impurity; w: week).

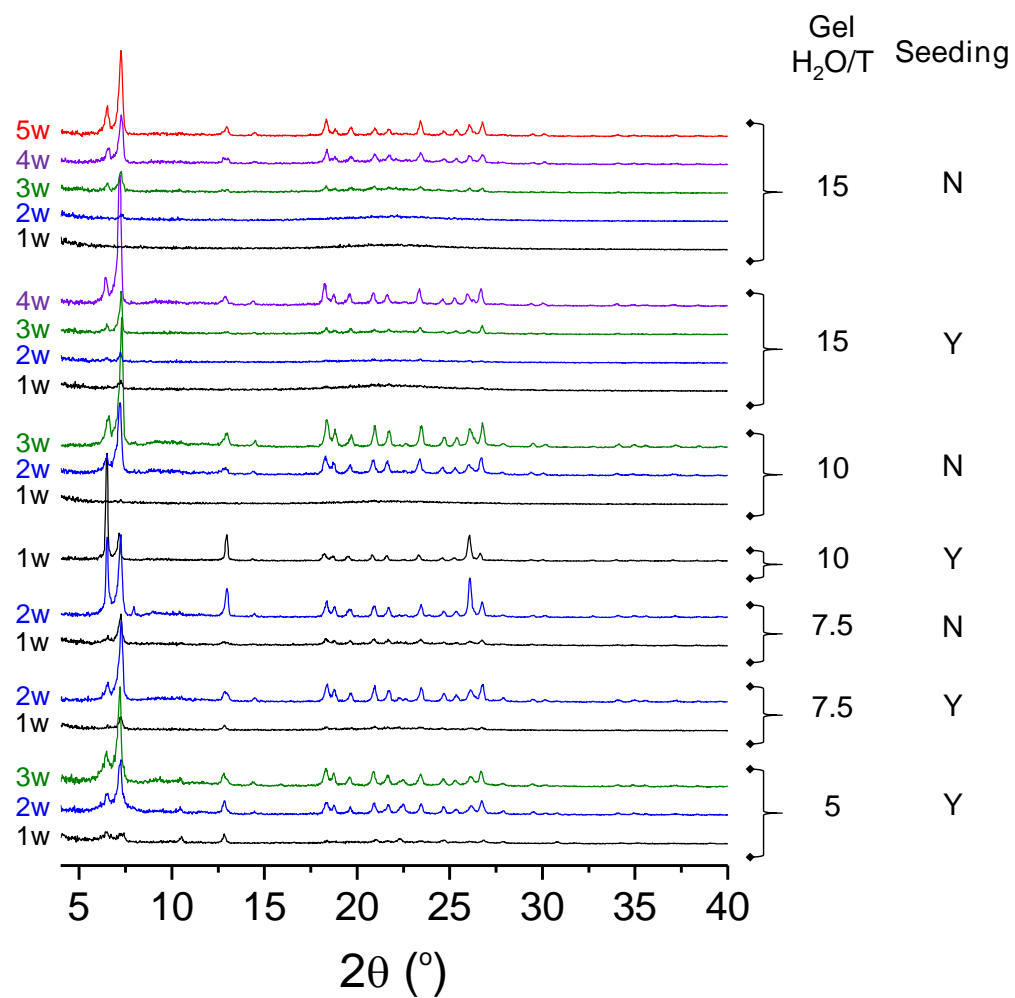


Figure B3. The effect of water levels in the gel on the crystallization of CIT-13 (w: week).

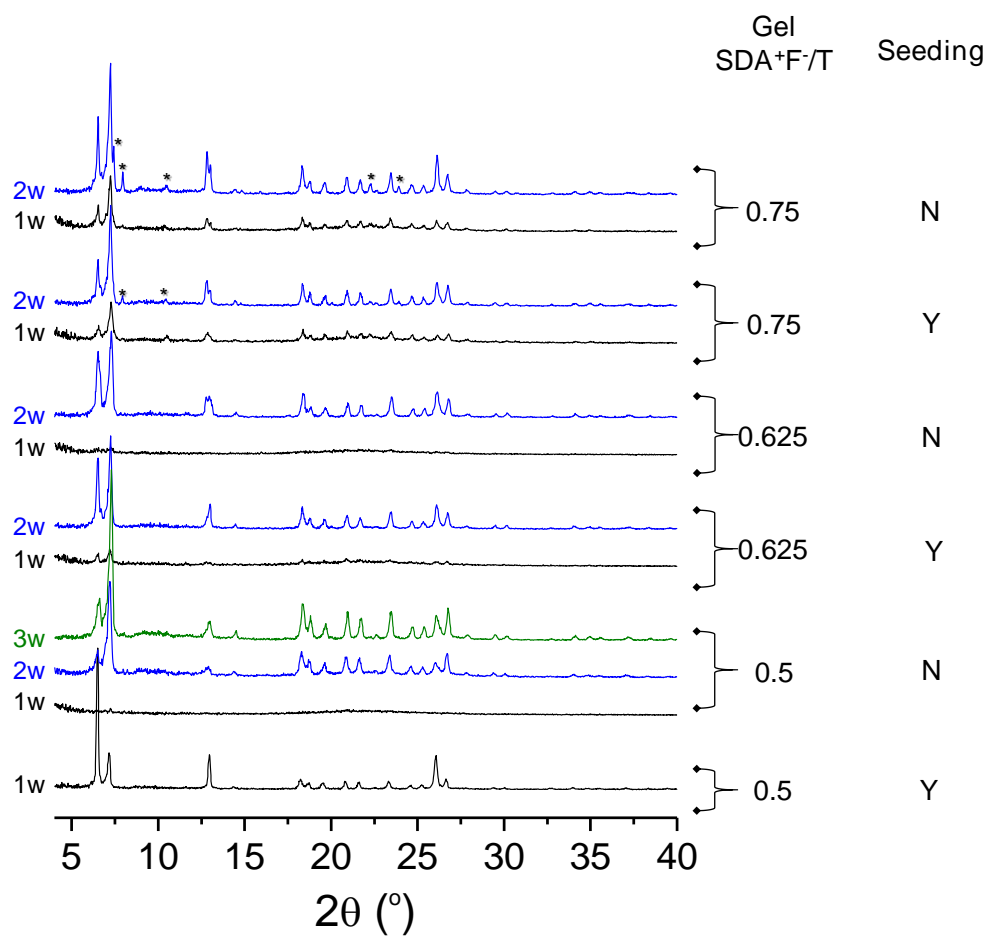


Figure B4. The effect of the amount of OSDA in the gel on the crystallization of CIT-13 (*: impurity; w: week).

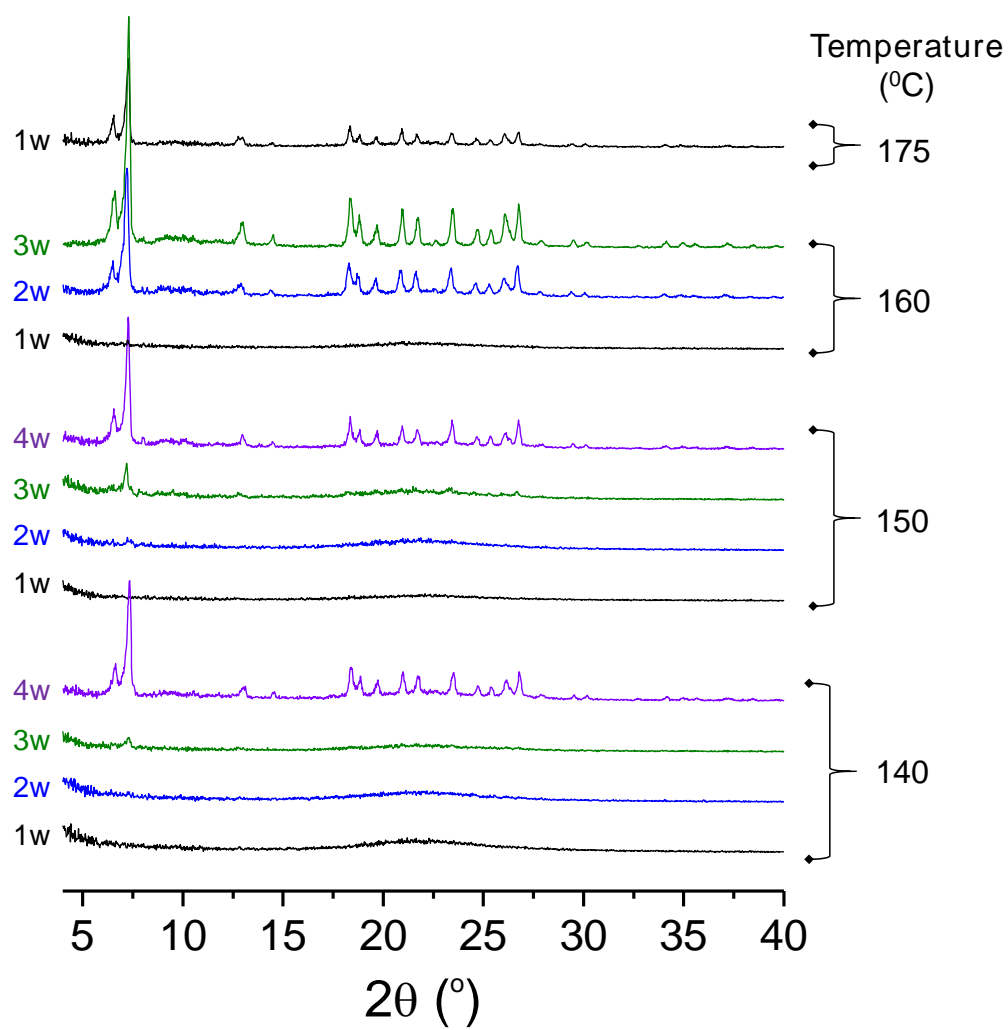


Figure B5. The effect of the crystallization temperature on the crystallization of CIT-13 (*: impurity; w: week).

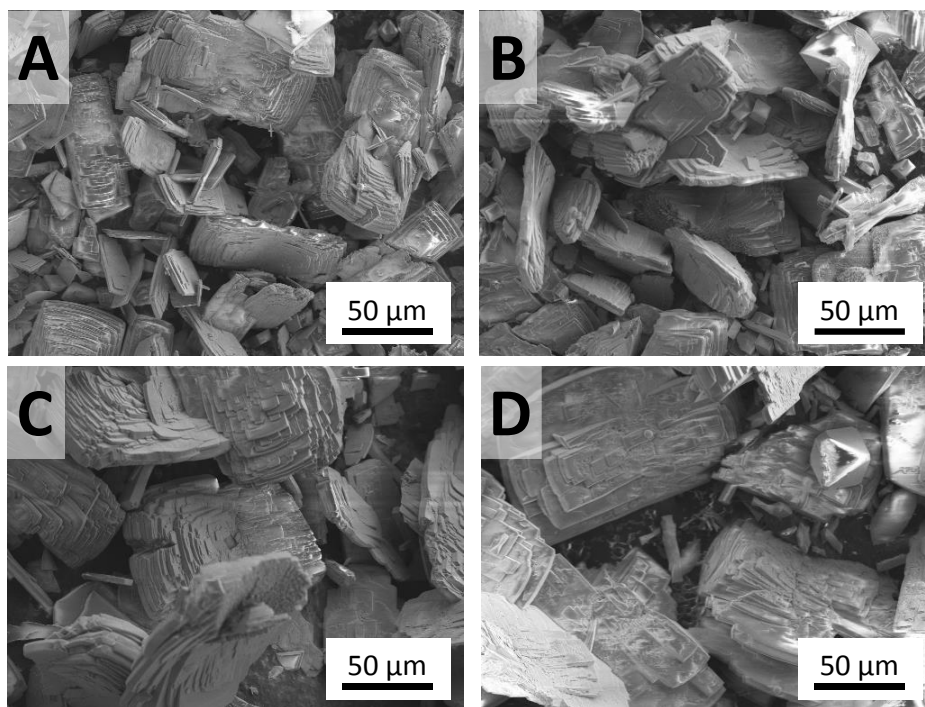


Figure B6. SEM micrographs of CIT-13 crystallized at (A) 140°C, (B) 150°C, (C) 160°C and (D) 175°C.

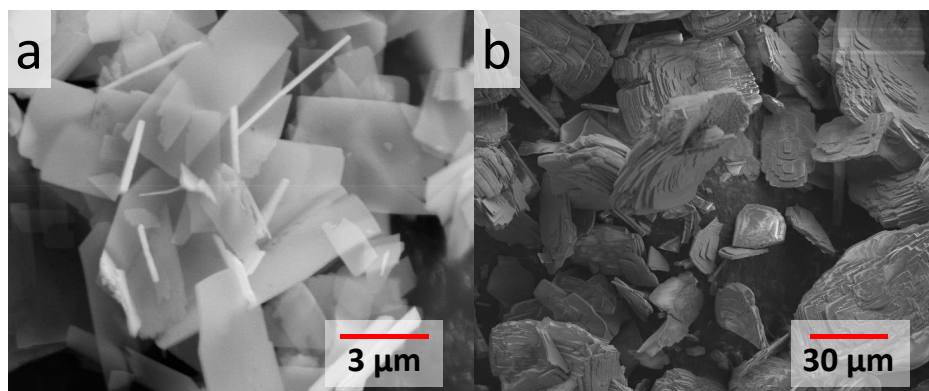


Figure B7. SEM micrographs of CIT-13 crystals prepared by heating (A) in a rotating autoclave and (B) in a static autoclave.

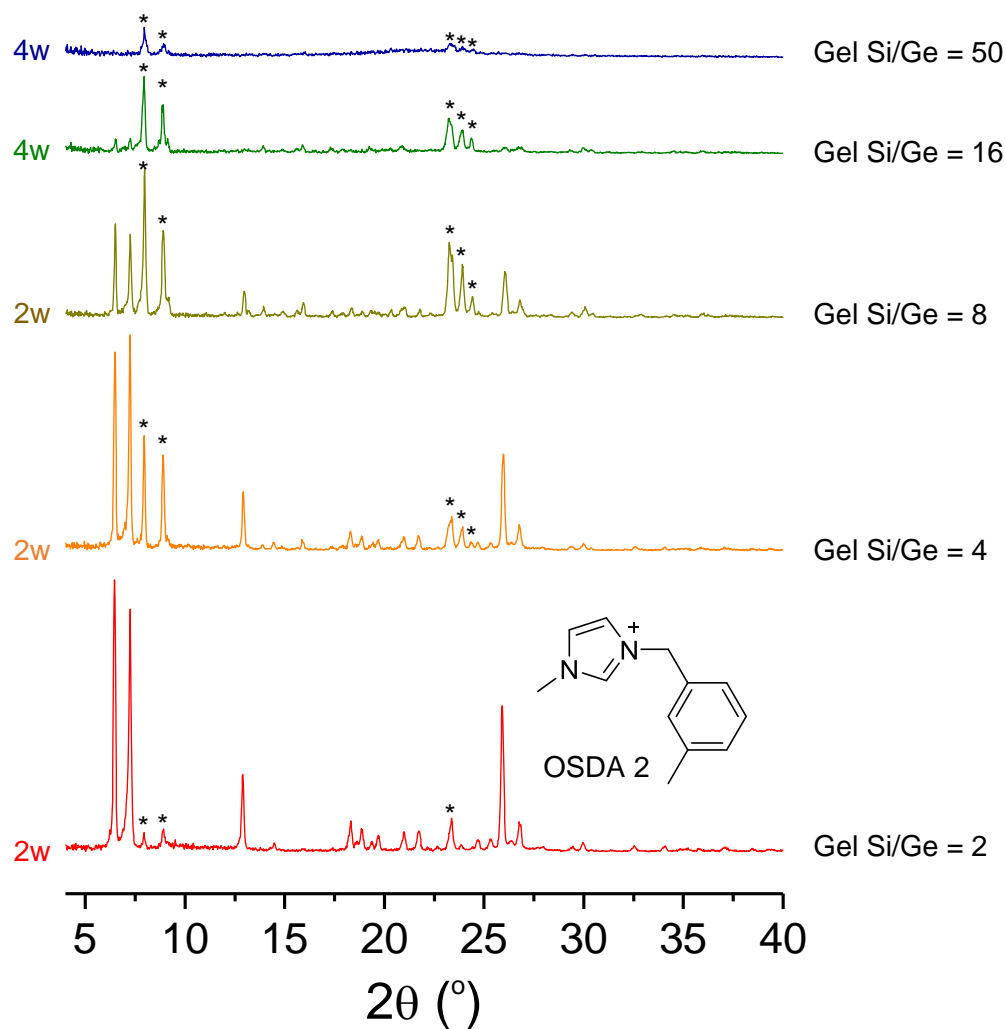


Figure B8. XPD patterns of germanosilicate samples that crystallized in the presence of **OSDA 2** and different Si/Ge ratios and in the gel (*: impurity; w: week). Here, the impurity phase was identified as an MFI-type material.

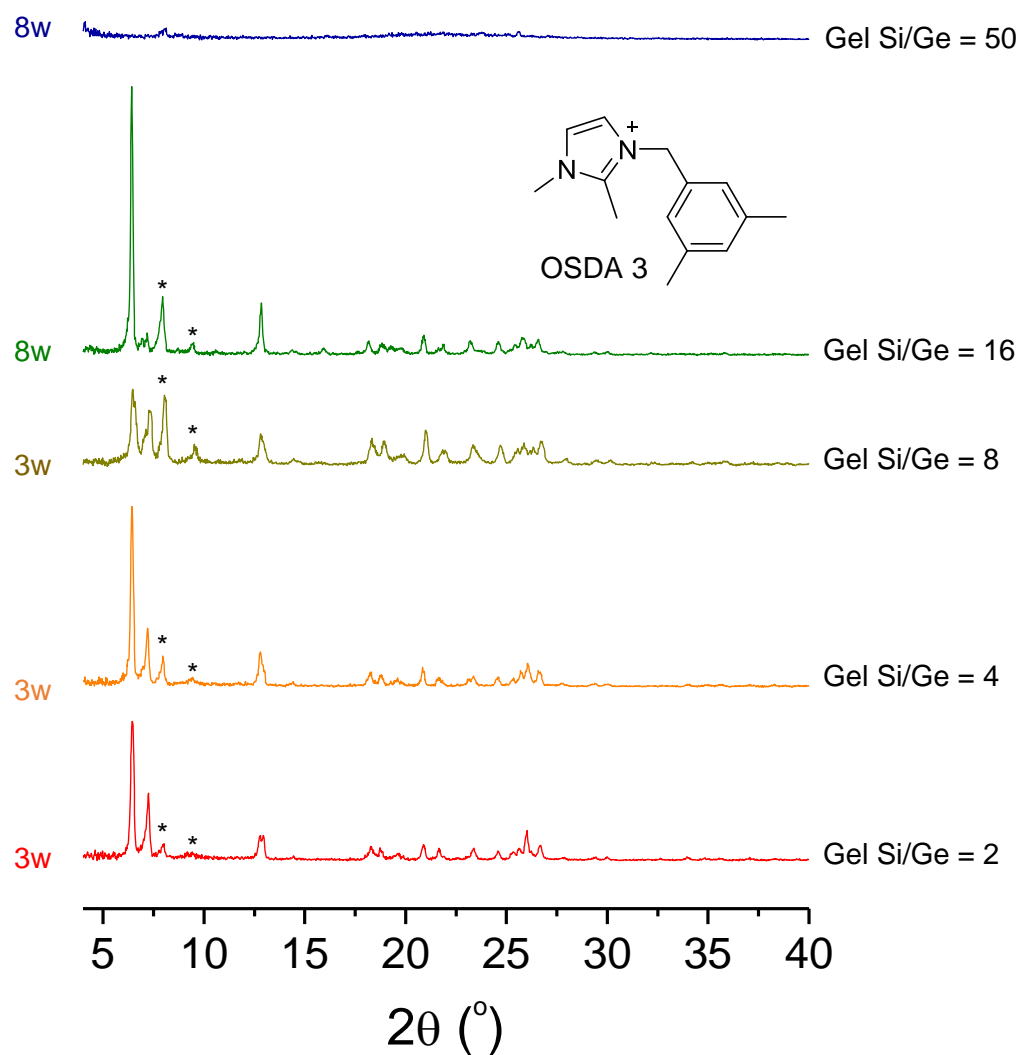


Figure B9. XPD patterns of germanosilicate samples that crystallized in the presence of **OSDA 3** and different Si/Ge ratios and in the gel (*: impurity; w: week).

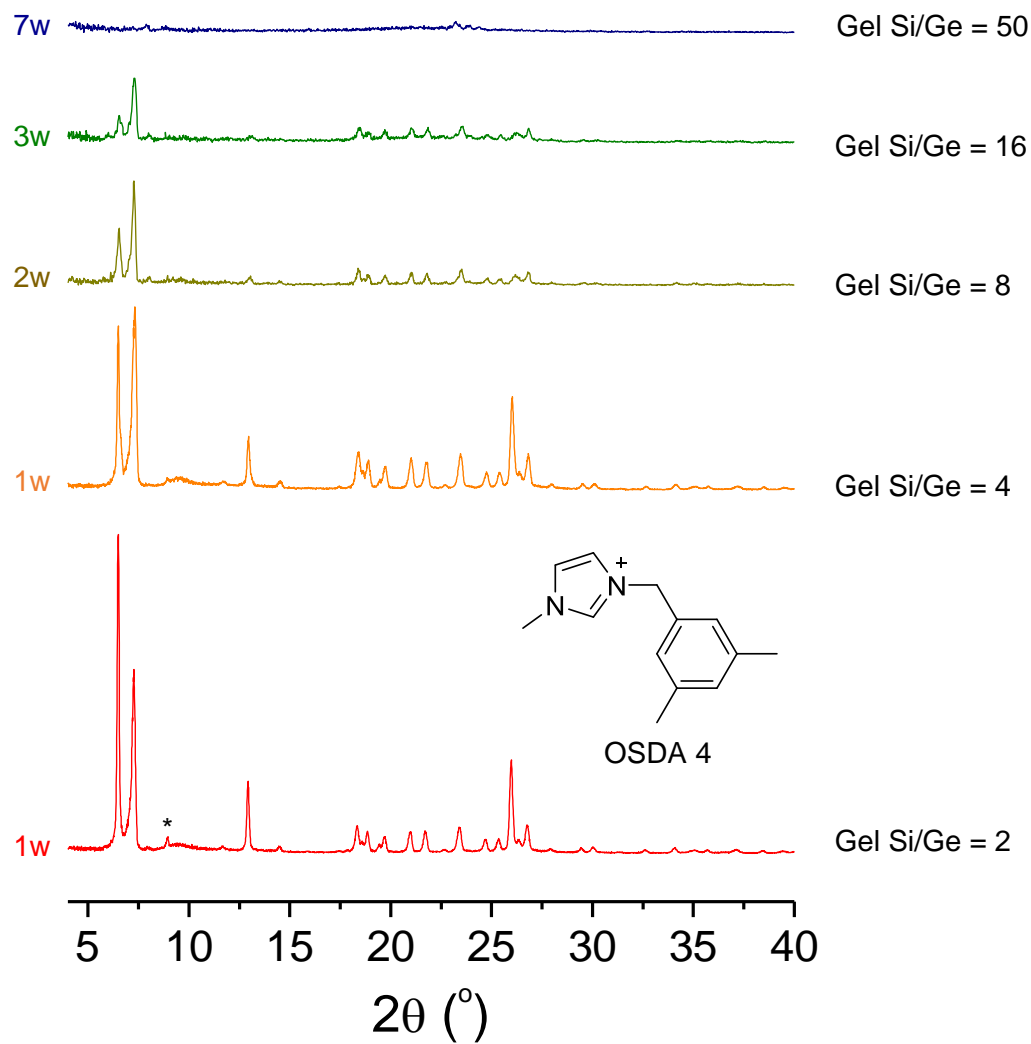


Figure B10. XPD patterns of germanosilicate samples that crystallized in the presence of **OSDA 4** and different Si/Ge ratios and in the gel (*: impurity; w: week).

Table B4. Summary of hydroxide-based CIT-13 synthesis conditions and results. ($x/(x+1)$ SiO_2 : $1/(x+1)$ GeO_2 : 0.5 ROH : y H_2O)

Sample	x	Si-source	ROH-type	y	T (°C)	Oven Type	Time (days)	Result [†]
1	2	TEOS	Ortho*	7.0	175	Rotating	14	P
2	2	TEOS	Ortho	10.0	175	Rotating	21	I
3	2	TEOS	1	7.0	175	Rotating	14	I
4	4	TEOS	1	7.0	175	Rotating	14	P
5	3	TEOS	1	7.0	175	Rotating	14	I
6	3	TEOS	1	7.0	175	Rotating	14	I
7	3	TEOS	1	7.0	175	Static	14	I
8	2	TEOS	1	7.0	175	Rotating	14	I
9	2	TEOS	1	7.0	175	Static	14	P
10	3	TEOS	1	6.0	160	Rotating	42	P
11	3	TEOS	1	6.5	160	Rotating	42	P
12	3	TEOS	1	7.5	160	Rotating	42	A
13	3	Cab-O-Sil	1	7.0	160	Rotating	14	P
14	3	Cab-O-Sil	1	6.0	160	Rotating	14	P

* “Ortho” is 1,2-dimethyl-3-(2-methylbenzyl)imidazolium hydroxide. [†]CIT-13 purity index: P = pure, I = impure, A = amorphous The purity of the products were assessed based on the PXRD patterns.

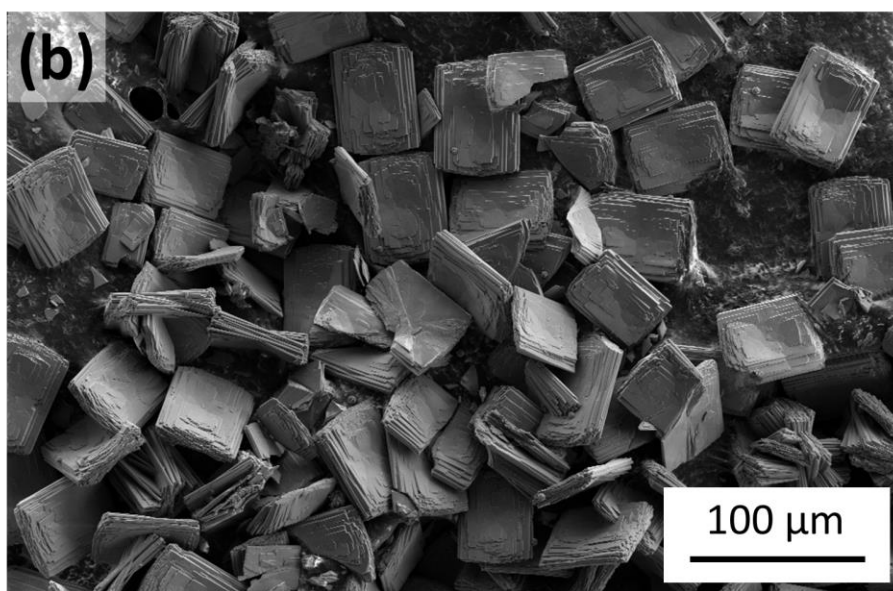
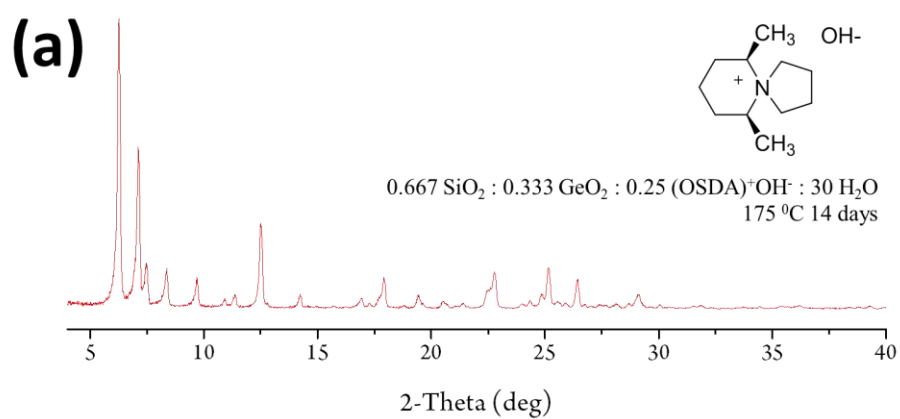


Figure B11. (A) An XPD pattern and (B) SEM image of a sample of the germanosilicate IM-12 synthesized in hydroxide medium (UTL framework type). The Si/Ge ratio was determined using EDS to be 4.5. This sample was used for comparison with CIT-13.

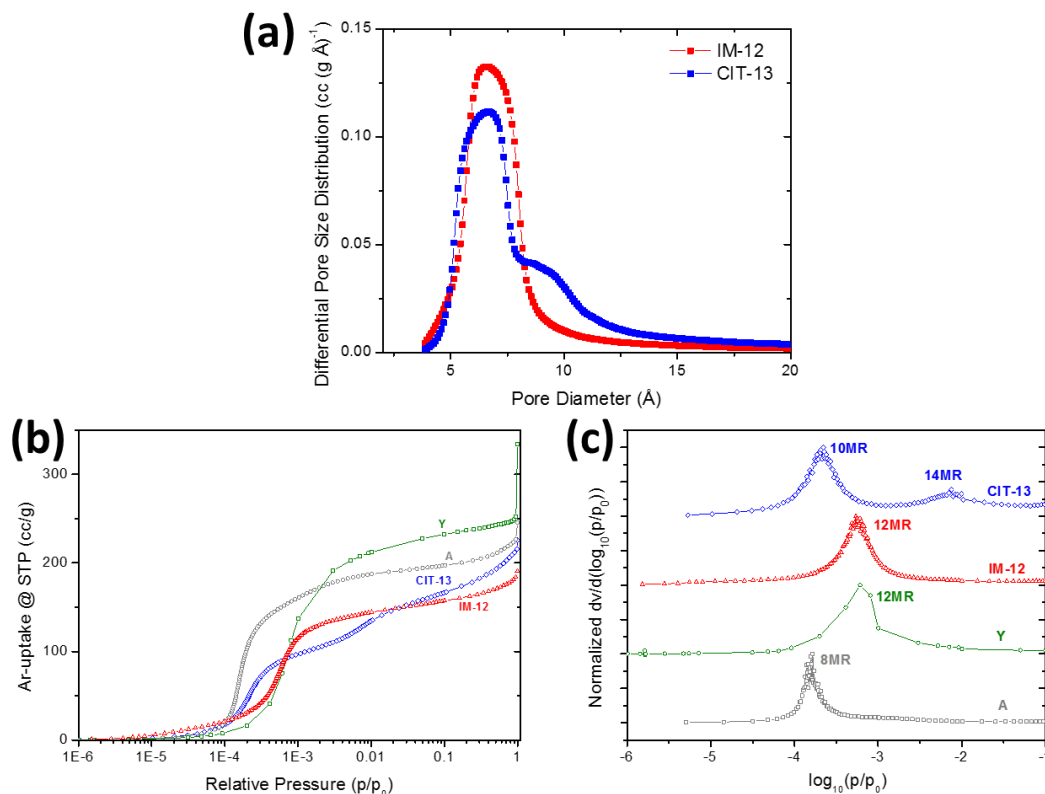


Figure B12. Porosity characterizations of CIT-13 and IM-13. (a) The Saito-Foley pore size distribution derived from the argon adsorption isotherm shown in Figure 8. (b) The log-plot of the Ar-isotherms of CIT-13, IM-12, zeolite Y and zeolite A. (c) The normalized differentiated log-plot of isotherms in (b) to allow a qualitative comparison. *Zeolite Y and Zeolite A data courtesy of Dr. Joel E. Schmidt.*

Since the small micropores are filled with argon atoms at a lower pressure than the large micropores, the position at which the inflection point in the log-plot is observed allows the pore size to be estimated qualitatively. For zeolite A (LTA) and zeolite Y (FAU), the inflection points are observed at $p/p_0 = 10^{-3.80}$ and $10^{-3.22}$ (Figure S13B and C), and these

correspond to 8-rings and 12-rings, respectively. IM-12 (UTL) shows the inflection point at $p/p_0 = 10^{-3.26}$, which is very close to that of zeolite Y, so this inflection point was assigned to 12-rings in IM-12. CIT-13 was the only framework that showed two inflection points. The first was observed at $p/p_0 = 10^{-3.66}$ and assigned to the 10-rings and the second at $p/p_0 = 10^{-2.13}$ to the 14-rings. This second inflection point corresponding to 14-ring was not observable in IM-12.

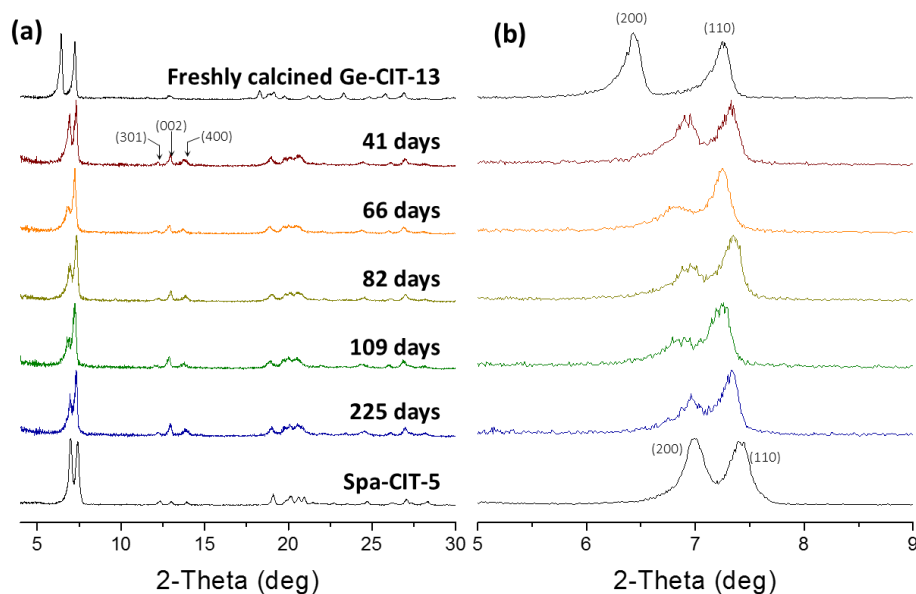


Figure B13. Transformation of Ge-CIT-13/F[4.11] to Ge-CIT-5 over time observed on the basis of PXRD patterns in 2-theta scanning ranges of (a) 4–30° and (b) 5–9°.

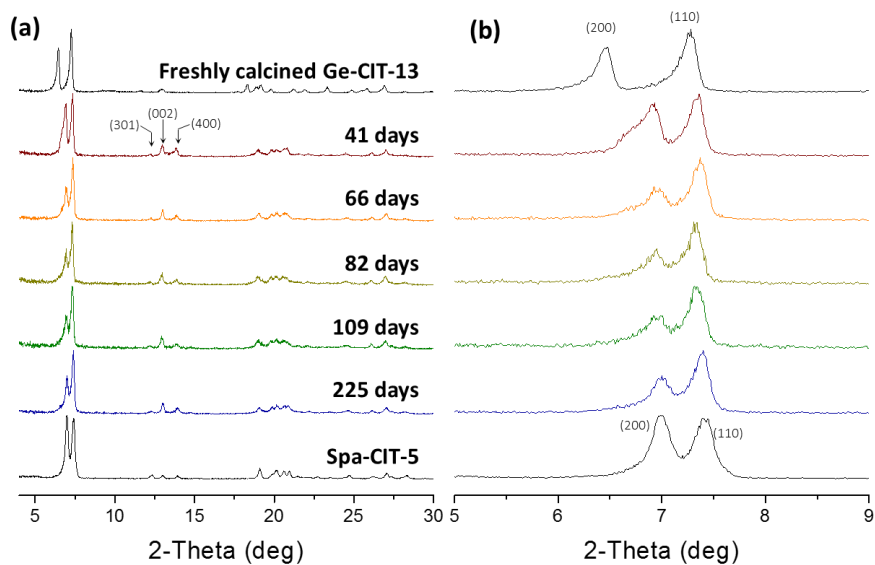


Figure B14. Transformation of Ge-CIT-13/F[4.22] to Ge-CIT-5 over time observed on the basis of PXRD patterns in 2-theta scanning ranges of (a) 4–30° and (b) 5–9°.

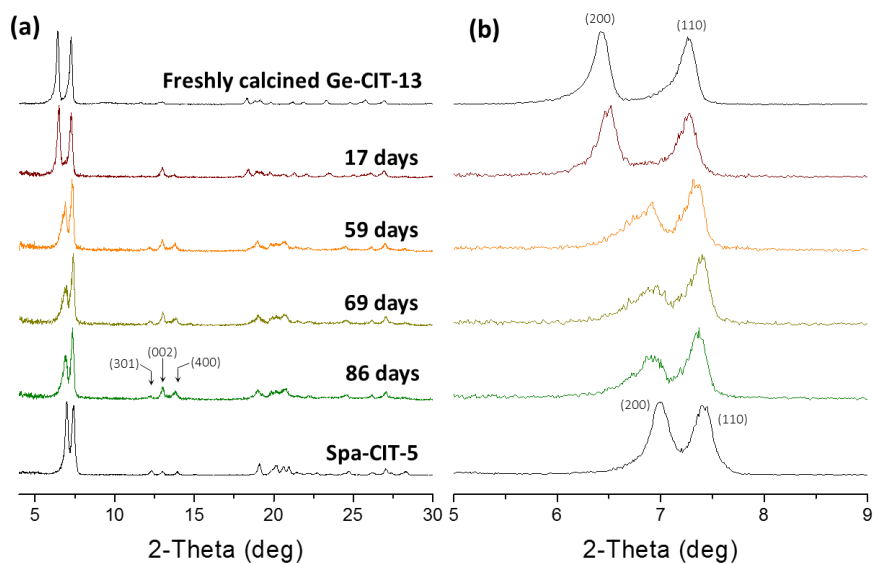


Figure B15. Transformation of Ge-CIT-13/F[4.27] to Ge-CIT-5 over time observed on the basis of PXRD patterns in 2-theta scanning ranges of (a) 4–30° and (b) 5–9°.

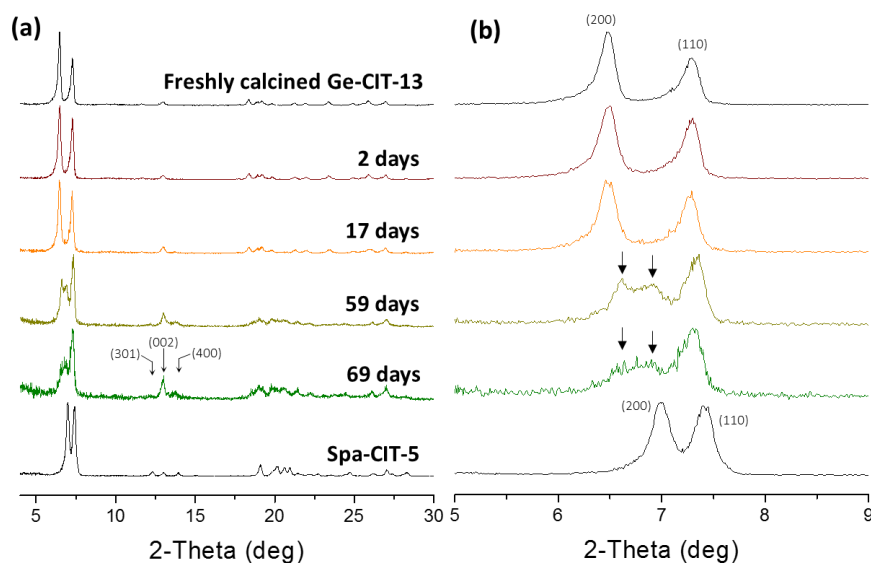


Figure B16. Transformation of Ge-CIT-13/F[4.65] to Ge-CIT-5 over time observed on the basis of PXRD patterns in 2-theta scanning ranges of (a) 4–30° and (b) 5–9°.

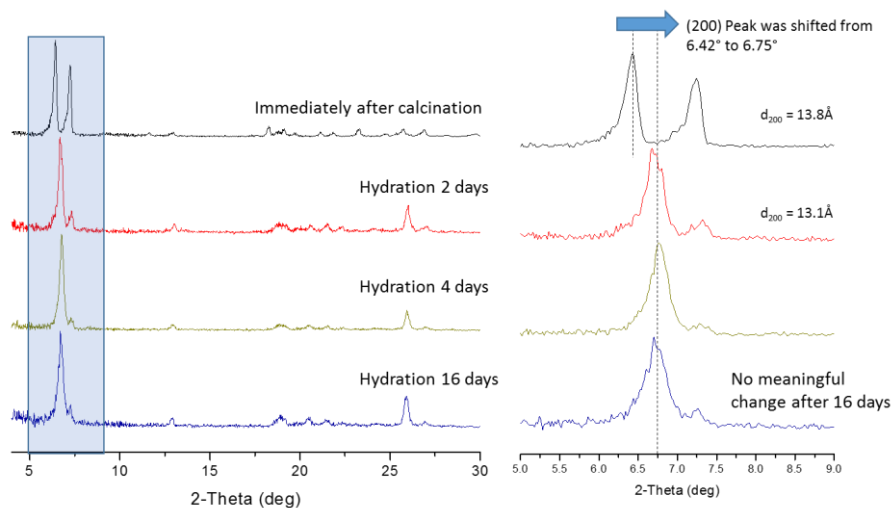


Figure B17. Structural change of Ge-CIT-13/F[4.31] upon extended exposure to saturated water vapor.

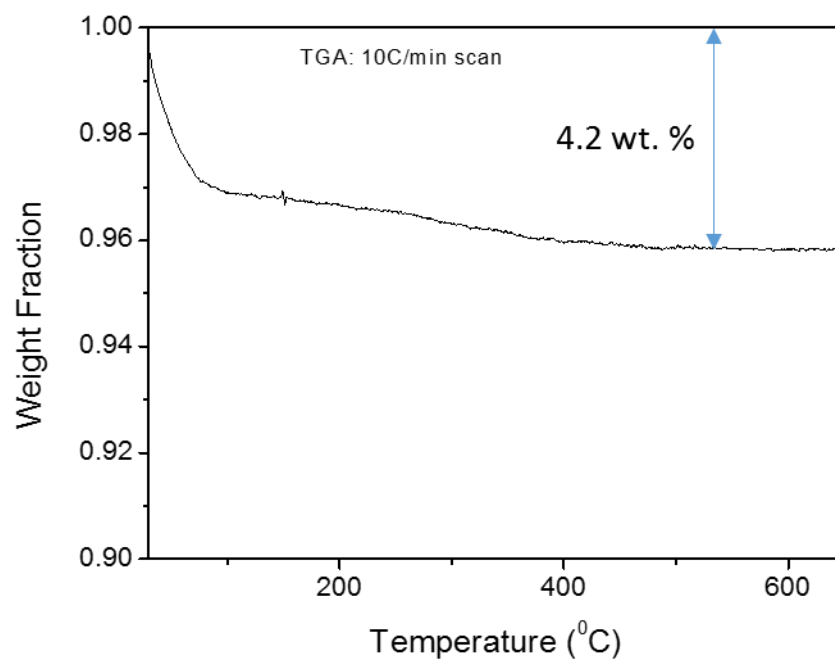


Figure B18. TGA profile of Ge-CIT-5 produced by exposing calcined Ge-CIT-13/F[4.31] to an ambient atmosphere for 4 months.

Table B5. Collection of all T-O-T angles of *CTH and CFI, and estimated positions and multiplicities of ^{29}Si NMR signals calculated using the empirical model by Thomas et al. (1983) which is visualized in Figure 7.15(b).

	M	T-O-T angles (CIT-13)				Average	Expected
		θ_1	θ_2	θ_3	θ_4	θ_{avg}	(ppm)
T1 (d4r)	16	140.3228	142.2268	150.8837	127.6139	140.2618	-106.694
T2 (reclusive)	8	173.5357	179.6750	169.2013	169.2013	172.9033	-125.603
T3 (channel)	16	164.4319	161.9671	169.2013	127.6139	155.8036	-115.697
T4 (channel)	8	180	143.2463	161.9672	161.9672	161.7952	-119.168
T5 (channel)	4	178.5357	178.5357	143.2463	143.2463	160.891	-118.644
T6 (channel)	8	180	143.0414	164.4319	164.4319	162.9763	-119.852
T7 (channel)	4	179.6750	179.6750	143.0414	143.0414	161.3582	-118.915
	M	T-O-T angles (CIT-5)				Average	Expected
		θ_1	θ_2	θ_3	θ_4	θ_{avg}	(ppm)
T1 (dzc)	16	144.6096	164.3356	164.3356	137.4945	152.6938	-113.896
T2 (reclusive)	8	179.9785	179.9785	169.4620	169.4620	174.7203	-126.655
T3 (channel)	16	169.4620	165.4495	165.4495	144.6095	161.2426	-118.848
T4 (channel)	16	144.4710	180	165.4495	165.4495	163.8425	-120.354
T5 (channel)	8	179.9785	179.9785	144.4710	144.4710	162.2248	-119.417

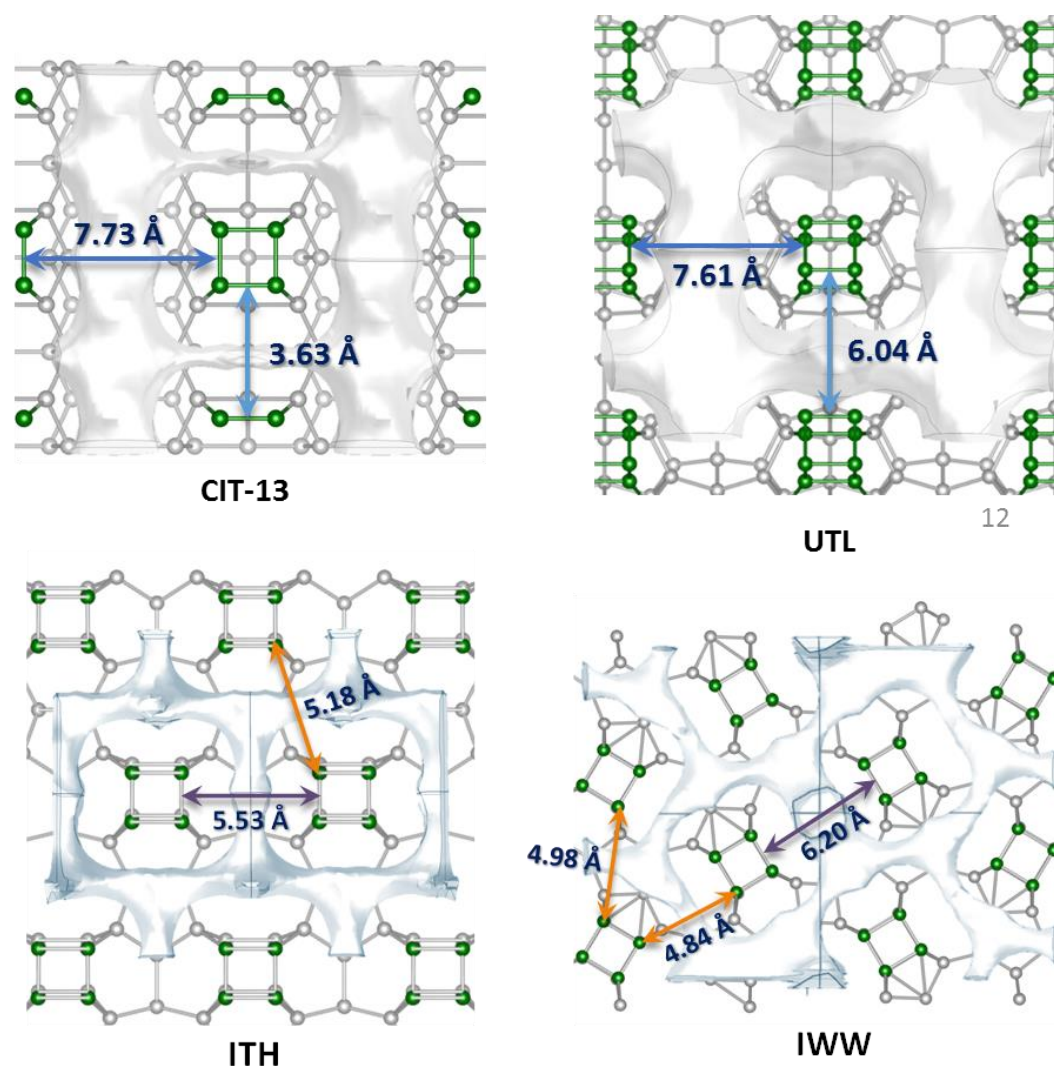


Figure B19. Channel structures and geometric arrangements of $d4r$ units of studied germanosilicates.

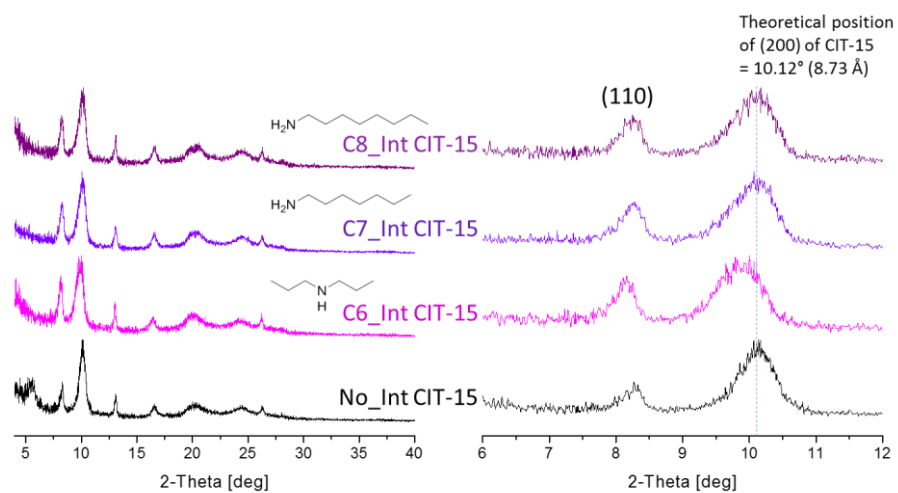


Figure B20. Reassembly abilities of various aliphatic amines for the condensation of CIT-13P to CIT-15 investigated on the basis of PXRD patterns.

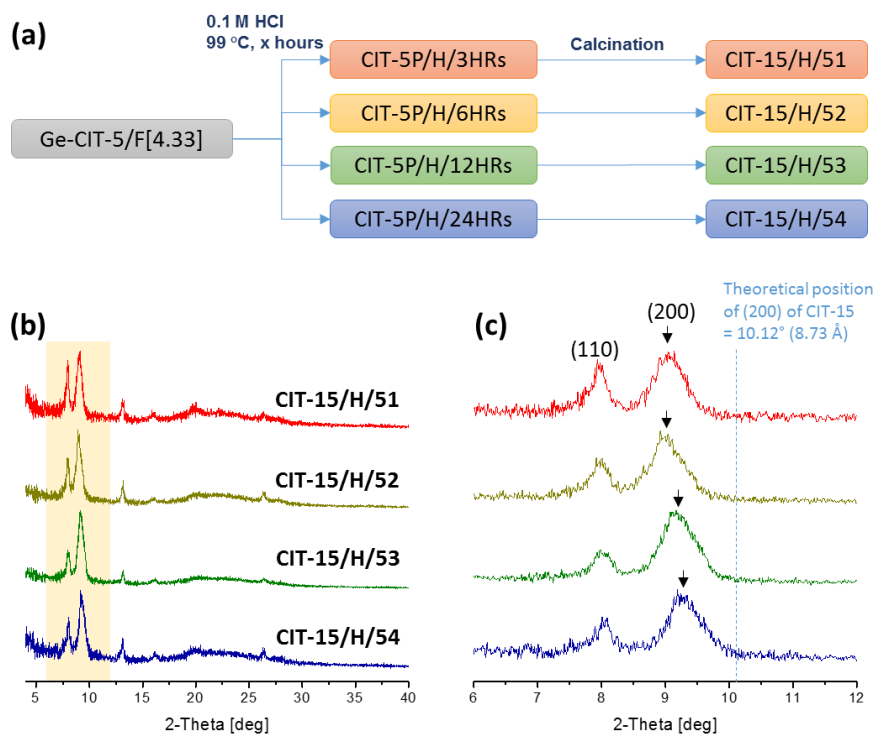


Figure B21. Influence of degree of delamination of Ge-CIT-5 on the formation of CIT-15-like layered materials (a) Design of experiment. PXRD patterns of the resultant layered materials in the range of (b) 4–40° and (d) 6–12°.